Doctoral Thesis

Quantum State Control of Two Interacting Rydberg Atoms

A dissertation
submitted in fulfillment of the requirements for the degree of
Doctor of Philosophy in Physics
by

Ankita Niranjan

IISER PUNE

Department of Physics
Indian Institute of Science Education and Research
Pune 411 008, India.
2021

© Ankita Niranjan All rights reserved. 2021.

Dedicated to my Mummi, Papa & Bhaiya

"Nothing in life is to be feared, it is only to be understood. Now is the time to understand more, so that we may fear less."

— *Marie Salomea Skłodowska Curie*

DECLARATION

I, **Ankita Niranjan**, declare that this written submission entitled "**Quantum State Control of Two Interacting Rydberg Atoms**" represents my idea in my own words and where others' ideas have been included; I have adequately cited and referenced the original sources. I also declare that I have adhered to all principles of academic honesty and integrity and have not misrepresented or fabricated or falsified any idea/data/fact/source in my submission. I understand that violation of the above will be cause for disciplinary action by the Institute and can also evoke penal action from the sources which have thus not been properly cited or from whom proper permission has not been taken when needed. The work reported in this thesis is the original work done by me under the guidance of Dr. Rejish Nath.

Ankita

Ankita Niranjan

CERTIFICATE

I certify that the thesis entitled "**Quantum State Control of Two Interacting Rydberg Atoms**" presented by **Ms. Ankita Niranjan** represents her original work which was carried out by her at IISER, Pune under my guidance and supervision during the period from 01 Aug, 2014 to 6 September, 2021. The work presented here or any part of it has not been included in any other thesis submitted previously for the award of any degree or diploma from any other University or institutions. I further certify that the above statements made by her in regard to her thesis are correct to the best of my knowledge.

Dr. Rejish Nath

Contents

Acknowledgements xv

List of Publications xix

Abstract xxi

Symbols & abbreviations xxiii

List of Figures xxiii

1 Introduction 1

1.1 Ultracold Rydberg atoms 4
1.1.1 Properties of Rydberg atoms 5
1.2 Rydberg-Rydberg Interactions 9
1.3 Rydberg Blockade 10
1.4 Quantum Dynamics 12
1.4.1 Rabi Dynamics 13
1.4.2 Quench Dynamics and LZ transitions 14
1.4.3 Dynamical stabilization in a periodically driven two-level atom 18
1.5 Quantum Correlations 20
1.6 Issues covered in this thesis 24

2 Dynamics and quantum correlations in two independently driven Rydberg Atoms 27

2.1 Introduction 27
2.2 Setup and Model 28
2.3 State Population Dynamics 30
2.3.1 Populations at large interaction strengths 30
2.3.2 Populations at small interaction strengths 31
2.4 Effective Hamiltonians 35
2.5 Entanglement Dynamics 42
2.6 Dissipative dynamics: Steady-states and quantum discord 45

2.7 Conclusion and outlook . . . 51

3 Landau-Zener transition dynamics under linear quench 53

3.1 Introduction . . . 53
3.2 Eigenspectrum of two Rydberg atoms . . . 55
3.3 Different LZ Models . . . 56
3.4 LZ dynamics for different initial states . . . 58
    3.4.1 Initial state: $|\psi(t_i)\rangle = |1\rangle$ . . . 59
    3.4.2 Initial state: $|\psi(t_i)\rangle = |2\rangle$ . . . 65
    3.4.3 Initial state: $|\psi(t_i)\rangle = |3\rangle$ . . . 67
3.5 Adiabatic Impulse approximation . . . 69
3.6 Summary and outlook . . . 72

4 Landau-Zener transition and adiabatic impulse approximation in a periodically driven pair of Rydberg atoms 75

4.1 Introduction . . . 75
4.2 Periodically driven single two-level atom . . . 76
    4.2.1 Time-evolution under AIA . . . 78
    4.2.2 Comparison with Multi-slit interference Pattern . . . 82
4.3 Periodic modulation in two-atoms . . . 83
    4.3.1 Case 1: $\delta = V_0/4 - \Delta_0$ . . . 86
    4.3.2 Case 2: $\delta = 3V_0/4 - \Delta_0$ . . . 89
    4.3.3 Case 3: $\delta = 5V_0/4 - \Delta_0$ . . . 93
4.4 Summary and outlook . . . 94

5 Population trapping in a pair of Rydberg atoms 97

5.1 Introduction . . . 97
5.2 Setup, Model, and Techniques . . . 98
    5.2.1 Effective Hamiltonian . . . 99
    5.2.2 Floquet Theory . . . 100
5.3 A two-level atom ($N = 1$) . . . 102
5.4 Two-atom chain . . . 105
    5.4.1 Resonances . . . 105
    5.4.2 Dynamical stabilization of product states . . . 107
    5.4.3 Dynamical stabilization of maximally entangled Bell states . . . 115
5.5 Experimental Parameters . . . 118
5.6 Summary . . . 120

6 Summary and Outlook 121

A Steady State Results **125**

A.1 Analytical results for the steady state density matrices and purity of the system and subsystems . . . 125

B Underlying Group Symmetries **127**

B.1 Two-level system and SU(2) . . . 127

B.2 Three level system and SU(3) . . . 128

B.2.1 SU(3) . . . 128

B.2.2 LZT matrix . . . 129

Bibliography **131**

Acknowledgements

I am thankful to many people for the successful completion of my PhD thesis. First, I am thankful to my mother, my father, and my brother for their unconditional and unwavering support through all my journeys, for never giving up on me, for nurturing curiosity in me, and for reminding me of my strengths time and again. I extend my thanks to my sister in-law for bringing a bright presence in our lives.

I owe my gratitude to my PhD supervisor, Dr Rejish Nath for his guidance across the various projects. His extensive knowledge and persuasion helped in writing the papers included in the thesis. I thank my collaborators Dr Weibin Li and Dr Sebastian Wüster for useful discussions and feedback. I am grateful to my collaborators Kumar and Vineesha whose contribution to our research work is invaluable. I extend my gratitude to my RAC members, Prof Bhas Bapat and Dr Arun Thalapilil for broadening the perspective in physics, and inspecting the thesis progress throughout the years. I heartfully thank Bhas Sir for his constant encouragement, support, feedback, and discussions on physics and career.

I would like to thank IISER Pune for providing me with the opportunity to conduct research in physics. The earlier and present Directors, Dr K.N. Ganesh and Dr J. Udgaonkar, have brought a beautiful campus to life and created a nurturing environment. I am also thankful to the institute for my fellowship during the early years of my Int. PhD from Aug-2014 to Oct-2018, and to UGC-CSIR for my fellowship since Nov. 2018. I thank the Dept. of Physics, IISER Pune for travel support during conferences. I am also thankful to OIST, Okinawa for full funding to attend the workshop in Coherent Quantum Dynamics. I am thankful to UGC-UKIERI and Dr Weibin Li for a fruitful research visit to the University of Nottingham, UK.

I further extend my gratitude to Sayalee ma'am and Tushar Sir from the administrative office who took care of fellowship documents, and Prabhakar and Dhanashree ma'am from the physics office who helped in other official work go smoothly.

I would like to thank all past and present group members of our Theoretical Atom Optics group: Chinamyee, Yashwant, Supriti, Dhiya, Ratheejit, Sandra, Kumar, Komal, Banibrata, Jugal, Sagarika, Gopal, Vighnesh, Pranay, Chirag, Gautam, Ashwath and others for the useful discussions during weekly group meetings. Among these, I am especially grateful to my officemates Yashwant and Chinmayee. Yash-

want, for his many insightful discussions on Rydberg physics and applications, for being there during my frustrations, and most of all for inspiring a career outside of Physics in Finance. Chinmayee, for helping me through various stages in my PhD and for being a great companion. Her in-depth knowledge of BEC, creativity in presentations, and digital artistry is inspiring. Be it heated discussions on social topics, movie nights, dressed-up dinners, photoshoots, shopping, or getaways, these guys were a constant and amazing company to have. I am also grateful to our past group members. Supriti has been a clear-hearted and thoroughly supportive friend; her perseverance and rise beyond social stigma have taught me to do the same. Jugal, our BS-MS colleague and a social butterfly, has presented a different unstigmatized outlook during our discussions; and Komal has taught me to embrace the introvert in me.

My friends at IISER have been very crucial pillars of emotional support and encouragement for me. I am grateful to have found Tejal and I profoundly enjoyed our morning walks and cooking time which were interspersed with discussions on physics and life, alike. Her unconditional friendship and perspectives make my life richer in every way. I would like to thank Deepak for showing his insightful support during difficult times. I cherish the incredible amount of time I have spent with him. Be it Diwali, Holi, national holidays, or our many trips to Reliance Mart, shopping malls, countless dine-ins and dine-outs, group outings, Ral's fitness regimen, gym/badminton sessions, or inputs during my comprehensive, RAC or pre-synopsis; he made it easier/bearable, and fun. I am thankful to Mayur for being an avid listener during my PhD, for converting me to a dog-lover, for being my badminton partner, and for his appreciation towards the simple joys of life. He is equal parts adorkable and wise. I sincerely express my gratitude to them for standing with me through the ups and downs of this wondrous journey. I want to thank Sumit for indulging me with his joyful singing from an enormous list of old Hindi songs. It has been an incredible journey at IISER with this amazing bunch.

I would also like to thank my old friends Nikita, Priyanka, Surbhi, Raaisa; my school friends; my IISER batchmates Sayali, Punita and others, and my mama, mami and mausi who keep me rooted and give me a broader perspective. Many thanks are due to my school teachers: Awasthi Sir, Sanjay Sir, Tripathi Sir, and coaching teachers: Rajora Sir, AG Sir, VJ Sir who encouraged me to pursue science. I am also thankful to my professors from IIT-D: Dr P. Srivastava, Dr Santanu Ghosh, Dr R.K. Soni, and to Dr M.H. Modi, RRCAT who gave me exposure to research.

I further extend my gratitude to hostel managers Ramlal Sir and Irfana ma'am for taking care of our living arrangements, Santosh Sir from Gym, and Ral (LivEzy) for their fitness course. I am grateful to have had IISER sports facility, IISER counsellors, IC, and medical staff dedicated to students. I am also thankful for our mess, Shivsagar, and MDP canteen staff for their catering services. I also thank our housekeeping and security staff who keep the campus clean and safe. In the end, I would like to thank arXiv, Wikipedia, Stack Exchange, Coursera, and edX for making knowledge accessible to everyone.

List of Publications

1. Vineesha Srivastava, **Ankita Niranjan**, and Rejish Nath, Dynamics and quantum correlations in two independently driven Rydberg atoms with distinct laser fields. J. Phys. B: At. Mol. Opt. Phys. **52** 184001 (2019)
2. **Ankita Niranjan**, Weibin Li, and Rejish Nath, Landau-Zener transitions and adiabatic impulse approximation in an array of two Rydberg atoms with time-dependent detuning. Phys. Rev. A **101**, 063415 (2020).
3. S. Kumar Mallavarapu, **Ankita Niranjan**, Weibin Li, Sebastian Wüster, and Rejish Nath, Population trapping in a pair of periodically driven Rydberg atoms. Phys. Rev. A **103**, 023335 (2021).

Abstract

The field of ultracold Rydberg atoms has made enormous progress in recent years and emerges at the forefront to probe quantum properties of matter. Individually controlled Rydberg atoms prove to be a versatile platform to test phenomena significant to condensed matter physics, quantum optics, atomic and molecular physics. Systems of many-body interacting Rydberg atoms have an enormous potential to solve long-standing problems in physics. On the other hand, the interest in two-body Rydberg systems is motivated by applications of local quantum control and deterministic local state preparation in a larger array. Our work pertains to manipulating the state dynamics of the two-atom system which is achieved by tuning the atom-light couplings and detunings, both in weakly and strongly interacting systems.

First, we investigate the effect of an offset in Rabi coupling between two Rydberg atoms both in coherent and dissipative systems. The interplay of Rabi frequency offset and tunable interactions reveals fascinating features. In the strongly interacting regime, we find a novel phenomenon of Rydberg-biased freezing where amplification of the Rabi frequency of one atom suppresses the dynamics in the second atom. In the weak interaction regime, we discuss the double excitation dynamics as a function of interaction for very small offsets in the Rabi frequencies. We further propose a dynamic control over quantum correlations upon dynamic variation of the Rabi frequency of the second atom.

In the second part of the thesis, we use time-dependent atom-laser detuning to manipulate collective quantum states. We first consider a linear variation of the detuning. We observe that for different values of Rydberg-Rydberg interaction, the system can emulate different three-level Landau-Zener models such as bow-tie and triangular Landau-Zener models. Our central result is that Landau-Zener excitation dynamics exhibit nontrivial dependence on the initial state, the quench rate, and the interaction strengths. We further use analytical techniques such as Adiabatic Impulse approximation in the strongly interacting regime to capture the non-trivial dynamics.

In the last section, we consider the application of periodic atom-laser detuning on the pair of Rydberg atoms. We review the single two-level periodically driven atom and highlight the similarity of the final state population with the intensity pattern obtained in an antenna array. We further use a single atom to characterize the phenomenon of population trapping and dynamical stabilization using Floquet quasienergies and the Inverse participation ratio. In the two atom setup, we test the validity of the Adiabatic Impulse approximation under periodic driving.We further explain the interesting phenomenon of a state-dependent population trapping that emerges due to Rydberg-Rydberg interactions. We specify the regimes where populations in experimentally significant states such as product and Bell entangled states can be frozen for a significantly longer duration.

This thesis is a study of the manipulation of coherent dynamics of a setup of two two-level Rydberg atoms. We achieve the above goal by tuning the atom-light couplings and detunings, both in weakly and strongly interacting systems. Our study shows that the minimal setup can be used to create non-trivial dynamics and exert local control, or as an atom-interferometer. Our investigations also serve as a building block that can be extended to multi atom setups.

Symbols & abbreviations

Physical Constant

$\hbar$ - Planck's constant

ϵ_0 - Vacuum permittivity

Abbreviations

RRI - Rydberg-Rydberg Interactions
vdW - Van der Waals
LZ - Landau-Zener
LZT - Landau Zener Transition
AIA - Adiabtaic impulse approximation
DS - Dynamical Stabilization
SU(n) - Special Unitary Group of $n \times n$

List of Figures

1.1 Radial probability density $r^2|R(r)|^2$ and (red) the expectation value $\langle r \rangle = \langle \phi_{n,l,m}|r|\phi_{n,l,m}\rangle$ of (a) $5S_{1/2}$ (ground state) with $\langle r \rangle = 5.3a_0 \sim 3$ Å and (b) $100S_{1/2}$ (a Rydberg state) having $\langle r \rangle = 14075a_0 \sim 0.7$ μm for ^{85}Rb atom. Figures obtained using ARC library [107]. 7

1.2 Schematic representation of energy levels of two atoms, each of which their ground state coupled to Rydberg state with Rabi frequency Ω (for more details, see Sec. 1.4.1). The energy of $|rr\rangle$ state is a function of the distance between atoms (R) in the van der Waals regime varies as C_6/R^6 . Ω is the excitation linewidth caused by the power broadening of the light field. (a) When the separation between atoms is large, a complete transition to $|rr\rangle$ is possible. (b) When the separation is smaller than R_b, it leads to a 'blockade' of $|rr\rangle$ excitation. A corroborative dynamics is shown in Fig. 1.3. 10

1.3 The population dynamics in $|gg\rangle, |+\rangle$ and $|rr\rangle$ states. (a) For $V_0 = 0$, the state $|rr\rangle$ gets populated via $|+\rangle$ state. (b) When $V_0/\Omega = 10$, it causes a blockade of double excitation and results in coherent population transfer between $|gg\rangle$ and entangled state $|+\rangle$. The oscillation frequency is enhanced to $\sqrt{2}\Omega$. 11

1.4 A two-level atom. The two energy levels are separated by a transition with frequency ω_{gr}. The atom is driven by a monochromatic field of frequency ω. Two key parameters govern the dynamics of the atom-light interaction - the detuning $\Delta = \omega - \omega_{gr}$, and the Rabi frequency Ω which describes the strength of the atom-field coupling. 13

1.5 Time evolution of population in the ground and excited state. (a) Rabi dynamics of a single two-level atom at resonance ($\Delta = 0$). The population of ground state transfers coherently to excited state and oscillate with a time-period $2\pi/\Omega$. (b) The Rabi dynamics with detuning $\Delta/\Omega = 1.5$. A finite detuning results in an imperfect population transfer within a Rabi cycle with a shorter time-period $2\pi/\bar{\Omega}$. For a large enough detuning, the population effectively remains trapped in the initial state. 14

1.6 (a) (Top) The energy values of instantaneous eigenstates (solid red/blue) and diabatic states (dashed-black) corresponding to (Bottom) a linear change of detuning. The energy-gap at avoided-level crossing is equal to the Rabi frequency Ω. (b) (Top) The inverse of energy gap between adiabatic energy levels $1/(E_+ - E_-)$ is plotted whilst (Bottom) a transition from ground ($|-\rangle$) to excited state ($|+\rangle$) occurs when subjected to a linear quench in the detuning. The dashed-blue line is obtained from AIA model [Eq. (1.22)] where an impulse transition is approximated at avoided-level crossing. 16

1.7 Stable and unstable equilibrium positions of (a) simple normal pendulum (b) periodically driven Kapitza or inverted pendulum. The usual position of unstable equilibrium can be stabilized with periodic driving. 19

1.8 (a) Detuning is periodicaly varied across the avoided level crossing in a two-level atom, as $\Delta(t) = \Delta_0 + \delta\sin(\omega t)$ where Δ_0 is the initial detuning, δ is the strength and ω is the frequency of modulation (b) The populations of ground and excited states for periodically varying detuning with $\Delta_0 = 0, \omega/\Omega = 6.0, \delta/\omega = 2.404$. 20

1.9 Quantum Mutual Information: $\mathcal{I} = \mathcal{S}_A + \mathcal{S}_B - \mathcal{S}_{AB}$ where $\mathcal{S}_A$ ($\mathcal{S}_B$) is the Von Neumann entropy of the subsystem A (B), and $\mathcal{S}_{AB}$ is the joint entropy of A and B. 22

2.1 A schematic of two Rydberg atoms trapped in distinct microtraps with a separation of R. Each of the atoms is driven independently by different laser fields while resonantly coupling the ground state $|g\rangle$ to the same Rydberg state $|r\rangle$. 29

2.2 The figure shows energy level scheme of composite two-atom system in the product basis $\{|gg\rangle, |gr\rangle, |rg\rangle, |rr\rangle\}$ with their associated Rabi couplings. The doubly excited state $|rr\rangle$ is populated from ground state $|gg\rangle$ via $|gr\rangle$ and $|rg\rangle$ as shown by curved arrows. V_0 is the Rydberg-Rydberg interaction which detunes the $|rr\rangle$ state from resonance. 29

2.3 The population dynamics for strongly interacting case $V_0/\Omega = 10$ with (a) small Rabi-offset $\omega/\Omega = 0.5$ which causes asymmetry in P_{gr} and P_{rg}, (b) large Rabi-offset $\omega/\Omega = 5$ which freezes the dynamics of state $|rg\rangle$. P_{rr} is suppressed at strong interactions causing Rydberg-blockade. 30

2.4 The time average populations as a function of ω/Ω for $V_0 = 25\Omega$, and $\Omega\tau = 5000$. Since $V_0 \gg \Omega$, the numerical results (solid points) are in excellent agreement with the analytic results (solid lines) given in Eqs. (2.7)-(2.9) 31

2.5 Color density plot for long time averaged populations: (a) $\bar{P}_{gg}$, (b) $\bar{P}_{rr}$, (c) $\bar{P}_{gr}$ and (d) $\bar{P}_{rg}$ plotted against V_0/Ω and ω/Ω conditioned to $|\psi(t=0)\rangle = |gg\rangle$ till time $\Omega\tau = 5000$. For stronger interactions V_0/Ω and large Rabi-offset ω/Ω both $\bar{P}_{rr}$ and $\bar{P}_{rg}$ are negligible, leading to Rydberg-biased freezing. Also note in (b) that the blockade condition only gets weakly affected due to Rabi-offset ω. 32

2.6 The population dynamics for $V_0/\Omega = 0.1$ with (a) a small Rabi-offset $\omega/\Omega = 0.1$ and (b) a large Rabi-offset $\omega/\Omega = 5.0$. For small Rabi-offset, the faster oscillations (having frequency $\sim \Omega$) exist between $|gg\rangle \leftrightarrows |rr\rangle$, and $|gr\rangle \leftrightarrows |rg\rangle$, with a small envelope frequency ($\sim \omega$). For the large Rabi-offset, the faster oscillations with frequency ($\sim \omega$) exist between the strongly coupled states $|gg\rangle \leftrightarrows |gr\rangle$, and $|rg\rangle \leftrightarrows |rr\rangle$, with a faster envelope frequency ($\sim \Omega$), as visible from the time-scale. 33

2.7 The time average populations: (a) $\bar{P}_{gg}$, (b) $\bar{P}_{rr}$, (c) $\bar{P}_{gr}$ and (d) $\bar{P}_{rg}$ as a function of V_0/Ω for different ω/Ω, with $\Delta = \delta = 0$, $|\psi(t=0)\rangle = |gg\rangle$ and $\Omega\tau = 5000$. For very small values of ω/Ω, the populations $\bar{P}_{rr}$, $\bar{P}_{rg}$ and $\bar{P}_{gr}$ depend non-monotonously on $|V_0|$. 34

2.8 The half of the peak separation V_0^P in $\bar{P}_{rr}$ (see inset) as a function of ω/Ω. The dashed line is the analytical result given by Eq. (2.30) obtained for small ω. 35

2.9 The population dynamics of states (a) $|gg\rangle$, (b) $|rr\rangle$ and (c) $|gr\rangle$ from exact numerics (solid lines) and from analytical results (dashed lines) obtained using Eq. (2.21) for $V_0/\Omega = 0.1$. 40

2.10 Comparison of results from exact numerical solution (solid lines) and the effective Hamiltonian $\hat{H}_{eff}^{(\Omega)}$ (dashed line) for $\omega/\Omega = 0.1$. (a) is for the time-averaged populations $\bar{P}_{gg}$ and $\bar{P}_{rr}$ and (b) is for $\bar{P}_{gr}$ and $\bar{P}_{rg}$. 42

2.11 The first atom is subsystem A and the second atom is referred to as subsystem B. When interacting, the joint system state is no longer a simple tensor product of subsystems A and B. 43

2.12 (a)-(e) The time evolution of the entanglement entropy $\mathcal{S}_A(t)$ obtained from the reduced density matrix of the first atom for different ω/Ω and V_0/Ω corresponding to the coherent dynamics discussed in the Sec. 2.3. In this case $\mathcal{S}_A$ is same as the discord $\mathcal{D}$. The values of ω/Ω and V_0/Ω are indicated in the left and top sides respectively. 44

2.13 The maximum of $\mathcal{S}_A(t)$ as a function of ω/Ω and V_0/Ω corresponding to the coherent dynamics discussed in the Sec. 2.3. The lower cutoff of $V_0/\Omega = 0.5$ in the vertical axis is because for smaller values, the time taken to attain maximum $\mathcal{S}_A(t)$ becomes extremely large. 45

2.14 (a) The dynamics of $\mathcal{S}_A(t)$ when the Rabi-offset ω is varied in time with $\alpha = 0.1\Omega$ (see text), $V_0/\Omega = 10$ and $\omega_{max}/\Omega = 8$. When ω reaches the maximum, $\mathcal{S}_A(t)$ is significantly suppressed, and is retrieved back to the initial dynamics once ω is brought back to zero. (b) shows the overlap of $|\psi(t)\rangle$ on the states $|gg\rangle$ and $|+\rangle$ for the dynamics shown in (a). 46

2.15 The steady-state populations: (a) ρ_{gg}, (b) ρ_{rr}, (c) ρ_{gr} and (d) ρ_{rg} as a function of ω/Ω and V_0/Ω with $\Gamma/\Omega = 0.1$. 47

2.16 The steady-state purity of the subsystems (a) A and (b) B, and (c) the total system (AB) as a function of ω/Ω and V_0/Ω. (d) shows the purity and the quantum discords as a function of ω/Ω for $V_0/\Omega = 10$ (blockade region). $\Gamma/\Omega = 0.1$ for all figures. In (d) the solid lines are the analytical results given in A.1 and points are from the full numerical calculations for the steady-state purity. Dashed lines show the quantum discords. The open squares show $\mathrm{Tr}\,(\hat{\rho}^2_{\mathrm{A}}) \times \mathrm{Tr}\,(\hat{\rho}^2_{\mathrm{B}})$ which matches to $\mathrm{Tr}\,(\hat{\rho}^2_{\mathrm{AB}})$ at large ω values. 48

2.17 The steady-state quantum discords (a) $\mathcal{D}(B:A)$ and (b) $\mathcal{D}(A:B)$ as a function of ω/Ω and V_0/Ω for $\Gamma/\Omega = 0.1$. For $\omega \neq 0$ we have $\mathcal{D}(B:A) \neq \mathcal{D}(A:B)$. For $\omega = 0$, the correlations maximally saturate at large V_0 due to Blockade, and they start to diminish as ω increases. Discords vanish in the Rydberg-biased freezing regime where the system is described by a product state. 49

2.18 (a) The populations vs time for $\omega/\Omega = V_0/\Omega = 5$ and $\Gamma/\Omega = 0.1$. The inset shows the same for the initial period of time. (b) shows the time evolution of both the quantum discords, and the purity of the total system and subsystems, for the dynamics shown in (a). 50

3.1 Energy eigenvalues E_j as a function of detuning (which varies linearly in time as shown in y-axes) for (a) $V_0 = 0.1\Omega$ and (b) $V_0 = 5\Omega$. The diabatic energy levels are shown by the dashed lines. The level crossings/avoided crossings in (a) form a three-level bow-tie model, and in (b) form a triangular LZ model. The inset in (b) shows the avoided level crossing at $V_0/2$. The asymptotic eigenstates at $t \to \pm\infty$ are given towards the left and right end of the energy level diagrams. (c) shows the energy gaps $\overline{\Delta E}_\alpha = \Delta E_\alpha/\Omega$ at the avoided crossings as a function of V_0. The inset shows the schematic setup for the LZ interferometer in which the first (S_1) and the second (S_2) crossings act as beam splitters. At the last crossing, O mixing takes place. 57

3.2 Multistate Landau-Zener models. (a) The three level bow-tie model, (b) a triangular LZ model (figures adapted from [223]), and (c) a four-level bow-tie model (figure adapted from [246]). 58

3.3 The dynamics of populations in the adiabatic (a)-(b), and the diabatic (c)-(d) states for the initial state $|\psi(t_i)\rangle = |1\rangle \sim |gg\rangle$, $v = (1\Omega^2, 10\Omega^2)$, and $V_0 = 0.1\Omega$. The first LZT takes-place in the vicinity of $t = 0$. The thin arrows show the times around which the second (t_2) and the third (t_3) LZTs occur. Since the LZTs are not resolvable, so a single arrow is shown. The dashed horizontal lines in the right column show the results from the non-interacting model. 60

3.4 The dynamics of populations in the adiabatic (a)-(b) and the diabatic (c)-(d) states for the initial state $|\psi(t_i)\rangle = |1\rangle \sim |gg\rangle$, $v = (1\Omega^2, 10\Omega^2)$, and $V_0 = 10\Omega$. The first LZT takes-place in the vicinity of $t = 0$. The thin arrows show the times around which the second (t_2) and the third (t_3) LZTs occur. The dashed horizontal lines in the bottom row show the results from the non-interacting model. 61

3.5 The final population in (a) $|1\rangle \sim |rr\rangle$, (b) $|2\rangle \sim |s\rangle$ and (c) $|3\rangle \sim |gg\rangle$, after the linear quench, as a function of v and V_0 for the initial state $|\psi(t_i)\rangle = |1\rangle$, $\Delta(t_i) = -10\Omega$, and $\Delta(t_f) = 30\Omega + 10v/\Omega$. 62

3.6 (a) The final population in the adiabatic/diabatic states as a function of v for $V_0 = 0.1\Omega$ with the initial state $|1\rangle \sim |gg\rangle$. (b) The same as in (a) but as a function of V_0 for $v = 2\Omega^2$. The solid lines show exact results, and the filled squares, circles, and triangles are the theoretical prediction for small V_0 in the limit $t_f \to \infty$. 63

3.7 The dynamics of populations in the adiabatic (a)-(b) and the diabatic (c)-(d) states for the initial state $|\psi(t_i)\rangle = |2\rangle \sim |s\rangle$, $v = (1\Omega^2, 5\Omega^2)$, and $V_0 = 0.1\Omega$. The three LZTs are not resolvable in time hence depicted by a single arrow. The dashed horizontal lines in (c) and (d) show the results from the non-interacting model. 65

3.8 The dynamics of populations in the adiabatic (a)-(b) and the diabatic (c)-(d) states for the initial state $|\psi(t_i)\rangle = |2\rangle \sim |s\rangle$, $v = (1\Omega^2, 5\Omega^2)$, and $V_0 = 10\Omega$. The first LZT takes-place in the vicinity of $t = 0$. 66

3.9 The final population in (a) $|1\rangle \sim |rr\rangle$, (b) $|2\rangle \sim |s\rangle$ and (c) $|3\rangle \sim |gg\rangle$, after the linear quench, as a function of v and V_0 for the initial state $|\psi(t_i)\rangle = |2\rangle$, $\Delta(t_i) = -10\Omega$, and $\Delta(t_f) = 30\Omega + 10v/\Omega$. 67

3.10 The dynamics of population in the adiabatic (a)-(b) and diabatic (c)-(d) states for the initial state $|\psi(t_i)\rangle = |3\rangle \sim |rr\rangle$ with different values of v while keeping $V_0 = 10\Omega$. The thin arrows show the times around which the second (t_2) and the third (t_3) LZTs occur. 68

3.11 The final population in (a) $|1\rangle \sim |rr\rangle$, (b) $|2\rangle \sim |s\rangle$ and (c) $|3\rangle \sim |gg\rangle$, after the linear quench, as a function of v and V_0 for the initial state $|\psi(t_i)\rangle = |2\rangle$, $\Delta(t_i) = -10\Omega$, and $\Delta(t_f) = 30\Omega + 10v/\Omega$. 69

3.12 (a) The beats in the dynamics of $P_s(t)$ for $V_0 = 2\Omega$, $v = 5\Omega^2$, and different initial states. (b) The instantaneous energy eigenspectrum for $\Delta(t) = vt$ for large V_0. The adiabatic and non-adiabatic regimes are marked by the operators $\hat{U}_{1,2,3,4}$ and $\{\hat{G}1_{LZ}, \hat{G}2_{LZ}, \hat{G}3_{LZ}\}$. 70

3.13 The final population in the adiabatic/diabatic states as a function of both V_0 and v for the initial state $|1\rangle$ (a)-(b), $|2\rangle$ (c)-(d), and $|3\rangle$ (e)-(f). For the first column, $v = 2\Omega^2$ and for the second column, $V_0 = 2\Omega$. The solid lines show exact results, and the filled squares, circles, and triangles are from AIA. 71

4.1 The top panel shows the instantaneous energy eigenvalues $E_\pm$ and the energy gap at avoided-crossing is Ω. The bottom panel depicts periodic time dependence of $\Delta(t)$. Away from the avoided crossing, adiabatic evolution takes place while at the avoided-crossing, instantaneous impulse transition occurs under the AIA. 77

4.2 (a) (Top) The periodic modulation of $\Delta(t)$ as a function of time. $\tau_{j=0,1,2}$ indicate the instants at which the avoided crossing is encountered during one cycle. (b) (Bottom) The instantaneous energy eigenvalues $E_\pm$ corresponding to the time-dependent detuning. At the avoided crossings, $t = \tau_{2n}(\tau_{2n+1})$ LZT occurs and is described by the operator $\hat{G}_{LZ}(\hat{G}^T_{LZ})$. On either side of the avoided-crossing, an adiabatic evolution takes place which is determined by $\hat{U}_1$ and $\hat{U}_2$. The shaded areas indicates the phase accumulated ($\zeta_\pm$) during the adiabatic evolution. 78

4.3 The transition probability to the excited state as a function of ω when the atom is initially prepared in the ground state for ($\delta = 20\Omega$, $\Delta_0 = 5\Omega$) at $t_i = \pi/2\omega$ after (a) one cycle and (b) 10 cycles. The solid line shows the exact results, and the dashed line is the same but from AIA. In (b), the peak at $\omega/\Omega = 2.5$ corresponds to the resonance $2\omega = \Delta_0$. (c) Interference pattern obtained using AIA: the long-time averaged population in the excited state ($\bar{P}_+$) as a function of Δ_0/Ω and δ/Ω for $\omega = 0.32\Omega$. The density peaks correspond to the resonances, and the solid lines mark the validity of AIA. 81

4.4 The excitation probability after ten cycles as a function of α for $\delta/\Omega = 20$, $\Delta_0 = 0$ and ω is varied. A given α is not associated with a unique value of ω, leading to the scattered points, but bounded by a maximum value of $\sin^2 k\alpha$ shown by the solid line. 82

4.5 The above panel depicts the adiabatic (colored-solid lines) and diabatic (dashed-black lines) energy levels $E_{j=1,2,3}$ plotted as a function of Δ. The energy gap at $\Delta(t) = 0$ is $\Delta E_0 = \Omega'$, at the second avoided-crossing $\Delta(t) = V_0/2$ it is $\Delta E_{V_0/2} = \Omega''$, and for the third one at $\Delta(t) = V_0$ the gap is $\Delta E_{V_0} = \Omega'''$. In the bottom panel, the periodic time-dependence of $\Delta(t)$ is shown. The hollow circles in the bottom panel show the instants at which the corresponding avoided-crossing is traversed. Away from the avoided-crossings, adiabatic evolution takes place while at the avoided-crossing, instantaneous impulse transition takes place in the adiabatic impulse approximation. 85

4.6 (a) The periodic time dependence of the detuning for $\delta = V_0/4 - \Delta_0$. The expected durations for adiabatic evolution are T_a and T'_a. (b) shows the corresponding instantaneous energy eigenvalues. The instants ($\tau_0^{(1)}$, $\tau_1^{(1)}$, $\tau_2^{(1)}$) at which the LZTs occur between states $|1\rangle$ and $|2\rangle$ are shown by shaded stripes. The operators $\hat{U}_j$ and $\hat{G}1_{LZ}$ indicate the adiabatic regimes and the impulse points, respectively. Between the origin and the dashed vertical line, we have one complete cycle. 86

4.7 The numerical results (solid lines) and that of AIA (dashed lines) for P_1 after (a) 10 and (b) 100 cycles, as a function of ω for the initial state $|1\rangle \sim |gg\rangle$, $\Delta_0 = -15\Omega$, $V_0 = 40\Omega$ and $\delta = 25\Omega$. (b) shows that at longer times, AIA deviates from exact dynamics especially, at high ω. 87

4.8 (a) The exact results (solid lines) for $\bar{P}_{1,2}$, and the same from the AIA (dashed lines) over a period of 100 cycles, as a function of ω for the initial state $|1\rangle \sim |gg\rangle$, $\Delta_0 = -15\Omega$, $V_0 = 40\Omega$ and $\delta = 25\Omega$. The dips (peaks) in $\bar{P}_1$ ($\bar{P}_2$) indicate the resonances at $n\omega = |\Delta_0|$. The six resonances are seen at $\omega/\Omega = 15, 7.5, 5, 3.75, 3, 2.5$ corresponds to $n = 1, 2, 3, 4, 5, 6$, respectively. (b) shows the coherent oscillation between $|gg\rangle$ and $|s\rangle$ at the resonance $\omega/\Omega = 7.5$ and (c) shows the same between $|1\rangle$ and $|2\rangle$ states. . 88

4.9 (a) The exact results (solid lines) and that from AIA (dashed lines) of $\bar{P}_2$ over 100 cycles, as a function of ω for the initial state $|2\rangle \sim |s\rangle$. The dips indicate the resonances, and the five (broader) of them at $\omega/\Omega = 15, 7.5, 5, 3.75, 3$ correspond to $n\omega = |\Delta_0|$ with $n = 1, 2, 3, 4, 5$, respectively. The narrow ones at $\omega/\Omega = 18.33, 13.75, 11$ correspond to $n\omega = |\Delta_0 - V_0|$ with $n = 3, 4, 5$, respectively, which are not captured by AIA. 89

4.10 (a) The periodic time dependence of the detuning for $\delta = 3V_0/4 - \Delta_0$. The adiabatic durations are marked by T_{a1}, T_{a2}, and T'_{a1}. (b) shows the instantaneous energy eigenvalues. The instants ($\tau_0^{(1)}$, $\tau_0^{(2)}$, $\tau_1^{(2)}$, $\tau_1^{(1)}$, $\tau_2^{(1)}$, $\tau_2^{(2)}$) at which the LZTs occur are shown by shaded stripes. The $\hat{U}$ and $\hat{G}$ operators indicate the adiabatic regimes and the impulse points, respectively. Between the origin and the dashed vertical line, we have one complete cycle. 90

4.11 The exact results (solid lines) for the time-averaged populations ($\bar{P}_{1,2,3}$) and the same from the AIA (dashed lines) for a period of 100 cycles, as a function of ω for $\Delta_0 = -15\Omega$, $V_0 = 40\Omega$ and $\delta = 45\Omega$ with the initial state (a) $|1\rangle \sim |gg\rangle$, (b) $|2\rangle \sim |s\rangle$ and (c) $|3\rangle \sim |rr\rangle$. In (c) AIA completely failed to capture any resonances. 91

4.12 (a) The periodic time dependence of the detuning for $\delta = 5V_0/4 - \Delta_0$ and (b) shows the instantaneous energy eigenvalues. The adiabatic durations are marked by T_{a1}, T_{a2}, T_{a3}, and T'_{a1}. The instants ($\tau_0^{(1)}$, $\tau_0^{(2)}$, $\tau_0^{(3)}$, $\tau_1^{(3)}$, $\tau_1^{(2)}$, $\tau_1^{(1)}$, $\tau_2^{(1)}$, $\tau_2^{(2)}$, $\tau_2^{(3)}$) at which the LZTs occur between different adiabatic states are shown by shaded stripes. The $\hat{U}$ and $\hat{G}$ operators represent the adiabatic regions and impulse points, respectively. Between the origin and the dashed vertical line, we have one complete cycle. 92

4.13 The numerical results (solid lines) for the time-averaged populations ($\bar{P}_{1,2,3}$) in the adiabatic states, and the same from the AIA (dashed lines) over a period of 100 cycles, as a function of ω for the initial state (a) $|1\rangle$, (b) $|2\rangle$ and (c) $|3\rangle$. Other parameters are $\Delta_0 = -15\Omega$, $V_0 = 40\Omega$ and $\delta = 65\Omega$. In (a) the major peaks correspond to the resonances $n\omega = |\Delta_0|$ (between $|gg\rangle$ and $|s\rangle$ states) and smaller ones indicate the resonances at $n\omega = |\Delta_0 - V_0|$ (between $|rr\rangle$ and $|s\rangle$ states). In (b) the peaks/dips indicate the resonances at $n\omega = |\Delta_0|$ and $n\omega = |\Delta_0 - V_0|$, with no traces on the resonances at $n\omega = |2\Delta_0 - V_0|$. In (c) except the resonances at $n\omega = |\Delta_0|$, other two types are seen. AIA results are in excellent agreement with the numerics in all three cases. 93

5.1 Floquet mode properties of a driven single two-level atom with $\omega = 8\Omega$ for the case of primary resonance, $\Delta_0 = 0$ ($n_1 = 0$). The crossings of ϵ_k in (a) and the zeros of $\Pi_0^{|g\rangle}$ in (b) coincides with the zeros of $J_0(\alpha)$. The plots (a) and (b) are the special case of population trapping corresponding to the dynamical stabilization. The parameter α is varied by changing δ and keeping ω constant. 102

5.2 The IPR ($\Pi_1^{|g\rangle}$) as a function of α and Δ_0 for $\omega = 8\Omega$. The pearl-stripes are along the α axis at the resonances $n\omega = \Delta_0$. The local minima ($\Pi_1^{|g\rangle} = 0$) along the first stripe are the points of DS for which $J_0(\alpha)$=0. The parameter α is varied by changing δ and keeping ω constant. 103

5.3 Population dynamics for the resonance type R1 ($n_1\omega = \Delta_0$) for the initial states (a) $|I\rangle = |gg\rangle$ and (b) $|I\rangle = |rr\rangle$. The same, but with the resonance type R2 ($n_2\omega = \Delta_0 - V_0$) for the initial state (c) $|I\rangle = |gg\rangle$ and (d) $|I\rangle = |rr\rangle$ with $\Delta_0 = 2\Omega$. In (a) we see the Rabi oscillations between $|gg\rangle$ and $|+\rangle$ states, whereas in (b) we observe no dynamics. Similarly, (c) shows the absence of dynamics, and the Rabi oscillations between $|+\rangle$ and $|rr\rangle$ states is shown in (d). We took $V_0 = 10\Omega$, $\delta = 15\Omega$, and $\omega = 8\Omega$ for all plots. The value of Δ_0 is taken such that $n_1 = 1$ for (a) and (b), and for (c) and (d) we have $n_2 = -1$. 106

5.4 The quasi-energy spectrum ϵ_k and IPR ($\Pi_2^{|gg\rangle}$, $\Pi_2^{|rr\rangle}$) for $N = 2$, $\Delta_0 = 0$, and $\omega = 8\Omega$, as a function of α for different V_0. (a) shows ϵ_n for $V_0 = 0\Omega$ (dashed lines), and $V_0 = 0.2\Omega$ (solid lines), and (b) and (c) show the same for $V_0 = 2\Omega$ and $V_0 = 8\Omega$, respectively. Since $\Delta_0 = 0$, in (a) and (b), the level crossings take place at the zeros of $J_0(\alpha)$. In (a)-(c) the color bar indicates the probability of the finding the state $|gg\rangle$ in each of the Floquet modes. The dashed vertical lines in (c) mark $J_0(\alpha) = 0$, and at those points the central Floquet mode consists purely of $|gg\rangle$ state, which indicates dynamical stabilization. (d) and (e) show the IPR $\Pi_2^{|gg\rangle}$ and $\Pi_2^{|rr\rangle}$, respectively. In (f), we show the Bessel functions $J_0(\alpha)$ (solid line) and $J_{-1}(\alpha)$ (dashed line). The parameter α is varied by changing δ and keeping ω constant. 110

5.5 The IPR (a) $\Pi_2^{|gg\rangle}$ and (b) $\Pi_2^{|rr\rangle}$ as a function of V_0 and α for $N = 2$, $\Delta_0 = 0$ (R1 resonance), and $\omega = 8\Omega$. The regions of $\Pi_2^{|gg\rangle} = 0$ correspond to the dynamical stabilization of $|gg\rangle$, those where both $\Pi_2^{|gg\rangle} \sim 1$ and $\Pi_2^{|rr\rangle} \sim 0$ indicate the population trapping of $|rr\rangle$, and $\Pi_2^{|gg\rangle} = 2$ signals the Rydberg anti-blockade in which the system exhibits Rabi oscillations between $|gg\rangle$ and $|rr\rangle$ via the intermediate state $|+\rangle$. The intricate patterns arise due to the competition between the Rabi-couplings for the transitions $|gg\rangle \leftrightarrow |+\rangle$ [$\propto J_{n_1}(\alpha)$] and $|+\rangle \leftrightarrow |rr\rangle$ [$\propto J_{n_2}(\alpha)$]. If R2 is satisfied with $V_0 = \Delta_0$ instead of R1 (a) is $\Pi_2^{|rr\rangle}$ and (b) is $\Pi_2^{|gg\rangle}$. The parameter α is varied by changing δ and keeping ω constant. 112

5.6 (a) The IPR ($\Pi_2^{|gg\rangle}$) as a function of α for $\omega = 30\Omega$ for different V_0 satisfying the R3 resonance with $n_3 = 0$, i.e., $2\Delta_0 = V_0$. (b) The same as in (a), but for different ω and $V_0 = 6\Omega$. In (c), we show the dynamics for the initial state $|gg\rangle$ assuming R1 and R3 are met ($n_1 = n_3 = 0$) at the first root of $J_0(\alpha)$, $\omega = 15\Omega$ and $V_0 = 6\Omega$. In (d), we show the same as in (c), except that the initial state is $|rr\rangle$ and for the resonances R2 and R3, i.e. for $n_2 = n_3 = 0$. The parameter α is varied by changing δ and keeping ω constant. 114

5.7 (a) IPR $\Pi_2^{|+\rangle}$ as a function of α and V_0 for $\omega = 8\Omega$ and $\Delta_0 = 0$. The parameter α is varied by changing δ and keeping ω constant. (b) The general behavior of the dynamics of the entanglement entropy $\mathcal{S}_A$ for $\Pi_2^{|+\rangle} = 0$ (solid line), indicating dynamical stabilization and for $\Pi_2^{|+\rangle} = 1$ (dashed line). 116

5.8 Population dynamics in $|B1\rangle$ (red-dashed lines), $|B2\rangle$ (blue-solid), $|gg\rangle$ (magenta dash-dotted) and $|rr\rangle$ (green-dotted) conditioned to initial state $|B1\rangle = (|gg\rangle + |rr\rangle)/\sqrt{2}$, (a) with small interaction strengths $V_0 = 0.01\Omega$, $\omega/\Omega = 8.0$ and modulation amplitude corresponding to first Bessel root $\delta = 2.404\omega$, (b) for strong interactions, $V_0/\Omega = 15$ but without periodic modulation, $\delta = 0$ 119

B.1 Each crossing in the triangular shaped $SU(3)$ model can be considered as a combination of three crossings each having $SU(2)$ symmetry. 128

Chapter 1

Introduction

The field of ultracold atomic physics has made enormous progress since the remarkable observation of Bose-Einstein condensate (BEC) in 1995 [1–3], and remains at the forefront of probing quantum properties of matter. Over the last few decades, the study of ultracold atomic systems has encompassed a wide variety of phenomena significant to atomic, molecular, optical, condensed matter, and nuclear physics.

In the early experiments, a weakly-interacting Bose gas of alkalis (Rubidium [1], Sodium in [2] and Li in [3]) were confined in magnetic traps and cooled down to nanoKelvin temperatures. A feature of the magnetic trap is that the spin degrees of freedom of the atoms remain frozen. Nevertheless, upon using an optical trap the spin degrees of freedom were made available to probe [4] which led to the observation of spin-textures [5] and spin domains in the spinor condensates [6]. Soon after the observation of BEC, the possibility of realizing a Fermionic condensate was set in motion which held the potential to closely investigate an idea central to high-temperature superconductivity, that of BCS-BEC crossover. Facilitated by Feshbach resonance the strength of interaction between ultracold atoms could be tuned [7, 8], and remarkably a low-density degenerate Fermi gas was actualized [9]. The BEC-BCS crossover in a degenerate Fermi gas was then observed from the BEC side in [10, 11] and from the BCS side in [12, 13].

More recently, the emphasis has shifted towards strongly interacting and correlated systems of bosons. Significant efforts are focused on inducing strong interactions within BEC which have led to the realization of dipolar condensate and quantum ferrofluids of atoms with permanent magnetic dipole moment namely, Cr [14, 15], Dy [16] and Er [17]. More recently, the dipolar BEC were shown to exhibit quantum droplets whose theoretical description goes beyond the mean-field theory [18]. The discovery has further led physicists on a quest of finding exotic supersolids which possess superfluidity in a crystalline order [19, 20]. Another interesting platform to study the interacting quantum matter is polar molecules. However, their energy scheme is non-trivial and it poses a further challenge towards a complete control [21]. Another approach to induce long-range interactions within ultracold gas is to make use of the strong van der Waals interactions between high lying, Rydberg, states. The tunable and controllable on and off nature of Rydberg interactions make Rydberg atoms very appealing to quantum simulation and quantum information processing [22, 23]. The strong interaction properties are used to create logic gates [24–27], study quantum many-body physics [28], correlations in Rydberg-dressed ground states [29, 30], and makes them useful to non-linear quantum optics [31, 32].

In this regard, optical lattice [33–35] and, the more versatile and programmable, optical tweezer array [36–39] emerged as a toolbox that can be used to generate strong tunable periodic potentials for ultracold atomic gases mimicking a defect-free crystal lattice of a solid in 1D and 2D. The shape, depth, and dimensionality of lattice are fully controllable along with the inter-particle interactions making them a unique platform for the realization of unconventional phases of matter. In particular, the optical tweezers, created using micron-sized focused beams, offer great flexibility in manipulating atoms individually. Ultracold gases in optical lattices serve as ideal systems to study a tunable version of Hubbard models [40] (with Bosons [41, 42], repulsive fermions [43], Bose-Fermi mixtures [44]), extended Hubbard models [45], or quantum magnetism [46] in frustrated systems of triangular [47], kagome lattices [48] which may lead to exotic phases like quantum spin liquids [49]. Rydberg atoms become a very promising platform to study interaction-based physics and quantum spin models [28] when equipped with deterministic preparation of arrays by optical tweezers, single-atom manipulation [50, 51] and detection techniques [52]. Ultracold Rydberg atoms in optical tweezers are also used to study frustrated magnets where they give an added advantage of longer coherence times [53, 54]. Furthermore, exotic many-body localized phases of matter have been probed with ultracold gases in optical lattice [55, 56], and tweezer arrays [57]. Notably, the gauge theories in *high-energy* physics can also be configured by the *low-energy* ultracold atoms in optical lattices [58], and by interacting ultracold Rydberg atoms in tweezer arrays [59]. Moreover, ultracold Strontium gases in optical lattice have been used to create the most accurate atomic clock in the world to date [60, 61] where a potential to further enhance the precision by using tweezers exists [62]. A single site-resolved detection of Bosons [63, 64] and Fermions [65, 66] was a crucial step in forwarding the quantum simulation based on optical lattice and tweezer systems [67]. In recent years, an unprecedented amount of progress has been made with ultracold Rydberg atom arrays created using controllable optical tweezers. Most notably, quantum simulators ranging to 256 atoms have been recently demonstrated [68–70]. A 51 atom quantum simulator [71] brought into light the first signatures of quantum many-body scars [72]. Such poignant experimental and theoretical discussions indicate an exciting age for ultracold Rydberg atom physics. Rydberg excitation dynamics is also used to study disorder-induced many-body localization [73].

Studying physics in small systems becomes relevant at this time where physicists can probe at the level of individual atoms. In particular, two atoms in small traps are of fundamental interest for understanding the role of interactions in an assembly of cold atoms, and for the creation of quantum gates with single-atom traps [74]. Among open systems, the two atom dissipative systems provide a clean system where the effects from the environment can be understood clearly whereas acquiring such an understanding in poly-atomic systems is limited by the complexity of the underlying Hamiltonian [75]. In the past, the two-atom systems have been useful for validation of fundamental properties such as the measurement and control of the Rydberg-Rydberg interactions both in van der Waals regime [76] and dipole-dipole regime [77–79]; and controlled entanglement of neutral atoms through Rydberg blockade both in Rydberg states [26, 27, 80, 81] and Rydberg-dressed ground states [82]. In the current scenario, the two-atom system is routinely used to create more resilient and high-fidelity entangled quantum gates [24, 26, 27, 80, 81, 83], and as a testbed for dynamics control such as in [84] where the dynamics of collective states is manipulated through a single atom addressing, or in [79] where freezing of excitation dynamics is demonstrated through controlling transition frequencies. Beyond that, the two-atom setup and can also be used for quantum optics applications such as building quantum routers [85]. Thus, studies in few-body systems can broaden our fundamental understanding of isolated quantum systems, serve as an ideal platform for testing new unconventional tools to bring more control and desirable dynamics to the forefront, and can also shed more light on non-equilibrium physics. Moreover, experiments on two ultracold atoms in traps are now readily accessible and have the flexibility to tune external knobs eg. laser parameters, distance, depth of potential, etc. as well as internal knobs such as tunable interactions which can verify the effectiveness of newly engineered Hamiltonians.

We draw a current focus on testing new techniques of quantum control on a distinctly addressable system of two-atoms. Our techniques of Hamiltonian engineering in a two-atom setup not only uncover newer methods to control state through Rabi-offset [86], quench [87], and periodic drive [88]; but also brings fundamental insights into the physics of two-body systems which are the building blocks of many-body systems.

Other qubit architectures— Current efforts to realize a quantum simulator and computer go beyond the ultracold atoms [89]. The ultracold atom-based quantum simulators have the advantage of scalability and identicalness of qubits and are backed by recent studies of many-body physics in a large number of atoms. Other quantum systems provide unique advantages and pose distinctive limitations. For eg., trapped ions demonstrate coherence and long lifetimes along with qubit identicalness but lack scalability. Nevertheless, a quantum simulator with 100s coherently controlled trapped ions have come into existence [90]. Recently, quantum squeezed states of light generated on a silicon chip emerged as a candidate for implementing quantum algorithms that offer a quantum advantage [91]. Interacting photonic qubits in nonlinear cavity arrays, especially those generated by Rydberg gases [92] also create simulation possibilities [93, 94]. Among solid-state devices, one of the most popular platforms is superconducting qubits where the fabricated qubit is fully controllable by external voltages and magnetic fields [95]. In semiconductor-based quantum dots, a single electronic spin serves as a qubit [96]. Despite the tremendous progress in solid-state devices, [97], their central challenges lie in the variability of different qubits and their scalability. Other platforms such as nitrogen-vacancy centres in diamonds have the unique advantage of inter-connectivity and hold the potential to build long-distance quantum networks but have a long way to go [98]. NMR-based qubits have also demonstrated universal control, and remain an indispensable resource for quantum computation among a few qubits [99].

1.1 Ultracold Rydberg atoms

In this section, we focus on ultracold Rydberg atoms: their origin, important properties, relevance, and typical techniques used to cool, generate and detect them. Rydberg states are named after the Swedish physicist Johannes Rydberg who in 1890 predicted the presence of higher-lying frequencies in Hydrogen atom spectra. Subsequently, any atom having one or even more electrons in a highly excited (Rydberg) electronic state is called the Rydberg atom. We, particularly, focus on alkali Rydberg atoms where only the outermost valence electron is promoted to a state with a large principal quantum number (n). As a result, the orbital of the outer electron has a low overlap with the ionic core and the resultant energy structure becomes similar to that of the Hydrogen atom. Thus, the Rydberg states are hydrogenic and have properties that scale with n. Larger the n, more exaggerated are the properties. Rydberg atoms tend to have incredibly large sizes ($\propto n^2 \sim \mu$m) and possess large dipole moments ($\propto n^2 \sim$ kDebye) which leads to them having a remarkably long lifetime ($\propto n^3 \sim 100\mu$s) compared to their non-excited/lowly-excited counterparts. Furthermore, due to the loosely bound outer electron, Rydberg states inherit extreme sensitivity to external electric fields with polarizability scaling as n^7 [100]. Resultantly, Rydberg atoms are sensitive even to the electric field generated by their nearby counterparts which essentially means that two Rydberg atoms are strongly interacting in nature. It was, however, with the invention of laser cooling techniques in the 1970s that it became possible to tap into the regime of energy scale inversion where the interaction could dominate the kinetic energy. It is indeed the strong interactions along with long lifetimes which make Rydberg atoms an exciting platform to investigate strongly correlated phenomena central to many-body physics. The nature of Rydberg atoms' interaction is dipole type at short distances and van der Waals type at longer distances [23]. A more detailed derivation of the central properties is done in Sec. 1.1.1.

We now briefly mention the experimental tools typically used in an ultracold Rydberg atom setup. First, the ground state atoms are cooled down. A typical setup for achieving ultracold temperature enlists a magneto-optical trap or an optical trap. Using Doppler cooling techniques, the temperature is first brought down to microKelvins and later to nanoKelvins through evaporative cooling. The atoms are then excited to Rydberg states. For most alkali atoms, the energies are well described by the Quantum defect theory. The simplicity of their energy structure makes the excited states accessible with the application of limited laser frequencies. Furthermore, the commercial availability of high-power diode lasers allows for efficient excitation to Rydberg states [101]. Due to this reason, a majority of laboratories around the world study Rydberg states in heavy alkali atoms: Rubidium and Cesium at ultracold temperatures. This is especially true of the experiments involving individual ultracold Rydberg atoms [102]. The excitation is made to a principal quantum number ranging as $n \sim 20 - 100$. The systems of ultracold Rydberg atoms are often referred to as "frozen Rydberg gases" [103, 104]. The atoms remain stationary on the time scale of experiments ($\sim \mu$s) and typically exhibit large atomic densities which manifest strong interactions. Lastly, the detection of Rydberg atoms in gas is usually done by field ionization techniques which are accurate up to 90% [102]. On the other hand, the atoms trapped in optical tweezers can also be detected by negative fluorescence spectroscopy [105]. The central idea of the latter technique is that when excited, the atoms leave the trap whereas the ground state atoms remain trapped. Thus a zero fluorescence signal signifies loss of the atom from the trap or, equivalently, its excitation to a Rydberg state.

1.1.1 Properties of Rydberg atoms

Up until this point, we have only mentioned the n-scaling of Rydberg atoms' properties. In this subsection, we sketch a theoretical framework to describe it quantitatively. The discussion in this subsection is intended to provide a deeper knowledge of quantum numbers, wavefunctions, dipole moments, lifetimes, etc., and helps to understand the exact behaviour of systems of alkali Rydberg atoms.

Energy levels—

In the semiclassical picture of alkali atoms mentioned above, the valence electron gets excited to a Rydberg state and thus samples the effective potential of an ionic core making it hydrogenic. The energies E_{nlj} can be calculated using Quantum defect theory:

$$E_{nlj} = -\frac{R_y}{n_*^2}, \tag{1.1}$$

where $n_* = (n - \delta_l)$ is the effective principal quantum number, and δ_l is the quantum defect which is experimentally determined. The mass-corrected Rydberg constant is, $R_y = R_\infty M/(m_e + M)$, with $Ry_\infty = \frac{e^4 m_e}{16\pi^2\epsilon_0^2\hbar^2}$ as the Rydberg constant, and m_e, M as the mass of electron and atomic mass, respectively.

Hamiltonian—

Now, we aim to solve the the 3-dimensional Schrödinger equation for the alkali atoms $H\psi_{nlj}(r,\theta,\phi) = E_{nlj}\psi_{nlj}(r,\theta,\phi)$. However, due to multiple charge-body interactions, the potential experienced by the outermost electron becomes very complicated. Marinescu et. al [106] proposed a simpler parametric description of the potential as,

$$V(r) = \frac{Z_{nl}}{r} - \frac{\alpha_c}{2r^4}(1 - e^{-(r/r_c)^6}), \tag{1.2}$$

which at long range is hydrogenic ($\propto 1/r$), and at short range accounts for the finite size of the core with the help of static polarizability α_c and a cut-off radius r_c. The effective radial charge is given by $Z_{nl}(r) = 1 + (Z-1)e^{-a_1 r} - r(a_3 + a_4 r)e^{-a_2 r}$, where Z is the nuclear charge of the neutral atom. Using it we describe the Hamiltonian for the valence electron of the alkali atom as,

$$H = -\frac{\hbar^2}{2\mu}\nabla_r^2 + \frac{L^2}{2\mu r^2} + V(r) + V_{SO}(r), \tag{1.3}$$

where $\mu = Mm_e/(M + m_e)$ is the reduced mass, and r is the distance of valence electron from the atom core. The four terms in the Hamiltonian indicate kinetic, centrifugal, coulombic interaction, and spin-orbit coupling, respectively. The spin-orbit interaction is $V_{SO}(r) = \alpha \mathbf{L}.\mathbf{S}/(2r^3)$, where α is the fine structure constant. Due to the spin-orbit coupling, the eigenstates are expressed in the fine-structure basis $|nljm_j\rangle$ instead of uncoupled basis $|nlm_l\rangle$. The hyperfine structure is negligible for the highly excited states and thus can be neglected.

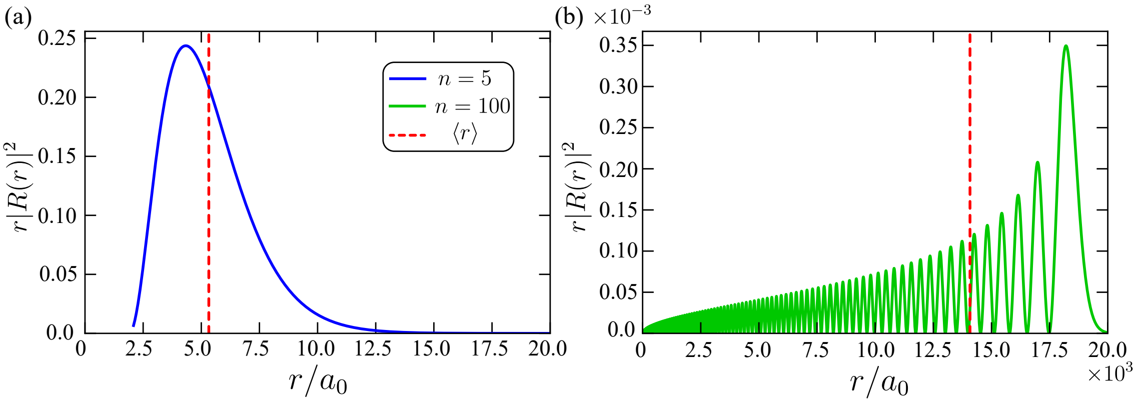

Figure 1.1: Radial probability density $r^2|R(r)|^2$ and (red) the expectation value $\langle r \rangle = \langle \phi_{n,l,m}|r|\phi_{n,l,m}\rangle$ of (a) $5S_{1/2}$ (ground state) with $\langle r \rangle = 5.3a_0 \sim 3$ Å and (b) $100S_{1/2}$ (a Rydberg state) having $\langle r \rangle = 14075a_0 \sim 0.7$ μm for ^{85}Rb atom. Figures obtained using ARC library [107].

Rydberg Atom wavefunction—

Owing to a spherically symmetric potential, the eigenfunctions in spherical coordinates for the Rubidum atom can be split into radial and spherical components: $\psi_{nlj}(r,\theta,\phi) = Y_{l,m_l}(\theta,\phi)R_{nl}(r)$ in the uncoupled basis. The radial wavefunctions can be obtained using the Schrödinger's equation,

$$\left[-\frac{1}{2\mu}\left(\frac{\mathrm{d}^2}{\mathrm{d}r^2} + \frac{2}{r}\frac{\mathrm{d}}{\mathrm{d}r}\right) + \frac{l(l+1)}{2\mu r^2} + V(r) + \frac{\alpha}{2r^3}F(j,l)\right] R_{nlj}(r) = E_{nl}R_{nlj}(r). \quad (1.4)$$

with $F(j,l) = j(j+1) - l(l+1) - 3/4$. The equation can be solved numerically using Numerov's method. It is found that $\langle r^\alpha \rangle \sim n^{2\alpha}$ for $\alpha > 0$ and for inverse powers $\langle r^\alpha \rangle \sim n^{-3}$ [100]. The n-dependence of $\langle r \rangle$ can be seen in Fig. 1.1, where for Rb ground state is $\langle r \rangle \sim 1$Å and on excitation to $n = 100$, the size approaches ~ 1 μm.

Dipole matrix elements—

As the electric field only couples to the orbital angular momentum (l) of the electron, it is, therefore, necessary to transform from the fine-structure basis into the uncoupled basis to evaluate the dipole matrix elements. The strength of coupling between the states at fine-structure splitting, $|nljm_j\rangle$ and $|n'l'j'm'_j\rangle$ is given by the dipole matrix element $\langle nljm_j|e\mathbf{r}|n'l'j'm'_j\rangle$. The matrix elements are evalauted using the Wigner-Eckart theorem [108] as

$$\langle nljm_j|r_q|n'l'j'm'_j\rangle = (-1)^{j-m_j}\begin{pmatrix} j & 1 & j' \\ -m_j & q & m'_j \end{pmatrix}\langle j||r||j'\rangle, \quad (1.5)$$

where $q = -1, 0, 1$ corresponds to σ^+, π and σ^- transitions. The j-reduced matrix element further equates through a Wigner-6j symbol to the uncoupled basis

$$\langle j||r||j'\rangle = (-1)^{l+s+j'+1}\delta_{s,s'}\sqrt{(2j+1)(2j'+1)}\begin{Bmatrix} j & 1 & j' \\ l' & s & l \end{Bmatrix}\langle l||r||l'\rangle. \tag{1.6}$$

The l-reduced matrix element in the above equation are related to the radial matrix element as

$$\langle l||r||l'\rangle = (-1)^{l}\sqrt{(2l+1)(2l'+1)}\begin{pmatrix} l & 1 & l \\ 0 & 0 & 0 \end{pmatrix}\langle nl|r|n'l'\rangle, \tag{1.7}$$

where the parenthesis denote Wigner-3j symbols. The radial matrix element represents the overlap integral between the radial wavefunctions and the dipole moment

$$\langle nl|r|n'l'\rangle = \int_{r_i}^{r_o} R_{n,l}(r) r R_{n',l'}(r) r^2 dr. \tag{1.8}$$

This integral can be evaluated by numerical integration over the wavefunctions calculated above. The dipole matrix elements between neighbouring levels $n \approx n'$ scale as the orbital radius n^2.

Rydberg state Lifetimes—

With the knowledge of dipole matrix elements, the radiative lifetimes of alkali atoms can be evaluated. First, we determine the Einstein A-coefficient that defines the spontaneous decay from $|nl\rangle$ to $|n'l'\rangle$ [100]

$$A_{nl\rightarrow n'l'} = \frac{4\omega_{nn'}^3}{3c^3}\frac{l_{\max}}{2l+1}|\langle nl|r|n'l'\rangle|^2 \tag{1.9}$$

where $\omega_{nn'}$ is the frequency of transition, and $l_{\max} = \max\{l, l'\}$. The effective lifetime is then given by summation over the radiative decay to lower states. At finite temperatures, the black-body radiation (BBR) which accounts for stimulated emission and absorption also becomes important. So, the lifetime of a Rybderg state is given by [107]

$$\tau_{nl} = \left[\sum_{nl>n'l'} A_{nl\rightarrow n'l'} + \sum_{n'l'} \frac{A_{nl\rightarrow n'l'}}{e^{\hbar\omega_{nn'}/k_B T} - 1}\right]^{-1}, \tag{1.10}$$

where $n'l'$ in the latter (BBR) term also includes states which are higher in energy. For $n \gg 1$ and low orbital angular momentum states (s and p), the lifetime $\tau \propto n^3$. To give an example, the lifetime of $30S$ state for ^{85}Rb is 10 μs. On the other hand, for circular states $l = n - 1$, the lifetime scales as $\tau \propto n^5$.

1.2 Rydberg-Rydberg Interactions

The natural consequence of the large dipole moment featured by the Rydberg atoms is the large interaction between the two of them. In fact, one of the main advantages that Rydberg atoms offer is a tunable, anisotropic, controllable interaction. We see this in more detail in this section. When the two atoms are separated by distance R, the dipole-dipole interaction is given by [109],

$$\hat{V}(\mathbf{r}) = \frac{1}{4\pi\epsilon_0 r^3}\left(\hat{\mathbf{d}}_1.\hat{\mathbf{d}}_2 - 3(\hat{\mathbf{d}}_1.\mathbf{n})(\hat{\mathbf{d}}_2.\mathbf{n})\right), \tag{1.11}$$

where $\hat{\mathbf{d}}_j$ is the electric dipole moment and $\mathbf{n} = \mathbf{r}/R$ is the unit vector of distance. A pair of atoms in $|e\rangle \otimes |e\rangle$ state couple via $\hat{V}(\mathbf{r})$ to $|e'\rangle \otimes |e''\rangle$ state. For simplicity, let's assume the atoms are initially in $|ns, ns\rangle$ state. The dominant contribution to the interaction arises from nearby states as it has the largest dipole moment. Thus, the coupling is effectively restricted to $|np, (n-1)p\rangle$ state with the dipole matrix elements, $\hat{\mathbf{d}}_1 = \langle ns|e\mathbf{r}|np\rangle$ and $\hat{\mathbf{d}}_2 = \langle ns|e\mathbf{r}|(n-1)p\rangle$. In the basis $\{|ns, ns\rangle, |np, (n-1)p\rangle\}$, the interaction is described by the Hamiltonian

$$H = \begin{pmatrix} 0 & C_3/R^3 \\ C_3/R^3 & \Delta \end{pmatrix}, \tag{1.12}$$

where $\Delta = 2E_{ns} - E_{(n-1)p} - E_{np}$ is the energy difference, and the coupling is $\langle ns, ns|\hat{V}|np, (n-1)p\rangle = C_3/R^3$. The dressed states' energies are given by eigenvalues,

$$\Delta E_\pm = \frac{1}{2}\left(\Delta \pm \sqrt{\Delta^2 + 4\left(\frac{C_3}{R^3}\right)^2}\right). \tag{1.13}$$

At short range, $C_3/R^3 \gg \Delta$ and the splitting of the energy is $\pm C_3/R^3$. This corresponds to a resonant dipole-dipole regime and the energy-shift scales as $C_3 \propto d^2 \sim n^4$. The dressed states are maximally mixed $|\pm\rangle = \frac{1}{\sqrt{2}}(|ns, ns\rangle \mp |np, (n-1)p\rangle)$ at short ranges.

At long ranges, $C_3/R^3 \ll \Delta$, the energy-shift of $|ns, ns\rangle$ state is of second order $\frac{1}{2\Delta}\left(\frac{C_3}{R^3}\right)^2$ and the mixing of ns states with p states is minimal. This is known as the van der Waals regime. The energy-shift has the form C_6/R^6 where $C_6 = \frac{C_3^2}{2\Delta}$ is called the dispersion coefficient. It scales with n as $C_6 \sim n^{11}$, due to scaling of $C_3 \sim d^2$ combined with $\Delta \sim n^{-3}$. Furthermore, the attractive/repulsive nature of interaction is determined by the sign of Δ. The transition between these two regimes occurs at the the van der Waals radius $R_{vdW} = \sqrt{C_6/|\Delta|} \sim \mu$m. In the systems we consider below, we assume the atom-atom separation large enough so that the

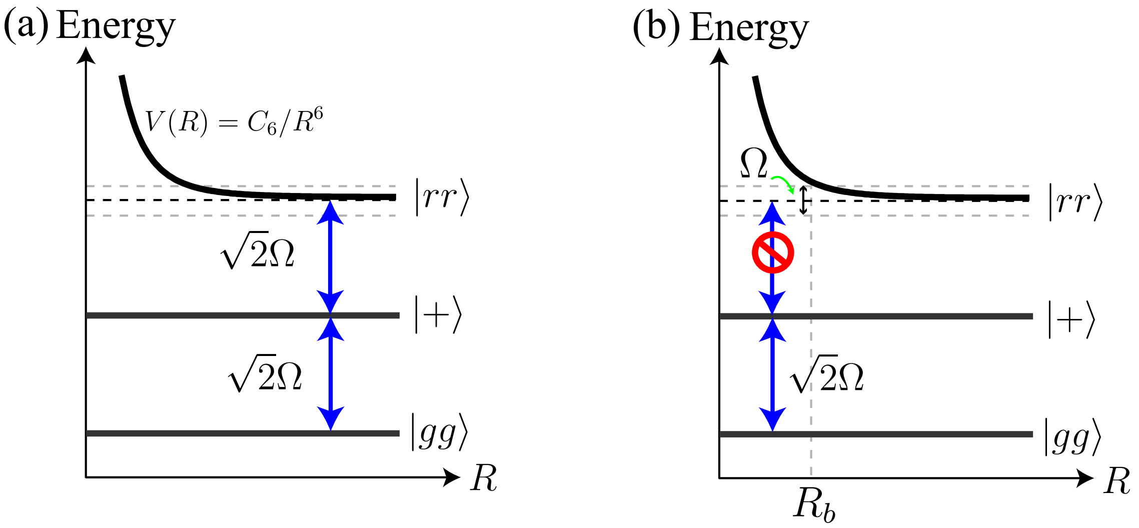

Figure 1.2: Schematic representation of energy levels of two atoms, each of which their ground state coupled to Rydberg state with Rabi frequency Ω (for more details, see Sec. 1.4.1). The energy of $|rr\rangle$ state is a function of the distance between atoms (R) in the van der Waals regime varies as C_6/R^6 . Ω is the excitation linewidth caused by the power broadening of the light field. (a) When the separation between atoms is large, a complete transition to $|rr\rangle$ is possible. (b) When the separation is smaller than R_b, it leads to a 'blockade' of $|rr\rangle$ excitation. A corroborative dynamics is shown in Fig. 1.3.

Rydberg-Rydberg interactions are of the van der Waals type.

1.3 Rydberg Blockade

One of the most significant consequences of strong interactions between the Rydberg atoms is the 'blockade' of another excitation in the vicinity of an already excited atom [24, 110, 111]. An early proposal to utilize these properties in quantum information science was made by Jaksch *et al.*, in which two neutral Rydberg atoms were proposed to create a quantum logic gate [24]. In this approach, different atomic states act as the qubit basis states. Soon after, the idea was extended to mesoscopic systems by Lukin *et al.* where the role of each qubit was played by a *superatom* [25]. A decade later, these ideas were successfully implemented in [26, 27]. In this section, we discuss this concept in detail. Consider two two-level atoms separated by a distance R. The ground state $|g\rangle$ and Rydberg state $|r\rangle$ of each atom is coupled with Rabi frequency Ω. When the two atoms are in the state $|rr\rangle$, they experience a strong interaction, and the energy of this state gets shifted by an amount given by vdW interaction: $V(R) = C_6/R^6$. Consequently, a laser resonant with the excitation of one atom becomes out of resonance with the excitation of the other atom, provided that the energy shift $V(R)$ is larger than the linewidth of the excitation ($\hbar\Omega$). The critical separation is called blockade radius. This is the phenomenon of "Rydberg blockade" *i.e.*, within the blockade regime, the excitation of one atom

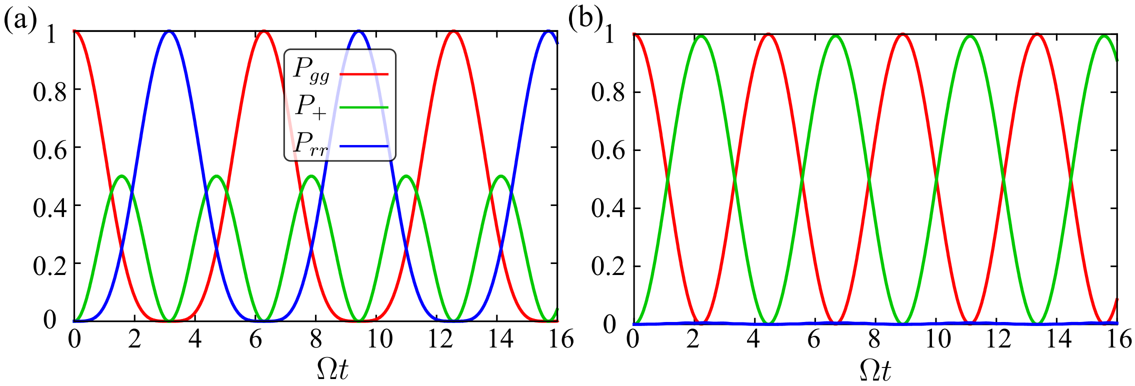

Figure 1.3: The population dynamics in $|gg\rangle, |+\rangle$ and $|rr\rangle$ states. (a) For $V_0 = 0$, the state $|rr\rangle$ gets populated via $|+\rangle$ state. (b) When $V_0/\Omega = 10$, it causes a blockade of double excitation and results in coherent population transfer between $|gg\rangle$ and entangled state $|+\rangle$. The oscillation frequency is enhanced to $\sqrt{2}\Omega$.

prevents excitation of another. The radius R_b of the blockaded sphere is set by the bandwidth of the excitation. In the case of van der Waals interaction:

$$R_b = \left(\frac{\hbar\Omega}{C_6}\right)^{1/6}. \tag{1.14}$$

We schematically depict the idea in Fig. 1.2. Within this radius, the two-atom system will oscillate between the bare ground state $|gg\rangle$ and entangled $|+\rangle = \frac{|gr\rangle+|rg\rangle}{\sqrt{2}}$ with Rabi frequency modified by a factor of $\sqrt{2}$, *i.e.* $\Omega_{new} = \sqrt{2}\Omega$ [111], where Ω is the Rabi frequency for single atom. The blockade dynamics is shown in Fig. 1.3(b) and the population dynamics is contrasted with the case of no interaction [Fig. 1.3(a)]. The details of the single-atom Rabi model are discussed in Sec. 1.4.1.

The effect of the blockade is not unique to Rydberg atoms and is present and observed in other quantum systems having similar strong interaction properties, such as electrons experiencing the coulomb blockade [112], or photons in a cavity experiencing a photon blockade [113]. Furthermore, atoms may experience interaction blockade due to s-wave collisions [114]. However, these systems may not have the same level of controllability as a Rydberg atom setup. Thus, the latter may help in revealing similar physics native to other systems. Further use of the Rydberg blockade mechanism is to produce a many-body entangled state in large cold atomic ensembles which lead to $\sqrt{N}$ modification of collective Rabi oscillation [52]. The same concept can be applied to create a spatially ordered structure of the Rydberg atoms with non-overlapping blockade spheres [115]. In addition to entangled gates [22, 116–119], it has also emerged as a useful tool in quantum state preparation such as deterministic loading of a single-atom in an optical lattice [120], creation of spin squeezed states of atoms [121] and scalable collective qubit states [122, 123]. Exotic concomitant of the Rydberg blockade effect include preparation of single-atom and single-photon sources [120].

1.4 Quantum Dynamics

Controllable, coherent dynamics in quantum systems provide insights into the fundamental properties of quantum matter and unveil new computational tools to exert local control in two-body or many-body systems. In many-body systems, the state and correlation dynamics have been used to understand phenomena of fundamental importance. These include pre-thermalization and quantum thermalization [124, 125], investigation of different quantum phases [68], measuring entanglement entropy in a many-body system [126, 127], understanding the critical dynamics of quantum phase transitions in Ising model [71, 128] and in the Kibble-Zurek mechanism [129], simulating the growth of magnetization in 2D antiferromagnets [69]. Quantum state dynamics is also used to observe the dynamical growth of entanglement using quantum state tomography [130]. Such systems are often studied through quenching the system - a change in the Hamiltonian from H^i to H^f - in an otherwise isolated quantum system resulting in non-equilibrium quantum physics. Often a sudden change of Hamiltonian is accompanied by a phase transition. The examples include disordered to ferromagnetic phase transitions in Ising models [131, 132], superfluid to Mott insulator quantum phase transitions in ultracold gases [133], or demonstration of quantum many-body scar states in Rydberg atom arrays [71, 72, 134]. On the other hand, a slow change of Hamiltonian (adiabatic following) enables the creation of entangled states such as GHZ and W states [135], or dynamical crystallization in ultracold atoms [136]. Furthermore, a periodic change in the Hamiltonian of Rydberg atom arrays has emerged as a robust tool used to dynamically localize excitations, in addition to enhancing the regime of the blockade and creating regions of anti-blockade [137].

Quantum dynamics in two atoms have been used to observe entangled quantum gates [26] and collective excitations [76]. Two-atom setups have been essential to devise methods to enhance gate fidelity [81], gate coherence [80], robustness [138]; and further allows for ultrafast control of the Rydberg states [139] and build resilient quantum gates [83]. The study of quantum dynamics, thus, brings fundamental insights into the physics of two-body systems which are the building blocks of many-body systems. In the following subsections, we give an overview of the quantum dynamics in a single two-level atom whereas the dynamics in a two-atom system will be studied in the rest of the chapters of this thesis.

1.4.1 Rabi Dynamics

Rabi dynamics is one of the fundamental concepts associated with two-level systems. In this section, we give a brief overview of the same. We consider a two-level atom coupled to a classical light field, and treat the problem under electric dipole approximation. The two-level atom is illustrated in Fig. 1.4. The atom has a ground state $|g\rangle$ and an excited state $|r\rangle$, and the states are coupled by an electric dipole transition of frequency ω_{gr}. The atom interacts with a monochromatic oscillatory radiation field of frequency ω, which is detuned by an amount $\Delta = \omega - \omega_{gr}$ from resonance.

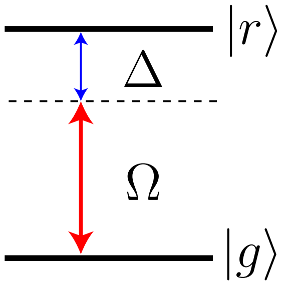

Figure 1.4: A two-level atom. The two energy levels are separated by a transition with frequency ω_{gr}. The atom is driven by a monochromatic field of frequency ω. Two key parameters govern the dynamics of the atom-light interaction - the detuning $\Delta = \omega - \omega_{gr}$, and the Rabi frequency Ω which describes the strength of the atom-field coupling.

The evolution of this system is governed by the time-dependent Schrödinger equation ($\hbar = 1$),

$$i\frac{\partial \Psi(\mathbf{r}, t)}{\partial t} = \hat{H}\Psi(\mathbf{r}, t). \tag{1.15}$$

The total Hamiltonian $\hat{H} = \hat{H}_0 + \hat{V}$ is composed of atomic Hamiltonian ($\hat{H}_0$) and a perturbation due to light field ($\hat{V}$). The electric field of the monochromatic light field is given by $\hat{E} = \hat{\epsilon} E_0 \cos(k\mathbf{r} - \omega t)$. Under the electric-dipole approximation to write the perturbation as $\hat{V} = \hat{d} \cdot \hat{E}$ where $\hat{d}$ is the dipole matrix element associated with the coupled atomic states *i.e.* $|g\rangle \leftrightarrow |r\rangle$ transition. The unperturbed atom is described by $\hat{H}_0$ whose eigenstates are bare atomic states $|g\rangle$ and $|r\rangle$. The time-evolved wavefunction can be expanded using the unperturbed eigenbasis as, $\Psi(\mathbf{r}, t) = c_g(t)|g\rangle + c_e(t)|r\rangle e^{-i\omega_{gr}t}$.

For initial state, $t = 0$, $c_g = 1$ and $c_e = 0$, the probability for the atom to be in the excited state $|c_e(t)|^2$:

$$P_e = \frac{\Omega^2}{\bar{\Omega}^2} \sin^2 \left[\frac{\bar{\Omega} t}{2}\right] \tag{1.16}$$

where $\Omega = E_0 \langle r|\hat{d} \cdot \hat{\epsilon}|g\rangle$ depends on atom-light coupling through the amplitude of the radiation field (E_0) and strength of the atomic response (dipole moment $\hat{d}$),

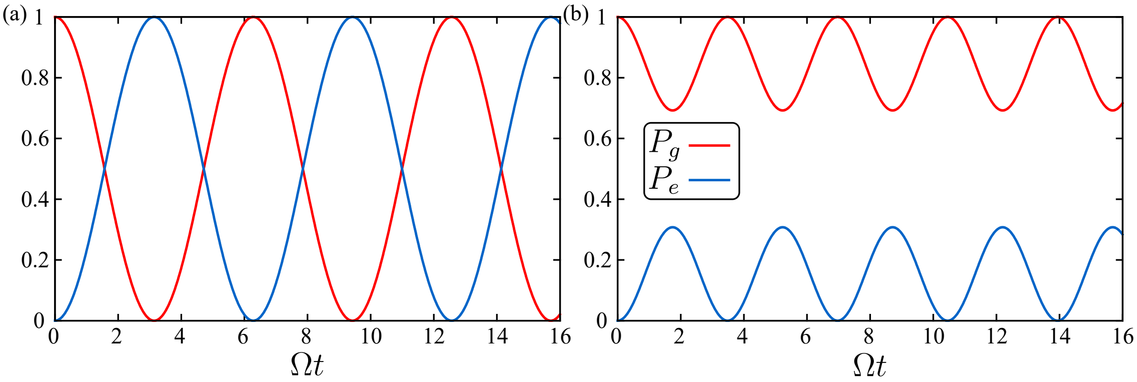

Figure 1.5: Time evolution of population in the ground and excited state. (a) Rabi dynamics of a single two-level atom at resonance ($\Delta = 0$). The population of ground state transfers coherently to excited state and oscillate with a time-period $2\pi/\Omega$. (b) The Rabi dynamics with detuning $\Delta/\Omega = 1.5$. A finite detuning results in an imperfect population transfer within a Rabi cycle with a shorter time-period $2\pi/\bar{\Omega}$. For a large enough detuning, the population effectively remains trapped in the initial state.

and is commonly known as *Rabi frequency*. The term $\bar{\Omega} = \sqrt{\Omega^2 + \Delta^2}$ is the effective Rabi frequency in presence of the atom-light detuning Δ. The probability of system to be in state $|r\rangle$ undergoes *Rabi* oscillations at frequency $\bar{\Omega}$, as shown in Fig. 1.5.

In the case of two two-level atoms, where each atom is resonantly coupled from ground $|g\rangle$ to a highly excited or Rydberg state $|r\rangle$ with Rabi frequency Ω, strong interactions cause energy shift in the $|rr\rangle$ state. As a result, only one atom can be excited to the Rydberg state if the interaction energy shift is larger than the excitation linewidth. Within this blockade radius, the excitation to the doubly excited state is greatly suppressed [see Sec. 1.3 for details].

In Chapter 2, we study a system of two two-level Rydberg atoms where each atom is driven independently by distinct Rabi-frequency and investigate the effects of an offset in the Rabi frequencies on the dynamics and quantum correlations.

1.4.2 Quench Dynamics and LZ transitions

As mentioned before, quenching drives the system out of equilibrium and enables investigation of interesting quantum dynamics, especially when driven across the *avoided-level crossing* [140]. The simplest understanding of such non-adiabatic transition comes from looking at a two-state quantum system, where a degenerate pair of (unperturbed) energy levels 'repel' each other to create an avoided-level crossing. When the two (unperturbed) levels have far different energies, the electron resides almost definitely in one of the unperturbed eigenstates. However, at degeneracy, the electron finds itself in a superposition of the two states. If the Hamiltonian is dynamically varied such that the system is driven across the avoided crossing, the electron makes a dynamic non-adiabatic transition from one eigenstate to the other.

This is called a Landau-Zener Transition (LZT). The classic example is the Landau-Zener (LZ) model in which the Hamiltonian of a two-level system is varied linearly in time. The probability of transition between the two eigenstates is given by the LZ formula first shown by L. Landau, C. Zener, E. Stückelberg, and E. Majorana [141–144] in 1932.

The two-level atom consists of a ground state $|g\rangle$ and an excited state $|r\rangle$ and is driven by a laser field associated with a Rabi frequency Ω and a time-dependent atom-light detuning $\Delta(t)$. Considering the atom to be frozen with negligible kinetic energy, we can describe the system by Hamiltonian (assume $\hbar = 1$),

$$\hat{H} = \frac{\Omega}{2}\hat{\sigma}_x - \Delta(t)\hat{\sigma}_{rr}, \tag{1.17}$$

where $\hat{\sigma}_{rr} = |r\rangle\langle r|$ is a projection operator and $\hat{\sigma}_x = |g\rangle\langle r| + |r\rangle\langle g|$ is the transition operator. The off-diagonal Rabi-coupling Ω manifests as the energy gap at the avoided-level crossing in Fig. 1.6(a).

Two sets of basis are important for considering the LZ physics: the so-called diabatic states $\{|g\rangle, |r\rangle\}$ which are the eigenstates of the unperturbed Hamiltonian under $\Omega = 0$, and the adiabatic basis $\{|\phi_+(t)\rangle, |\phi_-(t)\rangle\}$ which is composed of the instantaneous eigenstates of the Hamiltonian, $\hat{H}(t)|\phi_\pm(t)\rangle = E_\pm(t)|\phi_\pm(t)\rangle$. The instantaneous energies of these states are

$$E_\pm(t) = \pm\bar{\Omega}(t)\beta_\mp(t) \tag{1.18}$$

with $\beta_\pm(t) = \frac{\bar{\Omega}(t)\pm\Delta(t)}{2\bar{\Omega}(t)}$ and $\bar{\Omega}(t) = \sqrt{\Delta(t)^2 + \Omega^2}$. The variation of $E_\pm(t)$ with a linear detuning is shown in Fig 1.6(a). The adiabatic and diabatic bases are connected with each other via the time-dependent coefficients $\beta_\pm(t)$,

$$|\phi_\pm(t)\rangle = \pm\sqrt{\beta_\pm(t)}|g\rangle + \sqrt{\beta_\mp(t)}|r\rangle. \tag{1.19}$$

Asymptotically away from the avoided-level crossing $|\Delta| >> \Omega$ ($\beta_\pm \rightarrow \{1, 0\}$), the adiabatic states coincide with the diabatic states [see Fig. 1.6(a)]. At the avoided-level crossing, they are equal superposition of $|g\rangle$ and $|r\rangle$. We can write the system state in adiabatic basis as $|\psi(t)\rangle = a_+(t)|\phi_+(t)\rangle + a_-(t)|\phi_-(t)\rangle$, where $a_\pm(t)$ are the time-dependent coefficients for locating the atom in the adiabatic states $|\phi_\pm(t)\rangle$. We obtain the state dynamics by numerically solving the corresponding Schrödinger equation $i\partial/\partial t|\psi(t)\rangle = \hat{H}|\psi(t)\rangle$. In the Landau-Zener model, the detuning is varied linearly with time $\Delta(t) = vt$, where v is the rate of change of detuning or the quench rate. The model is analytically solvable with the exact solution obtainable in the form of Weber's functions. In the asymptotic limit, the detuning varies from $(-\infty, \infty)$, and we get the LZ formula for transition probability

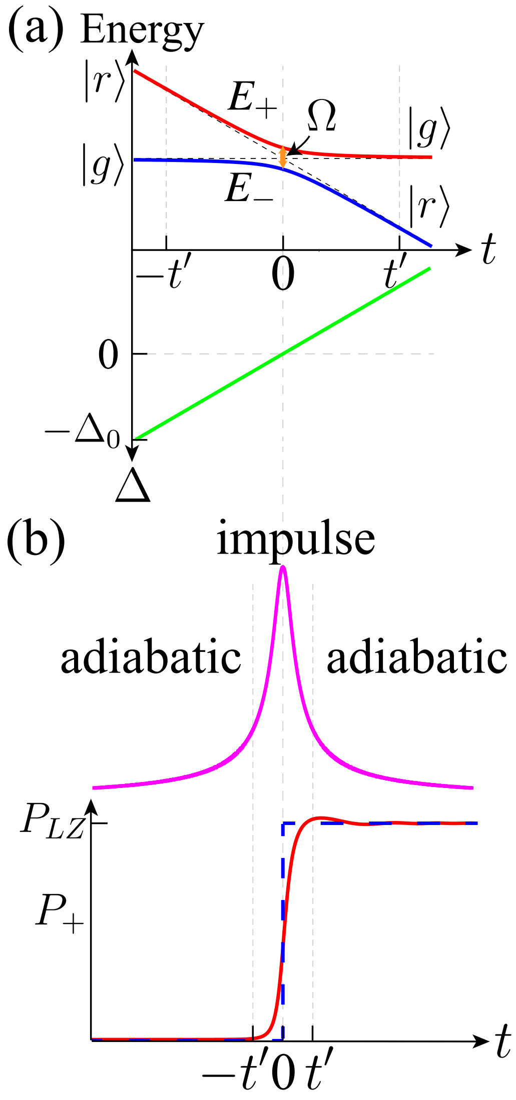

Figure 1.6: (a) (Top) The energy values of instantaneous eigenstates (solid red/blue) and diabatic states (dashed-black) corresponding to (Bottom) a linear change of detuning. The energy-gap at avoided-level crossing is equal to the Rabi frequency Ω. (b) (Top) The inverse of energy gap between adiabatic energy levels $1/(E_+ - E_-)$ is plotted whilst (Bottom) a transition from ground ($|-\rangle$) to excited state ($|+\rangle$) occurs when subjected to a linear quench in the detuning. The dashed-blue line is obtained from AIA model [Eq. (1.22)] where an impulse transition is approximated at avoided-level crossing.

[141, 142].

A simplified understanding of the LZ model emerges by assuming an Adiabatic Impulse type evolution across time. The central idea of the Adiabatic-Impulse model is to divide the time-evolution into discrete regimes of adiabatic and non-adiabatic or impulse evolution as demonstrated in Fig. 1.6(b) [145, 146]. In the regime of adiabatic-evolution, the system evolves to remain in the instantaneous eigenstate of the Hamiltonian whereas, during the impulse regime, a non-adiabatic transition (LZT) happens. We now apply the AIA to the LZ model. The two-level system with linear detuning and Rabi-coupling Ω is shown in Fig. 1.6(a) where the energy gap between the two adiabatic levels (E_+ and E_-) is minimum at $t = 0$ with value Ω, and away from the avoided-level crossing, the gap is large. As per AIA, the system will evolve adiabatically when $(E_+ - E_-)^2/v \gg 1$ and non-adiabatically elsewhere. We show these regimes in Fig. 1.6(b). Although the transition is not instantaneous and spans over an extended duration ($2t'$) near the avoided-level crossing, while implementing the Adiabatic-Impulse model, we assume $t' \to 0$ due to its versatility [147]. The time-evolution across the avoided level crossing after a single sweep can, therefore, be discretized into adiabatic and non-adiabatic matrices as

$$|\psi(t_\infty)\rangle = U(t_\infty, +0)\hat{G}_{LZ}U(-0, t_{-\infty})|\psi(t_{-\infty})\rangle, \tag{1.20}$$

with $|\psi(t)\rangle = (a_+(t), a_-(t))^T$ as the probability amplitude in adiabatic basis. The adiabatic evolution far away from the avoided-level crossing governed by the unitary evolution matrix (written in the adiabatic basis $\{|\phi_+\rangle, |\phi_-\rangle\}$),

$$\hat{U}(t_2, t_1) = \begin{pmatrix} e^{-i\zeta_+} & 0 \\ 0 & e^{-i\zeta_-} \end{pmatrix}$$

where $\zeta_\pm(t_2, t_1) = \int_{t_1}^{t_2} dt E_\pm(t)$ are the aggregated dynamical phases. In the vicinity of avoided-level crossing, the LZ transition matrix $\hat{G}_{LZ}$ governs the evolution. We obtain it by taking an asymptotic limit in time of exact solution $\bar{\psi}(t)$ as,

$$\hat{G}_{LZ} = \begin{pmatrix} e^{-i\tilde{\phi}_s}\sqrt{1 - P_{LZ}} & -\sqrt{P_{LZ}} \\ \sqrt{P_{LZ}} & e^{i\tilde{\phi}_s}\sqrt{1 - P_{LZ}} \end{pmatrix} \tag{1.21}$$

where $\tilde{\phi}_s = \gamma(\ln\gamma - 1) + \arg\Gamma(1 - i\gamma) + \frac{\pi}{4}$ is the Stoke's phase, and $\gamma = \Omega^2/4v$ is the adiabaticity parameter along with Γ as the gamma function. Therefore, an atom residing in the ground state ($|\phi_-\rangle$) when undergoes a linear quench of detuning makes a transition to the excited state ($|\phi_+\rangle$) with the probability

$$P_{LZ} = \exp\left(-\pi\frac{\Omega^2}{2|v|}\right). \tag{1.22}$$

wwhich is the well-known LZ formula. For an adiabatic transition ($v \to 0$ or $\gamma \gg 1$), the transition probability is negligible ($P_{LZ} \to 0$) which is in accordance with the adiabatic approximation, whereas for a sudden quench ($v \to \infty$ or $\gamma \ll 1$), the $|r\rangle$ state is excited with a maximum probability ($P_{LZ} \to 1$). The exact dynamics are more intricate as shown Fig. 1.6(b), regardless the simple Landau-Zener model gives an accurate estimate of the final excitation probability and reveals parameter dependence.

LZ transitions have been studied using Rydberg atoms, where the two coupled levels of the atom play the role of qubit states. Most studies pertain to a single atom, such as measuring LZ transition probability [148], and populating the Rydberg levels via multi-photon using a chirped frequency pulse across an avoided crossing [149–151], or a selective field ionization employing LZT [152]. More recent works include enhancement of LZ transition probability across the avoided crossing [153], and observation of quantum beats in the ionization field upon exciting three Rydberg sublevels in an ultracold gas [154]. In a system of two "frozen" Rydberg atoms, the LZ interferences have been probed across Förster resonance [155] but a detailed study of LZ transition in such a system with linear quench was not yet made.

We study Landau-Zener (LZ) dynamics in a setup of two Rydberg atoms with time-dependent detuning comprehensively in Chapters 3 and 4.

1.4.3 Dynamical stabilization in a periodically driven two-level atom

In this section, we give a brief overview of the dynamics of periodically driven systems. Periodically driven or Floquet systems have a long history. The periodic drive is specified by a time-dependent Hamiltonian $H(t) = H(t+T)$ with a constant time period T. The behaviour of Floquet systems is very rich, in particular, they display counter-intuitive effects such as dynamical localization and dynamical stabilization. One paradigmatic example in classical physics is that of Kapitza inverted pendulum. In contrast to a simple gravity pendulum which oscillates about its equilibrium position at the lowest point in its trajectory [Fig 1.7(a)], the Kapitza pendulum displays equilibrium behaviour at the highest point. The dynamical stabilization at the inverted point is evoked by a periodic movement of the suspension point of the pendulum [see Fig 1.7(b)]. Other examples of dynamical localization are the Fermi-Ulam model of a particle moving between a fixed and periodically oscillating wall [156], classical and quantum kicked rotors [157, 158].

In the quantum world, an idea closely related to the Kapitza pendulum is population trapping in a two-level atom coupled with light [146, 159, 160]. We briefly discuss it here; a detailed discussion can be found in Chapter 5. Under periodic modulation of the light frequency [see Fig. 1.8(a)], the population can be trapped in an initial quantum state for a significant period, where the state would otherwise evolve into the other state through Rabi oscillations. Thus, effectively, the periodic variation suppresses the Rabi coupling between the states, as shown in Fig. 1.8(b). Population trapping, however, crucially depends on both the modulation frequency and amplitude. For high frequencies, at

$$\Delta_0 = n\omega \tag{1.23}$$

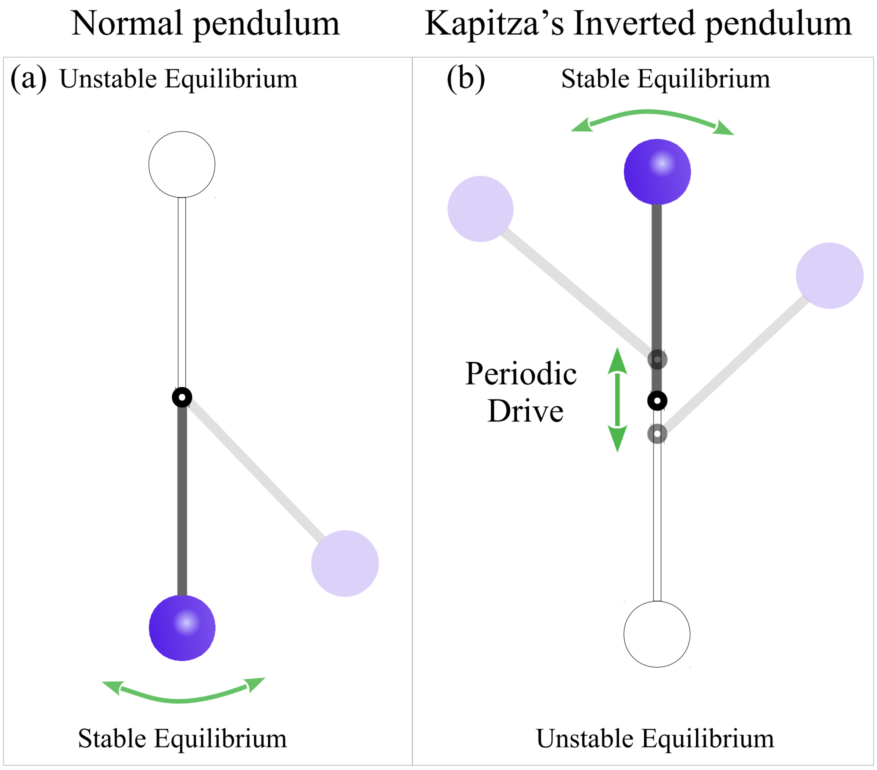

Figure 1.7: Stable and unstable equilibrium positions of (a) simple normal pendulum (b) periodically driven Kapitza or inverted pendulum. The usual position of unstable equilibrium can be stabilized with periodic driving.

we get *resonance* *i.e.* a coherent population transfer between the ground and excited state. However, at $J_n(\delta/\omega) = 0$, the coherent transfer halts, and the population trapping occur. Population trapping is synonymous with dynamical stabilization if the initial detuning is not too large. In particular, for $n = 0$ *i.e.* at the Bessel zero roots, we get dynamical stabilization. Further details are given in chapter 5.

In quantum systems, examples of dynamical stabilization include coherent destruction of tunnelling (CDT) in a double-well potential [161–163] where the tunnelling between double well is brought to an almost complete stop when perturbed by a monochromatic driving force. Analogous phenomena are observed in several other physical setups, for instance, a moving charged particle may be localized with a time-periodic electric field [164, 165], or localization of a wavepacket in a periodic lattice may occur due to periodic shaking of the lattice [166–169] or due to a modulation of the inter-particle interactions [170]. In the same vein, a temporal modulation results in a minimized decoherence of a spin-half particle coupled to a bath [171]. From the above examples, we conclude that periodic perturbations are useful in exploring exciting physical phenomena in quantum few-body and many-body systems. Combined with the tunable engineering of ultracold atoms, periodic driving establishes itself as a flexible tool to coherently manipulate the states of quantum systems.

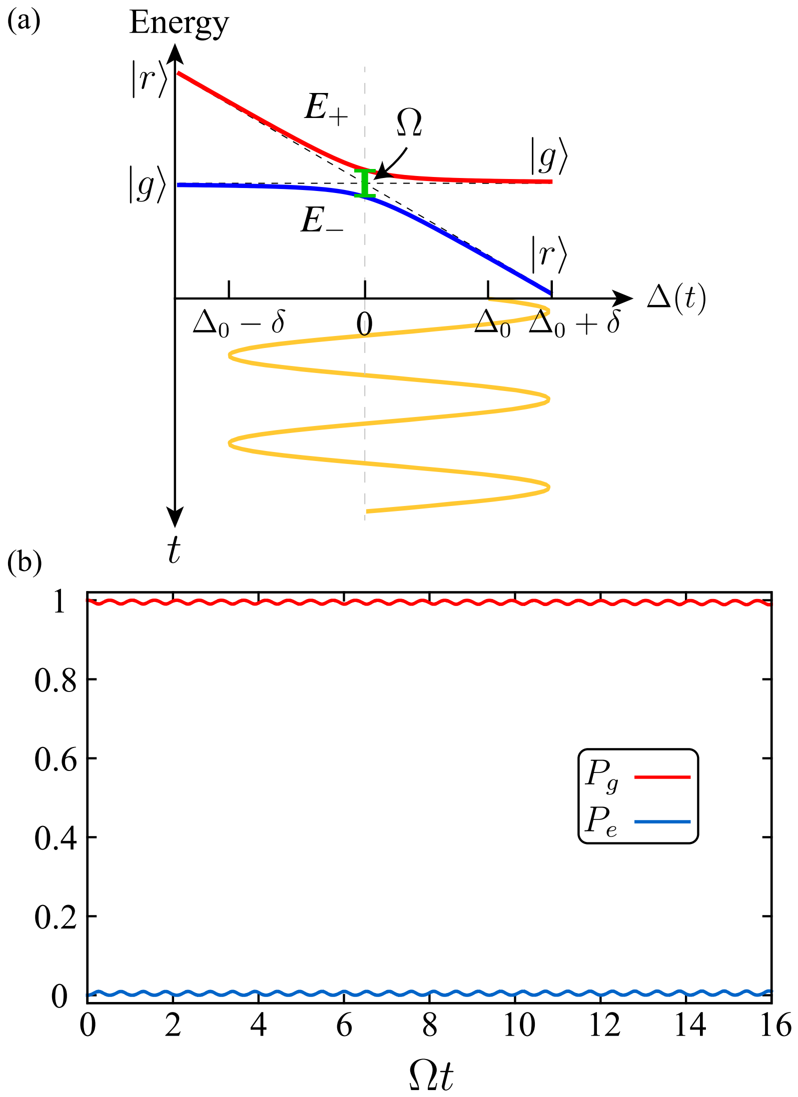

Figure 1.8: (a) Detuning is periodicaly varied across the avoided level crossing in a two-level atom, as $\Delta(t) = \Delta_0 + \delta \sin(\omega t)$ where Δ_0 is the initial detuning, δ is the strength and ω is the frequency of modulation (b) The populations of ground and excited states for periodically varying detuning with $\Delta_0 = 0, \omega/\Omega = 6.0, \delta/\omega = 2.404$.

In Chapter 5, we study the population trapping extensively in a periodically driven Rydberg pair. We observe that the Rydberg-Rydberg interactions lead to a state-dependent population trapping.

1.5 Quantum Correlations

Entanglement is not only a useful resource in quantum information science and quantum computations [172], but is often used to characterize quantum phases in condensed matter systems [173–180], including topologically ordered ones [178, 181–183], and spin liquids [184, 185]. Interestingly, even the elementary two-qubit systems can reveal non-trivial features such as revivals [186], decay [187] and sudden death of entanglement [188, 189]. There is, however, no unique measure of entanglement, and quantifying and characterizing entanglement is an active area of research [172]. The von Neumann entropy is one "good" measure to characterize a pure state's entanglement [190, 191]. Another disparate way to measure purely quantum correlations is through the *quantum discord* [192, 193]. Quantum discord captures non-classical correlations different from entanglement entropy. Such non-classical correlations can allow for computational speed-up even with single qubit systems [180, 194–196].

To quantify entanglement, we partition the bipartite quantum system equally into subsystems A and B. If the two subsystems are uncorrelated, the state of subsystem A does not depend on the state of subsystem B in any way. In particular, the probability of A being in any of its states does not depend on the state of B, and vice versa. However, if the subsystems are interacting, the quantum state of the composite system cannot be written as a tensor product of the states of A and B which in turn means that the states of A and B are entangled, in general. We look both at the Von-Neumann entanglement entropy, the quantum analogue of Shannon entropy, and quantum discord to describe the quantum correlations. Note that for pure states, the quantum discord turns out to be equal to entanglement entropy [197]. The Von-Neumann entanglement entropy of the subsystems is,

$$\mathcal{S}_A = -\operatorname{Tr}(\hat{\rho}_A \log_2 \hat{\rho}_A), \quad \text{and} \quad \mathcal{S}_\mathrm{B} = -\operatorname{Tr}(\hat{\rho}_\mathrm{B} \log_2 \hat{\rho}_\mathrm{B}), \tag{1.24}$$

with $\hat{\rho}_A$ ($\hat{\rho}_B$) being the reduced density matrix for subsystem A (B). A reduced density matrix can be obtained by taking partial trace over the complete density matrix, $\hat{\rho} = |\psi(t)\rangle\langle\psi(t)|$,

$$\hat{\rho}_A = -\operatorname{Tr}_B(\hat{\rho}), \quad \text{and} \quad \hat{\rho}_\mathrm{B} = -\operatorname{Tr}_\mathrm{A}(\hat{\rho}). \tag{1.25}$$

Partial trace is how we describe 'the state of subsystem(s)' when the joint quantum state is correlated. Any outcome of a measurement on A (or B) can be determined by the reduced density matrix $\hat{\rho}_A$(or $\hat{\rho}_B$). Nevertheless, if ρ_A is a pure state, the entanglement is zero. The easiest way to calculate the von Neumann entropy $\mathcal{S}_A$ is by taking the trace $\operatorname{Tr}\left(\hat{O}\right)$ in the eigenbasis of $\hat{\rho}_A$: $|\lambda_{1,2}\rangle$ which has eigenvalues $\lambda_{1,2}$. This gives us

$$\mathcal{S}_A = -\sum_{i=1}^{2} \lambda_i \log_2 \lambda_i. \tag{1.26}$$

The same is valid for $\mathcal{S}_B$. For a pure state of the system $(\operatorname{Tr}(\rho)^2 = 1)$, the entropy of the complete system is zero $S_{AB} = 0$, and that of the subsystems are equal to each other, $\mathcal{S}_A = \mathcal{S}_B$.

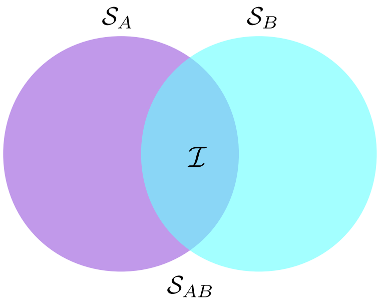

Figure 1.9: Quantum Mutual Information: $\mathcal{I} = \mathcal{S}_A + \mathcal{S}_B - \mathcal{S}_{AB}$ where $\mathcal{S}_A$ ($\mathcal{S}_B$) is the Von Neumann entropy of the subsystem A (B), and $\mathcal{S}_{AB}$ is the joint entropy of A and B.

Another quantity which is useful to quantify entanglement in not only pure states $(\mathrm{Tr}(\rho)^2 = 1)$ but also mixed states $(\mathrm{Tr}(\rho)^2 < 1)$ is quantum discord, a measure of *quantumness* of correlations. Quantum discord has its roots in Quantum and Classical Information theory. In classical Information theory, the Shannon entropy $H(p) = \sum_i p_i \log p_i$ is used to quantify information in a subsystem A (or B). Correlation between subsystems A and B are defined by the classical mutual information $\mathcal{I} = H_A + H_B - H_{AB}$ where H_{AB} is the joint entropy of A and B. Bayes' rule says that the conditional entropy is $H_{B|A} = H_{AB} - H_B$ which is the information about B given that we know about A. The quantum mutual information is then equivalent to $\mathcal{J} = H_B - H_{B|A}$. Although in the classical information theory $\mathcal{I} = \mathcal{J}$, the same is not true in its quantum analogue. In Quantum Information theory, the Von Neumann entropy is used to measure the information in a quantum state. The quantum mutual information is then defined as $\mathcal{I} = \mathcal{S}_A + \mathcal{S}_B - \mathcal{S}_{AB}$. However the quantum version of $\mathcal{J}(B : A) = \mathcal{S}_B - \mathcal{S}_{B|A}$, requires the knowledge of conditional entropy $\mathcal{S}_{B|A}$ which is the entropy of subsystem B after a measurement has been performed on A. Each measurement fundamentally alters the state of the system ρ_{AB}. Every possible outcome is one of the vectors comprising the basis of eigenvectors of the chosen observable. The observable can be any self-adjoint operator however we focus on projective measurement which are defined by $\{\hat{\Pi}^i_A = |i\rangle_A\langle i|_A\}$ whose probability of outcome is $p^i = \mathrm{Tr}_{AB}[(\hat{\Pi}^i_A \otimes \mathbb{1}_B)\rho_{AB}]$. After each measurement the state of subsystem B is given by $\hat{\rho}^i_B = \mathrm{Tr}_A[(\hat{\Pi}^i_A \otimes \mathbb{1}_B)\rho_{AB}(\hat{\Pi}^i_A \otimes \mathbb{1}_B)]/p^i$. The conditional entropy of the subsystem B is an average of all such outcomes weighted by probability p_i, $\mathcal{S}_{B|A} = \sum_i p^i S(\hat{\rho}^i_B)$. As the conditional entropy is still basis dependent, the quantum information $\mathcal{J}(B : A)$ is not equal to the quantum mutual information $\mathcal{I}$. However, the inequality between the two ways provides an opportunity to find basis independent classical correlations [192]

$$\tilde{\mathcal{J}}(B : A) = \max_{\{\hat{\Pi}^i_A\}} \left[\mathcal{S}_B - \sum_i p^i \mathcal{S}_{B|i}\right] = \mathcal{S}_B - \min_{\{\hat{\Pi}^i_A\}} \left[\sum_i p^i \mathcal{S}(\hat{\rho}^i_B)\right] \tag{1.27}$$

by maximizing ($\max_{\{\hat{\Pi}_A^i\}}$) across all the possible orthonormal measurement bases $\{\hat{\Pi}_A^i\}$ of the subsystem A. In particular, for two-level atoms the orthonormal measurement bases is extensively spanned by $|i\rangle = \cos\theta|g\rangle + e^{i\phi}\sin\theta|r\rangle$ and $|j\rangle = \cos\theta|g\rangle - e^{i\phi}\sin\theta|r\rangle$, upon varying $\theta \in [-\pi/2, \pi/2]$, and $\phi \in [0, 2\pi)$ with N_θ and N_ϕ values respectively. The minimization is performed over all possible combinations of N_θ and N_ϕ values,

$$\min_{\{\hat{\Pi}_A^k\}} \left(\mathcal{S}_{B|A}\right) = \min_{\{N_\phi, N_\theta\}} \left(p^i \mathcal{S}(\rho_B^i) + p^j \mathcal{S}(\rho_B^j)\right). \tag{1.28}$$

which gives us $\mathcal{S}_{B|A} = 0$ and $\tilde{\mathcal{J}}(B:A) = \mathcal{S}_B$. Similarly one can obtain $\tilde{\mathcal{J}}(A:B)$ where the measurement is performed on subsystem B rather than A. The *quantumness* of correlations can then be found by $\mathcal{I} - \tilde{\mathcal{J}}$. The quantum discord can be defined corresponding to both A and B as,

$$\mathcal{D}(A:B) = \mathcal{I} - \tilde{\mathcal{J}}(A:B), \tag{1.29}$$

and $\mathcal{D}(B:A) = \mathcal{I} - \tilde{\mathcal{J}}(B:A)$. In general, the two are not equal to each other as they are basis-dependent. For a pure system of two interacting two-level atoms, we get $\mathcal{D}(A:B) = \mathcal{S}_A$ and $\mathcal{D}(B:A) = \mathcal{S}_B$. Due to the atoms being identical, $\mathcal{S}_A = \mathcal{S}_B$ and $\mathcal{D}(A:B) = \mathcal{D}(B:A)$. In summary, the quantum conditional entropy is eigenbasis dependent which results in a disagreement between $\mathcal{I}$ and $\mathcal{J}(B:A)$ (or $\mathcal{J}(A:B)$). The difference between these two defines quantum discord. For a bipartite pure system described by $|\psi(t)\rangle$, the quantum discord is same as the Von Neumann entanglement entropy, i.e., $\mathcal{D}(A:B) = \mathcal{D}(B:A) = \mathcal{S}_A = \mathcal{S}_B$ [197].

However, for a dissipative system, the system is driven to a mixed state even when initially prepared in a pure state. For a mixed state system, the discord is no longer equal to entanglement entropy; and, in fact, since $\mathcal{S}_{A,B}$ fails to distinguish between classical and quantum correlations, it has been ruled out as a good measure of quantum correlations [190, 198, 199]. On the other hand, quantum discord remains a good measure. For a mixed state the conditional entropy is not symmetric for all states [174], and therefore, in general, $\mathcal{D}(A:B) \neq \mathcal{D}(B:A)$. An exception occurs when the states are symmetric under the exchange of A and B allowing $\mathcal{D}(A:B) = \mathcal{D}(B:A)$ to hold.

In Chapter 3, we study the growth and dynamics of quantum correlations in coherent dynamics. Furthermore, in Chapter 5, we analyze the dynamics of the entangled bell state when the two-atom system is driven periodically.

1.6 Issues covered in this thesis

In this thesis, we study systems of two interacting Rydberg atoms and propose mechanisms to engineer the quantum state of the collective system in a frozen pair of Rydberg atoms where each atom is considered to be trapped in an optical tweezer.

In chapter 2, we study the population and entanglement dynamics of two interacting Rydberg atoms by varying their Rabi frequency independently by distinct laser fields. We find a novel phenomenon that we term as Rydberg-biased freezing where amplification of the Rabi frequency of one atom at large Rydberg-Rydberg interaction freezes the dynamics in the second atom. Furthermore, we discuss a double-peak structure in the doubly Rydberg state population as a function of interaction for very small offsets in the Rabi frequencies. We then study the quantum correlations in the Rydberg pair and demonstrate the control over correlations that manifests due to attenuation of Rabi frequency of the second atom. Lastly, we look at the dissipative dynamics in the system.

In chapter 3, we propose a time-dependent atom-laser detuning of linear variation to manipulate the final occupation probabilities of the two-atom states. This brings new ways to control the state dynamics of the Rydberg pair which may be useful in quantum state preparations. By varying the Rydberg-Rydberg interaction strengths, the system can emulate different three-level LZ models, for instance, bow-tie and triangular LZ models. The LZ dynamics exhibit nontrivial dependence on the initial state, the quench rate, and the interaction strengths. We also use the analytical technique of the Adiabatic Impulse model to reveal the web of phases in the dynamics. We also mention the emergent $SU(3)$ symmetry in the two-atom setup.

In chapter 4, we study the effect of periodic atom-laser detuning on the pair of Rydberg atoms. First, we review the single two-level periodically driven atom. We highlight the similarity of the final state population with the intensity pattern obtained in an antenna array. In the two atom setup, we test the validity of analytical results of population dynamics obtained using the Adiabatic-Impulse approximation under periodically drive. We show that when all avoided crossings are incorporated, the dynamics is well captured by AIA. The latter may find applications in quantum state preparation, quantum phase gates, and atom interferometry.

In chapter 5, we study the interesting phenomenon of dynamical stabilization which is observed at certain parameter regimes when periodically driving the Rydberg pair. The periodic modulation of the atom-light detuning effectively suppresses the Rabi couplings. We characterize the phenomenon of population trapping and dynamical localization using Floquet quasienergies and the Inverse participation ratio of Floquet states. We elucidate the phenomenon of state-dependent population trapping which emerges due to Rydberg-Rydberg interactions. We further specify the regimes where populations in experimentally significant states such as product and bell entangled states can be frozen for a significantly longer duration. The behaviour of the entangled states is further characterized by the bipartite entanglement entropy.

Chapter 2

Dynamics and quantum correlations in two independently driven Rydberg Atoms

The current chapter is an adaptation of the research article "Dynamics and quantum correlations in two independently driven Rydberg atoms with distinct laser fields" [86]. We study both the population and quantum correlation dynamics in a pair of Rydberg atoms where the Rabi coupling of the atoms with laser is non-identical. The first part of the chapter deals with coherent dynamics and in the regime of strong interactions, we are introduced to a novel phenomenon: an amplification in the Rabi frequency of one atom freezes the dynamics of the second atom which at the same time is accompanied by reduced quantum correlations. We call this phenomenon as *Rydberg-biased freezing.* Alongside, the weak-interaction case is also investigated and a peculiar non-monotonic behaviour is obtained. We accompany the above numerical results with the analytical results obtained by an effective Hamiltonian. The later part of the chapter deals with a more realistic scenario of spontaneous emission and we study dissipative population and quantum correlation dynamics in the system.

2.1 Introduction

The setup of Rydberg atoms driven by *identical* lasers has been a usual scenario in many of the Rydberg-based experimental studies. Of primary interest have been studies in strongly interacting Rydberg atoms which have found applications from quantum many-body physics to quantum information protocols. However, in recent years, the technology has advanced in such a way that it has become possible to probe and manipulate the Rydberg atoms individually using optical tweezers and optical microtraps [51, 84, 200] which enables further control over the system. For instance, single atom addressing by *distinct* lasers has been employed to study decay processes in individually trapped atoms [74], achieve controlled local operations [84], entangle two different Rydberg isotopes at a nearby site [201], quantify the imperfections in Rabi oscillations [202], control resonant dipole-dipole interaction between Rydberg atoms [79] as well as to implement fast entangled gates between identical Rydberg atoms [81, 203, 204]. Such technological advancements strive to reach new regimes and discover new tools which would ultimately allow addressing the unsolved problems in many-body physics and quantum information protocols.

We are motivated by the potential offered by distinct lasers on ultracold atoms, and thus conduct a systematic study of the effect of applying distinct lasers on a minimal setup of two ultracold trapped Rydberg atoms. In particular, we focus on the case wherein the interacting atoms are driven at different Rabi frequencies. The Rabi frequencies for the atoms can be simply tuned by illuminating the two atoms with different light field intensities. We show that the offset in Rabi frequency could be an experimental tool to control the state populations and quantum correlations.

We study the population and entanglement dynamics of the two-atom system. We begin by identifying intriguing features in the state population dynamics in the strongly interacting regime where on amplifying the Rabi frequency of one of the Rydberg atoms the other atom freezes to its ground state. Later, we analyze the state dynamics in the weakly interacting regime where a small Rabi-frequency offset causes a non-monotonic behaviour at small interaction values. We further use an effective Hamiltonian picture in different limiting cases of system parameters to capture the physics simplistically and intuitively. We further analyze the temporal evolution of Von-Neumann entanglement entropy or the quantum discord and demonstrate that a Rabi-frequency offset is a viable tool to control quantum correlations in the composite two-qubit systems. Lastly, we consider the spontaneous emission from the Rydberg state and analyze the population dynamics, steady-state purities, and quantum correlations.

2.2 Setup and Model

We consider two identical neutral two-level atoms with electronic ground state $|g\rangle$ and a Rydberg state $|r\rangle$. Each is strongly confined in independent optical microtraps separated by a distance R [see Fig. 2.1]. Both are driven by distinct but resonant light fields having a Rabi frequency Ω for the first atom, and $\Omega+\omega$ for the second atom, where ω is the offset in Rabi-frequencies henceforth called as Rabi-offset. The strength of Rydberg-Rydberg interaction between the excited atoms is given by $V_0 = C_6/R^6$. In the frozen gas limit, the internal state dynamics of the

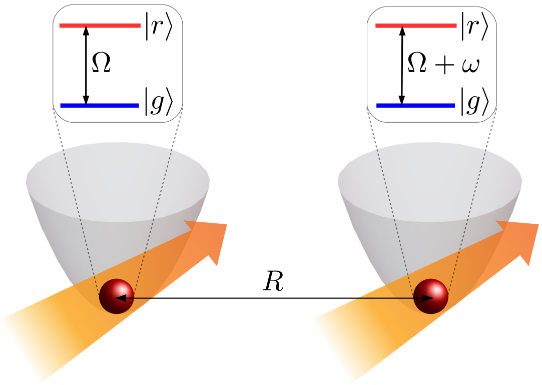

Figure 2.1: A schematic of two Rydberg atoms trapped in distinct microtraps with a separation of R. Each of the atoms is driven independently by different laser fields while resonantly coupling the ground state $|g\rangle$ to the same Rydberg state $|r\rangle$.

quantum system is described by the Hamiltonian ($\hbar = 1$):

$$\hat{H} = \frac{\Omega}{2}\sum_{i=1}^{2}\hat{\sigma}_x^{(i)} + \frac{\omega}{2}\hat{\sigma}_x^{(2)} + V_0\hat{\sigma}_{rr}^{(1)}\hat{\sigma}_{rr}^{(2)}. \tag{2.1}$$

where $\hat{\sigma}_{rr}^{(i)} = |r^{(i)}\rangle\langle r^{(i)}|$ is the atomic projection operator, and $\hat{\sigma}_x^{(2)} = \hat{\sigma}_{rg}^{(2)} + \hat{\sigma}_{gr}^{(2)}$ is the Pauli's X operator with $\hat{\sigma}_{ab}^{(2)} = |a^{(2)}\rangle\langle b^{(2)}|$ being the state transition operator corresponding to the second atom. We obtain the coherent dynamics of the composite system by numerically solving the Schrödinger equation, $i\partial/\partial t|\psi(t)\rangle = \hat{H}|\psi(t)\rangle$. The initial state is chosen as both atoms in their electronic ground state, $|\psi(t=0)\rangle = |gg\rangle$. We work in the two-atom product basis $\{|gg\rangle, |gr\rangle, |rg\rangle, |rr\rangle\}$ whose energy levels alongwith their Rabi-couplings are outlined in Fig. 2.2. We also pictorially depict that the $|rr\rangle$ state is getting populated via $|gr\rangle$ and $|rg\rangle$ states from the initial state $|gg\rangle$.

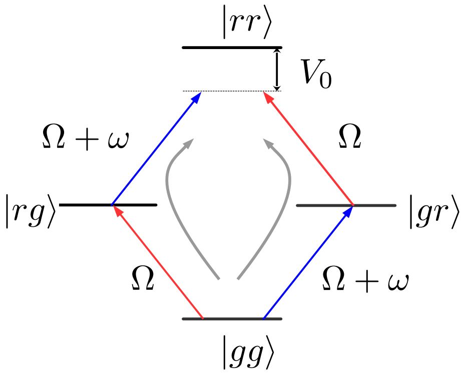

Figure 2.2: The figure shows energy level scheme of composite two-atom system in the product basis $\{|gg\rangle, |gr\rangle, |rg\rangle, |rr\rangle\}$ with their associated Rabi couplings. The doubly excited state $|rr\rangle$ is populated from ground state $|gg\rangle$ via $|gr\rangle$ and $|rg\rangle$ as shown by curved arrows. V_0 is the Rydberg-Rydberg interaction which detunes the $|rr\rangle$ state from resonance.

2.3 State Population Dynamics

In this section, we investigate how the Rydberg excitation dynamics change for a non-zero Rabi-offset ω. We analyze both the temporal evolution and the long time-averaged of occupation probability in the product basis states $\{|gg\rangle, |gr\rangle, |rg\rangle, |rr\rangle\}$ obtained after solving the system numerically. The population in each state is given by the projection of final state $|\psi(t)\rangle$ onto it, $P_{\alpha\beta}(t) = |\langle\alpha\beta|\psi(t)\rangle|^2$ where $\alpha, \beta \in \{r, g\}$ and the time-averaged population is $\bar{P}_{\alpha\beta} = \frac{1}{\tau}\int_0^\tau P_{\alpha\beta}(t)dt$.

2.3.1 Populations at large interaction strengths

In the regime of strong interaction $V_0/\Omega \gg 1$, the doubly Rydberg $|rr\rangle$ state gets detuned from resonance and leads to Rydberg blockade wherein the population coherently oscillates between $|gg\rangle$ and entangled state $|+\rangle = (|gr\rangle + |rg\rangle)/\sqrt{2}$ [see Sec. 1.3]. Further introducing a Rabi-offset ω breaks the symmetry between the two atoms, and therefore not only the entangled state $|+\rangle$ lose significance but the population among non-identical $|gr\rangle$ and $|rg\rangle$ states is controlled by the Rabi-offset ω. Note however that, the blockade doesn't necessarily result in the emergence of symmetric entangled state $|+\rangle$ which happens in the special case of $\omega = 0$. For a finite value of ω, the second atom is driven strongly compared to the first atom which causes an enhancement of P_{gr} at the cost of P_{rg}, as shown in Fig. 2.3(a). Interestingly when a large Rabi-offset is applied $\omega/\Omega \gg 1$ to strongly interacting atoms $V_0/\Omega \gg 1$, the population of the weakly driven excited state P_{rg} minimizes indicating that the dynamics of the first atom nearly freezes to its ground state. Subsequently, the system displays coherent Rabi oscillations between the ground state $|gg\rangle$ state and strongly driven excited $|gr\rangle$ state whereas both $P_{rr} \approx 0$ and

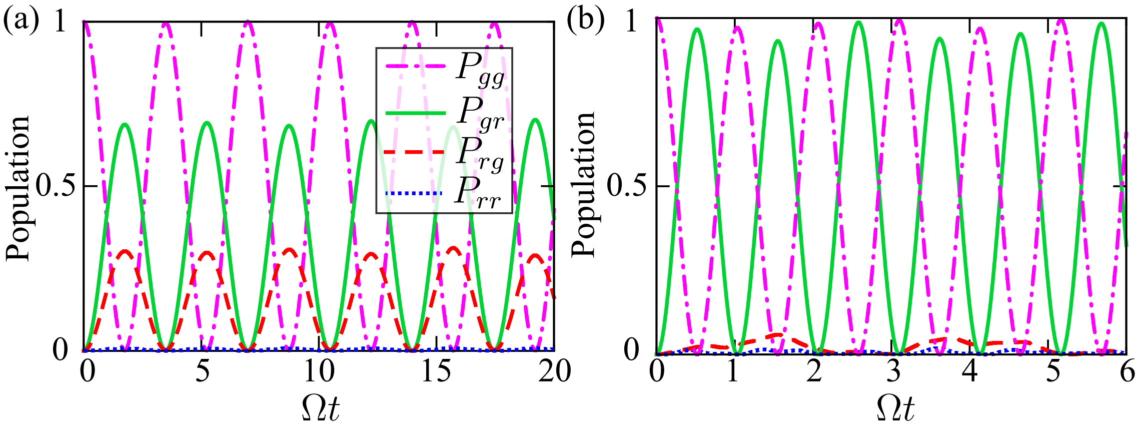

Figure 2.3: The population dynamics for strongly interacting case $V_0/\Omega = 10$ with (a) small Rabi-offset $\omega/\Omega = 0.5$ which causes asymmetry in P_{gr} and P_{rg}, (b) large Rabi-offset $\omega/\Omega = 5$ which freezes the dynamics of state $|rg\rangle$. P_{rr} is suppressed at strong interactions causing Rydberg-blockade.

$P_{rg} \approx 0$, as shown in Fig. 2.3(b). In effect, only the atom driven by an amplified Rabi frequency gets excited and the dynamics of the other atom freezes to its ground state [also see Fig. 2.4]. Remarkably, we can thus freeze the dynamics of one atom by selectively amplifying the Rabi frequency of the second atom. Note that the freezing of the first atom emerges as a combined effect of both the Rydberg blockade from large interactions and the strong driving in the second atom, and we designate this phenomenon as Rydberg-biased freezing.

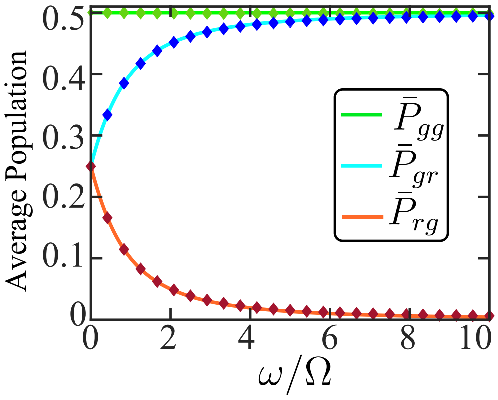

Figure 2.4: The time average populations as a function of ω/Ω for $V_0 = 25\Omega$, and $\Omega\tau = 5000$. Since $V_0 \gg \Omega$, the numerical results (solid points) are in excellent agreement with the analytic results (solid lines) given in Eqs. (2.7)-(2.9)

A complete variation of ω/Ω and V_0/Ω is shown in the time-averaged population plots in Fig. 2.5 which shows fascinating attributes. The regime of $\{\omega/\Omega, V_0/\Omega\} \gg 1$ is that of Rydberg-biased freezing where both the $|gg\rangle$ and $|gr\rangle$ states have high occupation probabilities while the populations in $|rr\rangle$ and $|rg\rangle$ states are suppressed. At large interactions V_0 but small Rabi-offset ω, $P_{gr} \geqslant P_{rg}$ with a non-zero P_{rg}, and both the $|gr\rangle$ and $|rg\rangle$ states coherently oscillate with $|gg\rangle$; while the $|rr\rangle$ state population remains minimal. We further note in Fig. 2.5(b) that the time-averaged $|rr\rangle$ state population is minimally affected by Rabi-offset ω, except at very small V_0 and ω which we discuss in the Sec. 2.3.2. Nevertheless, for strongly interacting atoms $V_0/\Omega \gg 1$, the $|rr\rangle$ state population vanishes irrespective of the Rabi-offset ω value. As a consequence, we conclude that the condition of blockade $V_0 \gg \Omega$, remains unchanged by the Rabi-offset ω. It is the lowest of the two Rabi-couplings which determine the blockade. For small Rabi-offsets, particularly at large $|V_0|$, $\bar{P}_{gr}$ increases at the cost of $\bar{P}_{rg}$ upon increasing the Rabi-offset ω since the second atom is more strongly driven.

2.3.2 Populations at small interaction strengths

To analyze dynamics in this regime, we first look at the exactly solvable case of non-interacting atoms $V_0 = 0$ having a Rabi-offset ω. In the absence of Rydberg-Rydberg

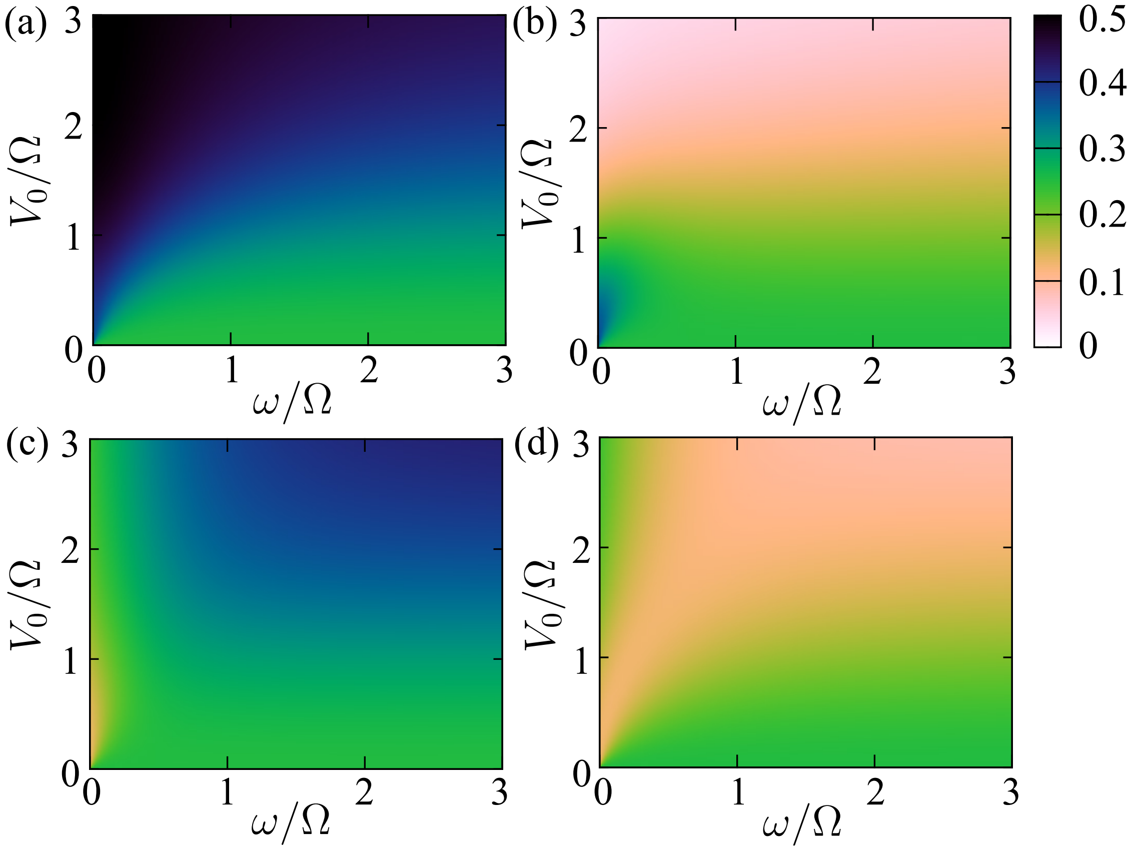

Figure 2.5: Color density plot for long time averaged populations: (a) $\bar{P}_{gg}$, (b) $\bar{P}_{rr}$, (c) $\bar{P}_{gr}$ and (d) $\bar{P}_{rg}$ plotted against V_0/Ω and ω/Ω conditioned to $|\psi(t=0)\rangle = |gg\rangle$ till time $\Omega\tau = 5000$. For stronger interactions V_0/Ω and large Rabi-offset ω/Ω both $\bar{P}_{rr}$ and $\bar{P}_{rg}$ are negligible, leading to Rydberg-biased freezing. Also note in (b) that the blockade condition only gets weakly affected due to Rabi-offset ω.

interactions, population in the two-atom basis states are obtained by a product of the populations in corresponding single-atom states *i.e.* $P_{\alpha\beta}(t) = P_\alpha(t)P_\beta(t)$. The single two-level atom population is well known in the Rabi-problem [see Sec. 1.4.1]. For the two-atom system having initial state $|\psi(t=0)\rangle = |gg\rangle$, we obtain

$$P_{gg}(t) = \cos^2\frac{\Omega t}{2}\cos^2\frac{(\Omega+\omega)t}{2}, \tag{2.2a}$$

$$P_{gr}(t) = \cos^2\frac{\Omega t}{2}\sin^2\frac{(\Omega+\omega)t}{2}, \tag{2.2b}$$

$$P_{rg}(t) = \sin^2\frac{\Omega t}{2}\cos^2\frac{(\Omega+\omega)t}{2}, \tag{2.2c}$$

$$P_{rr}(t) = \sin^2\frac{\Omega t}{2}\sin^2\frac{(\Omega+\omega)t}{2}. \tag{2.2d}$$

In the absence of a Rabi-offset the time-averaged populations are

$$\bar{P}_{gg} = \bar{P}_{rr} = 0.375, \bar{P}_{gr} = \bar{P}_{rg} = 0.125, \quad \text{for} \quad \omega = 0. \tag{2.3}$$

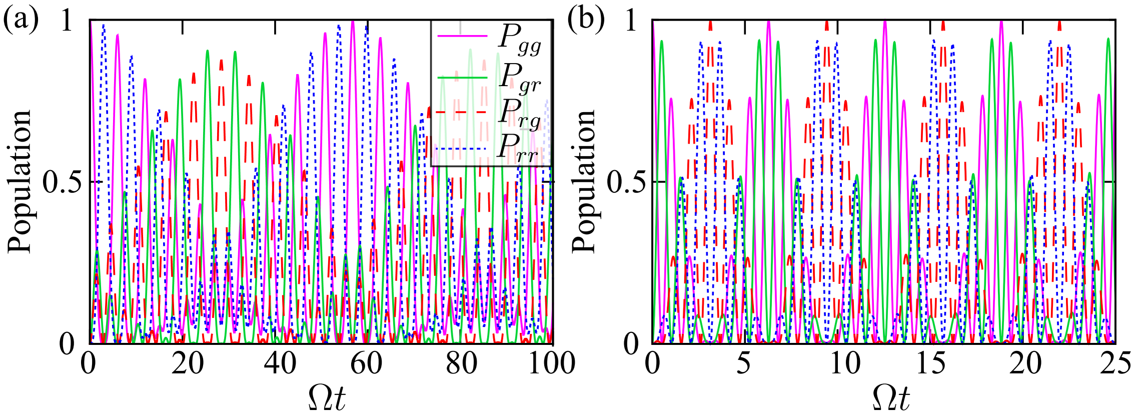

Figure 2.6: The population dynamics for $V_0/\Omega = 0.1$ with (a) a small Rabi-offset $\omega/\Omega = 0.1$ and (b) a large Rabi-offset $\omega/\Omega = 5.0$. For small Rabi-offset, the faster oscillations (having frequency $\sim \Omega$) exist between $|gg\rangle \leftrightarrows |rr\rangle$, and $|gr\rangle \leftrightarrows |rg\rangle$, with a small envelope frequency ($\sim \omega$). For the large Rabi-offset, the faster oscillations with frequency ($\sim \omega$) exist between the strongly coupled states $|gg\rangle \leftrightarrows |gr\rangle$, and $|rg\rangle \leftrightarrows |rr\rangle$, with a faster envelope frequency ($\sim \Omega$), as visible from the time-scale.

Their higher doubly-ground and doubly-excited probabilities are due to in-phase but independent Rabi-oscillation of each atom. As soon as a non-zero Rabi-offset is present, the atoms' Rabi oscillations mismatch and it manifests in an equal occupation probability among the four basis states,

$$\bar{P}_{gg} = \bar{P}_{rr} = \bar{P}_{gr} = \bar{P}_{rg} = 0.25 \quad \text{for} \quad \omega \neq 0. \tag{2.4}$$

We further discuss the case of finite but small interactions $V_0 \ll \Omega$. The time-evolution of populations for the initial state $|gg\rangle$ is shown in Fig. 2.6. Upon changing the Rabi-offset from small to large values, key features characterizing the dynamics change. For a small Rabi-offset, the faster oscillations exist between $|gg\rangle \leftrightarrows |rr\rangle$, and $|gr\rangle \leftrightarrows |rg\rangle$ state having frequency $\sim \Omega$. Additionally, the dynamics has another smaller envelope frequency ($\sim \omega$) during which the system goes from a predominantly $\{|gg\rangle, |rr\rangle\}$ to $\{|gr\rangle, |rg\rangle\}$. On the other hand, for a large Rabi-offset the faster oscillations with frequency ($\sim \omega$) exist between the strongly coupled states $|gg\rangle \leftrightarrows |gr\rangle$, and $|rg\rangle \leftrightarrows |rr\rangle$, with a faster envelope frequency ($\sim \Omega$). A large Rabi-offset not only governs the fast frequency but the states involved in faster oscillations get switched. Note however that the population in neither the $|rg\rangle$ nor $|rr\rangle$ state get suppressed at small or large Rabi-offsets for small interactions. It affirms the notion that Rydberg-biased freezing [see Sec. 2.3.1] is a phenomenon central to strongly interacting systems.

An intriguing feature emerges for a small Rabi-offset in the weakly interacting regime. A non-monotonic behaviour in a time-averaged population of doubly excited state $\bar{P}_{rr}$ and that of excitation in second-atom $\bar{P}_{gr}$ can be seen near the

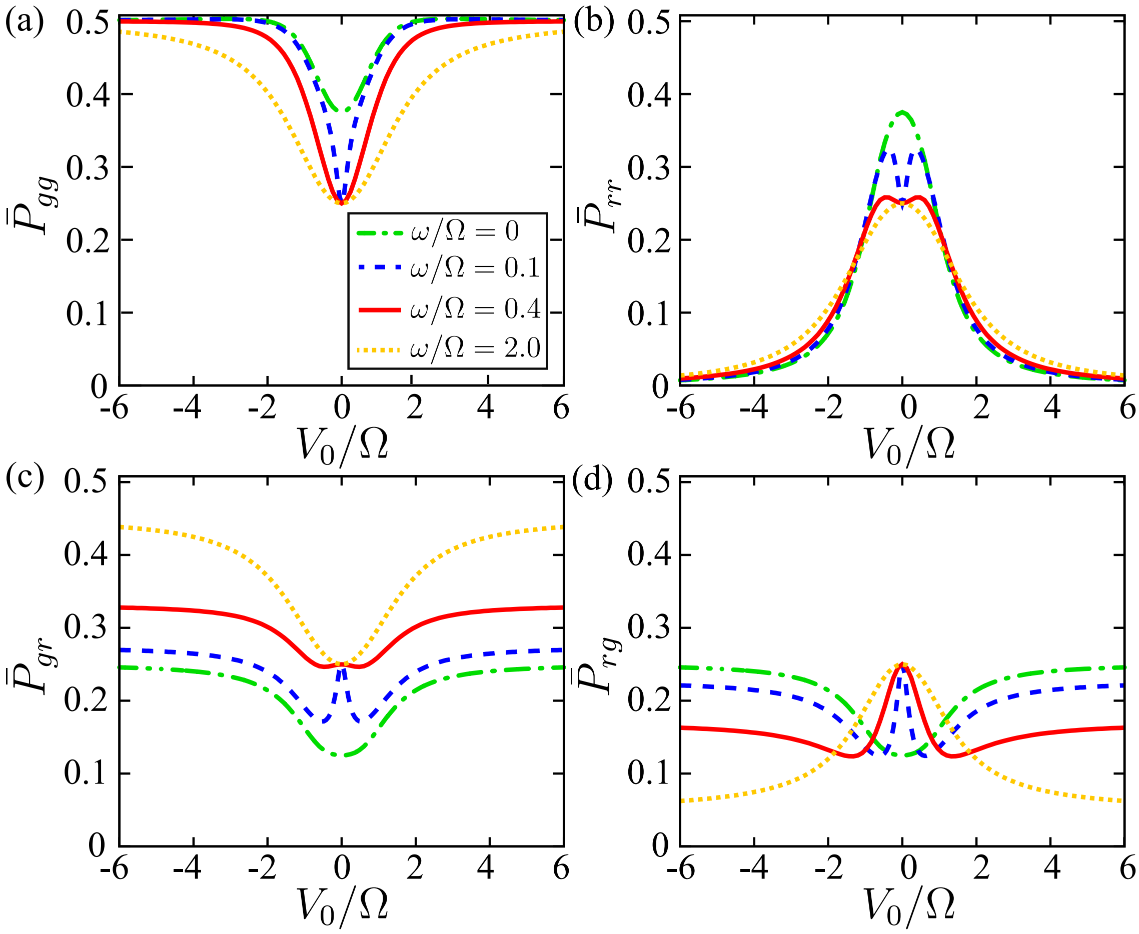

Figure 2.7: The time average populations: (a) $\bar{P}_{gg}$, (b) $\bar{P}_{rr}$, (c) $\bar{P}_{gr}$ and (d) $\bar{P}_{rg}$ as a function of V_0/Ω for different ω/Ω, with $\Delta = \delta = 0$, $|\psi(t=0)\rangle = |gg\rangle$ and $\Omega\tau = 5000$. For very small values of ω/Ω, the populations $\bar{P}_{rr}$, $\bar{P}_{rg}$ and $\bar{P}_{gr}$ depend non-monotonously on $|V_0|$.

origin of Figs. 2.5(b) and 2.5(c). To gain more insights into this behaviour, we show explicitly the time-averaged populations as a function of V_0/Ω for different values of ω/Ω in Figs. 2.7. Without a Rabi-offset, $\bar{P}_{rr}$ exhibits a Lorentzian profile when plotted as a function of interaction strength V_0. For $\omega = 0$ and $V_0 \neq 0$, the population gets transferred from the initial ground state $|gg\rangle$ via the symmetric entangled state $|+\rangle = (|gr\rangle + |rg\rangle)/\sqrt{2}$ to the doubly Rydberg state $|rr\rangle$. Upon increasing the interaction strength $|V_0|$, the $|rr\rangle$ state slowly becomes off-resonant with the light field due to interaction-induced energy-shift, and consequently a time-averaged population in $|rr\rangle$ state $\bar{P}_{rr}(t)$ decrease, resulting in a Lorentizan profile. On the other hand, the population of entangled state $\bar{P}_{+}$ as well as that of doubly ground state P_{gg} increase, saturating to 0.5 in limit of large $|V_0|$ [see Figs. 2.7]. For a finite Rabi-offset $\omega \neq 0$, the symmetry between atoms and hence $|gr\rangle$ and $|rg\rangle$ gets broken leading to $\bar{P}_{gr} \neq \bar{P}_{rg}$. As a result, the Lorentzian profile of $\bar{P}_{gr}, \bar{P}_{rg}$ and $\bar{P}_{rr}$ gets deformed. The doubly excited state population, in particular, shows a non-monotonic behaviour having peaks at small interaction strengths ($\pm V_0^p$), as shown

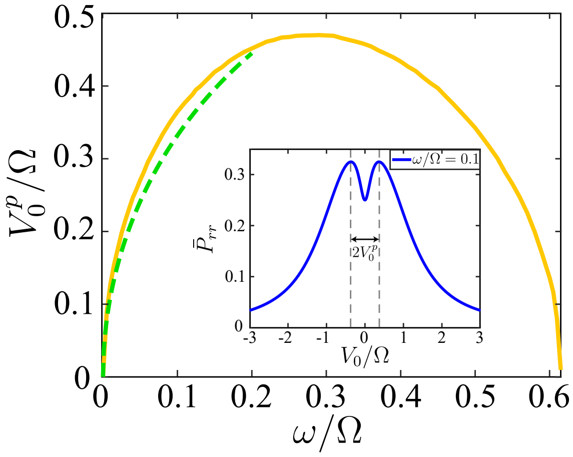

Figure 2.8: The half of the peak separation V_0^P in $\bar{P}_{rr}$ (see inset) as a function of ω/Ω. The dashed line is the analytical result given by Eq. (2.30) obtained for small ω.

in Figs. 2.7(b) and 2.8. The splitting in $\bar{P}_{rr}$ happens due to a competition between the terms associated with V_0 and ω in Eq. (2.1) for small values of V_0 and ω. The non-monotonic behaviour in $\bar{P}_{gr}, \bar{P}_{rg}$ as well as split in $\bar{P}_{rr}$ eventually saturates to another Lorentizian profile with a lowered maxima value $(= 0.25)$ at larger values of Rabi-offsets $(\omega \gg 1)$.

Focusing on $\bar{P}_{rr}$, for small Rabi-offsets $\omega \ll \Omega$ such that $\bar{P}_{gr} \approx \bar{P}_{rg}$, a small $|V_0|$ compensates for the effect from a small Rabi-offset ω, leading to the recovery of $\bar{P}_{rr}$. However, a further increase in V_0 leads to interaction-induced shift of $|rr\rangle$ state (blockade effect) and $\bar{P}_{rr}$ starts to decrease thereby giving rise to peak in average population. The maximum value of the peak decreases with increasing ω until there is no longer a peak. However, the separation between peaks $(2V_0^p)$ increases with increasing ω first and later decreases, reaching zero. After this point, V_0 can no longer compensate for the effect of ω, see Fig. 2.8. Hence, when ω remains greater than a certain value, the $|rr\rangle$ state population $\bar{P}_{rr}$ again becomes a Lorentzian function of V_0. The separation between the peaks abide $V_0^p \propto \sqrt{\omega}$ for smaller values of ω. In the Sec. 2.4, we use effective Hamiltonian picture derived in the limit $\{\omega, V_0\} \ll \Omega$, to explain the initial increment of $\bar{P}_{rr}$ in V_0 at small values of ω. Notably, the partial splitting of $|rr\rangle$ state population $\bar{P}_{rr}$ bears resemblance to the Autler-Townes effect [205].

2.4 Effective Hamiltonians

In this section, we derive the effective Hamiltonian picture which also describes the long-time dynamics of the two-atom system in various limits [206, 207].

Case I: $\mathbf{V_0} \gg \{\boldsymbol{\Omega}, \omega\}$ We first consider the strongly interacting regime $V_0 \gg \{\Omega, \omega\}$. Switching to a rotating frame $|\psi'(t)\rangle = \hat{U}|\psi(t)\rangle$ with unitary transformation, $\hat{U} = \exp(iV_0\hat{\sigma}^1_{rr}\hat{\sigma}^2_{rr}t)$ eliminates V_0 in favor of fast oscillations associated with the smaller energies $\{\Omega, \omega\}$. In this frame, the wavefunction $|\psi'(t)\rangle$ satisfies the Schrödinger equation corresponding to the new Hamiltonian, $\hat{H}' = \hat{U}\hat{H}\hat{U}^\dagger + i(d\hat{U}/dt)\hat{U}^\dagger$, where $\hat{H}$ is the same as in Eq. (2.1). Explicitly, the new Hamiltonian is,

$$\begin{aligned}\hat{H}'(t) = \frac{\Omega}{2}\Big[|gg\rangle\langle gr| + |gg\rangle\langle rg| + e^{-iV_0t}(|gr\rangle\langle rr| + |rg\rangle\langle rr|) + \text{H.c.}\Big] \\ + \frac{\omega}{2}\Big[|gg\rangle\langle gr| + |rg\rangle\langle rr|e^{-iV_0t} + \text{H.c.}\Big]. \qquad (2.5)\end{aligned}$$

As the rotated Hamiltonian is time-periodic with periodicity $T = 2\pi/V_0$, it can be expanded perturbatively in T as: $\hat{H}'(t) = \sum_l \hat{H}'_l e^{ilTt}$. An effective (Floquet) Hamiltonian can be obtained by a High Frequency expansion (HFE): $\hat{H}_{eff} = \hat{H}_0 + \sum_{l>0}[\hat{H}'_l, \hat{H}'_{-l}]/lT + \mathcal{O}(T^{-2})$ which gives the evolution of the system at stroboscopic times $(2\pi n/V_0)$ [207]. Here $\hat{H}_0$ is the time-independent part of the Hamiltonian. This method is identical to a Schieffer-Wolff Transformation (SWT). Alternatively $\hat{H}_{eff}$ can be obtained using Magnus expansion where the zeroth order term is a single time-period averaged Hamiltonian, $\hat{H}_{eff} = (1/T)\int_0^T \hat{H}'(t)dt$, which is identical to $\hat{H}_0$ [208]. With either of the above methods, we get effective Hamiltonian for the limit $V_0 \gg \{\Omega, \omega\}$ as,

$$\hat{H}^{(V_0)}_{eff} = \frac{(\omega + \Omega)}{2}\hat{\sigma}^1_{gg}\hat{\sigma}^2_x + \frac{\Omega}{2}\hat{\sigma}^1_x\hat{\sigma}^2_{gg}. \qquad (2.6)$$

In obtaining the above Hamiltonian, we essentially have made a rotating wave approximation where the faster oscillating terms are removed while the zeroth-order terms survive [145]. We note that even though we have eliminated the interaction V_0 dependent terms, the effective Hamiltonian $\hat{H}^{(V_0)}_{eff}$ cannot be replaced by a combination of single atom Hamiltonian which means that $\hat{H}^{(V_0)}_{eff}$ represents a correlated system. The two terms in $\hat{H}^{(V_0)}_{eff}$ [Eq. (2.6)] can be interpreted as follows: The first term drives the second atom with Rabi-coupling $\Omega + \omega$ while letting the first atom rest in the ground state. The second term has the reverse true but it drives the first atom with a smaller Rabi coupling Ω. This type of coupling is also called correlated Rabi coupling [137]. An identical phenomenon in an optical lattice is the density-assisted tunnelling of atoms [209]. Notably in Eq. (2.6), for the situation where $\omega \gg \Omega$, the second term reduces to being a small perturbation with the first term contributing primarily to the dynamics. This is exactly the dynamics we observe in Rydberg-biased freezing [see Sec. 2.3.1]. Now we solve the Schrödinger equation corresponding to $\hat{H}^{(V_0)}_{eff}$. At large time scales, the dynamics due to $\hat{H}^{(V_0)}_{eff}$ and due to

$H'(t)$ will coincide.

In the effective Hamiltonian picture, the $|rr\rangle$ state gets removed from the dynamics hence we can truncate our basis to only $\{|gg\rangle, |gr\rangle, |rg\rangle\}$. Here the benefit of using this picture is clear: the Schrödinger equation is now exactly solvable. We solve $i|\dot{\psi'}\rangle = \hat{H}_{eff}^{(V_0)}|\psi'\rangle$ with intial condition $|\psi'(0)\rangle = |\psi(0)\rangle = |gg\rangle$. The initial condition remains unchanged in the transformed frame since at $t = 0$, the unitary transformation operator is Identity $\hat{U}(0) = \mathbb{1}$. We obtain the populations as

$$P_{gg}(t) = \cos^2 \beta t \tag{2.7}$$

$$P_{gr}(t) = \left(\frac{\Omega + \omega}{2\beta}\right)^2 \sin^2 \beta t \tag{2.8}$$

$$P_{rg}(t) = \left(\frac{\Omega}{2\beta}\right)^2 \sin^2 \beta t, \tag{2.9}$$

where $\beta^2 = \left[(\Omega + \omega)^2 + \Omega^2\right]/4$. It is clear from Eqs. (2.8) and (2.9) that for $\omega \ll \Omega$, we get $P_{gr} \approx P_{rg}$, leading to $\bar{P}_{gr} \approx \bar{P}_{rg}$ which is in agreement with the numerical solution obtained and shown in Figs. 2.5. For $\omega \gg \Omega$ we can see that the P_{gr} gets augmented at the cost of P_{rg} at the a large ω while the population in $|gg\rangle$ is not compromised. We also have $P_{gr}(t) \approx \sin^2 \beta t$ with $\beta \approx \omega/2$, which indicate Rabi oscillations in the $|gg\rangle$ state and $|gr\rangle$ state occur with a frequency $2\beta \approx \omega$. Additionally, note that the Rabi-oscillations in states $|gg\rangle$ and $|rg\rangle$, counterintuitively, have an enhanced Rabi-frequency same as 2β but with a much smaller magnitude. The time-averaged populations with the above solution are:

$$\bar{P}_{gg} = 1/2, \bar{P}_{gr} = \left[(\Omega + \omega)/2\beta\right]^2/2, \bar{P}_{rg} = (\Omega/2\beta)^2/2. \tag{2.10}$$

The above analytical solutions are compared with the exact results obtained by numerically solving the Schrödinger equation for the complete Hamiltonian given in Eq. (2.1). Both are in very good agreement with each other within the limit $V_0 \gg \Omega$ [see Fig. 2.4].

Case II: $\omega \gg \{\mathbf{\Omega}, \mathbf{V_0}\}$ We now obtain the effective Hamiltonian in the limit $\omega \gg \{\Omega, V_0\}$ by using a similar methodology as specified above. We move to a rotating frame with a local unitary transformation $\hat{U} = \exp(i\omega\hat{\sigma}_x^{i=2}t/2)$ which acts only on the second atom. The new Hamiltonian in the rotating frame is,

$$\hat{H}' = \frac{\Omega}{2}\sum_{i=1}^{2}\hat{\sigma}_x^i + V_0\left(\frac{1-\cos\omega t}{2}\hat{\sigma}_{rr}^1\hat{\sigma}_{gg}^2 + \frac{1+\cos\omega t}{2}\hat{\sigma}_{rr}^1\hat{\sigma}_{rr}^2 - \frac{\sin\omega t}{2}\hat{\sigma}_{rr}^1\hat{\sigma}_y^2\right). \tag{2.11}$$

An effective Hamiltonian can be obtained by selecting the time-independent terms (HFE) in Eq.(2.11) or equivalently taking a time-average of Eq.(2.11) over a time period of $T = 2\pi/\omega$ (Magnus expansion). The effective Hamiltonian is,

$$\hat{H}^{(\omega)}_{eff} = \frac{\Omega}{2}\sum_{i=1}^{2}\hat{\sigma}^i_x + \frac{V_0}{2}\hat{\sigma}^1_{rr}. \tag{2.12}$$

Note here that $\hat{H}^{(\omega)}_{eff}$ can be seen as a sum of two Hamiltonians corresponding to single atoms where the first atom has a detuning of $V_0/2$ with resonance. Note that, in the new rotating frame the Rabi couplings of both the atoms are reduced to Ω. It is thus clear that for $V_0 \gg \Omega$, the excitation of the first atom is not favoured, resulting in the phenomenon of Rydberg-biased freezing. $\hat{H}^{(\omega)}_{eff}$ also indicative that the two-atom correlations will get suppressed in the large ω limit irrespective of V_0 [see Sec. 2.5]. Both Cases I and Case II explain the Rydberg-biased freezing with unique intuitions.

Case III: $\{\mathbf{V_0}, \omega\} \ll \mathbf{\Omega}$ We now finally consider the limit $\{V_0, \omega\} \ll \Omega$. This limit is particularly important in explaining the non-monotonic behaviour of $\bar{P_{rr}}$ and $\bar{P_{gr}}$ near the origin of Figs 2.3(b) and 2.3(c). With a similar idea as in the above cases, we move to a rotating frame by an application of the unitary transformation operator $\hat{U} = e^{i\Omega(\hat{\sigma}^1_x + \hat{\sigma}^2_x)t/2}$. We obtain the new Hamiltonian as,

$$\begin{aligned}\hat{H}' = V_0\Big[&\sin^2(\Omega t/4)\,\hat{\sigma}^1_{gg}\hat{\sigma}^2_{gg} + \cos^2(\Omega t/4)\,\hat{\sigma}^1_{rr}\hat{\sigma}^2_{rr} \\ &+ \frac{\sin^2\Omega t}{4}\Big(\big(\hat{\sigma}^1_{gg}\hat{\sigma}^2_{rr} + \hat{\sigma}^1_{rr}\hat{\sigma}^2_{gg}\big) + \big(\hat{\sigma}^1_{gr}\hat{\sigma}^2_{rg} - \hat{\sigma}^1_{gr}\hat{\sigma}^2_{gr} + \text{H.c.}\big)\Big)\Big] + \frac{\omega}{2}\hat{\sigma}^2_x \\ &+ \frac{i}{2}V_0\sin\Omega t\Big[\sin^2(\Omega t/2)\,(\hat{\sigma}^1_{gg}\hat{\sigma}_{gr} + \hat{\sigma}^1_{gr}\hat{\sigma}^2_{gg}) + \cos^2(\Omega t/2)\,(\hat{\sigma}^1_{rr}\hat{\sigma}^2_{gr} + \hat{\sigma}^1_{gr}\hat{\sigma}^2_{rr}) + \text{H.c.}\Big].\end{aligned} \tag{2.13}$$

An effective Hamiltonian is then obtained by time-averaging Eq.(2.13) over the period $T = 2\pi/\Omega$,

$$\hat{H}^{(\Omega)}_{eff} = \frac{3V_0}{8}\Big[\hat{\sigma}^1_{gg}\hat{\sigma}^2_{gg} + \hat{\sigma}^1_{rr}\hat{\sigma}^2_{rr}\Big] + \frac{V_0}{8}\Big[\hat{\sigma}^1_{gg}\hat{\sigma}^2_{rr} + \hat{\sigma}^1_{rr}\hat{\sigma}^2_{gg} + \big(\hat{\sigma}^1_{gr}\hat{\sigma}^2_{rg} - \hat{\sigma}^1_{gr}\hat{\sigma}^2_{gr} + \text{H.c.}\big)\Big] + \frac{\omega}{2}\hat{\sigma}^2_x. \tag{2.14}$$

Since the wavefunction transforms as $|\psi_R(t)\rangle = \hat{U}|\psi(t)\rangle$. The $\hat{H}^{(\Omega)}_{eff}$ can be applied on the transformed basis vectors $\hat{U}\{|gg\rangle, |gr\rangle, |rg\rangle, |rr\rangle\}$. Noting that the unitary transformation $\hat{U}$ can be written as,

$$\hat{U} = \cos^2(\Omega t/2)\mathbb{1} + \frac{i}{2}\sin\Omega t(\sigma^1_x + \sigma^2_x) - \sin^2(\Omega t/2)\sigma^1_x\sigma^2_x, \tag{2.15}$$

we find the transformed basis as

$$\begin{aligned}
\hat{U}|gg\rangle = &\quad \cos^2(\Omega t/2)|gg\rangle + \tfrac{i}{2}\sin\Omega t\,(|gr\rangle + |rg\rangle) - \sin^2(\Omega t/2)|rr\rangle \\
\hat{U}|gr\rangle = &\quad \tfrac{i}{2}\sin\Omega t\,(|gg\rangle + |rr\rangle) + \cos^2(\Omega t/2)|gr\rangle - \sin^2(\Omega t/2)|rg\rangle \\
\hat{U}|rg\rangle = &\quad \tfrac{i}{2}\sin\Omega t\,(|gg\rangle + |rr\rangle) - \sin^2(\Omega t/2)|gr\rangle + \cos^2(\Omega t/2)|rg\rangle \\
\hat{U}|rr\rangle = &\ -\sin^2(\Omega t/2)|gg\rangle + \tfrac{i}{2}\sin\Omega t\,(|gr\rangle + |rg\rangle) + \cos^2(\Omega t/2)|rr\rangle.
\end{aligned} \tag{2.16}$$

Using both Eq.(2.13) and Eq.(2.16), we can estimate the time-averaged populations for small ω and V_0. As an example, we verify our expectations for the case of $V_0 = \omega = 0$. The initial state $|\psi(t=0)\rangle = |gg\rangle$ remains undisturbed in the rotating frame $|\psi_R(t=0)\rangle = \hat{U}|\psi(t=0)\rangle = |gg\rangle$. Since the $\hat{H}_{eff}^{(\Omega)} = 0$, the time-averaged populations are obtained directly from $\hat{U}|gg\rangle$ upon projection in the non-rotated basis $\{|gg\rangle, |gr\rangle, |rg\rangle, |rr\rangle\}$, $\bar{P}_{gg} = \bar{P}_{rr} = 0.375$, and $\bar{P}_{gr} = \bar{P}_{rg} = 0.125$, which is as expected. However, when either of these parameters are non-zero: $\omega \neq 0$ or $V_0 \neq 0$, we first need to consider the long-time evolution using $\hat{H}_{eff}^{(\Omega)}$. For the non-interacting case $V_0 = 0$, with a Rabi-offset $\omega \neq 0$ we have $\hat{H}_{eff}^{(\Omega)} = (\omega/2)\hat{\sigma}_x^2$ and in the rotating frame, for initial state $|gg\rangle$ we observe

$$|\psi_R(t)\rangle = \cos\frac{\omega t}{2}|gg\rangle - i\sin\frac{\omega t}{2}|gr\rangle, \tag{2.17}$$

i.e. the initial state $|gg\rangle$ makes coherent Rabi oscillations with state $|gr\rangle$. In the laboratory frame, the population in $|\alpha\beta\rangle$ state can be obtained by simply projecting $|\psi_R(t)\rangle$ along the rotated basis $\hat{U}|\alpha\beta\rangle$ where $\alpha, \beta \in \{g, r\}$. This exercise gives us the same result as we obtain previously in the Sec. 2.3.2. Now, we move on to the interacting case and take $V_0 \ll \Omega$ with $\omega = 0$. The time-evolution with $\hat{H}_{eff}^{(\Omega)}$ for initial state $|gg\rangle$ results in

$$|\psi_R(t)\rangle = \left[\cos\frac{V_0 t}{8}|gg\rangle + i\sin\frac{V_0 t}{8}|rr\rangle\right]\exp(-i3V_0 t/8) \tag{2.18}$$

when we project on to the rotated basis states given in Eqs. (2.16) to obtain the final population in non-rotated basis,

$$\begin{aligned}
P_{gg}(t) &= \cos^4\frac{\Omega t}{2}\cos^2\frac{V_0 t}{8} + \sin^4\frac{\Omega t}{2}\sin^2\frac{V_0 t}{8} \qquad (2.19)\\
P_{gr}(t) &= P_{rg}(t) = \frac{1}{4}\sin^2\Omega t \qquad (2.20)\\
P_{rr}(t) &= \cos^4\frac{\Omega t}{2}\sin^2\frac{V_0 t}{8} + \sin^4\frac{\Omega t}{2}\cos^2\frac{V_0 t}{8}. \qquad (2.21)
\end{aligned}$$

These results indeed match very well with the numerical solution obtained by solving the Schrödinger equation using the Hamiltonian in Eq. (2.1) when $V_0 \ll \Omega$ is

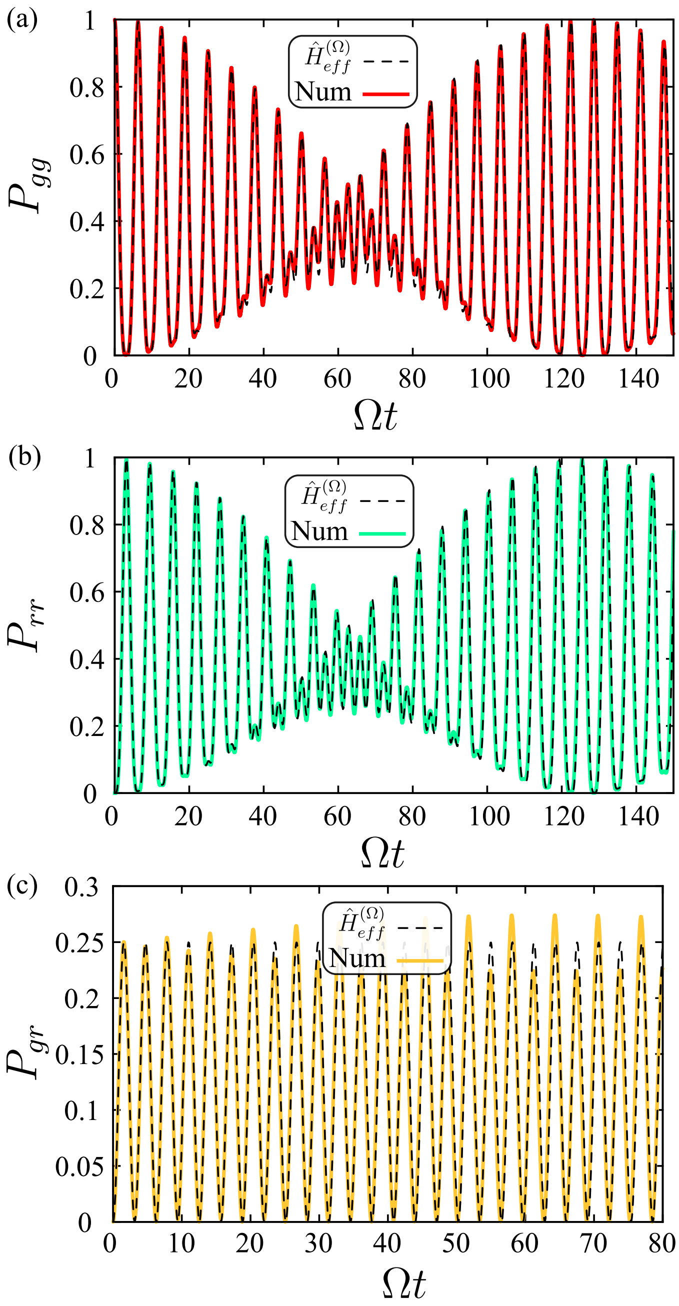

Figure 2.9: The population dynamics of states (a) $|gg\rangle$, (b) $|rr\rangle$ and (c) $|gr\rangle$ from exact numerics (solid lines) and from analytical results (dashed lines) obtained using Eq. (2.21) for $V_0/\Omega = 0.1$.

satisfied as shown in Fig. 2.9. Finally, we consider the non-interacting case, $V_0 \ll \Omega$ with small Rabi-offset, $\omega \ll \Omega$. With the initial state as $|gg\rangle$, the unitary evolution with $H^{(\Omega)}_{eff}$ gives the final state as

$$\begin{aligned} |\Psi_R(t)\rangle \quad = \quad & e^{-iV_0 t/4} \times \frac{1}{2\eta}\Big[\left(\eta \left(\cos\omega t/2 + \cos\eta t/4\right) - iV_0 \sin\eta t/4\right)|gg\rangle \\ & -i\left(\eta \sin\omega t/2 + 2\omega \sin\eta t/4\right)|gr\rangle + i\left(\eta\sin\omega t/2 - 2\omega\sin\eta t/4\right)|rg\rangle) \\ & - \left(\eta\left(\cos\eta t/4 - \cos\omega t/2\right) - iV_0 \sin\eta t/4\right)|rr\rangle\Big], \qquad (2.22) \end{aligned}$$

and then projecting to the rotated basis states given in Eqs. (2.16) we obtain the populations for $\{V_0, \omega\} \ll \Omega$ as,

$$\begin{aligned} P_{gg}(t) &= \tfrac{1}{4}\left(\cos\tfrac{(\omega+2\Omega)t}{2} + \cos\tfrac{\eta t}{4}\right)^2 + \tfrac{V_0^2}{4\eta^2}\sin^2\tfrac{\eta t}{4} && (2.23)\\ P_{gr}(t) &= \left(\tfrac{1}{2}\sin\tfrac{(\omega+2\Omega)t}{2} + \tfrac{\omega}{\eta}\sin\tfrac{\eta t}{4}\right)^2 && (2.24)\\ P_{rg}(t) &= \left(\tfrac{1}{2}\sin\tfrac{(\omega+2\Omega)t}{2} - \tfrac{\omega}{\eta}\sin\tfrac{\eta t}{4}\right)^2 && (2.25)\\ P_{rr}(t) &= \tfrac{1}{4}\left(\cos\tfrac{(\omega+2\Omega)t}{2} - \cos\tfrac{\eta t}{4}\right)^2 + \tfrac{V_0^2}{4\eta^2}\sin^2\tfrac{\eta t}{4}, && (2.26) \end{aligned}$$

where $\eta = \sqrt{V_0^2 + 4\omega^2}$. The time-averaged populations are

$$\begin{aligned} \bar{P}_{gg} = \bar{P}_{rr} &= 1/4 + V_0^2/(8\eta^2), && (2.27)\\ \bar{P}_{gr} = \bar{P}_{rg} &= 1/8 + \omega^2/(2\eta^2). && (2.28) \end{aligned}$$

For $\omega = 0$, we recover the previous results. For $\omega \neq 0$, $\bar{P}_{rr}$ is an increasing function of V_0 which concurs with the initial increase with $|V_0|$ as seen in $\bar{P}_{rr}$ at small values of ω. Furthermore, the point corresponding to the peak value V_0^P that exists at small ω and V_0 values, is plotted in Fig. 2.8. It can be estimated by the V_0 value at which $\bar{P}_{rr}$ from the effective Hamiltonian Eq. (2.27) equates to the following Lorentzian function

$$f(V_0/\Omega) = \frac{3\Omega^2}{8[\Omega^2 + (V_0/\nu_{rr})^2]}. \qquad (2.29)$$

The above Lorentzian profile of $\bar{P}_{rr}$ is obtained at $\omega = 0$ whose half-width ν_{rr} is a parameter. The plot is fitted with the exact numerics to obtain nu_{rr}. An analytical equation of the peak value can thus be obtained as,

$$V_0^p = \sqrt{\frac{2}{3}}\sqrt{\omega\left(-2\omega + \sqrt{4\omega^2 + 3\nu_{rr}^2\Omega^2}\right)}. \qquad (2.30)$$

The above equation is plotted as a dashed green line against the exact numerical result in Fig. 2.8. Furthermore, we plot the initial increase of peak value using the numerics as well as from the effective Hamiltonian in Fig. 2.10 and they are in good agreement with each other. Note that we cannot explain the further decrease from this effective Hamiltonian picture. As V_0 becomes comparable to Ω the above effective Hamiltonian picture is not useful. Nevertheless, it is clear that within this regime there is a competition between ω and V_0 which manifests as non-monotonicity of time-averaged populations.

The effect of ω can thus be summarized as follows: For no offset, the $|rr\rangle$ population is coherently populated via $|gr\rangle$ and $|rg\rangle$. A non-zero value of ω breaks this

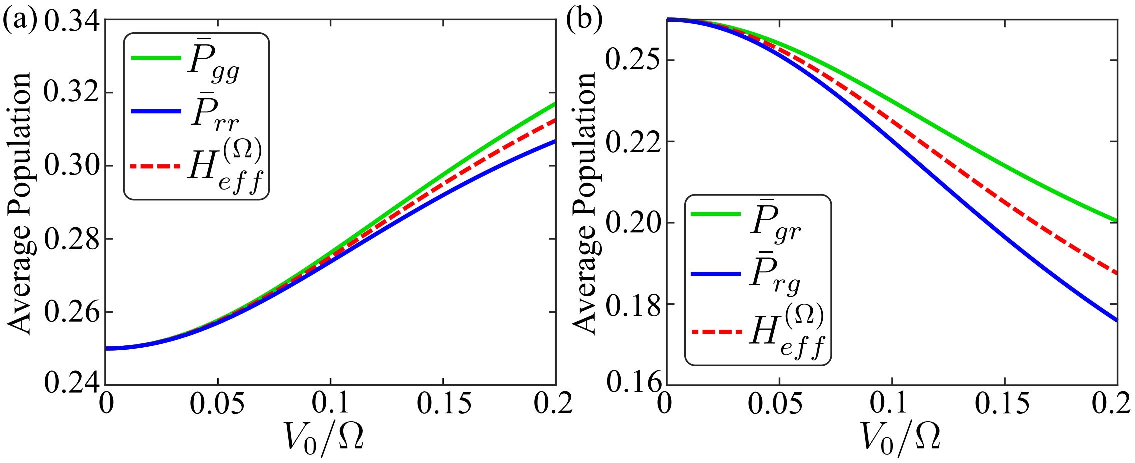

Figure 2.10: Comparison of results from exact numerical solution (solid lines) and the effective Hamiltonian $\hat{H}^{(\Omega)}_{eff}$ (dashed line) for $\omega/\Omega = 0.1$. (a) is for the time-averaged populations $\bar{P}_{gg}$ and $\bar{P}_{rr}$ and (b) is for $\bar{P}_{gr}$ and $\bar{P}_{rg}$.

symmetry and thus the previously identical route become non-identical, resulting in a decrease in time-averaged populations of $\bar{P}_{gg} = \bar{P}_{rr}$ from 0.375 to 0.25; and an increase in $\bar{P}_{gr} = \bar{P}_{rg}$ from 0.125 to 0.25. At small values of ω, the decrease in time-averaged population $\bar{P}_{rr}$ due to a small Rabi-offset can be partially compensated by a small V_0 (seen as a peak in $\bar{P}_{rr}$). Moreover, in the time-evolution of population, we observe an envelope (frequency $\sim \omega$) superposed with beats having frequency Ω. At slightly larger ω ($\sim \Omega$), both the envelope and beat frequencies are similar; and the decrease of $|rr\rangle$ population can no longer be compensated by any value of V_0. At significantly large values of either V_0 or ω, the effective Hamiltonian pictures mentioned throughout Case I and Case II adequately describe the time-evolution of the population as well as time-averaged dynamics.

The effect of V_0 is not monotonic but dependent upon the value of ω. For small ω values a small value of V_0 affects the time-dynamics in such a way that $\bar{P}_{rr}$ increases. However, at large V_0 we get the expected blockade dynamics irrespective of ω.

2.5 Entanglement Dynamics

We now look at the evolution of the quantum correlations in the two-atom system. We partition the system equally with the first atom as subsystem A and the second atom as subsystem B. As mentioned in the Sec.1.5, the quantum correlations for a pure state system can be measured by the entanglement entropy $\mathcal{S}_A = -\operatorname{Tr}(\hat{\rho}_A \log_2 \hat{\rho}_A)$ with $\hat{\rho}_A$ being the reduced density matrix for subsystem A, or equivalently by Quantum discord $\mathcal{D}(A:B)$.

In particular, we analyze the temporal evolution of bipartite entanglement, at different interaction strengths and Rabi-offsets. In Fig. 2.12, we show the time

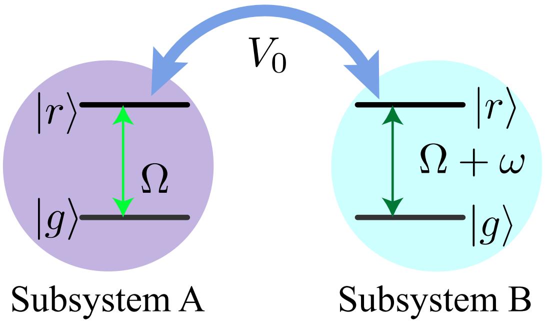

Figure 2.11: The first atom is subsystem A and the second atom is referred to as subsystem B. When interacting, the joint system state is no longer a simple tensor product of subsystems A and B.

evolution of $\mathcal{S}_A(t)$ for several values of V_0/Ω and ω/Ω to ascertain the effect of ω on entanglement. Each row contains four plots for different values of V_0/Ω while keeping ω/Ω fixed and vice versa is true for the columns. Since we start with a product state $|gg\rangle$ as the initial state, there is no quantum correlation at $t=0$, $\mathcal{S}_A(0)=0$. With time, the subsystems coherently entangle and disentangle with each other leading to oscillations in $\mathcal{S}_A(t)$. For $\omega=0$, at $V_0=0$, the quantum correlations are non-existent since the atoms are non-interacting (case not shown). However, at finite values of V_0, $\mathcal{S}_A(t)$ oscillates with time between a minimum value of zero (*product state*) and a variable maximum value. Moreover, the frequency of oscillations in $\mathcal{S}_A(t)$ increases in proportion to V_0. At sufficiently large V_0 such that blockade condition is satisfied, $\mathcal{S}_A(t)$ oscillates perfectly between the minimum, 0, and the maximum attainable value of 1, indicative of coherent oscillations between $|gg\rangle$ and maximally entangled state $|+\rangle$. On increasing ω to finite values, the growth of entanglement is slowed down for lower values of V_0/Ω without much affecting the maximum attainable value, as evidenced in the first and second column of Figs. 2.12(a)-(e). It indicates that ω effectively reduces the effect of interaction strengths between the two atoms for small V_0 or in other words, there exists a competition between V_0 and ω as we pointed out earlier in Secs. 2.3 and 2.4. However, for larger values of V_0/Ω, the maximum of entanglement entropy decreases significantly, as shown in the third and last column of Figs. 2.12(a)-(e). In particular, when both $\omega/\Omega \gg 1$ and $V_0/\Omega \gg 1$, the quantum correlations get suppressed due to the phenomenon of Rydberg-biased freezing [see the last figure in Figs. 2.12(e)].

The maximum attainable value of entanglement $\mathcal{S}_A(t)$ is plotted with respect to V_0/Ω and ω/Ω in Fig. 2.13. We introduced a lower cutoff for V_0/Ω here as the time required to achieve the maximum correlation value becomes increasingly large for such small values of V_0, particularly at larger ω values. The above discussion on the growth and maximum attainable entanglement allows us to present a possibility where the quantum correlations in the bipartite system of the two atoms can be

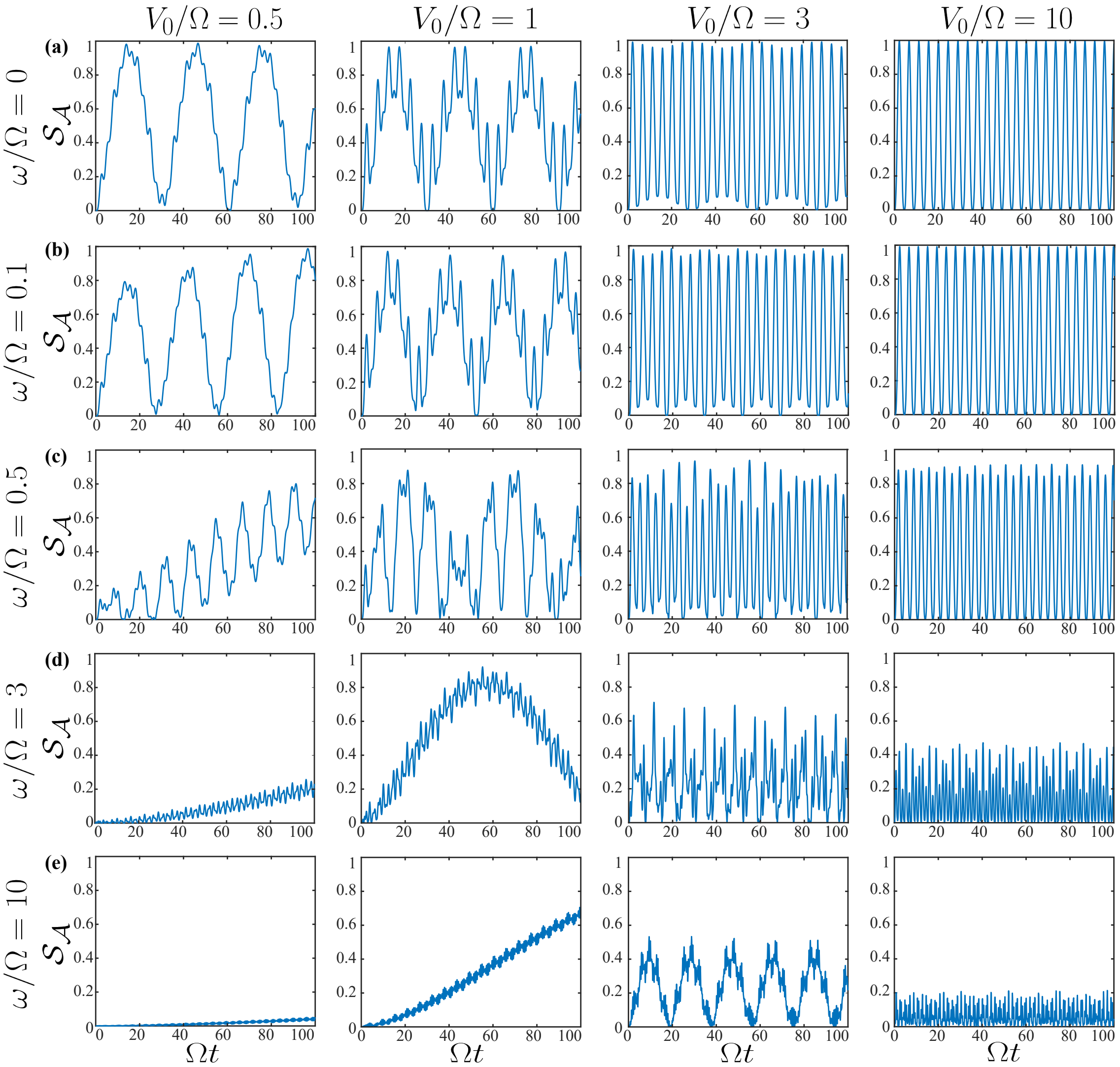

Figure 2.12: (a)-(e) The time evolution of the entanglement entropy $\mathcal{S}_A(t)$ obtained from the reduced density matrix of the first atom for different ω/Ω and V_0/Ω corresponding to the coherent dynamics discussed in the Sec. 2.3. In this case $\mathcal{S}_A$ is same as the discord $\mathcal{D}$. The values of ω/Ω and V_0/Ω are indicated in the left and top sides respectively.

designed and controlled through a dynamic variation of Rabi-offset while keeping the interaction value fixed.

Now, we demonstrate how to dynamically control the entanglement using Rabi-offset ω. For this, we consider ω to be a time-dependent function [see Fig. 2.14(a)] which varies as follows:

$$\omega(t)/\omega_{\max} = \begin{cases} 0, & 0 \leq \alpha t \leq \pi/2 \\ \cos^2(\alpha t), & \pi/2 \leq \alpha t \leq \pi \\ 1, & \pi \leq \alpha t \leq 2\pi \\ \cos^2(\alpha t), & 2\pi \leq \alpha t \leq 5\pi/2 \\ 0, & 5\pi/2 \leq \alpha t \leq 3\pi \end{cases} \tag{2.31}$$

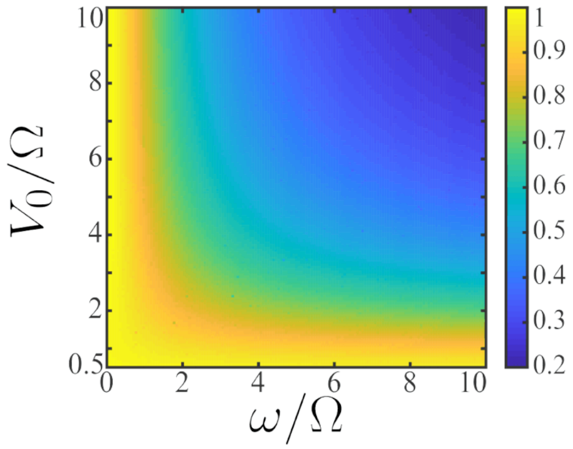

Figure 2.13: The maximum of $\mathcal{S}_A(t)$ as a function of ω/Ω and V_0/Ω corresponding to the coherent dynamics discussed in the Sec. 2.3. The lower cutoff of $V_0/\Omega = 0.5$ in the vertical axis is because for smaller values, the time taken to attain maximum $\mathcal{S}_A(t)$ becomes extremely large.

where α determines the rate of change in ω. We keep the interaction strength large at all times so that the bipartite system is in the blockade regime. At $t = 0$, we start with $|gg\rangle$ state with the correlation zero. As long as ω remains null, we see a complete periodic oscillation of entanglement entropy between 0 and 1 corresponding to blockaded oscillation between $|gg\rangle$ and bell-entangled $|+\rangle$ state. However, upon a dynamic change of ω to $\omega_{\text{max}} = 8.0$, we see that the quantum correlations decrease significantly. This regime corresponds to the Rydberg-biased freezing. In Fig. 2.14(b), the population of $|gg\rangle$ state and $|+\rangle$ is shown. As expected, in the regime of Rydberg-biased freezing the lower correlations are accompanied by lower population in the entangled state.

Upon reducing $\omega(t)$ back to zero, the correlations again begin to build up in the system and attain the maximum correlation of signified by $\mathcal{S}_A = 1$ as ω vanishes. In Figs. 2.14(b), the value of both α and ω_{max} is chosen such that the maximum correlations are completely retrieved at later times along with blockaded regime dynamics. This can be seen in 2.14(c) where the probabilities $|\langle X|\psi(t)\rangle|^2$ with $|X\rangle \in \{|gg\rangle, |+\rangle\}$ exhibit perfect Rabi oscillations at later times.

2.6 Dissipative dynamics: Steady-states and quantum discord

At this point, we discuss the effect of spontaneous emission from the Rydberg state $|r\rangle$ on the dynamics of two-atom system. Once the spontaneous emission is taken into account, the dissipative dynamics and the steady-state correlations are analyzed

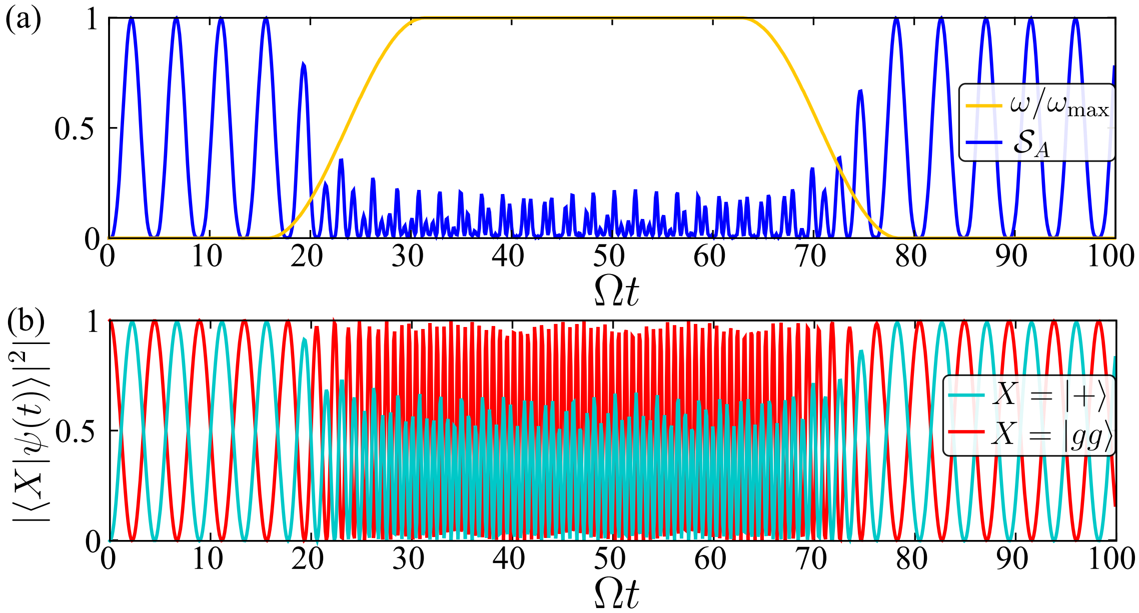

Figure 2.14: (a) The dynamics of $\mathcal{S}_A(t)$ when the Rabi-offset ω is varied in time with $\alpha = 0.1\Omega$ (see text), $V_0/\Omega = 10$ and $\omega_{max}/\Omega = 8$. When ω reaches the maximum, $\mathcal{S}_A(t)$ is significantly suppressed, and is retrieved back to the initial dynamics once ω is brought back to zero. (b) shows the overlap of $|\psi(t)\rangle$ on the states $|gg\rangle$ and $|+\rangle$ for the dynamics shown in (a).

using the master equation for the two-particle density matrix $\hat{\rho}$,

$$\partial_t \hat{\rho} = -i\left[\hat{H}, \hat{\rho}\right] + \mathcal{L}[\hat{\rho}], \tag{2.32}$$

where the Lindblad superoperator given by

$$\mathcal{L}[\hat{\rho}] = \sum_{i=1}^{2} \hat{C}_i \hat{\rho} \hat{C}_i^\dagger - \frac{1}{2}\sum_i \left(\hat{C}_i^\dagger \hat{C}_i \hat{\rho} + \hat{\rho} \hat{C}_i^\dagger \hat{C}_i\right) \tag{2.33}$$

with $\hat{C}_i = \sqrt{\Gamma}\hat{\sigma}^i_{gr}$ as the jump operator and Γ as the spontaneous decay rate of the Rydberg state $|r\rangle$. As time progresses, the dissipative mechanism allows the system to attain a steady-state which is characterized by $\partial_t \hat{\rho} = 0$. The eventual state will not be a pure state but a mixed state since the master equation describes only the two-atom system and not the spontaneously emitted light. Hence, even if the two-atom system is initially prepared in a pure state, the resultant steady-state is a mixed state. Furthermore, in this section, we only use quantum discord to quantify the quantum correlations in the two-atom system since the entanglement entropy does not prove to be a good measure for mixed states correlations [see Sec. 1.5 for details]. Moreover, for a mixed state, the quantum discord obtained after the measurement on the second atom $\mathcal{D}(A:B)$ may not be always equal to $\mathcal{D}(B:A)$ where the measurement is instead made on the first atom. In our two-atom setup

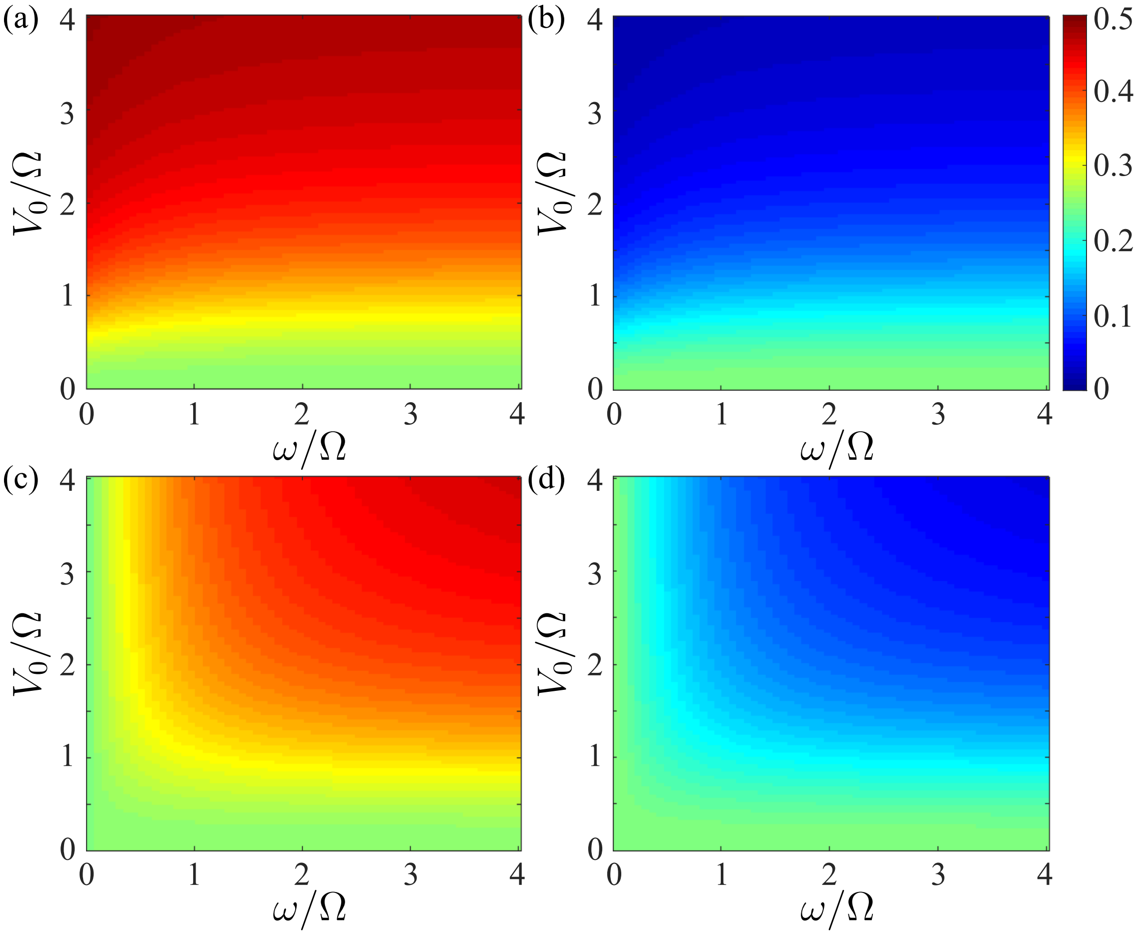

Figure 2.15: The steady-state populations: (a) ρ_{gg}, (b) ρ_{rr}, (c) ρ_{gr} and (d) ρ_{rg} as a function of ω/Ω and V_0/Ω with $\Gamma/\Omega = 0.1$.

with an initial state $\rho_{gg} = 1$, $\mathcal{D}(A : B) = \mathcal{D}(B : A)$ only holds at $\omega = 0$ where an exchange symmetry exists between the atoms. Furthermore, since the initial state is a product state ($|gg\rangle$), we get diminishing values for quantum discords at $t = 0$.

First, we look at the steady-state populations: ρ_{gg}, ρ_{gr}, ρ_{rg}, and ρ_{rr} as a function of ω/Ω and V_0/Ω with $\Gamma/\Omega = 0.1$ for the initial state $\rho_{gg} = 1$ in Fig. 2.15. Two features are directly evident from the Fig. 2.15(b): (i) the doubly excited state (ρ_{rr}) is completely suppressed at large V_0 due to the blockade, and (ii) for sufficiently large ω the blockade criteria remains independent of ω similar to that in the coherent dynamics. In the blockade regime with very small $\omega \ll \Omega$, we get $\rho_{gg} \approx 0.5$ and $\rho_{gr} \approx \rho_{rg} \approx 0.25$ at the steady-state. At sufficiently large values of V_0 and ω, both ρ_{rr} [Fig. 2.15(b)] and ρ_{rg} [Fig. 2.15(d)] approach zero and the steady-state populations are shared among ρ_{gg} [Fig. 2.15(a)] and ρ_{gr} [Fig. 2.15(c)]. These results are fairly consistent with the time-averaged populations in the coherent case which leads us to conclude that the phenomenon of Rydberg-biased freezing is robust against dissipation.

To obtain more insights into the steady-state populations, we measure the purity

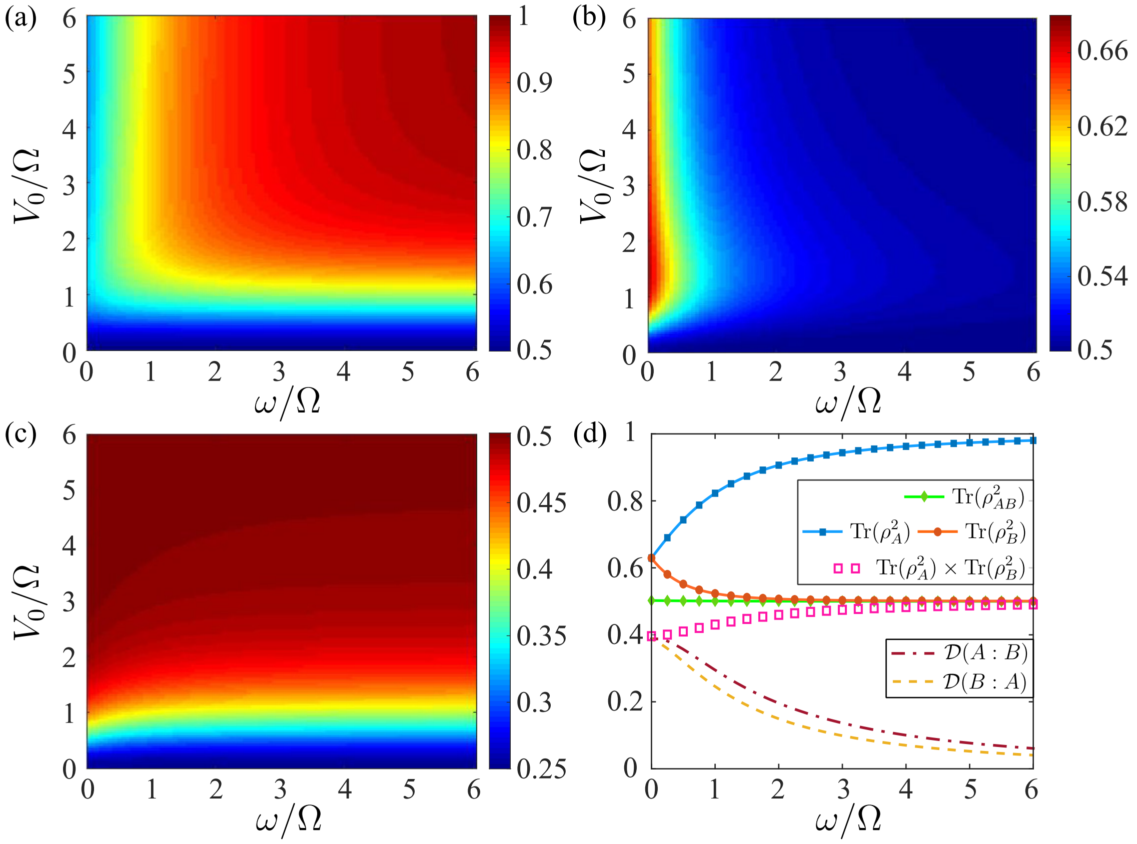

Figure 2.16: The steady-state purity of the subsystems (a) A and (b) B, and (c) the total system (AB) as a function of ω/Ω and V_0/Ω. (d) shows the purity and the quantum discords as a function of ω/Ω for $V_0/\Omega = 10$ (blockade region). $\Gamma/\Omega = 0.1$ for all figures. In (d) the solid lines are the analytical results given in A.1 and points are from the full numerical calculations for the steady-state purity. Dashed lines show the quantum discords. The open squares show $\mathrm{Tr}\,(\hat{\rho}^2_{\mathrm{A}}) \times \mathrm{Tr}\,(\hat{\rho}^2_{\mathrm{B}})$ which matches to $\mathrm{Tr}\,(\hat{\rho}^2_{\mathrm{AB}})$ at large ω values.

of the total system (two-atom system denoted by AB) and its subsystems (first atom is subsystem A and the second atom is subsystem B) at the steady-state. The quantity $\mathrm{Tr}\,(\hat{\rho}^2_{\mathrm{AB}})$ measures the purity of the total system, and it fulfills the bounds $1/d \leq \mathrm{Tr}\,(\rho^2_{\mathrm{AB}}) \leq 1$, where d is the dimension of the Hilbert space. Only for pure states $\mathrm{Tr}\,(\rho^2_{\mathrm{AB}}) = 1$ and, therefore, if $\mathrm{Tr}\,(\rho^2_{\mathrm{AB}}) < 1$ the system is in a mixed state. The lower bound for a system of two-atoms is $1/4$ and it represents a maximally mixed state. Similarly, $\mathrm{Tr}\,(\hat{\rho}^2_{\mathrm{A}})$ $[\mathrm{Tr}\,(\hat{\rho}^2_{\mathrm{B}})]$ measures the purity of the subsystem A $[B]$. The maximally mixed state for the subsystems attains a value of $1/2$. We plot the purity of the total system and subsystems as a function of V_0 and ω in Fig. 2.16(a)-(c). For small values of $V_0 (\ll \Omega)$, independent of the value of ω, the total system $[\mathrm{Tr}\,(\hat{\rho}^2_{\mathrm{AB}}) \approx 1/4]$ as well as the subsystems $[\mathrm{Tr}\,(\hat{\rho}^2_{\mathrm{A}}) \approx 1/2$ and $\mathrm{Tr}\,(\hat{\rho}^2_{\mathrm{B}}) \approx 1/2]$ are completely mixed in the steady-state. Moreover, no quantum correlations exist between the subsystems in the steady-state, see Fig. 2.17 for the corresponding quantum discord values. Thus, the steady-state of the system can be approximately written as a

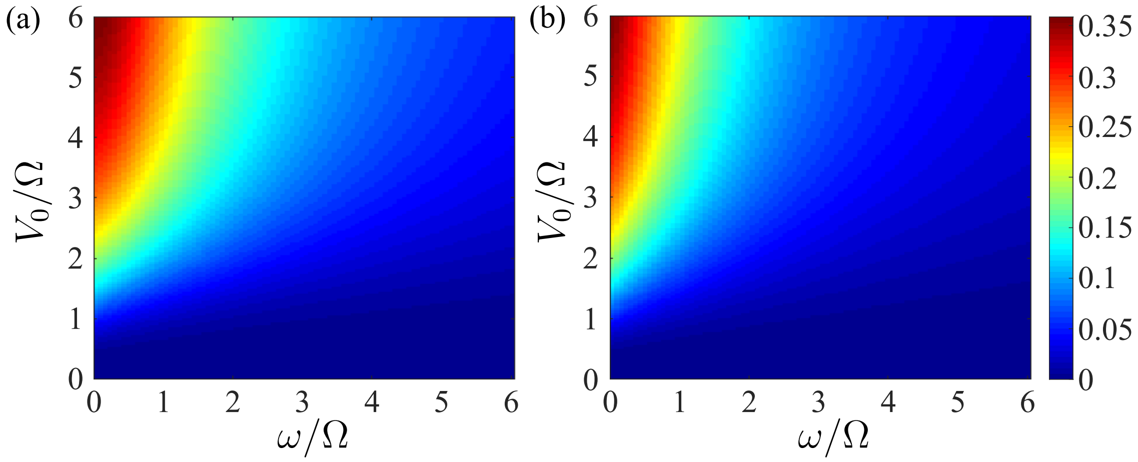

Figure 2.17: The steady-state quantum discords (a) $\mathcal{D}(B:A)$ and (b) $\mathcal{D}(A:B)$ as a function of ω/Ω and V_0/Ω for $\Gamma/\Omega = 0.1$. For $\omega \neq 0$ we have $\mathcal{D}(B:A) \neq \mathcal{D}(A:B)$. For $\omega = 0$, the correlations maximally saturate at large V_0 due to Blockade, and they start to diminish as ω increases. Discords vanish in the Rydberg-biased freezing regime where the system is described by a product state.

product state, $\hat{\rho}_{AB} = \hat{\rho}_A \otimes \hat{\rho}_B$ and consequently $\mathrm{Tr}\left(\hat{\rho}^2_{\mathrm{AB}}\right) = \mathrm{Tr}\left(\hat{\rho}^2_{\mathrm{A}}\right) \times \mathrm{Tr}\left(\hat{\rho}^2_{\mathrm{B}}\right)$. In other words, for sufficiently small V_0, the initial correlations which were build up from the interaction between the subsystems eventually got washed out due to the dissipation resulting in a maximally mixed state.

As V_0 increases, the purity $\mathrm{Tr}\left(\hat{\rho}^2_{\mathrm{AB}}\right)$ also increases and saturates to a value of 1/2 in the blockade region. Interestingly, the latter happens independent of the value of ω [Fig. 2.16(c)]. It may appear that a similar mechanism is responsible for $\mathrm{Tr}\left(\hat{\rho}^2_{\mathrm{AB}}\right) \approx 0.5$ at small or large values of ω in the blockade region. However, upon accessing $\mathrm{Tr}\left(\rho^2_{\mathrm{A}}\right)$ and $\mathrm{Tr}\left(\rho^2_{\mathrm{B}}\right)$ [Fig. 2.16(a)-(b)] along with the quantum correlations (Fig. 2.17), we see that the subsystems are indeed ω dependent. At small values of ω, the subsystems are correlated which is signified by $\{\mathrm{Tr}\left(\rho^2_{\mathrm{A}}\right), \mathrm{Tr}\left(\rho^2_{\mathrm{B}}\right)\} > 0.5$ as well as by a non-zero value of quantum discord. On the other hand, at large values of ω, the subsystems become uncorrelated (also seen in Fig. 2.17) as the subsystem A becomes pure $\mathrm{Tr}\left(\rho^2_{\mathrm{A}}\right) \to 1$ while the subsystem B remains mixed. The latter is the regime of Rydberg-biased freezing. We particularly look at the purities and quantum discord as a function of ω/Ω in the blockade region ($V_0/\Omega = 10$) in Fig. 2.16(d). As mentioned before, the system purity $\mathrm{Tr}\left(\rho^2_{\mathrm{AB}}\right) \sim 0.5$ is independent of ω at large V_0, but the purity of the subsystems depends strongly on ω/Ω as shown in Fig. 2.16(a)-(b). The purity in the strongly driven atom (subsystem B) decreases as a function of ω/Ω and becomes maximally mixed at sufficiently large ω, whereas that of the first atom (subsystem A) increases with ω and eventually becomes a pure state at very large values of ω/Ω. Thus, the total system is in a product state for large V_0 and ω, and the purity of the system becomes $\mathrm{Tr}\left(\hat{\rho}^2_{\mathrm{AB}}\right) = \mathrm{Tr}\left(\hat{\rho}^2_{\mathrm{A}}\right) \times \mathrm{Tr}\left(\hat{\rho}^2_{\mathrm{B}}\right)$ as shown in Fig. 2.16(d).

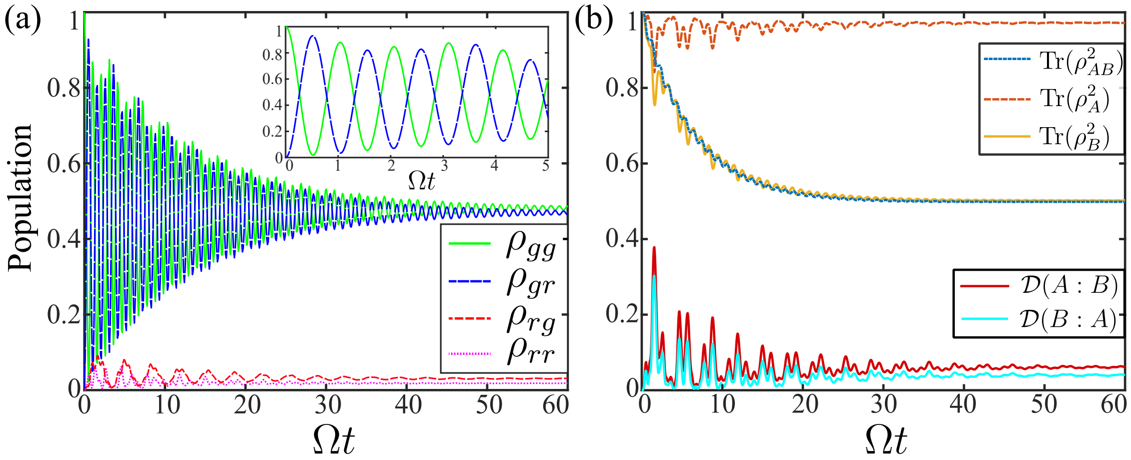

Figure 2.18: (a) The populations vs time for $\omega/\Omega = V_0/\Omega = 5$ and $\Gamma/\Omega = 0.1$. The inset shows the same for the initial period of time. (b) shows the time evolution of both the quantum discords, and the purity of the total system and subsystems, for the dynamics shown in (a).

When V_0 increases for sufficiently small ω, the quantum correlations survive in the steady-state as shown in Fig. 2.17, and its magnitude increases with an increase in V_0 eventually saturating to a constant value (which is Γ-dependent) at large values of $V_0(\sim 10\Omega)$. The strong correlations at large V_0 for small ω are attributed to the Rydberg blockade [210]. The maximum quantum discord possessed by the system at large V_0 decreases with an increase in the rabi-offset ω as shown in Fig. 2.16(d), similar to the case of the coherent dynamics discussed in the Sec. 2.5.

Since the Rydberg-biased freezing is one of the main features in our studies, we explicitly discuss the dissipative dynamics in that regime in Fig. 2.18. In Fig. 2.18(a) we show the time evolution of the populations [$\rho_{\alpha\beta}(t)$ with $\alpha, \beta \in \{g, r\}$] for $\omega/\Omega = V_0/\Omega = 5$ and $\Gamma/\Omega = 0.1$. At shorter times we see the damped Rabi oscillations between the populations in states $|gg\rangle$ and $|gr\rangle$ [inset of Fig 2.18(a)] whereas the populations in states $|rg\rangle$ and $|rr\rangle$ are suppressed. Eventually, the system reaches a steady-state with nearly equal populations between $|gg\rangle$ and $|gr\rangle$. To simplify the picture, the negligible $|rg\rangle$ and $|rr\rangle$ populations can be ignored making the scenario identical to a single atom (strongly driven second atom) with a spontaneously emitting excited state while the first atom remains in its ground state. The coherent field pumps in the excited state (of the second atom) whereas the decay rate causes the loss. Eventually, the excitation rate becomes equal to the decay rate of the excited state, and a steady-state is achieved [211]. Furthermore, the driving strength $(\Omega + \omega)$ is much stronger than the decay rate Γ ensuring a maximal mixing which results in the populations $\rho_{gg} \approx \rho_{gr} \approx 0.5$. Fig. 2.18(b) shows the corresponding dynamics of both the quantum discord and purities as a function of time. The purity of the first atom (subsystem A), $\mathrm{Tr}\,(\hat{\rho}^2_{\mathrm{A}})$ remains close to unity during the dissipative evolution; albeit it exhibits small initial fluctuations but as the system converges to the steady-state, the purity becomes more steady at unity. The unit value is the indication that a pure state exists. This is indeed true as the first atom remains frozen in the ground state due to the Rydberg-biased freezing and therefore exists in a pure state. At the same time, the purity of the second atom (subsystem B) $\mathrm{Tr}\,(\hat{\rho}_{\mathrm{B}}^2)$ decreases and eventually converges to $1/2$ indicating that it is in a completely mixed state i.e., a mixture of $|g\rangle$ and $|r\rangle$ with equal populations. As a consequence, the density matrix of the total system is not maximally mixed, and $\mathrm{Tr}\,(\hat{\rho}_{\mathrm{AB}}^2)$ converges to $1/2$. The dynamics of quantum discord is shown in Fig 2.18(b) which tell us that the correlations build up in the system during the initial stages of time evolution owing to large interactions but eventually converge to a small value as the system approaches steady-state due to the Rydberg-biased freezing.

Note that, we also obtained the analytical results for steady-state density matrices, the purity of the system and subsystems, see A.1, and these are in excellent agreement with the exact numerical calculations. The comparison is made in Fig. 2.16(d).

2.7 Conclusion and outlook

In conclusion, we studied the population dynamics and quantum correlations in a system of a pair of two-level Rydberg atoms which are envisioned as driven continuously and independently by two distinct light fields. In particular, we focused on finding the effect of a Rabi-offset corresponding to the two atoms on the excitation dynamics and quantum correlations when the atoms are interacting with each other. In the coherent dynamics, we identified the novel feature of Rydberg-biased freezing in the system, wherein augmenting the driving in one atom attenuates the population dynamics of the second atom, in the strong interaction regime. In addition to the effect of Rydberg-biased freezing, a non-monotonic behaviour in the double Rydberg excitation at both small Rabi-offsets and interaction strengths is observed. We accompanied the numerical results with analytical calculations derived from the effective Hamiltonians obtained via unitary transformations at various limits of system parameters. These are in very good agreement with the full numerical results. In addition, quantum discord is studied to measure quantum correlations in the system. Furthermore, we demonstrated that the quantum correlations can be controlled using a dynamic time-dependent Rabi-offset. We further studied the dissipative regime where spontaneous emissions from the Rydberg states are considered. We obtain steady-state dynamics and measure the entanglement in the mixed state via quantum discord. It is noteworthy that the Rydberg-biased freezing is a robust phenomenon even with dissipation. We also showed the purity of the two-atom system as well as its subsystems at the steady-state. Our study opens up a new avenue to control quantum states or quantum correlations in a pair of Rydberg atoms or equivalently in any other coupled two-level system. A recent study conducted in the NMR architecture corroborates our central result of the Rydberg-biased freezing in two and three qubits [212]. They experimental demonstrate the population attenuation of the qubit driven with lower amplitude in the strongly interacting regime. Furthermore, their quantum discord results show that the two qubits are uncorrelated in the regime of strong interaction and strong Rabi-offset as predicted by our study. The above study also extends the setup to three qubits wherein they demonstrated a local quantum control based on Rydberg-biased freezing. This experimental verification supports the possibility of quantum control in an even larger chain of qubits using a local quantum control of two qubits by varying the Rabi-offsets [213]. As an outlook, our study in the minimal setup of two Rydberg atoms can be extended to a large number of Rydberg atoms or other qubits either in a linear chain or in different geometries. In conclusion, the Rabi-offset (in particular, Rydberg-biased freezing) may serve as a useful tool to control local state dynamics and quantum correlations while studying quantum many-body physics using Rydberg atoms or equivalent systems.

Chapter 3

Landau-Zener transition dynamics under linear quench

The current chapter is adapted from the research article "Landau-Zener transitions and adiabatic impulse approximation in an array of two Rydberg atoms with time-dependent detuning" [87]. We analyze the population dynamics of a linearly quenched pair of interacting Rydberg atoms. The variable interaction allows the two-atom system to emulate different three-level Landau-Zener models ranging from bow-tie to triangular. Our results show that the population dynamics non-trivially depend on the initial state, the rate of quench, and the interaction strengths. We further describe the dynamics for the strongly interacting case which is most commonly occurring in experiments, using the analytical model of Adiabatic Impulse Approximation.

3.1 Introduction

In the ubiquitously found two-level quantum systems, often the eigenenergy levels 'repel' each other to create an avoided-level crossing. A dynamical variation of Hamiltonian across such avoided crossings leads to non-adiabatic transitions. In particular, if the variation of Hamiltonian is linear, the probability of transition between the two eigenstates is given by the Landau-Zener formula [Eq. 1.22] [141–144]. It is commonly known as the Landau-Zener (LZ) model after the pioneering scientists L. Landau and C. Zener. An idea closely related to the LZ model is that of adiabatic impulse approximation (AIA). As described in the two-level system [see Sec. 1.4.2], under the AIA the time-evolution away from the avoided crossing is considered adiabatic where the system only acquires dynamical phases; whereas, the evolution exactly at the avoided crossing is considered non-adiabatic or an impulse transition. The adiabatic and impulse transition matrices, in this case, are found using the exactly solvable two-level LZ model. It encapsulates the underlying SU(2) symmetry of the two-level system. The applicability of AIA, however, reaches beyond the linearly driven LZ model [214].

The Landau-Zener model has been generalized to both multi-level systems [215–230] and many-body setups [178, 231–238]. If driven periodically across an avoided level crossing, the separate LZTs interfere and lead to Landau-Zener-Stückelberg (LZS) interferometry [214]. The interference is attributed to multiple exciting phenomena such as the coherent destruction of tunnelling [161], dynamical localization in quantum transport [164], and population trapping [159, 160]. On the application side, such interference features can be utilized to control the population in qubit state [239–241]. Ultracold Rydberg atoms provide a platform to study multi-state Landau-Zener models [155]. The advantage of using Rydberg atoms in an LZ study is twofold: firstly, an LZ transition can be used to prepare the collective state of the two-atom system. In particular, we note that the LZ transition in a pair of Rydberg atoms is not simply explained by a single three-level model but a variety of three-level models. The different models occur at different interaction strengths. At small interactions, the two-atom system acts like a three-level bow-tie model and at large interactions like a triangular model. In this study, we highlight the role of interactions in the study of LZ physics in a Rydberg atom setup. On the flip side, since ultracold Rydberg atoms act like a quantum simulator, various three (or four) level LZ models occurring in other systems such as quantum dots or spins systems can be simulated using Rydberg atoms. Furthermore, due to the resemblance of the triangular LZ model with an interferometer [242], atom interferometry can also be studied in Rydberg atoms-based setups.

In this chapter, we study Landau Zener transition dynamics in a system of two interacting two-level Rydberg atoms. The energy space of such a system is much more involved than that of the two-level atoms. The system has three avoided crossings, and the separation between each pair is tunable via Rydberg-Rydberg interactions. Due to the tunable interaction, the setup can emulate various three-level LZ models. Furthermore, due to multiple avoided crossings present in the system, interferences between multiple Landau-Zener transitions occur and prompt the emergence of several distinct features in the population dynamics. The resultant interference features can be utilized for quantum state preparation, implementation of quantum gates, or atom interferometry. Moreover, in the limit of strong interactions, the adiabatic impulse approximation is able to closely match the numerical results.

3.2 Eigenspectrum of two Rydberg atoms

We consider two two-level atoms each of which is driven by a light field having Rabi frequency Ω, and detuning Δ from resonance. The field couples the ground state $|g\rangle$ of atom to a Rydberg state $|r\rangle$ off-resonantly. In the frozen gas limit, the atom-light system is described by the Hamiltonian

$$\hat{H} = -\Delta \sum_{i=1}^{2} \hat{\sigma}_{rr}^{i} + \frac{\Omega}{2} \sum_{i=1}^{2} \hat{\sigma}_{x}^{i} + V_0 \hat{\sigma}_{rr}^{1} \hat{\sigma}_{rr}^{2}, \tag{3.1}$$

where $\hat{\sigma}_{rr} = |r\rangle \langle r|$ and $\hat{\sigma}_x = |g\rangle \langle r| + |r\rangle \langle g|$ are projection and transition operators, respectively; and, $V_0 = C_6/R^6$ describes the van der Waals interaction between two Rydberg excited atoms separated by a distance R. For $V_0 = 0$, the atoms are decoupled, and each of them exhibit dynamics independent of the other.

As with the case of single atom, two sets of bases are important to the LZ physics which are described below. First, the reduced diabatic basis $\{|gg\rangle, |s\rangle, |rr\rangle\}$, where $|s\rangle = (|gr\rangle + |rg\rangle)/\sqrt{2}$ is the symmetric state, which form the eigenstates of the Hamiltonian when $\Omega = 0$. Second, the adiabatic basis $\{|1\rangle, |2\rangle, |3\rangle\}$ which are the eigenstates of system Hamiltonian $\hat{H}$. The two bases are related as

$$|j\rangle = \frac{1}{A}\left(-\frac{V_0 - 2\Delta - E_j}{E_j}|rr\rangle - \frac{\sqrt{2}\,(V_0 - 2\Delta - E_j)}{\Omega}|s\rangle + |gg\rangle\right), \tag{3.2}$$

where $j \in \{1, 2, 3\}$ and A is the normalization constant. Furthermore, the adiabatic states $|j\rangle$ approach the diabatic ones asymptotically,

$$\lim_{\Delta\to-\infty} |1\rangle = |gg\rangle, \lim_{\Delta\to\infty} |1\rangle = |rr\rangle, \tag{3.3a}$$

$$\lim_{\Delta\to\pm\infty} |2\rangle = |s\rangle, \tag{3.3b}$$

$$\lim_{\Delta\to-\infty} |3\rangle = |rr\rangle, \lim_{\Delta\to\infty} |3\rangle = |gg\rangle. \tag{3.3c}$$

For $\Omega = 0$, the Hamiltonian becomes diagonal in the reduced diabatic basis and the energy of these states are simply obtained as the diagonal elements of unperturbed Hamiltonian: $\{0, -\Delta, -2\Delta + V_0\}$. On the other hand, the energies of adiabatic states E_n are found by diagonalizing the Hamiltonian H. These are obtained from the roots of cubic polynomial: $f(E) = -E^3 + (V_0 - 3\Delta)E^2 + (V_0\Delta - 2\Delta^2 + \Omega^2)E - V_0\Omega^2/2 + \Delta\Omega^2$ as,

$$E_n = \frac{1}{3}\left[V_0 - 3\Delta + 2|C| \cos(\theta_n/3)\right], \tag{3.4}$$

where $n \in \{1, 2, 3\}$, $\theta_n = 3 \arccos(\mathrm{Re}(C)/|C|) + \lambda_n$ with $\lambda_n = 2(3 - n)\pi$, and

$C = \left[\left(D_1 - \sqrt{D_1^2 - 4D_0^3}\right)/2\right]^{1/3}$ having $D_0 = V_0^2 - 3V_0\Delta + 3\Delta^2 + 3\Omega^2$, and $D_1 = 2V_0^3 - 9V_0^2\Delta + 9V_0\Delta^2 - 9V_0\Omega^2/2$.

For sufficiently large V_0, when plotted as a function of detuning Δ, the energies of diabatic states exhibit three level-crossings. At the same time, the adiabatic energy levels display three separate avoided-level crossings, [see Fig. 3.1(b)]. However, for weakly interacting atoms $V_0/\Omega \ll 1$, the avoided crossings are not resolvable [see Fig. 3.1(a)]. Note that the time axis in Fig 3.1 can be simply interpreted as Δ-axis, as the variation of detuning is linear. Each of these avoided crossings are located at

$$\text{(i)}\Delta = 0, (|1\rangle \leftrightarrow |2\rangle)\,, \tag{3.5a}$$

$$\text{(ii)}\Delta = V_0/2, (|2\rangle \leftrightarrow |3\rangle)\,, \tag{3.5b}$$

$$\text{(iii)}\Delta = V_0, (|1\rangle \leftrightarrow |2\rangle)\,. \tag{3.5c}$$

For sufficiently large V_0, the energy gaps at the avoided-level crossings $\Delta E_{\alpha\in\{0,V_0/2,V_0\}}$ are shown as a function of V_0 in Fig. 3.1(c). The energy gaps at the first ($\Delta = 0$) and third ($\Delta = V_0$) avoided level crossing are identical $\Delta E_0 = \Delta E_{V_0}$, and increase with V_0 while eventually saturating to $\sqrt{2}\Omega$. On the other hand, the gap across the second crossing $\Delta E_{V_0/2}$ decreases inversely with V_0, i.e., $\Delta E_{V_0/2} \sim 1/V_0$. The small value of $\Delta E_{V_0/2}$ at larger V_0 is indicative of the fact that $|gg\rangle$ and $|rr\rangle$ are not directly coupled to each other. Note that a small value of V_0 congregates the avoided-level crossings, and a sufficiently large V_0 isolates them from each other.

3.3 Different LZ Models

Now we consider the process where the detuning Δ is linearly changed with time starting from a large negative value to a large positive value,

$$\Delta = \Delta(t) = \omega_{gr} - \omega_L = vt \tag{3.6}$$

It can be implemented by linearly varying the frequency of the exciting light field (ω_L); or equivalently by changing the level separation (ω_{gr}), between the ground state $|g\rangle$ and Rydberg level $|r\rangle$, through the strength of an applied static electric field [243]. In the diabatic basis $\{|gg\rangle\,, |s\rangle\,, |rr\rangle\}$, the system of two Rydberg atoms describes the three-level LZ model [215, 219, 220] as,

$$\hat{H} = \begin{pmatrix} 0 & \frac{\Omega}{\sqrt{2}} & 0 \\ \frac{\Omega}{\sqrt{2}} & -vt & \frac{\Omega}{\sqrt{2}} \\ 0 & \frac{\Omega}{\sqrt{2}} & -2vt + V_0 \end{pmatrix}. \tag{3.7}$$

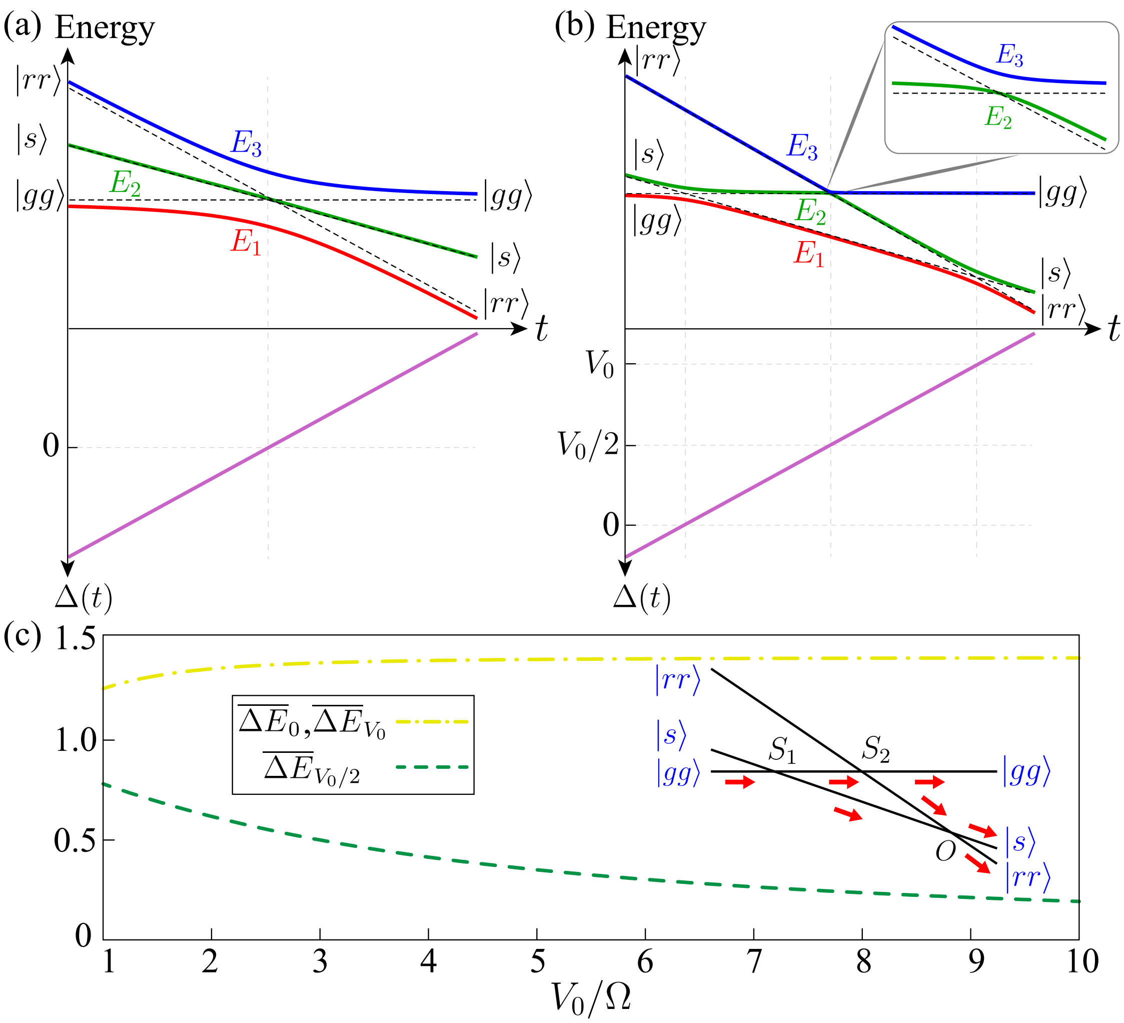

Figure 3.1: Energy eigenvalues E_j as a function of detuning (which varies linearly in time as shown in y-axes) for (a) $V_0 = 0.1\Omega$ and (b) $V_0 = 5\Omega$. The diabatic energy levels are shown by the dashed lines. The level crossings/avoided crossings in (a) form a three-level bow-tie model, and in (b) form a triangular LZ model. The inset in (b) shows the avoided level crossing at $V_0/2$. The asymptotic eigenstates at $t \to \pm\infty$ are given towards the left and right end of the energy level diagrams. (c) shows the energy gaps $\overline{\Delta E}_\alpha = \Delta E_\alpha/\Omega$ at the avoided crossings as a function of V_0. The inset shows the schematic setup for the LZ interferometer in which the first (S_1) and the second (S_2) crossings act as beam splitters. At the last crossing, O mixing takes place.

As mentioned before, the system has three avoided crossings [see Eq. 3.5 and Fig.3.1(b)]. We consider a linear sweep of detuning starting from the far left of the first avoided crossing ($\Delta = 0$) to the far right of the final avoided crossing ($\Delta = V_0$) encompassing all three avoided crossings in the process.

Among the diabatic states, $|s\rangle$ couples to both $|gg\rangle$ and $|rr\rangle$; but $|gg\rangle$ and $|rr\rangle$ are not coupled to each other. Therefore, for vanishing values of interactions, the two-atom setup converges to a three-level bow-tie model shown in Fig. 3.2(a) [215, 216, 244, 245]. The same atomic setup can also mimic a four-level bow-tie model [Fig. 3.2(c)] if we introduce an offset in Rabi frequencies or detunings of the two

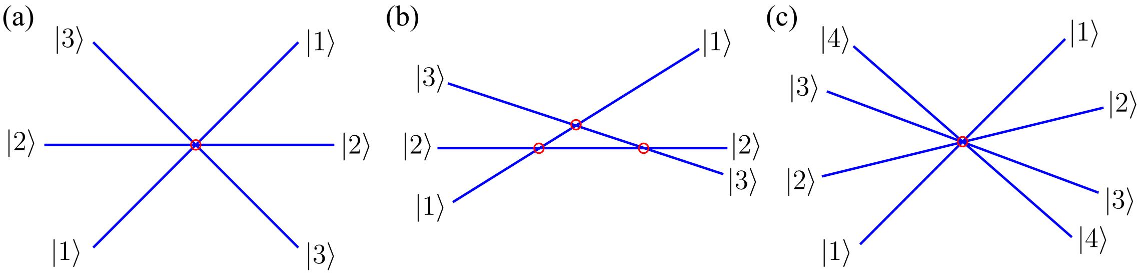

Figure 3.2: Multistate Landau-Zener models. (a) The three level bow-tie model, (b) a triangular LZ model (figures adapted from [223]), and (c) a four-level bow-tie model (figure adapted from [246]).

atoms [86, 230]. For sufficiently large V_0 (blockade regime), the avoided level crossings form a triangular geometry [Fig. 3.1(b)]. A triangular LZ model [Fig. 3.2(b)] exhibit beats and step patterns in the population dynamics which are strikingly different from the two-level LZ dynamics [222, 229]. The Hamiltonian describing two interacting Rydberg atoms in Eq. (3.1) is also identical to an anisotropic spin-1 model [221, 222]. With the mapping of states as $\{|gg\rangle, |s\rangle, |rr\rangle\} \to \{|-1\rangle, |0\rangle, |1\rangle\}$, we get

$$\hat{H}_s = \left[\Delta(t) - \frac{V_0}{2}\right]\hat{S}_z + \Omega\hat{S}_x + \frac{V_0}{2}(\hat{S}_z)^2, \tag{3.8}$$

where $\hat{S}_z$ and $\hat{S}_x$ are the spin-1 matrices which are the generators of SU(2) rotation of spinors; and V_0 lifts the trifold degeneracy of the unperturbed energy levels ($\Omega = 0$), hence called easy-axis anisotropy in spin systems. In the limit of $V_0 \to 0$ there's no anisotropy and the three avoided-level crossings merge at the point of zero detuning [see Fig. 3.1(a)]. The spin-1 Hamiltonian then exhibits SU(2) symmetry in accordance to that of non-interacting single atoms [220] [also see Appendix B.1]. However, in presence of Rydberg-Rydberg interactions, the underlying symmetry belongs to the class $SU(3)$. The model in Eq. (3.8) therefore is non-linear for the SU(2) generators *i.e.*, $\hat{S}_z$ and $\hat{S}_x$; however, the nonlinearity is removed when the Hamiltonian is expressed in terms of the generators of SU(3) group [222]. For details of representation see Appendix B.2.1. When V_0 is sufficiently large, the three avoided crossings get isolated from one another so that each avoided crossing comprises only two levels with underlying symmetry of SU(2) [see Fig. B.1].

3.4 LZ dynamics for different initial states

During the time-evolution, the first avoided crossing occurs at time $t_1 = 0$ between the states $|1\rangle$ and $|2\rangle$, the second avoided crossing between $|2\rangle$ and $|3\rangle$ occurs at time $t_2 = V_0/2v$, and the final one between the states $|1\rangle$ and $|2\rangle$ takes place at $t_3 = V_0/v$. As is evident, the adiabatic state $|3\rangle$ participates in only one LZT (at $t_2 = V_0/2v$), whereas the states $|1\rangle$ and $|2\rangle$ are each involved in two LZTs. Furthermore, if we scale time in the Schrödinger equation corresponding to the above Hamiltonian ($\tilde{t} = t/\sqrt{v}$), we observe that the rescaled Hamiltonian is only a function of two parameters: $\Omega/\sqrt{v}$ and $V_0/\sqrt{v}$ instead of three. Therefore, we can argue that the LZ transition probabilities will show a dependence on these parameters. In the following, we analyze the state population dynamics as a function of both v and V_0 conditioned to different initial states. The initial (t_i) and final (t_f) times of evolution are chosen such that the adiabatic states coincide with the diabatic ones.

3.4.1 Initial state: $|\psi(t_i)\rangle = |1\rangle$

Adiabatic states

The dynamics in adiabatic states is shown in the left columns of Figs. 3.3 and 3.4 for the initial state, $|\psi(t_i)\rangle = |1\rangle$, and initial time of sweep t_i is chosen such that $|1\rangle \approx |gg\rangle$.

Weakly interacting atoms — For $V_0 \ll \Omega$ due to indistinguishable avoided level crossings, the LZT transitions occur almost simultaneously from initial state $|1\rangle$ to the states $|2\rangle$ and $|3\rangle$, as seen in Figs. 3.3(a) and (b). The population transfer from state $|1\rangle$ is nearly complete for sufficiently large v. If v is small, although the transition times are coincident, the transfer of population is smaller [see Fig. 3.3(a)]. The small oscillations observed in the latter case eventually settle down to a steady value after a long time when the adiabatic states coincide with diabatic ones.

Strongly interacting atoms — For $V_0 \gg \Omega$, all three LZTs are resolved in the dynamics [see Figs. 3.4(a) and (b)]. Here, the first and third transitions which correspond to the population transfer from $|1\rangle$ to $|2\rangle$, can be seen as major dips in $P_1(t)$ near $t = 0$ and t_3. The rises and dips in $P_2(t)$ at $t = 0$, t_2, and t_3 reflect all three LZT of state $|2\rangle$. A singular rise in P_3 at time t_2 is due to the LZT between $|2\rangle$ and $|3\rangle$. As expected from the two-level LZ formula [Eq. 1.22], the transfer of populations across each avoided crossing is less for small v, and more for larger v. The final population in each state, is then estimated by a sequential application of each LZT [see Sec. 3.5].

We look at the final populations in the steady-state $P_j(t_f)$, as a function of v and V_0 in Fig. 3.5 drawing insights from the LZ formula. As initially, the entire population is in state $|1\rangle$, a sweep across the avoided crossings results in a decrease in P_1 across both the first $(\Delta = 0)$ and third avoided crossing $(\Delta = V_0)$. Per the LZ formula, the transfer is proportional to the quench rate v. This results in uniformly decreasing final population $P_1(t_f)$ in the state $|1\rangle$. On the other hand, the state $|3\rangle$ participates in only one crossing $(\Delta = V_0/2)$ across which the population transfer increases with a large quench rate v. Thus, $P_3(t_f)$ is a monotonically increasing

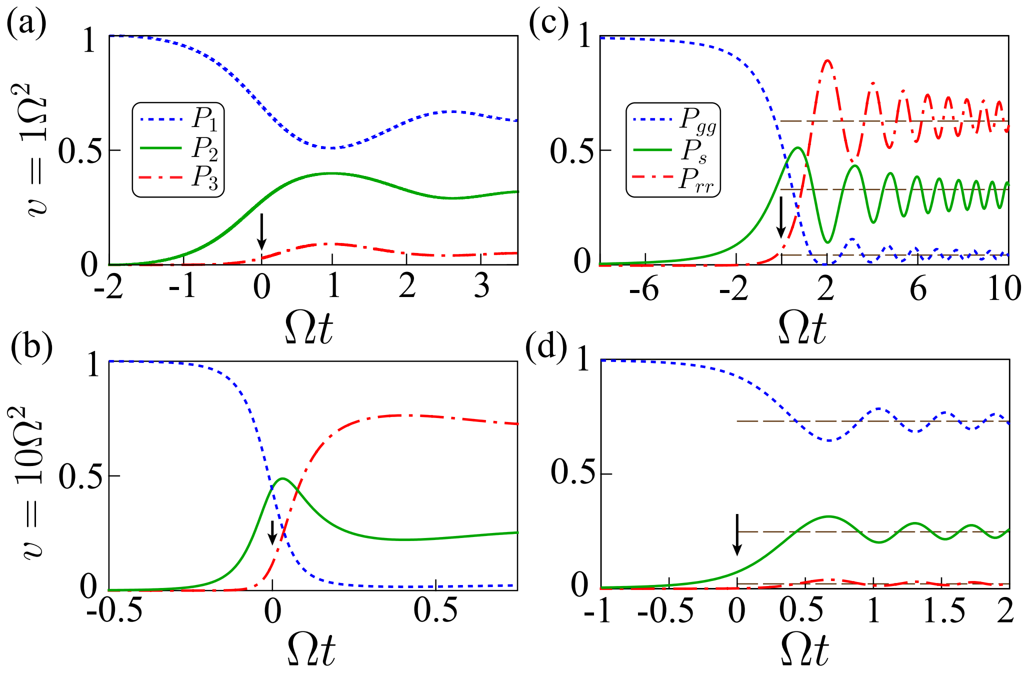

Figure 3.3: The dynamics of populations in the adiabatic (a)-(b), and the diabatic (c)-(d) states for the initial state $|\psi(t_i)\rangle = |1\rangle \sim |gg\rangle$, $v = (1\Omega^2, 10\Omega^2)$, and $V_0 = 0.1\Omega$. The first LZT takes-place in the vicinity of $t = 0$. The thin arrows show the times around which the second (t_2) and the third (t_3) LZTs occur. Since the LZTs are not resolvable, so a single arrow is shown. The dashed horizontal lines in the right column show the results from the non-interacting model.

function of v. However, $P_2(t_f)$ is non-monotonic with respect to v. We can reason that while there is an influx of population from P_1, there is also an outflux to P_3 which may result in a concave valued function.

Further non-triviality in the patterns can be better understood by looking at the energy gap across the avoided-level crossings. For instance, we expect that at large V_0, the steady state population $P_3(t_f)$ depends only depend on v. This is because both $\Delta E_0 = \Delta E_{V_0}$ saturates to $\sqrt{2}\Omega$ at large V_0 as well as $\Delta E_{V_0/2}$ becomes minimal ($\Delta E_{V_0/2} \ll \Omega$) at larger V_0. As a consequence of the former, after the first avoided crossing, $P_2(t)$ becomes independent of V_0. Furthermore, the narrow gap at the second avoided crossing allows for a swift transition from $|2\rangle$ to $|3\rangle$. Given v adequately large, the transfer is complete while for smaller values of v, the transition is swift but the occupation probability is less [visible from the (red) dashed-dotted line at t_2 in Fig. 3.4(a) and (b)]. As a result, the final population in $|3\rangle$ ($P_3(t_f)$) becomes independent of V_0, provided V_0 is sufficiently large. Counter-intuitively, we observe that even for smaller values of V_0, the steady-state $P_3(t_f)$ is invariant with respect to V_0 [see Fig. 3.5(c)]. It is better understood in terms of the dynamics of diabatic states (see below). On the other hand, both the states $|1\rangle$ and $|2\rangle$ take part in two crossings and therefore the phases acquired between the crossings (which may not be independent of V_0) become relevant and result in interference patterns seen

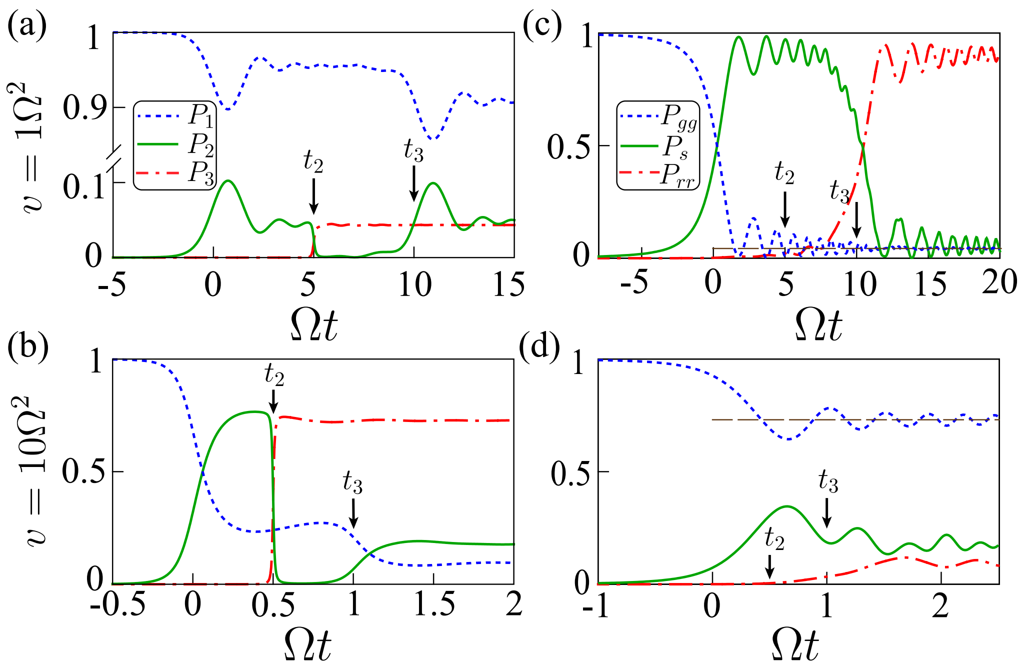

Figure 3.4: The dynamics of populations in the adiabatic (a)-(b) and the diabatic (c)-(d) states for the initial state $|\psi(t_i)\rangle = |1\rangle \sim |gg\rangle$, $v = (1\Omega^2, 10\Omega^2)$, and $V_0 = 10\Omega$. The first LZT takes-place in the vicinity of $t = 0$. The thin arrows show the times around which the second (t_2) and the third (t_3) LZTs occur. The dashed horizontal lines in the bottom row show the results from the non-interacting model.

across both Figs. 3.5 (a) and (b).

Diabatic states

In the right columns of Fig. 3.3 and 3.4, we also show the population dynamics in the diabatic states for the same parameters as in the left column of the respective figures. As opposed to adiabatic states, the population in the diabatic states exhibits clear oscillations (similar to Rabi oscillations) between different states. The amplitude of these oscillations reduces with time while the frequency increases. The amplitude damping occurs because a time-varying detuning produces dephasing in the coherent Rabi Oscillations. On the other hand, the frequency increases because the instantaneous effective Rabi frequency is proportional to detuning, which is growing with time [147]. As a note, the feature of oscillations exists in the impulse regime in the diabatic states for the two-level system as well. A detailed description of adiabatic and impulse regimes is given in Sec. 1.4.2. Below we look at weak and strong interaction cases separately.

Weak interaction— For small values of V_0 and v (*i.e.*, $V_0/\sqrt{v} \ll \Omega/\sqrt{v}$ and $\Omega/\sqrt{v} \gg 1$), the amplitude of oscillation is larger [see Fig. 3.3(b)]. We reason for it in the following manner: At a small value of V_0, all three avoided crossings are located nearby and the effective energy gap may be large compared to that between

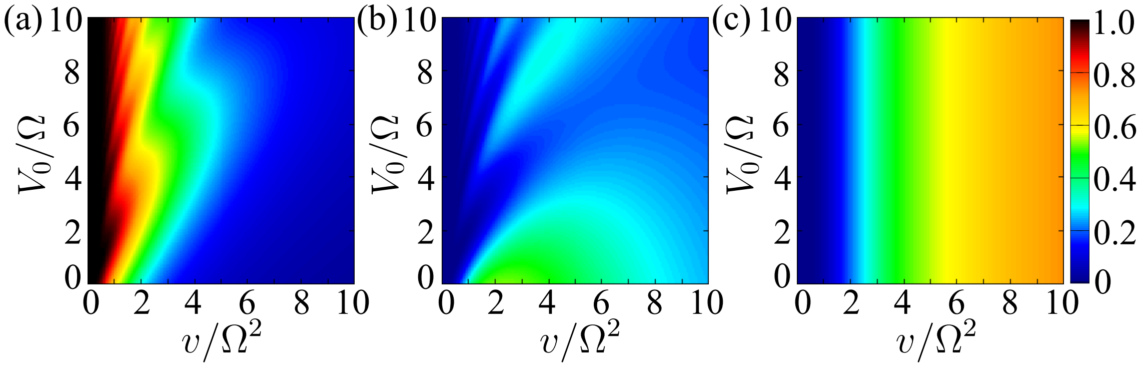

Figure 3.5: The final population in (a) $|1\rangle \sim |rr\rangle$, (b) $|2\rangle \sim |s\rangle$ and (c) $|3\rangle \sim |gg\rangle$, after the linear quench, as a function of v and V_0 for the initial state $|\psi(t_i)\rangle = |1\rangle$, $\Delta(t_i) = -10\Omega$, and $\Delta(t_f) = 30\Omega + 10v/\Omega$.

two such levels. Combined with smaller quench rates v, the system spends a long time at the impulse regime [see Sec. 1.4.2]. As a result, the system mixes through oscillations in the impulse regime before reaching the adiabatic regime where the amplitude damping occurs. Moving to the steady state populations, in the adiabatic limit ($v \to 0$), the initial population in $|gg\rangle$ completely transfers to $|rr\rangle$ independent of the value of V_0 [see Fig. 3.5]. As v increases, there is non-zero population in both $|s\rangle$ and $|rr\rangle$ states.

For larger quench rates $\Omega/\sqrt{v} \ll 1$ in the weak interaction regime, transfer of population from $|gg\rangle$ to both $|s\rangle$ and $|rr\rangle$ is suppressed near $t \approx 0$. This is because the system does not spend significant time near the avoided crossings, thus the effect of interactions is negligible. In this case, we can assume the atoms to be non-interacting and we have $P_3(t \to \infty) = P_{gg} = P_{LZ}^2, P_2(t \to \infty) = P_s = 2P_{LZ}(1 - P_{LZ})$, and $P_1(t \to \infty) = P_{rr} = (1 - P_{LZ})^2$ where P_{LZ} is same as in Eq. (1.22). Dashed horizontal lines in Fig. 3.3(c) and (d) show the results from the non-interacting approximation and are in a good agreement with the steady state numerical results. On the other hand, for smaller quench rates v, a finite but small V_0 instigates small corrections to the purely non-interacting results. To describe the steady state populations in this case, we take insight from the numerical result that $P_{gg}(t_f)$ remains independent of V_0 [see fig. 3.5(c)], and therefore, we simply consider $P_{gg}(t \to \infty) = P_{LZ}^2$. Further assuming that the correction factors depend on arguments ($\Omega/\sqrt{v}$ and $V_0/\sqrt{v}$), we intuitively come up with the analytical solutions as,

$$P_s(t \to \infty) \approx 1 - P_{LZ}^2 - (1 - Q_{LZ})^2, \tag{3.9}$$

and $P_{rr}(t \to \infty) \approx (1 - Q_{LZ})^2$ where

$$Q_{LZ} = P_{LZ} \exp\left(-\frac{\pi\Omega^2 V_0}{4v^{3/2}}\right). \tag{3.10}$$

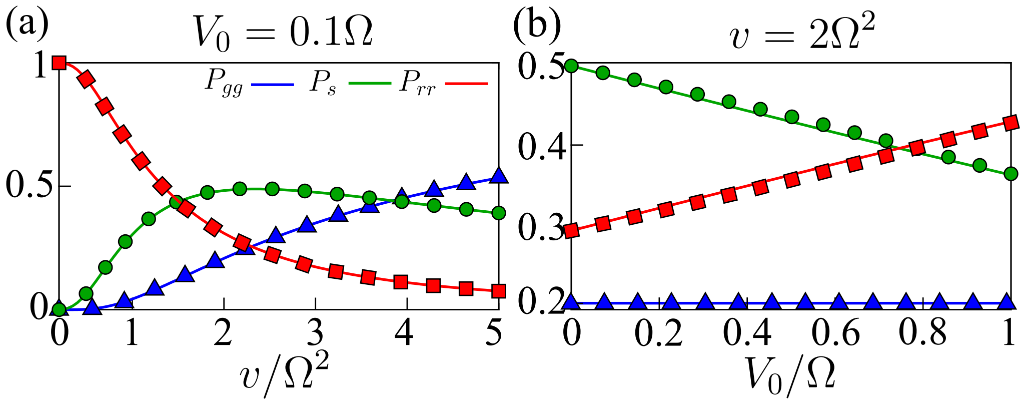

Figure 3.6: (a) The final population in the adiabatic/diabatic states as a function of v for $V_0 = 0.1\Omega$ with the initial state $|1\rangle \sim |gg\rangle$. (b) The same as in (a) but as a function of V_0 for $v = 2\Omega^2$. The solid lines show exact results, and the filled squares, circles, and triangles are the theoretical prediction for small V_0 in the limit $t_f \to \infty$.

These results are in an excellent agreement with the numerical results for $P_j(t_f)$ [see Fig. 3.6], even for reasonably large values of V_0.

Strong interaction— For $V_0 \gg \Omega$, the three avoided crossings are well separated. However, the dynamics observed in the diabatic states do not show signatures of all three LZTs. The reason is that $|gg\rangle$ is not directly coupled to $|rr\rangle$ and hence does not leave any trace of second LZT (near t_2) in the dynamics [see Figs. 3.4(c) and (d)]. After the first LZT ($t_1 = 0$), P_s increases at the cost of P_{gg}. For sufficiently small v, a near complete population transfer from $|gg\rangle$ to $|s\rangle$ occurs whereas for larger v, the transferred population is smaller. At the third LZT near t_3, population transfer from $|s\rangle$ to $|rr\rangle$ occurs. This poses an interesting scenario in the limit of $V_0/v \gg 1/\Omega$, namely that the system begins in an uncorrelated state ($|gg\rangle$), becomes entangled ($|s\rangle$) during the evolution, and eventually becomes uncorrelated again ($|rr\rangle$) state, as seen in Fig. 3.4(c). The population, as well as the duration of stay in either of the states, can be controlled by tuning v and V_0.

Interestingly, when the LZTs are resolved, the system is identical to an atom interferometer. Our Landau-Zener interferometer is based on the amplitude splitting at the (avoided) crossings. It is schematically shown in the inset of Fig. 3.1(c). The (avoided) crossings act like beam splitters [S_1 and S_2 in Fig. 3.1(c)] whose thickness is governed by the energy gaps and the quench rate v. At the final crossing O, the interference between $|s\rangle$ and $|rr\rangle$ occurs, and the final population in $|gg\rangle$ is taken as the residue leak from the interferometer.

Previously, we have seen that $P_3(t_f) \sim P_{gg}$ is independent of V_0 [see Fig. 3.5(c)]. This feature was partly explained, for large V_0, using the adiabatic basis. A simple and complete picture is obtained in the diabatic states, independent of the value of V_0. We know that in the three-level picture of two-atoms, the energy of $|rr\rangle$ state is shifted by an amount V_0 while that of $|gg\rangle$ and $|s\rangle$ states remain unchanged. Since the $|gg\rangle$ state is only coupled to $|s\rangle$, and both states are not directly affected by V_0, it plays no role in determining the population transfer from $|gg\rangle$ to $|s\rangle$. However, V_0 can affect the population transfer from the reverse channel since $|s\rangle$ is also coupled to $|rr\rangle$. In a single sweep of detuning with complete population initially in $|gg\rangle$, the reverse process is absent, which leaves the final population in $|gg\rangle$ independent of V_0. Similarly, as we shall see later, for initial state $|rr\rangle$, the final population $P_1(t_f) \sim P_{rr}$ remains independent of the value of V_0.

Adiabaticity Criteria

At this point, we comment briefly on the criteria of adiabaticity for sufficiently large V_0, which becomes state-dependent in three-level systems. The adiabaticity criteria are determined by the energy gap at the avoided crossing, which only affects the set of states involved in the LZT. The energy gaps at the three avoided crossings are obtained using Eq. (3.4) as,

$$\begin{aligned} \Delta E_0 = \Delta E_{V_0} &= -\frac{2}{\sqrt{3}}|C(t_1)|\sin\left(\frac{\theta_3(t_1)}{3}\right), \\ \Delta E_{V_0/2} &= \frac{2}{\sqrt{3}}|C(t_2)|\sin\left(\frac{\theta_1(t_2)}{3}\right), \end{aligned} \tag{3.11}$$

with $\theta_1 = 3\arccos(\mathrm{Re}(C)/|C|) + \pi$ and $\theta_3 = 3\arccos(\mathrm{Re}(C)/|C|)$ where $t_1 = 0$ and $t_2 = V_0/2v$ are the time at which the first and second avoided crossings are encountered. The above expression considerably simplifies at large V_0. The energy gap ΔE_0 saturates to a maximum value $\sqrt{2}\Omega$ while the leading order term for $\Delta E_{V_0/2}$ is $2\Omega^2/V_0$ and falls off with V_0, as seen in Fig. 3.1(c).

For initial state $|1\rangle$, the maximum gap $\Delta E_0 = \sqrt{2}\Omega$ (same as ΔE_{V_0}) decides the adiabatic limit. This is independent of V_0. On the other hand, on choosing the initial state as $|2\rangle$ or $|3\rangle$, the smallest gap (among the three) $\Delta E_{V_0/2} \approx 2\Omega^2/V_0$ determines the adiabatic limit. Therefore, for $V_0 \gg \Omega$, with the approximation that at each avoided level crossing only two levels participate, the adiabatic theorem requires $v \ll 2\Omega^2$ for the adiabatic evolution. Similarly, we need $v \ll 2\Omega^4/V_0^2$ for an adiabatic evolution if the chosen initial state is $|2\rangle$ or $|3\rangle$. Note that the small gap $\Delta E_{V_0/2}$ at large V_0 ensures almost a complete population transfer between the states $|2\rangle$ and $|3\rangle$ unless v is negligibly small. In other words, if the initial state is $|2\rangle$ or $|3\rangle$, an adiabatic evolution is not guaranteed for a large value of $V_0/\sqrt{v}$.

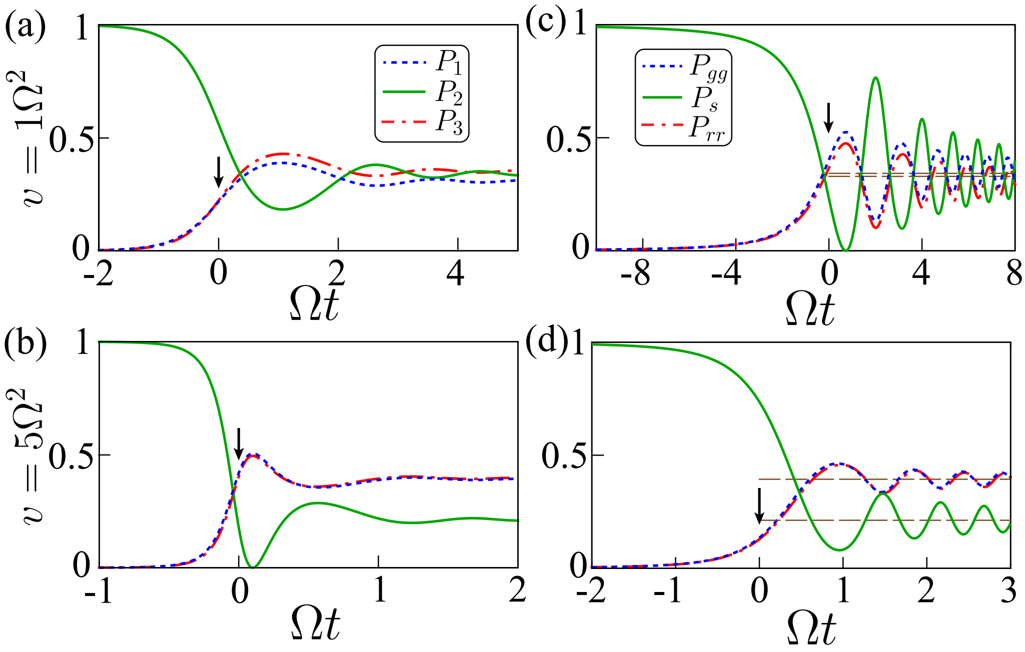

Figure 3.7: The dynamics of populations in the adiabatic (a)-(b) and the diabatic (c)-(d) states for the initial state $|\psi(t_i)\rangle = |2\rangle \sim |s\rangle$, $v = (1\Omega^2, 5\Omega^2)$, and $V_0 = 0.1\Omega$. The three LZTs are not resolvable in time hence depicted by a single arrow. The dashed horizontal lines in (c) and (d) show the results from the non-interacting model.

3.4.2 Initial state: $|\psi(t_i)\rangle = |2\rangle$

Adiabatic states

Weak interaction — The left panels of Figs. 3.7 show the population dynamics in adiabatic states for the initial state $|2\rangle$ in weakly interacting case. Keeping $V_0 \ll \Omega$, but with smaller v, Rydberg-Rydberg interactions introduces an offset in the dynamics of the states $|1\rangle$ and $|3\rangle$, i.e., $P_1(t) \neq P_3(t)$ [see Fig. 3.7(a)]. For small V_0 and larger v, (*i.e.* $V_0/\sqrt{v} \ll 1$), the interaction V_0 doesn't play any role, and we get $P_1(t) = P_3(t)$ as that of the non-interacting case [see Fig. 3.7(b)].

Strong interaction —The population dynamics in adiabatic states for the strongly interacting case is shown in the left panels of Figs. 3.8. For $V_0 \gg \Omega$, the population in $|2\rangle$ first gets transferred to $|1\rangle$ near $t = 0$. Afterwards, any remaining population in $|2\rangle$ gets nearly completely transferred to $|3\rangle$ at second avoided crossing owing to a small energy gap at t_2. Near t_3, when the system encounters the third avoided crossing, the state $|2\rangle$ partially gains back population from state $|1\rangle$. The transition probability between $|1\rangle$ and $|2\rangle$ depend on v whereas there is a complete transfer to $|3\rangle$ at the second avoided crossing for sufficiently large v.

The steady state population in the adiabatic/diabatic states as a function of v and V_0 for the initial state $|2\rangle$ is shown in Fig. 3.9. Contrary to the case with initial state as $|1\rangle$, here $P_3(t_f) \sim P_{gg}$ is a variable function of V_0 [see Fig. 3.9(c)]. Furthermore, the population $P_3(t_f)$ depends non-monotonically on v. For large V_0

this feature can be explained as follows: at smaller values of v, the transition from $|2\rangle$ is adiabatic near the first avoided crossing (to $|1\rangle$) while becomes non-adiabatic for the second avoided crossing (to $|3\rangle$) due to the small energy gap $\Delta E_{V_0/2}$. Hence, the transition probability to $|3\rangle$ increases with v and thus $P_3(t_f)$. However, for large enough values of v, the transition becomes non-adiabatic across the first avoided crossing as well, and the transition probability to state $|1\rangle$ increases with v while that to $|3\rangle$ saturates, in effect leading to a decrease in $P_3(t_f)$. The non-trivial patterns in $P_1(t_f)$ and $P_2(t_f)$ are due to the interference of LZTs at different avoided crossings.

Diabatic states

Now we shift our attention to the evolution in diabatic states which are shown in the right panels of Figs. 3.7 and 3.8. The system is initially prepared in $|s\rangle$ state.

Weak interaction — For larger values of v in the weakly interacting regime *i.e.* in the limit $V_0/\sqrt{v} \ll 1$, the population in $|s\rangle$ state transitions to $|gg\rangle$ and $|rr\rangle$ states with an equal probability, as seen (red and blue dotted lines) in Fig. 3.7(d). The final populations are similar to that obtained from the non-interacting LZ model shown as horizontal dashed lines in Figs. 3.7(c) and 3.7(d). The exact values of population in the non interacting case are, $P_{gg}(t \to \infty) = P_{rr}(t \to \infty) = 2P_{LZ}(1 - P_{LZ})$ and $P_s(t \to \infty) = 1 - 4P_{LZ}(1 - P_{LZ})$. At small interactions $V_0 \ll \Omega$ with smaller values of v, there is a slight difference in the population distribution among $|gg\rangle$ and $|rr\rangle$ [see Fig. 3.7(c)]. This is because, at smaller v, the system spends more time

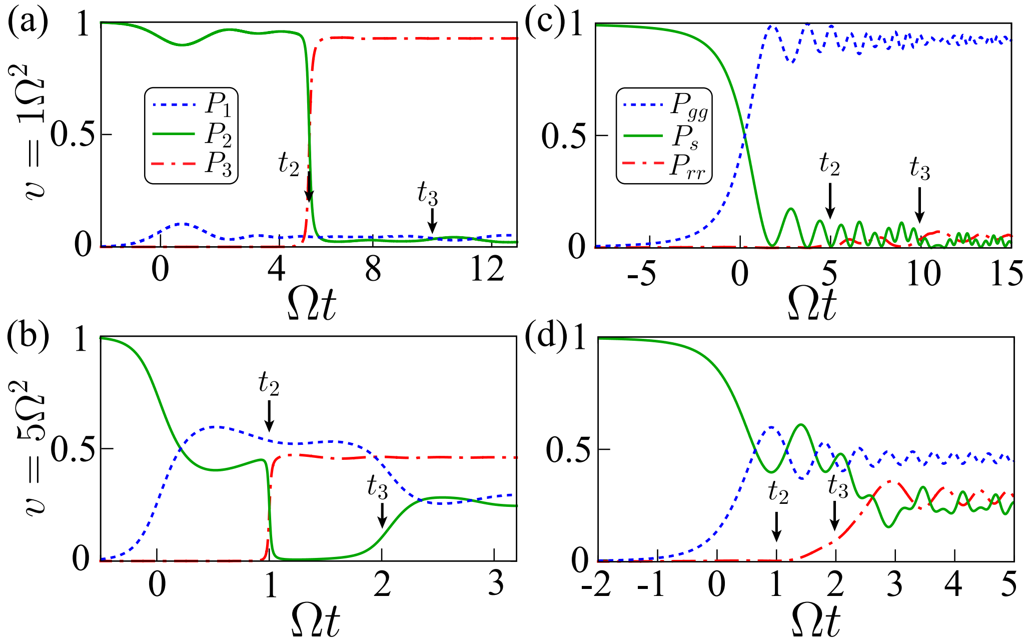

Figure 3.8: The dynamics of populations in the adiabatic (a)-(b) and the diabatic (c)-(d) states for the initial state $|\psi(t_i)\rangle = |2\rangle \sim |s\rangle$, $v = (1\Omega^2, 5\Omega^2)$, and $V_0 = 10\Omega$. The first LZT takes-place in the vicinity of $t = 0$.

in the impulse regime. Therefore, it experiences effects due to non-zero but small interaction and results in a deviation from the non-interacting case. A correction incorporates the effect of finite but small V_0 at smaller v values, similar to Eq. (5.4.2),

$$P_{gg}(t \to \infty) \approx 1 - P_{LZ}^2 - (1 - R_{LZ})^2, \tag{3.12}$$

$$P_{rr}(t \to \infty) \approx 1 - P_{LZ}^2 - (1 - Q_{LZ})^2, \tag{3.13}$$

$$P_s(t \to \infty) = 1 - P_{rr} - P_{gg} \tag{3.14}$$

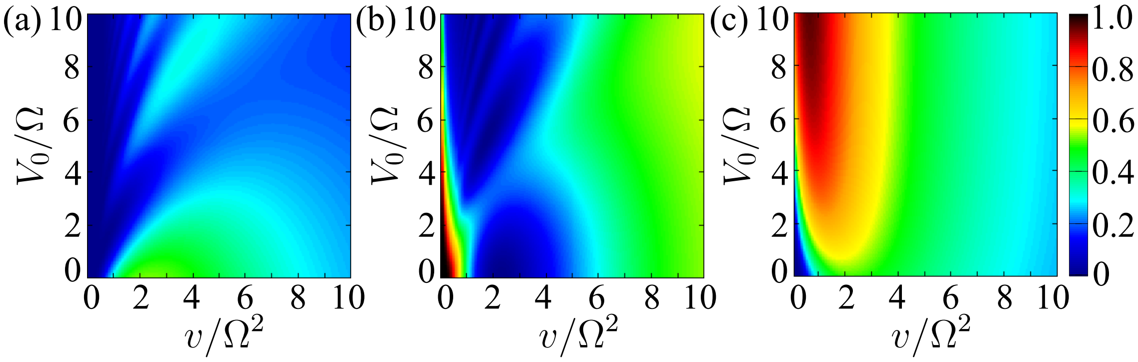

Figure 3.9: The final population in (a) $|1\rangle \sim |rr\rangle$, (b) $|2\rangle \sim |s\rangle$ and (c) $|3\rangle \sim |gg\rangle$, after the linear quench, as a function of v and V_0 for the initial state $|\psi(t_i)\rangle = |2\rangle$, $\Delta(t_i) = -10\Omega$, and $\Delta(t_f) = 30\Omega + 10v/\Omega$.

where $R_{LZ} = P_{LZ} \exp\left(-\frac{\pi\Omega^2 V_0}{2^{5/2} v^{3/2}}\right)$. These results are in excellent agreement with the exact numerical results (not shown).

Strong interaction — For $V_0 \gg \Omega$, the population transfer doesn't happen simultaneously. The first LZT takes place near $t = 0$ from $|s\rangle$ to $|gg\rangle$ as shown in Figs. 3.8(c) and 3.8(d). There is no signature of second LZT in the dynamics at t_2 since $|gg\rangle$ state is not coupled to $|rr\rangle$ state. In the vicinity of t_3, the population gets transferred from $|s\rangle$ to $|rr\rangle$. If the sweeping rate across first avoided crossing is sufficiently slow, the system is adiabatically brought to $|gg\rangle$, a state with no Rydberg excitations. This de-excitation is in stark contrast to the dynamical creation of excitations by adiabatically sweeping the detuning from negative to large positive values [136, 247, 248].

3.4.3 Initial state: $|\psi(t_i)\rangle = |3\rangle$

With the initial state as $|3\rangle$ and $V_0 \gg \Omega$, the first avoided crossing is irrelevant in the dynamics. So the first transition occurs near t_2 to state $|2\rangle$ [see Figs. 3.10(a) and 3.10(b)]. Afterwards, across the third avoided crossing, transition from $|2\rangle$ to $|1\rangle$ takes place. Thus, at large values of V_0 and sufficiently large v, we have $P_3(t_f) \sim 0$ [see Fig. 3.10(b)]. Regarding the diabatic states, the initial population is solely in $|rr\rangle$. Since the diabatic states do not experience the second avoided crossing, for $V_0 \gg \Omega$, only the third avoided crossing is relevant, and a singular population transfer happens to $|s\rangle$ near t_3 [see Figs. 3.10(c) and 3.10(d)]. At larger values of v, the transition between $|rr\rangle$ and $|s\rangle$ gets weaker. For $V_0 \ll \Omega$ with large v, in steady state we get the results for the final population using the non-interacting LZ model: $P_{rr} \approx P_{LZ}^2$, $P_s \approx 2P_{LZ}(1-P_{LZ})$, and $P_{gg} \approx (1-P_{LZ})^2$. However for smaller v, we incorporate the effect of a finite V_0 and obtain the rectified values as:

$$P_3(t_f \to \infty) = P_{gg} \approx (1-R_{LZ})^2, \tag{3.15}$$

$$P_2(t_f \to \infty) = P_s \approx 1 - P_{LZ}^2 - (1-R_{LZ})^2 \tag{3.16}$$

$$P_1(t_f \to \infty) = P_{rr} \approx P_{LZ}^2. \tag{3.17}$$

The final population in the adiabatic/diabatic states as a function of v and V_0 for the initial state $|3\rangle$ is shown in Fig. 3.11. Comparing final populations in Fig. 3.11 with Fig. 3.9 and Fig. 3.5, we observe that the patterns in the $v-V_0$ plane reoccurs. The identical patterns are (i) $P_3(t_f)$ with initial state $|1\rangle$ and $P_1(t_f)$ with initial state $|3\rangle$, (ii)$P_2(t_f)$ with initial state $|1\rangle$ and $P_1(t_f)$ with initial state $|2\rangle$ and (iii) $P_3(t_f)$ with initial state $|2\rangle$ and $P_2(t_f)$ with initial state $|3\rangle$. This implies that Rydberg-Rydberg interactions do not break the symmetry completely while swapping the states in the LZ model.

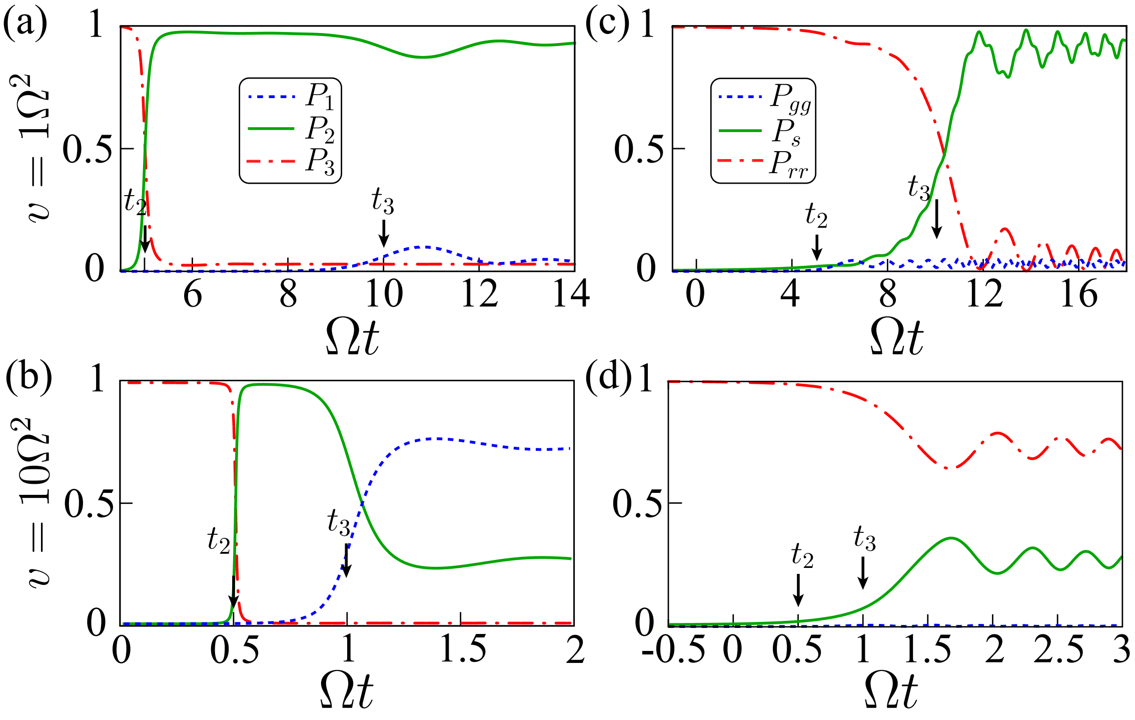

Figure 3.10: The dynamics of population in the adiabatic (a)-(b) and diabatic (c)-(d) states for the initial state $|\psi(t_i)\rangle = |3\rangle \sim |rr\rangle$ with different values of v while keeping $V_0 = 10\Omega$. The thin arrows show the times around which the second (t_2) and the third (t_3) LZTs occur.

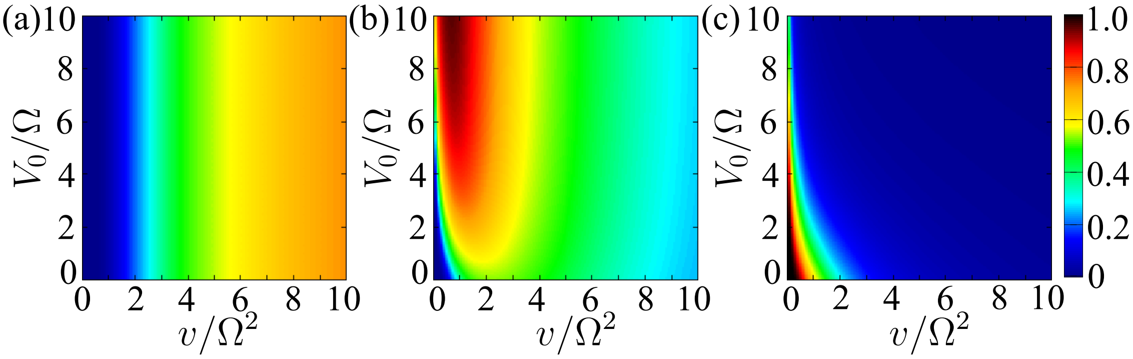

Figure 3.11: The final population in (a) $|1\rangle \sim |rr\rangle$, (b) $|2\rangle \sim |s\rangle$ and (c) $|3\rangle \sim |gg\rangle$, after the linear quench, as a function of v and V_0 for the initial state $|\psi(t_i)\rangle = |2\rangle$, $\Delta(t_i) = -10\Omega$, and $\Delta(t_f) = 30\Omega + 10v/\Omega$.

Beats

Depending on the geometric size of the triangle formed by the three avoided crossings [see Fig. 3.1(b)], the triangular LZ model exhibits beat and step patterns in the population dynamics of the diabatic states [154, 222]. These patterns arise due to the quantum interference of distinct LZTs. We only briefly comment on the beats pattern in our setup. The beats pattern is observed only in the population of the $P_s(t)$ as shown in Fig. 3.12(a) for different initial states. Based on the calculations in Ref. [222], we would expect a beat pattern in $P_s(t)$ if $\Omega^2/4v \ll 1$ and $V_0^2/4v < 1$. The envelope frequency is approximately $V_0/2$, and the fast oscillation frequency changes over time as approximately $vt/4$.

3.5 Adiabatic Impulse approximation

In this section, we employ the adiabatic impulse approximation to analyze the dynamics in the three-level LZ model described in Eq. (3.7). To separate adiabatic and non-adiabatic regimes, we require $V_0 \gg \Omega$ [see Figs. 3.1(b) and 3.12(b)]. When the avoided crossings are well isolated, we assume that only two adiabatic states are involved in each avoided crossings [also see Fig B.1]. It allows us to use the non-adiabatic matrices obtained in the two-level LZ model discussed in Sec. 1.4.2. The validity of AIA in the three-level LZ model requires the LZT time (τ_{LZ}) to be shorter than the duration during which the system evolves adiabatically between two LZTs ($T_a = V_0/2v$). Since $\Delta E_0 = \Delta E_{V_0} > \Delta E_{V_0/2}$ for $V_0 \neq 0$, the upper limit for τ_{LZ} is set by $\tau_{LZ} \approx (\frac{1}{2\sqrt{v}})\max\left(1, \sqrt{\Omega^2/4\mathrm{v}}\right)$. Therefore, for $v > \Omega^2/2$, we require $V_0^2 > v$ for AIA to be valid, whereas for $v < \Omega^2/2$, AIA is already satisfied in the

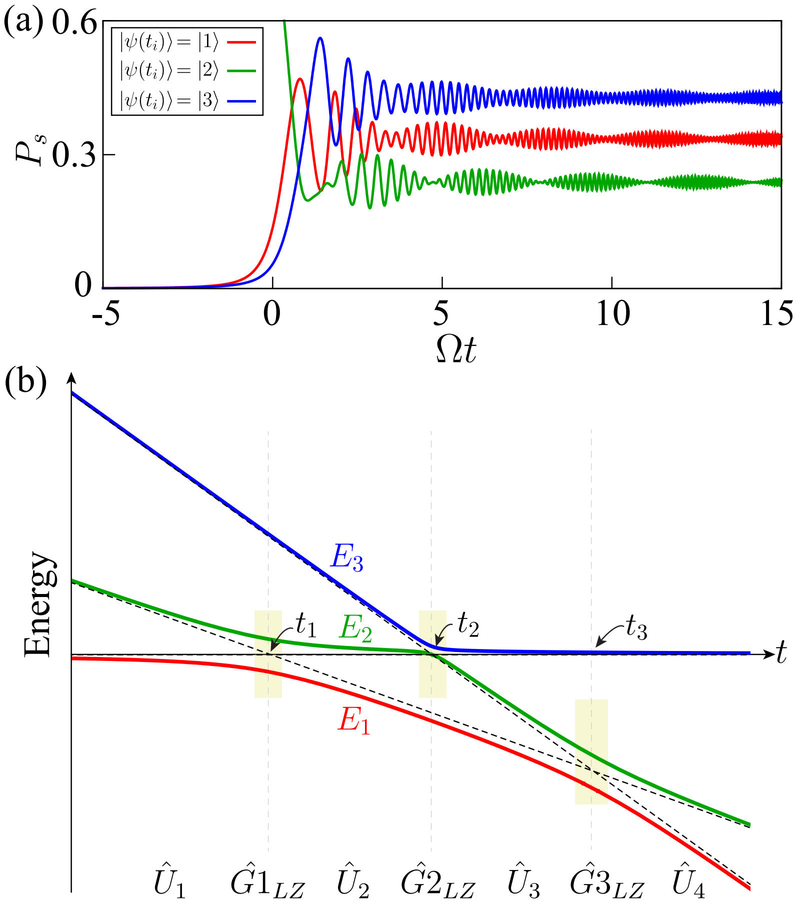

Figure 3.12: (a) The beats in the dynamics of $P_s(t)$ for $V_0 = 2\Omega$, $v = 5\Omega^2$, and different initial states. (b) The instantaneous energy eigenspectrum for $\Delta(t) = vt$ for large V_0. The adiabatic and non-adiabatic regimes are marked by the operators $\hat{U}_{1,2,3,4}$ and $\{\hat{G}1_{LZ}, \hat{G}2_{LZ}, \hat{G}3_{LZ}\}$.

strong interaction regime. The adiabatic evolution matrix is given by

$$\hat{U}_k = \begin{pmatrix} e^{-i\zeta_3^{\{k\}}} & 0 & 0 \\ 0 & e^{-i\zeta_2^{\{k\}}} & 0 \\ 0 & 0 & e^{-i\zeta_1^{\{k\}}} \end{pmatrix},$$

where $\zeta_j^{\{1\}} = \int_{t_i}^{t_1} dtE_j$, $\zeta_j^{\{2\}} = \int_{t_1}^{t_2} dtE_j$, $\zeta_j^{\{3\}} = \int_{t_2}^{t_3} dtE_j$, and $\zeta_j^{\{4\}} = \int_{t_3}^{t_f} dtE_j$ are the phases acquired between the avoided crossings. We define the non-adiabatic transition matrix $\hat{G}1_{LZ}$ at the impulse point t_1 in the basis $\{|1\rangle, |2\rangle, |3\rangle\}$ as,

$$\hat{G}1_{LZ} = \begin{pmatrix} 1 & 0 & 0 \\ 0 & \sqrt{1-P'_{LZ}}e^{-i\tilde{\phi}'_s} & -\sqrt{P'_{LZ}} \\ 0 & \sqrt{P'_{LZ}} & \sqrt{1-P'_{LZ}}e^{i\tilde{\phi}'_s} \end{pmatrix} \tag{3.18}$$

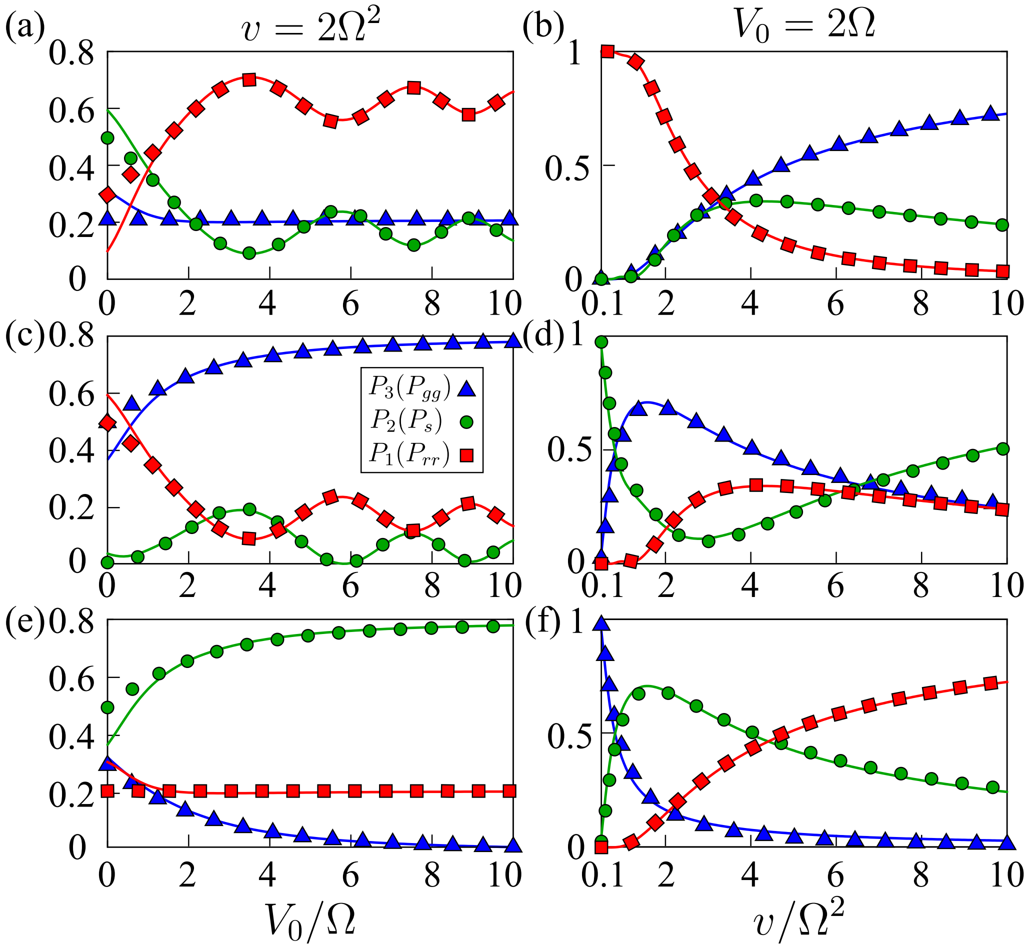

Figure 3.13: The final population in the adiabatic/diabatic states as a function of both V_0 and v for the initial state $|1\rangle$ (a)-(b), $|2\rangle$ (c)-(d), and $|3\rangle$ (e)-(f). For the first column, $v = 2\Omega^2$ and for the second column, $V_0 = 2\Omega$. The solid lines show exact results, and the filled squares, circles, and triangles are from AIA.

where $P'_{LZ} = \exp(-2\pi\Omega'^2/4v)$, and

$$\tilde{\phi}'_s = \pi/4 + \arg(\Gamma(1 - i\gamma')) + \gamma'(\ln\gamma' - 1) \tag{3.19}$$

with $\gamma' = \Omega'^2/4v$ and $\Omega' = \Delta E_0 \sim \sqrt{2}\Omega$. Similarly, the transition matrix at t_2 is

$$\hat{G}2_{LZ} = \begin{pmatrix} \sqrt{1 - P''_{LZ}}e^{-i\tilde{\phi}''_s} & -\sqrt{P''_{LZ}} & 0 \\ \sqrt{P''_{LZ}} & \sqrt{1 - P''_{LZ}}e^{i\tilde{\phi}''_s} & 0 \\ 0 & 0 & 1 \end{pmatrix} \tag{3.20}$$

with $P''_{LZ} = \exp(-2\pi\Omega''^2/8v)$ and

$$\tilde{\phi}''_s = \pi/4 + \arg(\Gamma(1 - i\gamma'')) + \gamma''(\ln\gamma'' - 1) \tag{3.21}$$

with $\gamma'' = \Omega''^2/8v$ and $\Omega'' = \Delta E_{V_0/2}$. We have $\hat{G}3_{LZ} = \hat{G}1_{LZ}$ since at t_3, the LZT involves $|1\rangle$ and $|2\rangle$. The complete evolution matrix in AIA is given by

$\hat{F}_L = \hat{U}_4\hat{G}3_{LZ}\hat{U}_3\hat{G}2_{LZ}\hat{U}_2\hat{G}1_{LZ}\hat{U}_1$. The resultant population obtained from AIA $|\psi(t_f)^{AIA}\rangle = \hat{F}|\psi(t_i)\rangle$ is compared with the exact dynamics. The final form of state $|\psi(t_f)^{AIA}\rangle$ thus obtained can be seen as a generalized rotation in $SU(3)$ [see Appendix B.2.2]. The final populations obtained from AIA and numerics are plotted as a function of v and V_0, for different initial states, and shown in Fig. 3.13. They exhibit good agreement even beyond the criteria discussed above. One reason could be that τ_{LZ} only sets the upper limit for the transition time, and the actual duration for transition can be much shorter than that.

As shown in Figs. 3.13(a) and 3.13(c), for a fixed v, the final population in states $|s\rangle$ and $|rr\rangle$ exhibit oscillations as a function of V_0, indicating the role of quantum interference between the distinct LZTs. On the other hand, for a fixed V_0, upon varying v we do not observe any oscillations. It indicates that the Stokes phases ($\tilde{\phi}'_s$ and $\tilde{\phi}''_s$) become irrelevant in the final populations if the initial state is one of the instantaneous eigenstates. We have verified this by setting $\tilde{\phi}'_s = \tilde{\phi}''_s = 0$ in the matrices $\hat{G}1_{LZ}$ and $\hat{G}2_{LZ}$, and the results are hardly affected by it. If the initial state is not the instantaneous eigenstate, the Stokes phases become important. In that case, we will observe oscillations in the final populations as a function of v keeping V_0 fixed. Ultimately, AIA reveals the different phases involved in the dynamics.

3.6 Summary and outlook

In summary, we analyzed the LZ dynamics in a setup of two Rydberg-atoms with a time-dependent linear detuning. We have shown, the Rydberg-atom setup realizes different LZ models such as the bow-tie model and the triangular LZ model. Since state-of-the-art Rydberg setups deal with strong Rydberg-Rydberg interactions (RRIs), the triangular LZ model can be tested in these systems through chirping the frequency of laser field, which couples the ground to the Rydberg state [149–151, 217, 249]. For two atoms (which can be easily realizable using optical tweezers or microscopic optical traps [76]), the LZ dynamics showed a non-trivial dependence on the initial state, the quench rate, and the interaction strength. We discussed in detail the validity of AIA in describing the dynamics for a linear variation of detuning. Interestingly, AIA reveals detailed information about the phases developed during the dynamics, which can be very useful for applications such as coherent control of quantum states, implementing quantum (phase) gates [138, 250], and atom-interferometry [251].

While implementing AIA, we rely on large RRIs for which the LZTs across each avoided crossing include only two adiabatic states. For small interactions, it is required to develop a multi-level AIA in which the LZTs take place among multiple levels at the same time. Our study can be extended to three two-level atoms, for which it will not be so straightforward to assume AIA would work at large values of interactions due to the complexity in the level structure.

Chapter 4

Landau-Zener transition and adiabatic impulse approximation in a periodically driven pair of Rydberg atoms

The current chapter is adapted from the research article "Landau-Zener transitions and adiabatic impulse approximation in an array of two Rydberg atoms with time-dependent detuning" [87]. We analyze the population dynamics of a periodically driven single two-level atom as well as a pair of interacting Rydberg atoms, both numerically and with adiabatic impulse approximation. In particular, the coherent resonances instigated by periodic driving are investigated for different initial states and driving amplitude. For the single atom case, we observe a striking similarity in the single-atom excitation probability with that of the intensity distribution in a uniform antenna array. For the two atom case, we show that for AIA to capture all the resonances, the periodic modulation should incorporate all the avoided crossings present in the system. Furthermore, AIA reveals the rich structure of phases involved in the dynamics which could be very relevant in coherent preparation of quantum states, implementation of entangled gates, and in Landau-Zener interferometry.

4.1 Introduction

Periodically driven quantum systems exhibit a wealth of rich dynamics that are not accessible within stationary quantum mechanics. In the single-particle case, notable phenomena such as coherent destruction of tunneling [161], dynamical localization [164, 252], and population trapping [159, 160] occur. Such dynamics emerge from the interferences among multiple LZTs when the system is driven periodically across an avoided crossing. The intricate interference pattern can be observed through Landau-Zener-Stückelberg (LZS) interferometry [214] in superconducting qubits [229, 242, 251, 253, 254], quantum dots [239, 241, 255], electronic qubits [256–258], dopant embedded in nanowires [259], or optical waveguides [260]. There is a growing interest in multi-particle systems where transition across multiple LZTs acts as a robust method to control the states or are used as a quantum gate operation using quantum dots [240], and Rydberg atoms [138, 250]. Periodically driven pair of Rydberg atoms can engineer the parameter space for Rydberg-blockade and anti-blockades [137]. To implement periodic driving in a Rydberg chain, one can modulate the light field which couples the ground to the Rydberg state. Another way is to apply additional radio-frequency or microwave fields, and they provide off-resonant couplings to other Rydberg states [261, 262]. To analyze the dynamics, the AIA approach is very useful in the context of periodic driving [263–266]. We have described AIA in Sec. 1.4.2 and further used it to describe the dynamics in a linearly driven system of two-atoms in Chapter 3. In this chapter, we extend the applicability of AIA to the periodically driven case.

We analyze the population dynamics of two-level Rubidium Rydberg atoms in which the ground state ($5S_{1/2}$) is coupled to a Rydberg state ($nS_{1/2}$) with a periodically time-dependent detuning in a single atom and a pair of Rydberg atoms. The dynamics are investigated with both numerics and AIA for different initial states, driving amplitudes, and cycles of periods in both adiabatic and diabatic states.

4.2 Periodically driven single two-level atom

In this section, we review the single two-level atom under the influence of a periodically varying detuning in consideration with adiabatic impulse approximation. As before, we consider the two-level atom with a ground state $|g\rangle$ and a Rydberg state $|r\rangle$. The two-level atom is driven continuously by a light field with Rabi frequency Ω and a periodically time-dependent detuning $\Delta(t) = \Delta_0 + \delta\sin(\omega t)$. Allowing the motional degrees of freedom to be frozen at ultracold temperatures under controlled experimental environment, the system can be described by the Hamiltonian ($\hbar = 1$),

$$\hat{H}(t) = \frac{\Omega}{2}\hat{\sigma}_x - \Delta(t)\hat{\sigma}_{rr},$$

where $\hat{\sigma}_x = \hat{\sigma}_{gr} + \hat{\sigma}_{rg}$ is one of the Pauli's operator and $\hat{\sigma}_{ab} = |a\rangle\langle b|$ are atomic operators with $a, b \in \{g, r\}$. The two important set of bases are (a) diabatic basis which consist of states $\{|g\rangle, |r\rangle\}$ and (b) the adiabatic basis $|\phi_{\pm}(t)\rangle$ which is given in Eq. (1.19). We especially note from Eq. (1.18) that the energies of the adiabatic levels exhibit an avoided-crossing at times when $\Delta(t) = 0$ [also see Fig. 1.6(a)].

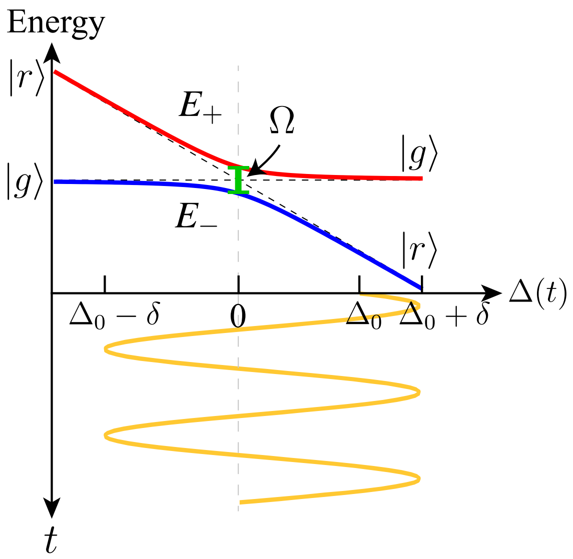

Figure 4.1: The top panel shows the instantaneous energy eigenvalues $E_\pm$ and the energy gap at avoided-crossing is Ω. The bottom panel depicts periodic time dependence of $\Delta(t)$. Away from the avoided crossing, adiabatic evolution takes place while at the avoided-crossing, instantaneous impulse transition occurs under the AIA.

Unlike a linear sweep where the avoided-crossing is encountered only at a single instant, under a periodic modulation of detuning, the avoided-crossing ($\Delta(t) = 0$) is encountered at multiple times during evolution, as shown in Fig. 4.1. Furthermore, under suitable parameter regimes, we can employ AIA in the system *i.e.* away from the avoided-crossing, we consider that an adiabatic evolution takes place in which the system remains in the instantaneous eigenstate of the Hamiltonian; whilst in the vicinity of avoided-crossing, the evolution is of impulse kind where a non-adiabatic transition (LZT) occurs, as indicated in Fig. 4.2(b). From the Sec. 1.4.2, we also know that for a single linear sweep across the avoided-crossing, transition probability between the adiabatic levels is $P_{LZ} = \exp\left(-\pi\frac{\Omega^2}{2|v|}\right)$.

For a periodic sweep, the multiple instants at which the avoided level crossing ($\Delta(t) = 0$) is encountered, are specified by the ordered set,

$$\tau_{2n} = [2n\pi + \sin^{-1}(-\Delta_0/\delta)]/\omega \tag{4.1}$$

$$\tau_{2n+1} = [(2n+1)\pi - \sin^{-1}(-\Delta_0/\delta)]/\omega, \tag{4.2}$$

where $n = 0, 1, 2, ...$, which are labelled in Fig 4.2(a) within one complete cycle of periodic detuning. At these instants, the detuning can be approximated, in the lowest order, as a linear function $\Delta(\tau_n \pm t) \approx \pm vt$ with $v = \omega\sqrt{\delta^2 - \Delta_0^2}$ through a Taylor's series expansion [214]. The linearity of detuning in fact makes each impulse evolution identical to a LZT with transition probability given by Eq. (1.22) and evolution matrix directed by Eq. (1.21). Away from the avoided-crossings, the adiabatic evolution matrix is given by unitary operator $\hat{U}(t_2, t_1)$ described in

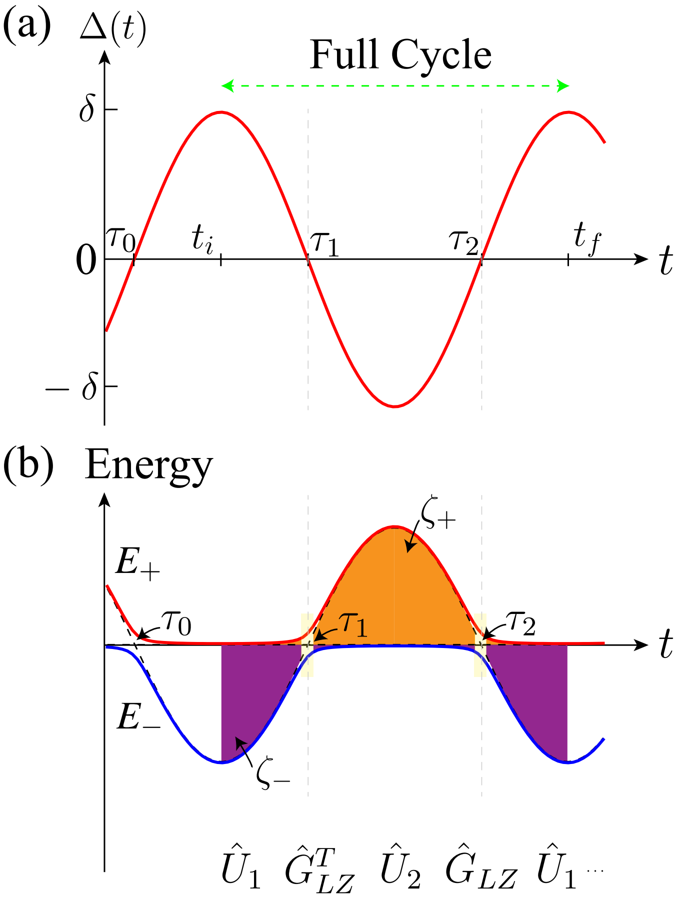

Figure 4.2: (a) (Top) The periodic modulation of $\Delta(t)$ as a function of time. $\tau_{j=0,1,2}$ indicate the instants at which the avoided crossing is encountered during one cycle. (b) (Bottom) The instantaneous energy eigenvalues $E_\pm$ corresponding to the time-dependent detuning. At the avoided crossings, $t = \tau_{2n}(\tau_{2n+1})$ LZT occurs and is described by the operator $\hat{G}_{LZ}(\hat{G}^T_{LZ})$. On either side of the avoided-crossing, an adiabatic evolution takes place which is determined by $\hat{U}_1$ and $\hat{U}_2$. The shaded areas indicates the phase accumulated ($\zeta_\pm$) during the adiabatic evolution.

Eq. (1.21). Note however when $\Delta_0 \neq 0$, there is a disparity in phases accumulated under adiabatic evolution to the left and right sectors of an avoided crossing and thus the two corresponding evolution matrices become dissimilar.

4.2.1 Time-evolution under AIA

We first consider evolution over a half-cycle, in particular from $t_i = \tau_1 - \pi/2\omega$ to $t_f = \tau_1 + \pi/2\omega$. Considering AIA, we can write the evolution matrix as $\hat{U}_2(t_f, \tau_1)\hat{G}^T_{LZ}\hat{U}_1(\tau_1, t_i)$

where we have defined the adiabatic matrices $\hat{U}_1$ and $\hat{U}_2$ as

$$\hat{U}_1(\tau_1, t_i) = \begin{pmatrix} e^{-i\zeta_+(\tau_1,t_i)} & 0 \\ 0 & e^{-i\zeta_-(\tau_1,t_i)} \end{pmatrix},$$

$$\hat{U}_2(\tau_2, \tau_1) = \begin{pmatrix} e^{-i\zeta_+(\tau_1,t_i)} & 0 \\ 0 & e^{-i\zeta_-(\tau_1,t_i)} \end{pmatrix},$$

with accumulated phases $\zeta_\pm(\tau_1, t_i) = \int_{t_i}^{\tau_1} dtE_\pm(t)$ and $\zeta_\pm(\tau_2, \tau_1) = \int_{\tau_1}^{\tau_2} dtE_\pm(t)$. The impulse transition at time τ_1 corresponds to a negative sweep rate and consequently the non-adiabatic evolution matrix is given by a transpose of $\hat{G}_{LZ}$,

$$\hat{G}_{LZ}^T = \begin{pmatrix} e^{-i\tilde{\phi}_s}\sqrt{1-P_{LZ}} & \sqrt{P_{LZ}} \\ -\sqrt{P_{LZ}} & e^{i\tilde{\phi}_s}\sqrt{1-P_{LZ}} \end{pmatrix}. \tag{4.3}$$

The final populations, in this case, are similar to the case of a single Landau-Zener transition and are given simply through Eq. (1.21). However, as we increase t_f to incorporate more avoided crossings during the evolution, the final population significantly diverges from the above case. As we'll see below, the transfer probabilities also become periodic with a maximum achievable value of unity and a minimum value of zero. As a general remark, the order of impulse and adiabatic matrices should be cautiously written depending on the avoided-crossing (τ_n), the initial (t_i), and final (t_f) times.

For the whole cycle, two LZTs actualize during the course of evolution. Upon employing adiabatic impulse approximation, we write the complete time-evolution operator for one time-period, assuming $\Delta_0 > 0$, starting at $t_i = 0$ till $t_f = 2\pi/\omega$ as, $\hat{F} = \hat{U}_1(2\pi/\omega, \tau_2)\hat{G}_{LZ}\hat{U}_2(\tau_2, \tau_1)\hat{G}_{LZ}^T\hat{U}_1(\tau_1, 0)$ [see Figs. 4.2(a) and 4.2(b)]. The same can be written as a matrix in the adiabatic basis $\{\phi_-, \phi_+\}$ as:

$$\hat{F} = e^{i\phi_G}\begin{pmatrix} g_{11} & -g_{21}^* \\ g_{21} & g_{11}^* \end{pmatrix}, \tag{4.4}$$

where $\phi_G = \exp\left(i\int_0^{2\pi/\omega}\Delta(t)dt/2\right)$ is the global phase, and adiabatic basis is given by Eq. (1.19). The survival and transition probability amplitudes are respectively,

$$g_{11} = e^{-i\eta_0}(1-P_{LZ}) + e^{-i\eta_1}P_{LZ}, \tag{4.5}$$

$$g_{21} = (e^{-i\eta_3} - e^{-i\eta_2})e^{i\tilde{\phi}_s}\sqrt{(1-P_{LZ})P_{LZ}}, \tag{4.6}$$

$$\text{where,}\quad \eta_0 = \frac{1}{2}\int_0^{2\pi/\omega}\bar{\Omega}dt + 2\tilde{\phi}_s, \quad \eta_1 = \frac{1}{2}\int_0^{2\pi/\omega}\bar{\Omega}dt - \int_{\tau_1}^{\tau_2}\bar{\Omega}dt,$$

$$\eta_2 = \frac{1}{2}\int_0^{2\pi/\omega} \bar{\Omega} dt - \int_{\tau_2}^{2\pi/\omega} \bar{\Omega} dt + 2\tilde{\phi}_s, \quad \eta_3 = \int_0^{\tau_1} \bar{\Omega} dt - \frac{1}{2}\int_0^{2\pi/\omega} \bar{\Omega} dt$$

are the dynamically accumulated phases. It follows that if the system is initially in the ground state, the transition probability to the excited state after a complete cycle of Hamiltonian is,

$$P_+^1 = |g_{21}|^2 = 4(1 - P_{LZ})P_{LZ} \sin^2 \phi_s, \tag{4.7}$$

in which the phase $\phi_s = \frac{1}{2}\int_{\tau_1}^{\tau_2} \bar{\Omega} dt + \tilde{\phi}_s$ is called the Stückelberg phase wherein $\bar{\Omega}(t) = \sqrt{\Delta(t)^2 + \Omega^2}$ and $\tilde{\phi}_s$ is the Stoke's phase defined in Eq. (1.21). The transition probability is a periodic function of Stückelberg phase ϕ_s and may range from 0 to a maximum value of $4(1 - P_{LZ})P_{LZ}$. Equivalently, we can reason that the distinct features of one-cycle transition probability are arising due to quantum interference between Landau-Zener transitions at τ_1 and τ_2. In conclusion, the accumulated phases between the LZTs as well as the phase change during the LZTs ($\tilde{\phi}_s$) play a crucial role in the characterization of the dynamics in a complete cycle.

The maxima and minima of Eq. (4.7) provide us the exact conditions for constructive or destructive interference for a single cycle. A constructive interference occurs at $\phi_s = (n + 1/2)\pi$ leading to $|g_{21}|^2 = 4(1 - P_{LZ})P_{LZ}$, and a destructive interference ($|g_{21}|^2 = 0$) occurs at $\phi_s = n\pi$ where $n = 0, 1, 2, \ldots$. Note that, so long as the LZT time (the duration for which the LZT takes place across an avoided crossing) is sufficiently shorter than the duration of adiabatic evolution between the two transitions, the AIA holds valid. Hence, for durations such that $\tau_{LZ} < [\pi - 2\sin^{-1}(-\Delta_0/\delta)]/\omega$, AIA gives a good approximation of the dynamics. An upper limit for the transition duration τ_{LZ} is given by $\left(\sqrt{\gamma}/\Omega\right) \max(1, \sqrt{\gamma})$ with $\gamma = \Omega^2/4v$, and therefore the validity of AIA requires $\delta - \Delta_0 > \Omega$ and $\delta\omega > \Omega^2$ [145, 146, 214]. In Fig. 4.3(a), we show the probability of transition from the ground state to excited state after evolution for a single cycle of detuning, $t_i = \pi/2\omega$, $t_f = 5\pi/2\omega$, for $\delta = 20\Omega$ and $\Delta_0 = 5\Omega$. The populations obtained under AIA are in an excellent agreement with the exact numerical results.

In a similar fashion, we can evaluate the evolution matrix after multiple cycles of detuning under AIA. For k cycles, we simply have k ordered full-cycle operators and the evolution operator is $\hat{F}^k = (\hat{U}_1 \hat{G}_{LZ} \hat{U}_2 \hat{G}_{LZ}^T \hat{U}_1)^k$. In the adiabatic basis $\{|\phi_-\rangle, |\phi_+\rangle\}$ the k-cycle evolution matrix is [214],

$$\hat{F}^k = e^{ik\phi_G} \begin{pmatrix} u_{11} & -u_{21}^* \\ u_{21} & u_{11}^* \end{pmatrix}, \tag{4.8}$$

where the survival probability amplitude is $u_{11} = \cos k\alpha + i\mathrm{Im}(g_{11}) \sin k\alpha / \sin\alpha$ while transition probability amplitude is $u_{21} = g_{21} \sin k\alpha / \sin\alpha$ with the angle α

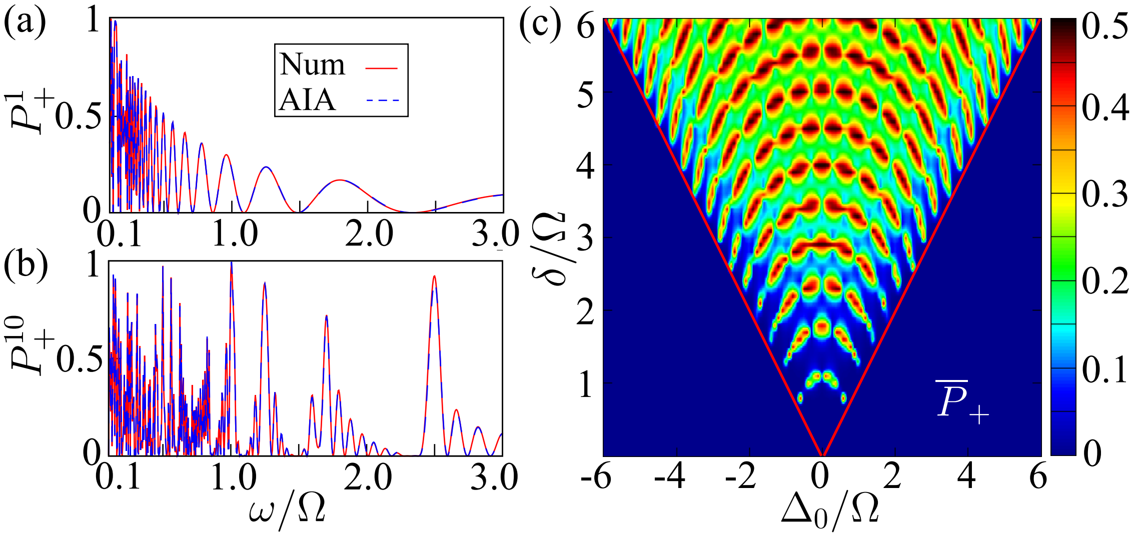

Figure 4.3: The transition probability to the excited state as a function of ω when the atom is initially prepared in the ground state for ($\delta = 20\Omega$, $\Delta_0 = 5\Omega$) at $t_i = \pi/2\omega$ after (a) one cycle and (b) 10 cycles. The solid line shows the exact results, and the dashed line is the same but from AIA. In (b), the peak at $\omega/\Omega = 2.5$ corresponds to the resonance $2\omega = \Delta_0$. (c) Interference pattern obtained using AIA: the long-time averaged population in the excited state ($\bar{P}_+$) as a function of Δ_0/Ω and δ/Ω for $\omega = 0.32\Omega$. The density peaks correspond to the resonances, and the solid lines mark the validity of AIA.

defined by $\cos\alpha = \mathrm{Re}(\mathrm{g}_{11})$. Therefore, the transition probability from the ground to the excited state after k-cycles of the periodic detuning is

$$P_+^k = |u_{21}|^2 = 4(1 - P_{LZ})P_{LZ}\sin^2\phi_s \frac{\sin^2 k\alpha}{\sin^2\alpha}. \tag{4.9}$$

We show the transition probabilities to the excited state after 10 cycles in Fig. 4.3(b). We can see that AIA is able to capture the resonances (sharp distinct peaks in 4.3(b)) which become a prominent feature in the dynamics when the system is taken through the avoided-crossing multiple times. To characterize the resonances and anti-resonances in the system, the long-time averaged populations are often useful. When $\omega \gg \Omega$, taking a time-average of dynamics is equivalent to taking an average of occupation probabilities over a large number of cycles ($k \gg 1$) [214]. The (cycle) averaged occupation probability in the excited state is given by,

$$\bar{P}_+ = \frac{2(1 - P_{LZ})P_{LZ}\sin^2\phi_s}{\sqrt{[4(1 - P_{LZ})P_{LZ}\sin^2\phi_s]^2 + \mathrm{Im}(g_{11})^2}}. \tag{4.10}$$

The maxima of the above equation gives criterion for a complete resonant transition between the adiabatic states allowing for both $\bar{P}_+ = \bar{P}_- = 1/2$. Thus, resonance occurs when $\mathrm{Im}(g_{11}) = -[(P_{LZ})\sin\eta_1 + (1 - P_{LZ})\sin\eta_0] = 0$. In the fast passage limit ($\gamma \gg 1$), $P_{LZ} \approx 1$ and the resonance criteria reduces to $\Delta_0 = n\omega$. The crest at $\omega/\Omega = 2.5$ in Fig. 4.3(b) is attributed to the resonance at $2\omega = \Delta_0$. In the slow

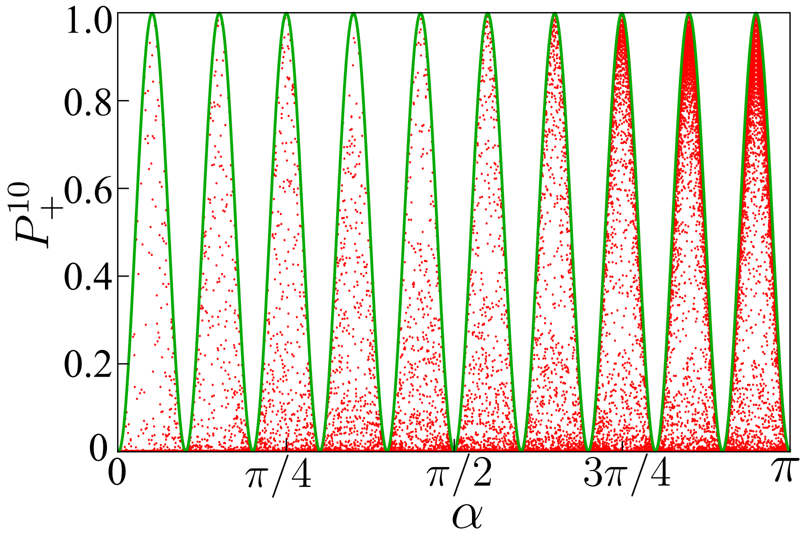

Figure 4.4: The excitation probability after ten cycles as a function of α for $\delta/\Omega = 20$, $\Delta_0 = 0$ and ω is varied. A given α is not associated with a unique value of ω, leading to the scattered points, but bounded by a maximum value of $\sin^2 k\alpha$ shown by the solid line.

passage limit we don't get a simplified expression for the resonance, but the resonances can be identified from the density peaks of $\bar{P}_+$ [see Fig. 4.3(c)] for smaller values of δ/Ω [267]. Note that a resonance defined by a complete transition among adiabatic states also implies coherent Rabi oscillations between the diabatic states, $|g\rangle$ and $|r\rangle$ [145].

4.2.2 Comparison with Multi-slit interference Pattern

We identify an interesting resemblance in the form of the Eq. (4.9) with the intensity distribution pattern obtained by an antenna array or simply a series of N identical uniformly spaced narrow slits separated by the same distances d. The N-slit interference pattern is of key importance in quantum mechanics due to its simplicity and key role in revealing the wave nature of both light and electrons. For the multi-slit array, the intensity due to multiple interference, along the direction θ is given by [268],

$$I(\theta) = I_0 \frac{\sin^2(k\phi/2)}{\sin^2(\phi/2)}, \tag{4.11}$$

where I_0 is the intensity from a single slit. The angle, $\phi = 2\pi d \sin\theta/\lambda$ is the phase difference between the consecutive slits where d is the spacing between the adjacent slits, and λ is the wavelength of incident light. Furthermore, I_0 is considered a constant upon neglecting the slit widths *i.e.* under narrow slit approximation. The N-slit intensity pattern takes a maximum value of $N^2 I_0$ for $\phi = 2n\pi$ where $n = 0, 1, 2, 3, ...$, and there are $k-1$ minima between two principal maxima which are located at $\phi = 2\pi/N, 4\pi/N, ..., 2(N-1)\pi/N$. Accordingly, there are also $N-2$ subsidiary maxima between two principal maxima.

Though the form of equations Eq. (4.9) and (4.11) is similar, the two have key differences. For instance, I_0 in Eq. (4.11) is independent of the angle ϕ, whereas the corresponding terms $|g_{21}|^2$ and α in Eq. (4.9) have common dependencies on variables such as ω and δ. In the latter case, a little algebra reveals that the maxima in the transition probability occur at $\cos k\alpha = 0$ or $\alpha = (2n+1)\pi/2k$, and the minima occur at $\sin k\alpha = 0$ or $\alpha = n\pi/k$. A key difference in the probability distribution is thus that $\alpha = 0$ doesn't correspond to a maximum for any value of k but instead, it is a minimum. This is in sharp contrast to the antenna array intensity distribution for which $\phi = 0$ always represents a principal maximum irrespective of the number of slits. Another major difference is that there are no secondary maxima in the excitation probability and consequently, only one minimum between the two maxima values. The corresponding probability distribution pattern obtained from AIA is shown in Fig. 4.4, which shows excitation probability after ten cycles ($k = 10$) as a function of α, for $\delta/\Omega = 20$ and $\Delta_0 = 0$ by varying ω (similar results can be obtained if δ or Δ_0 is varied). As there is no one-to-one correspondence between α and ω, it leads to a multi-valued plot with each scattered red-dot corresponding to different values of ω in Fig. 4.4. For a fixed α, the maximum value of P_+^k is provided by the condition $\mathrm{Im}(g_{11}) = 0$, and we have $(P_+^k)_{MAX} = \sin^2 k\alpha$, which is shown by the solid green curve in Fig. 4.4. As the number of cycles (k) increases, the number of peaks within the range $(0, \pi)$ increases and as a result, each peak also gets sharper. The number of peaks is equal to the number of cycles of the periodic drive. For example, for $k = 1$, there's only one maximum in $(0, \pi)$ while for $k = 10$, there are 10 maxima. These results imply that, by appropriately choosing the modulation parameters and the number of cycles k, we can control the transition probability in a two-level atom. In the following section, we consider the case of periodically driven two-atoms.

4.3 Periodic modulation in two-atoms

Now, we consider the two-atom case where the system is described by the Hamiltonian

$$\hat{H} = -\Delta(t)\sum_{i=1}^{2}\hat{\sigma}_{rr}^{i} + \frac{\Omega}{2}\sum_{i=1}^{2}\hat{\sigma}_{x}^{i} + V_0\hat{\sigma}_{rr}^{1}\hat{\sigma}_{rr}^{2}, \tag{4.12}$$

where $V_0 = C_6/R^6$ is the Rydberg-Rydberg vdW interaction between the atoms separated by a distance R with C_6 being the van der Waals coefficient. We consider the detuning as periodically varying with time $\Delta(t) = \Delta_0 + \delta\sin(\omega t)$ as the system is driven across the different avoided-crossings [see Fig. 4.5]. As discussed in chapter 3 and shown in Fig. 3.1, this Hamiltonian has three types of avoided-level crossings respectively at detunings $\Delta(t) = 0$, $\Delta(t) = V_0/2$, and $\Delta(t) = V_0$. We take $V_0 \gg \Omega$ so that the three avoided level crossings are well-isolated and we can implement AIA, as discussed in Sec. 3.5. We further choose a large negative offset in detuning at $t = 0$, *i.e.* $\Delta_0 \ll 0$ so that the adiabatic and diabatic states coincide with one another at the initial time $t_i = 0$. In what follows, we analyze the population dynamics for different initial states as a function of the experimentally controllable parameters δ and ω.

The avoided crossing at $\Delta(t) = 0$ involves states $|1\rangle$ and $|2\rangle$, and has a periodic occurence at times,

$$\tau_{2n}^{(1)} = [2n\pi - \sin^{-1}(\Delta_0/\delta)]/\omega, \tag{4.13}$$

$$\tau_{2n+1}^{(1)} = [(2n+1)\pi + \sin^{-1}(\Delta_0/\delta)]/\omega, \tag{4.14}$$

where $n = 0, 1, 2, ...$ Near these avoided-crossings $\tau_m^{(1)}$ the detuning is approximately a linear function of time, in the zeroth order, i.e., $\Delta(\tau_m^{(1)}+\tilde{t}) = \Delta_0+\delta\sin\omega(\tau_m^{(1)}+\tilde{t}) \approx \delta\omega\tilde{t}\cos\omega\tau_m^{(1)} = \left((-1)^m\omega\sqrt{\delta^2-\Delta_0^2}\right)\tilde{t}$. Thus, we obtain the quenching rate across the first avoided crossing, $v_1 = \pm\omega\sqrt{\delta^2-\Delta_0^2}$ and a LZT matrix can be used to describe the impulse transition. Note that, the approximation is valid as long as $\tilde{t} \ll 1/\omega$.

Similarly, the second set of avoided crossings that involves states $|2\rangle$ and $|3\rangle$) occur when $\Delta(t) = V_0/2$ at instants

$$\tau_{2n}^{(2)} = [2n\pi + \sin^{-1}((V_0/2-\Delta_0)/\delta)]/\omega \tag{4.15}$$

$$\tau_{2n+1}^{(2)} = [(2n+1)\pi - \sin^{-1}((V_0/2-\Delta_0)/\delta)]/\omega \tag{4.16}$$

with quench rates $v_2 = \pm\omega\sqrt{\delta^2-(\Delta_0-V_0/2)^2}$. Further, the third set of avoided crossings that involve states $|1\rangle$ and $|2\rangle$ again, occur when $\Delta(t) = V_0$ at times

$$\tau_{2n}^{(3)} = [2n\pi + \sin^{-1}((V_0-\Delta_0)/\delta)]/\omega, \tag{4.17}$$

$$\tau_{2n+1}^{(3)} = [(2n+1)\pi - \sin^{-1}((V_0-\Delta_0)/\delta)]/\omega. \tag{4.18}$$

with corresponding quench rates $v_3 = \pm\omega\sqrt{\delta^2-(\Delta_0-V_0)^2}$. The impulse evolution at every avoided crossing can be obtained by suitably replacing v by v_1, v_2, and v_3 in the LZT matrix in Eq. (3.18), Eq. (3.20) and Eq. (3.18), respectively giving us $\hat{G}1_{LZ}$, $\hat{G}2_{LZ}$, and $\hat{G}3_{LZ}$. Using the quench rates, we estimate the upper limit of the LZT durations across the avoided-crossings at $\tau_m^{(1)}$, and $\tau_m^{(3)}$ as

$$\begin{aligned}\tau_{LZ1} = & \frac{1}{2\sqrt{|v_1|}}\max\left(1, \sqrt{\Omega'^2/4|v_1|}\right), \\ \tau_{LZ3} = & \frac{1}{2\sqrt{|v_3|}}\max\left(1, \sqrt{\Omega'''^2/4|v_3|}\right),\end{aligned} \tag{4.19}$$

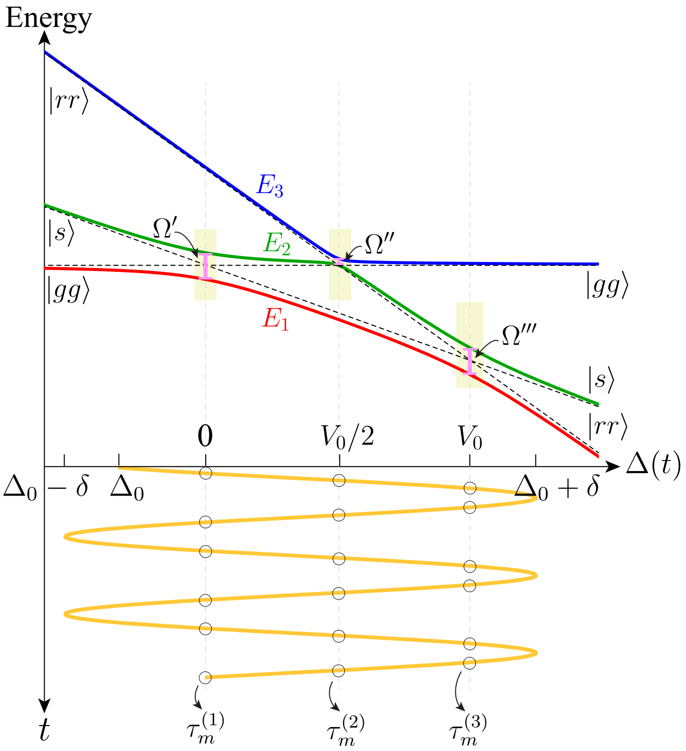

Figure 4.5: The above panel depicts the adiabatic (colored-solid lines) and diabatic (dashed-black lines) energy levels $E_{j=1,2,3}$ plotted as a function of Δ. The energy gap at $\Delta(t) = 0$ is $\Delta E_0 = \Omega'$, at the second avoided-crossing $\Delta(t) = V_0/2$ it is $\Delta E_{V_0/2} = \Omega''$, and for the third one at $\Delta(t) = V_0$ the gap is $\Delta E_{V_0} = \Omega'''$. In the bottom panel, the periodic time-dependence of $\Delta(t)$ is shown. The hollow circles in the bottom panel show the instants at which the corresponding avoided-crossing is traversed. Away from the avoided-crossings, adiabatic evolution takes place while at the avoided-crossing, instantaneous impulse transition takes place in the adiabatic impulse approximation.

respectively. The LZT duration for the impulse transition at $\tau_m^{(2)}$ is extremely small which is evident from the almost instantaneous transition from state $|2\rangle$ to $|3\rangle$ and vice-versa as shown in Fig. 3.8(a) and 3.8(b), for large values of V_0.

Note that, the periodic driving results in resonant transitions between different diabatic states [137] as well. For instance, in the high-frequency limit ($\omega \gg \Omega$) or the fast-passage limit $\left(\omega\sqrt{\delta^2 - \Delta_0^2} \gg \Omega\right)$, a resonant transition between $|gg\rangle$ and $|s\rangle$ occurs upon choosing $n\omega = \Delta_0$ where $n = 0, \pm1, \pm2....$ The resonance essentially implies a coherent Rabi oscillations between the two states. Similarly, for $n\omega = 2\Delta_0 - V_0$ resonant coherent Rabi oscillations between states $|gg\rangle$ and $|rr\rangle$ occurs, and for condition $n\omega = \Delta_0 - V_0$, coherent oscillations between $|s\rangle$ and $|rr\rangle$ states take place. To resolve the different resonances in the dynamics, we require sufficiently large RRIs. In the following, we analyze the population dynamics for a large value of V_0 as a function of δ and ω. Based on the value of δ, we consider three cases: (i) $\delta = V_0/4 - \Delta_0$, (ii) $\delta = 3V_0/4 - \Delta_0$, and (iii) $\delta = 5V_0/4 - \Delta_0$.

4.3.1 Case 1: $\delta = V_0/4 - \Delta_0$

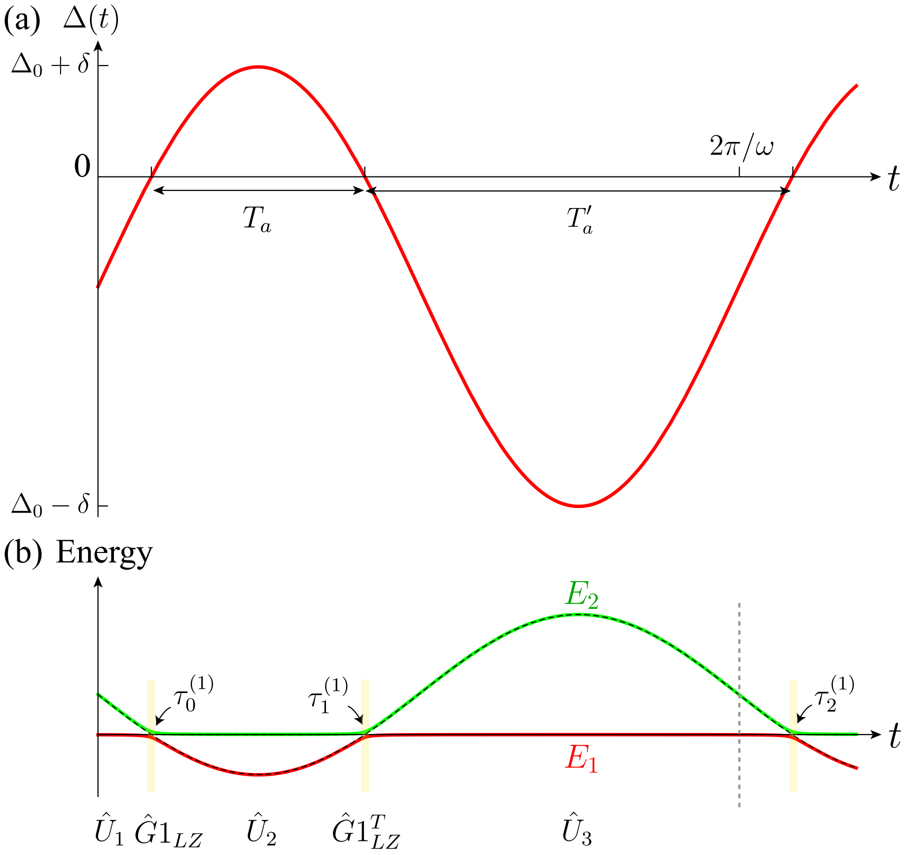

Figure 4.6: (a) The periodic time dependence of the detuning for $\delta = V_0/4 - \Delta_0$. The expected durations for adiabatic evolution are T_a and T'_a. (b) shows the corresponding instantaneous energy eigenvalues. The instants ($\tau_0^{(1)}$, $\tau_1^{(1)}$, $\tau_2^{(1)}$) at which the LZTs occur between states $|1\rangle$ and $|2\rangle$ are shown by shaded stripes. The operators $\hat{U}_j$ and $\hat{G}1_{LZ}$ indicate the adiabatic regimes and the impulse points, respectively. Between the origin and the dashed vertical line, we have one complete cycle.

In this case, we vary the detuning periodically across the first avoided crossing, and the maximum value that $\Delta(t)$ can take is chosen such that it lies midway between the first $\Delta(t) = 0$ and second avoided-crossing $\Delta(t) = V_0/2$. In this case, the state $|3\rangle$ is not part of the LZTs, and the evolution matrix for one complete cycle can be written as,

$$\hat{F} = \hat{U}_3 \hat{G}1^T_{LZ} \hat{U}_2 \hat{G}1_{LZ} \hat{U}_1. \tag{4.20}$$

There are three different time scales involved in the dynamics. One is the LZT duration τ_{LZ1} and the other two time-scales are the durations of adiabatic evolution

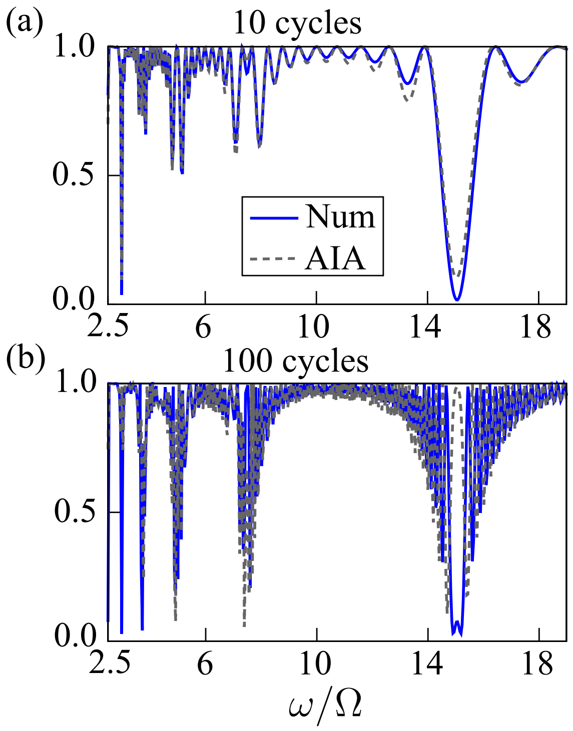

Figure 4.7: The numerical results (solid lines) and that of AIA (dashed lines) for P_1 after (a) 10 and (b) 100 cycles, as a function of ω for the initial state $|1\rangle \sim |gg\rangle$, $\Delta_0 = -15\Omega$, $V_0 = 40\Omega$ and $\delta = 25\Omega$. (b) shows that at longer times, AIA deviates from exact dynamics especially, at high ω.

between two consecutive LZTs:

$$T_a = \tau_1^{(1)} - \tau_0^{(1)} = \left(\pi - 2\arcsin(-\Delta_0/\delta)\right)/\omega, \tag{4.21}$$

$$T_a' = \tau_2^{(1)} - \tau_1^{(1)} = \left(\pi + 2\arcsin(-\Delta_0/\delta)\right)/\omega. \tag{4.22}$$

as shown in Fig. 4.6(a). Keeping $\Delta_0 < 0$, we have $T_a' > T_a$ and for the validity of AIA we only need $\tau_{LZ1} \ll T_a$. From Eqs. (4.19) and (4.22) we deduce that the ratio $\tau_{LZ1}/T_a \propto \sqrt{\omega}$ and it is clear that for some fixed values of (δ, Δ_0 ,V_0), sufficiently large values of ω may break down the AIA.

The final populations in the adiabatic state $|1\rangle$ after 10 and 100 cycles of periodic detuning, are plotted as a function of ω in Fig. 4.7, for the initial state $|\psi(t=0)\rangle = |1\rangle \sim |gg\rangle$, and ($\Delta_0/\Omega = -15$, $V_0/\Omega = 40$, $\delta/\Omega = 25$). The non-trivial oscillations observed in the final occupation probabilities are caused due to interferences between the different LZTs [see Fig. 4.7]. For smaller cycles, the final populations obtained under AIA are in very good agreement with that retrieved from numerics [see Fig. 4.7(a)]. The major dip in Fig. 4.7(a) is related to the resonance $\omega = |\Delta_0|$ and is well captured by the AIA. At longer periods, the results obtained from AIA start to deviate from numerics. This is evident in Fig. 4.7(b) where the final local minima obtained from numerics (blue-solid lines) is instead

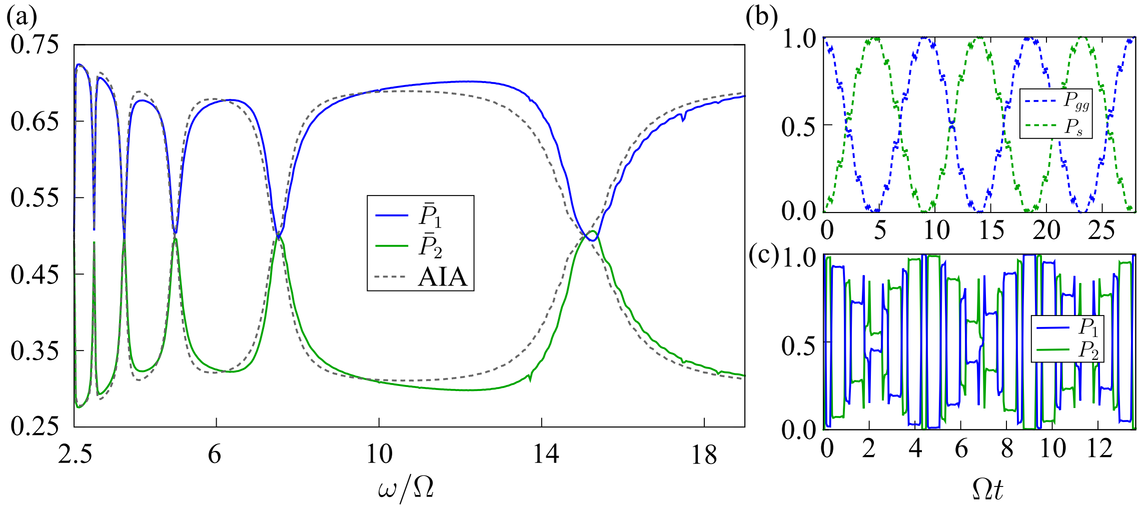

Figure 4.8: (a) The exact results (solid lines) for $\bar{P}_{1,2}$, and the same from the AIA (dashed lines) over a period of 100 cycles, as a function of ω for the initial state $|1\rangle \sim |gg\rangle$, $\Delta_0 = -15\Omega$, $V_0 = 40\Omega$ and $\delta = 25\Omega$. The dips (peaks) in $\bar{P}_1$ ($\bar{P}_2$) indicate the resonances at $n\omega = |\Delta_0|$. The six resonances are seen at $\omega/\Omega = 15, 7.5, 5, 3.75, 3, 2.5$ corresponds to $n = 1, 2, 3, 4, 5, 6$, respectively. (b) shows the coherent oscillation between $|gg\rangle$ and $|s\rangle$ at the resonance $\omega/\Omega = 7.5$ and (c) shows the same between $|1\rangle$ and $|2\rangle$ states.

realized as a maximum from AIA (gray-dashed). This happens because, at longer times, a significant population gets transferred to state $|3\rangle$ or $|rr\rangle$ but as the matrix $\hat{G}1_{LZ}$ does not include the transitions to $|3\rangle$, AIA cannot capture this effect thus breaking down in the long-time limit. Fig. 4.8(a) shows the time-averaged populations, $\bar{P}_j = (1/T)\int_0^T P_j(t)dt$ as a function of ω over a period of 100 cycles with the initial state $|1\rangle$ while the other variables are kept same as in Fig. 4.7. The resonances at $n\omega = |\Delta_0|$ are seen as troughs in $\bar{P}_1$ and peaks in $\bar{P}_2$. When the resonance condition is met, coherent Rabi oscillations between diabatic states $|gg\rangle$ and $|s\rangle$ take place [see Fig. 4.8(b)] or equivalently between the adiabatic states $|1\rangle$ and $|2\rangle$ [Fig. 4.8(c)]. This coherent dynamics is wholly identical to that of two Rydberg atoms under Rydberg-blockade without any periodic modulation. On following the procedure identical to that given in the Sec. 4.2, we obtain the transition probability to the state $|2\rangle$ after k-cycles as

$$P_2^k = 4(1 - P'_{LZ})P'_{LZ}\sin^2\phi_s \frac{\sin^2 k\alpha}{\sin\alpha} \tag{4.23}$$

where the modified LZ transition probability is $P'_{LZ} = \exp(-2\pi\Omega'^2/4v_1)$ with $\Omega' = \Delta E_0$ as the energy gap at instants $\tau_m^{(1)}$ where $\Delta(\tau_m^{(1)}) = 0$. The angle α is modified as $\cos\alpha = \mathrm{Re}\left((1 - P'_{LZ})e^{-i\eta_0} + P'_{LZ}e^{-i\eta_1}\right)$ and the new Stückelberg's phase is $\phi_s = \int_{\tau_0^{(1)}}^{\tau_1^{(1)}}(E_2 - E_1)dt/2 + \tilde{\phi}'_s$. The dynamical phases η_0 and η_1 are acquired during the adiabatic evolution, and Stoke's phase $\tilde{\phi}'_s$ is given by Eq. (3.19) after replacing v by v_1. Note that Eq. (4.23) is identical to Eq. (4.9) obtained in the single atom case,

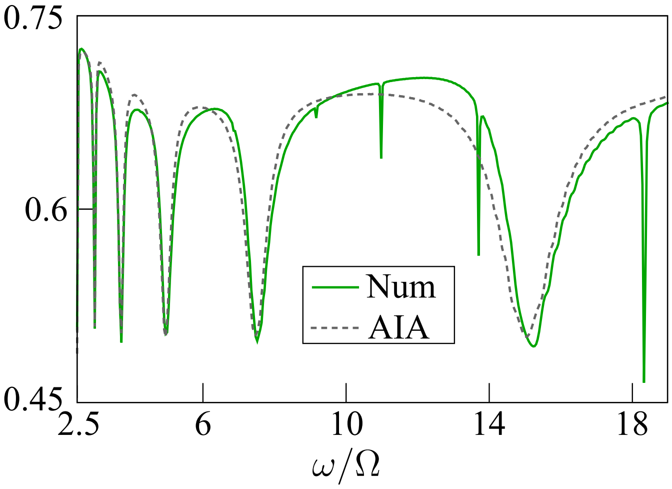

Figure 4.9: (a) The exact results (solid lines) and that from AIA (dashed lines) of $\bar{P}_2$ over 100 cycles, as a function of ω for the initial state $|2\rangle \sim |s\rangle$. The dips indicate the resonances, and the five (broader) of them at $\omega/\Omega = 15, 7.5, 5, 3.75, 3$ correspond to $n\omega = |\Delta_0|$ with $n = 1, 2, 3, 4, 5$, respectively. The narrow ones at $\omega/\Omega = 18.33, 13.75, 11$ correspond to $n\omega = |\Delta_0 - V_0|$ with $n = 3, 4, 5$, respectively, which are not captured by AIA.

and therefore, all the arguments made in the Sec. 4.2 are valid here.

For the initial state, $|\psi(t = 0)\rangle = |2\rangle \sim |s\rangle$ and time-evolution till 10 cycles, the time-averaged populations $\bar{P}_{1,2}$ are similar to that for the initial state $|1\rangle$ except that the role of states $|1\rangle$ and $|2\rangle$ are interchanged. The most prominent resonances appear at $n\omega = |\Delta_0|$ (results are similar to Fig. 4.8 with reversed color scheme for $|1\rangle$ and $|2\rangle$). However for 100 cycles, the resonances at $n\omega = \Delta_0 - V_0$, which are much narrower than those at $n\omega = |\Delta_0|$ also emerge in the exact dynamics [see green-solid lines in Fig. 4.9]. These narrow resonances at $n\omega = \Delta_0 - V_0$ are not captured by AIA. For the initial state $|\psi(t = 0)\rangle = |3\rangle \sim |rr\rangle$, AIA completely fails, as the state $|3\rangle$ is not involved in the LZT. In conclusion, in a multi-state periodically driven system, AIA may fail to capture the resonances emerging from nearby avoided crossings which are not incorporated in the impulse transition matrices, especially at larger times. The important message from this discussion is that AIA may not necessarily capture the exact dynamics unless all avoided crossings are incorporated in the impulse transitions.

4.3.2 Case 2: $\delta = 3V_0/4 - \Delta_0$

Now, we periodically drive across the first two avoided crossings such that the maximum of $\Delta(t)$ comes midway between the second and third avoided crossings *i.e.* $\max(\Delta(t)) = \Delta_0 + \delta = 3V_0/4$ [also see Fig. 3.12(b)]. In contrast to the previous case, all three adiabatic states are involved in the LZTs but the diabatic state $|rr\rangle$ is excluded. There are two LZT durations: τ_{LZ1} and τ_{LZ2} for the impulse transitions

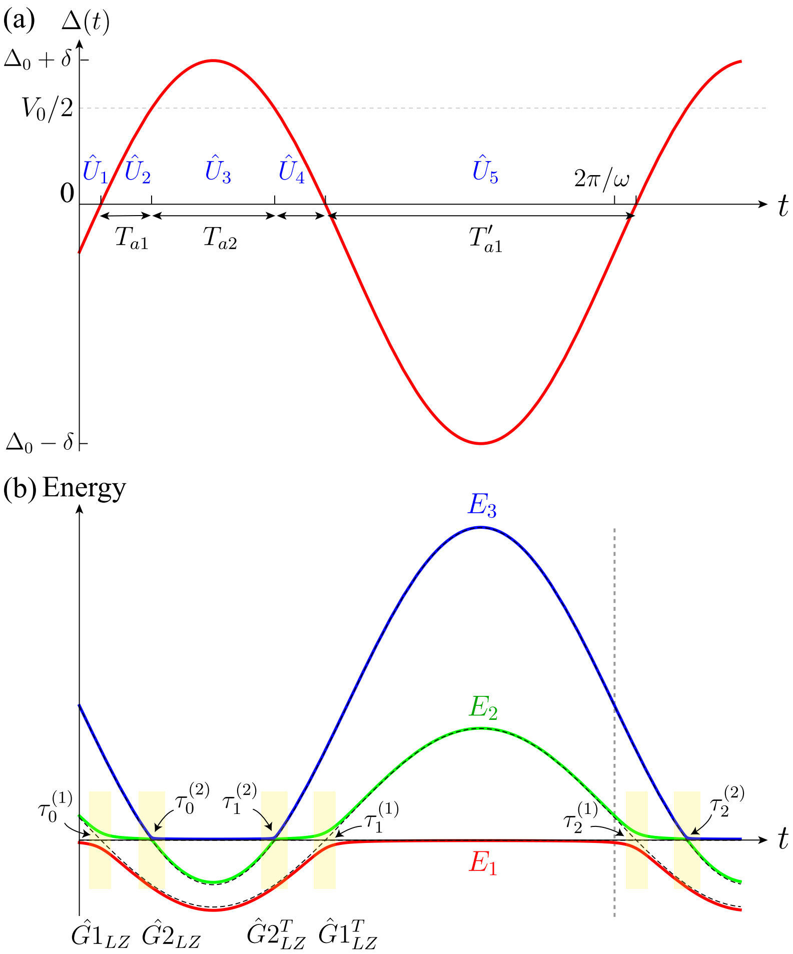

Figure 4.10: (a) The periodic time dependence of the detuning for $\delta = 3V_0/4 - \Delta_0$. The adiabatic durations are marked by T_{a1}, T_{a2}, and T'_{a1}. (b) shows the instantaneous energy eigenvalues. The instants ($\tau_0^{(1)}$, $\tau_0^{(2)}$, $\tau_1^{(2)}$, $\tau_1^{(1)}$, $\tau_2^{(1)}$, $\tau_2^{(2)}$) at which the LZTs occur are shown by shaded stripes. The $\hat{U}$ and $\hat{G}$ operators indicate the adiabatic regimes and the impulse points, respectively. Between the origin and the dashed vertical line, we have one complete cycle.

at $\Delta(t) = 0$ and $\Delta(t) = V_0/2$, respectively. The LZTs at $\tau_{2n}^{(1)}$ and $\tau_{2n}^{(2)}$ are characterized by the transition matrices $\hat{G}1_{LZ}$ and $\hat{G}2_{LZ}$ with v being replaced by v_1 and v_2, respectively. There are four different adiabatic intervals [see Fig. 4.10(a)], and as far as the validity of AIA is concerned, only the shortest among them matters. Once we fix $\delta = 3V_0/4 - \Delta_0$, the shortest adiabatic duration is given by

$$T_a = \tau_0^{(2)} - \tau_0^{(1)} = \left[\sin^{-1}(-[\Delta_0 - V_0/2]/\delta) - \sin^{-1}(-\Delta_0/\delta)\right]/\omega, \tag{4.24}$$

and the validity of AIA requires $T_a \gg \tau_{LZ1}, \tau_{LZ2}$. Again, the latter implies that for large values of ω, the AIA might break down. With two avoided crossings, the evolution matrix for one complete cycle becomes [also see Fig. 4.10(b)]

$$\hat{F} = \hat{U}_5 \hat{G}1_{LZ}^T \hat{U}_4 \hat{G}2_{LZ}^T \hat{U}_3 \hat{G}2_{LZ} \hat{U}_2 \hat{G}1_{LZ} \hat{U}_1 \tag{4.25}$$

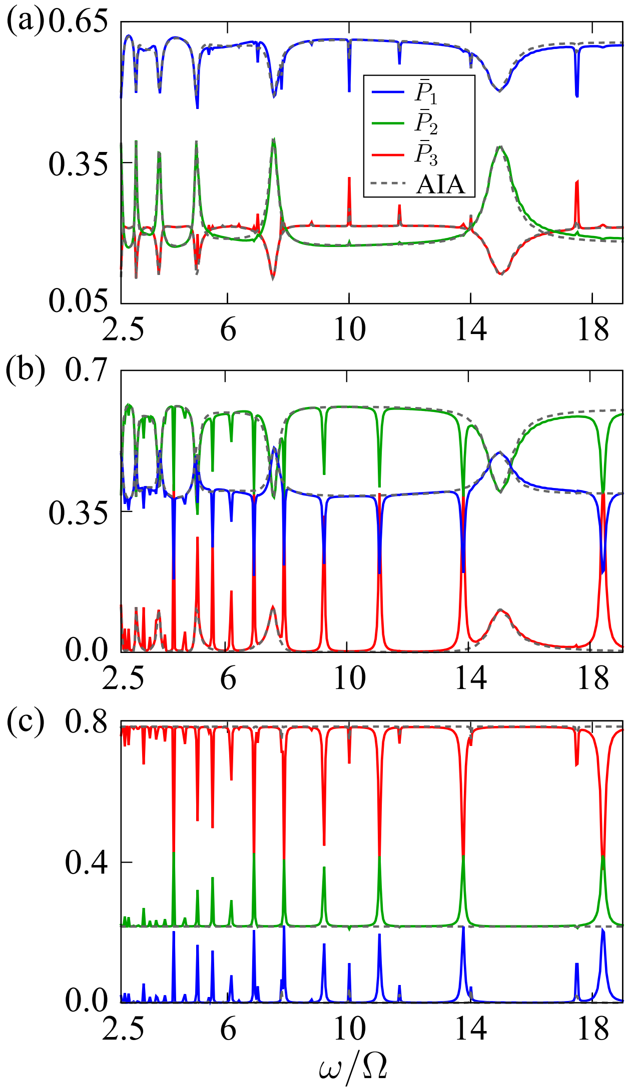

Figure 4.11: The exact results (solid lines) for the time-averaged populations ($\bar{P}_{1,2,3}$) and the same from the AIA (dashed lines) for a period of 100 cycles, as a function of ω for $\Delta_0 = -15\Omega$, $V_0 = 40\Omega$ and $\delta = 45\Omega$ with the initial state (a) $|1\rangle \sim |gg\rangle$, (b) $|2\rangle \sim |s\rangle$ and (c) $|3\rangle \sim |rr\rangle$. In (c) AIA completely failed to capture any resonances.

and for k-cycles it is $\hat{F}^k$. Fig. 4.11 shows the time-averaged populations in the adiabatic states as a function of ω over a period of 100 cycles for ($\Delta_0 = -15\Omega$, $V_0 = 40\Omega$, $\delta = 45\Omega$), with initial states $|\psi(t=0)\rangle = |1\rangle$, $|\psi(t=0)\rangle = |2\rangle$ and $|\psi(t=0)\rangle = |3\rangle$ in separate panels. The solid lines show the exact populations from numerics and the dashed lines are those obtained under AIA. The troughs or peaks in the time-averaged populations are indicative of the coherent Rabi oscillation between the corresponding states *i.e.*, of resonance. For the initial state $|\psi(t=0)\rangle = |1\rangle \sim |gg\rangle$ [see Fig. 4.11(a)], we observe troughs in $\bar{P}_1$ and $\bar{P}_3$ and corresponding peaks in $\bar{P}_2$, which indicates resonances (between $|gg\rangle$ and $|s\rangle$) at $n\omega = \Delta_0$. Furthermore, there are also another narrower set of troughs in $\bar{P}_1$ and corresponding narrow peaks in $\bar{P}_3$ indicative of resonance (between $|gg\rangle$ and $|rr\rangle$) at $n\omega = 2\Delta_0 - V_0$. Note

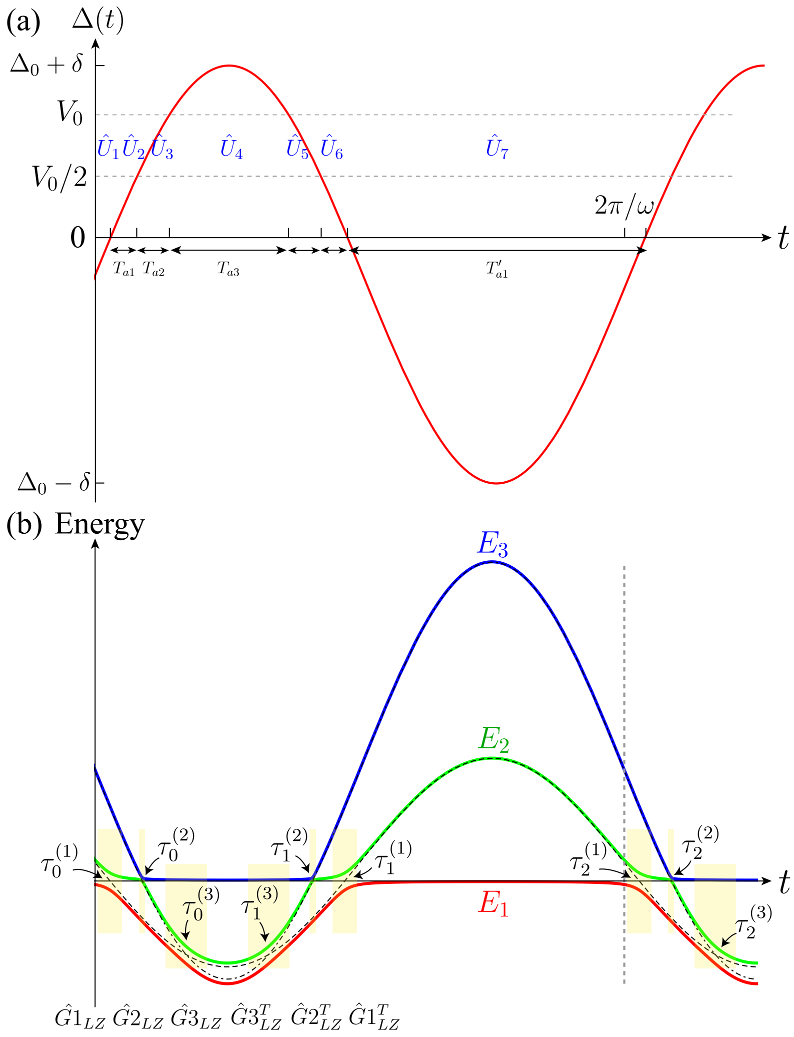

Figure 4.12: (a) The periodic time dependence of the detuning for $\delta = 5V_0/4-\Delta_0$ and (b) shows the instantaneous energy eigenvalues. The adiabatic durations are marked by T_{a1}, T_{a2}, T_{a3}, and T'_{a1}. The instants ($\tau_0^{(1)}$, $\tau_0^{(2)}$, $\tau_0^{(3)}$, $\tau_1^{(3)}$, $\tau_1^{(2)}$, $\tau_1^{(1)}$, $\tau_2^{(1)}$, $\tau_2^{(2)}$, $\tau_2^{(3)}$) at which the LZTs occur between different adiabatic states are shown by shaded stripes. The $\hat{U}$ and $\hat{G}$ operators represent the adiabatic regions and impulse points, respectively. Between the origin and the dashed vertical line, we have one complete cycle.

that, the last resonance in the plot ($\omega/\Omega = 17.5$) which correspond to the coherent transition between $|gg\rangle$ and $|rr\rangle$ (anti-blockades) is not captured by AIA since $|rr\rangle$ is not included in the LZT matrices involved in the AIA. Fig. 4.11(b) shows the time-averaged populations for the initial state $|\psi(t=0)\rangle = |2\rangle \sim |s\rangle$. The broader maxima and minima correspond to the resonance $n\omega = \Delta_0$ signifying transition between $|s\rangle$ and $|gg\rangle$, and the sharper transitions at $n\omega = \Delta_0 - V_0$ emerge due to $|s\rangle$ and $|rr\rangle$ transition. While the former resonance is captured by AIA, the latter is not as the $|rr\rangle$ state is not included in the AIA. On the other hand, with the initial state $|rr\rangle$, in the numerics, we observe the resonances associated with $|rr\rangle \leftrightarrow |s\rangle$ at $n\omega = \Delta_0 - V_0$, and $|rr\rangle \leftrightarrow |gg\rangle$ transitions at $n\omega = 2\Delta_0 - V_0$. Clearly, AIA does not capture features corresponding to the resonances which involve the state $|rr\rangle$

for the initial state $|rr\rangle$ as seen in Fig. 4.11(c).

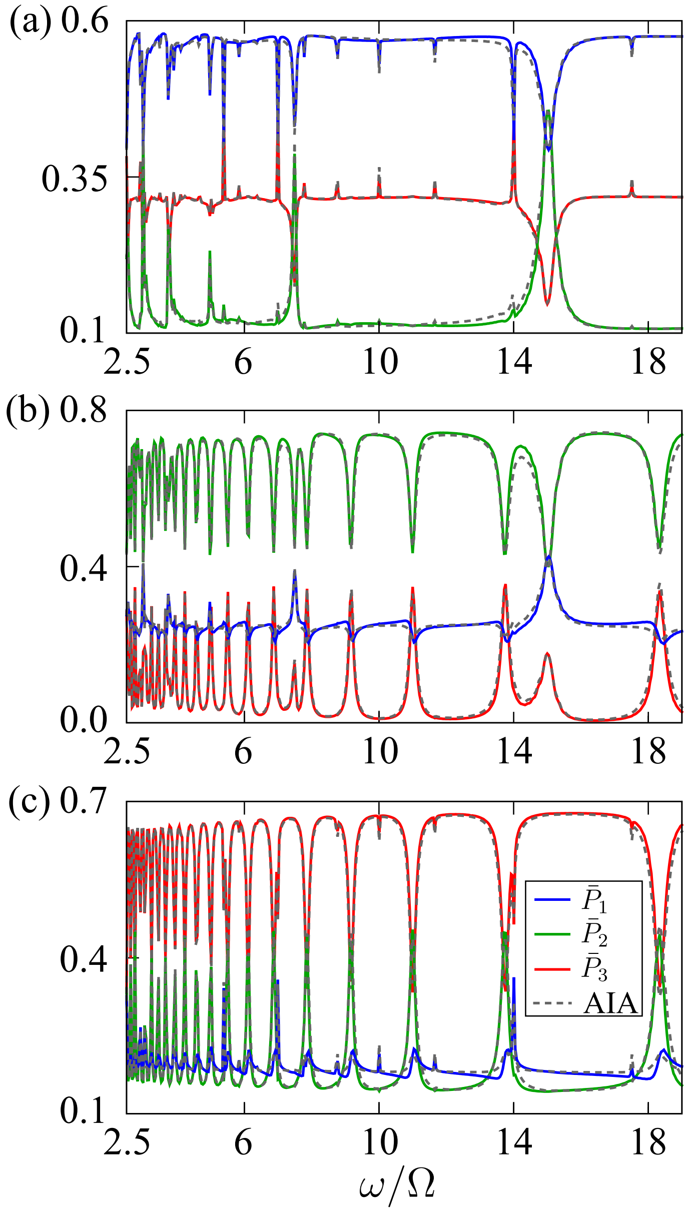

Figure 4.13: The numerical results (solid lines) for the time-averaged populations ($\bar{P}_{1,2,3}$) in the adiabatic states, and the same from the AIA (dashed lines) over a period of 100 cycles, as a function of ω for the initial state (a) $|1\rangle$, (b) $|2\rangle$ and (c) $|3\rangle$. Other parameters are $\Delta_0 = -15\Omega$, $V_0 = 40\Omega$ and $\delta = 65\Omega$. In (a) the major peaks correspond to the resonances $n\omega = |\Delta_0|$ (between $|gg\rangle$ and $|s\rangle$ states) and smaller ones indicate the resonances at $n\omega = |\Delta_0 - V_0|$ (between $|rr\rangle$ and $|s\rangle$ states). In (b) the peaks/dips indicate the resonances at $n\omega = |\Delta_0|$ and $n\omega = |\Delta_0 - V_0|$, with no traces on the resonances at $n\omega = |2\Delta_0 - V_0|$. In (c) except the resonances at $n\omega = |\Delta_0|$, other two types are seen. AIA results are in excellent agreement with the numerics in all three cases.

4.3.3 Case 3: $\delta = 5V_0/4 - \Delta_0$

For the last case, the modulation amplitude is chosen such that the system is periodically driven across all three avoided crossings. Therefore, all three adiabatic and diabatic states are involved in LZTs. There are three LZT durations involved in the dynamics: τ_{LZ1}, τ_{LZ2}, and τ_{LZ3} for the transitions at $\Delta(t) = 0$, $\Delta(t) = V_0/2$ and $\Delta(t) = V_0$, respectively, which are related as $\tau_{LZ2} \ll \tau_{LZ1}, \tau_{LZ3}$. As far as the validity of AIA is concerned, the shortest duration of adiabatic evolution [T_{a1} in Fig. 4.12(a)] should be larger than both τ_{LZ1} and τ_{LZ3}. The evolution matrix for one complete cycle in AIA [see Fig. 4.12(b)] is

$$\hat{F} = \hat{U}_7 \hat{G}1^T_{LZ} \hat{U}_6 \hat{G}2^T_{LZ} \hat{U}_5 \hat{G}3^T_{LZ} \hat{U}_4 \hat{G}3_{LZ} \hat{U}_3 \hat{G}2_{LZ} \hat{U}_2 \hat{G}1_{LZ} \hat{U}_1 \tag{4.26}$$

and for k-cycles, it is $\hat{F}^k$. The operators, $\hat{U}_j$ are the adiabatic evolution matrices, and the LZT matrices $\hat{G}1_{LZ}$ and $\hat{G}2_{LZ}$ are provided by Eqs. (3.18) and (3.20), with v being replaced by v_1 and v_2, respectively. The third LZT matrix is,

$$\hat{G}3_{LZ} = \begin{pmatrix} 1 & 0 & 0 \\ 0 & \sqrt{1 - P'''_{LZ}}e^{-i\tilde{\phi}_{s3}} & -\sqrt{P'''_{LZ}} \\ 0 & \sqrt{P'''_{LZ}} & \sqrt{1 - P'''_{LZ}}e^{i\tilde{\phi}_{s3}} \end{pmatrix}$$

where $P'''_{LZ} = \exp(-2\pi\Omega'''^2/4v_3)$ with $\Omega''' = \Delta E_{V_0}$, $\tilde{\phi}_{s3} = \frac{\pi}{4} + \arg(\Gamma(1 - i\gamma''')) + \gamma'''(\ln\gamma''' - 1)$ with $\gamma''' = \Omega'''^2/4v_3$ and $v_3 = \omega\sqrt{\delta^2 - (\Delta_0 - V_0)^2}$. In Fig. 4.13, we show the time-averaged populations in the adiabatic states as a function of ω over a period of 100 cycles with ($\Delta_0 = -15\Omega$, $V_0 = 40\Omega$, $\delta = 65\Omega$), and for all three initial states in different vertical panels. In Fig. 4.12(a), for the initial state $|\psi(t = 0)\rangle = |1\rangle \sim |gg\rangle$, we observe prominent broader peaks/troughs in $\bar{P}_j$ at resonances $n\omega = \Delta_0$, and smaller sharper peaks/troughs for the resonance at $n\omega = 2\Delta_0 - V_0$. For the initial state $|\psi(t = 0)\rangle = |2\rangle \sim |s\rangle$ [see Fig. 4.13(b)] we observe peaks/troughs in $\bar{P}_j$ corresponding to both resonances in which the state $|s\rangle$ is involved in: from $|s\rangle$ to $|gg\rangle$ at $n\omega = \Delta_0$ and from $|s\rangle$ to $|rr\rangle$ at $n\omega = \Delta_0 - V_0$. Finally, for the initial state $|\psi(t = 0)\rangle = |3\rangle \sim |rr\rangle$, both the resonances in which the state $|rr\rangle$ participates ($n\omega = \Delta_0 - V_0$ and $n\omega = 2\Delta_0 - V_0$) are observed. Contrary to the previous two cases, the AIA is able to capture all possible resonant transitions. From the above examples, we conclude that for AIA to be successful in a periodically driven multi-level system especially, at longer times, it is necessary to incorporate the transition matrices across all avoided crossings. Once successful, AIA reveals to us the web of phases involved in the dynamics which can find applications in developing quantum technologies.

4.4 Summary and outlook

In summary, we analyzed the LZ dynamics in a setup of two Rydberg-atoms with a periodic detuning. The periodically driven Rydberg setup, for instance, can be realized by frequency modulation [160]. We identified a striking similarity with the excitation probability in a single periodically driven two-level atom to the intensity distribution from a narrow antenna array. For two atoms, we discussed in detail the validity of AIA in describing the dynamics for the periodic variation of detuning. Interestingly, AIA reveals detailed information about the phases developed during the dynamics, which can be very useful for applications such as coherent control of quantum states, implementing quantum (phase) gates [138, 250], and atom-interferometry [251]. While implementing AIA, we rely on large RRIs for which the LZTs across each avoided crossings include only two adiabatic states. For small interactions, it is required to develop a multi-level AIA in which the LZTs take place among multiple levels at the same time. Our study can be extended to three two-level atoms, for which it will not be so straightforward to assume AIA would work at large interactions due to the complexity in the level structure.

Chapter 5

Population trapping in a pair of Rydberg atoms

The current chapter is adapted from the research article "Population trapping in a pair of periodically driven Rydberg atoms" [88]. We analyze the population trapping and dynamical stabilization in a pair of interacting Rydberg atoms whose atom-field detuning is periodically modulated. The periodic modulation can enhance or suppress the state population dynamics. In our setup, the dynamical stabilization exists as a special case of population trapping. We show that the presence of Rydberg-Rydberg interactions leads to state-dependent population trapping in a set of experimentally relevant states such as product and maximally entangled states.

5.1 Introduction

The behaviour of periodically driven or Floquet systems is very rich, in particular, they display counter-intuitive effects such as dynamical stabilization. A paradigmatic example is that of Kapitza's inverted pendulum which exhibits dynamical stabilization at the inverted point caused by a periodic movement of the suspension point of the pendulum [see chapter 1]. Other prominent examples of dynamical stabilization in quantum systems are coherent destruction of tunnelling [161–163], or localization of a wavepacket due to periodic shaking of the lattice [166–169] or modulation of the inter-particle interactions [170], and quantum kicked rotors [157, 158].

Among many-body physics, driven Floquet systems hold a special interest in the field of non-equilibrium quantum physics. Here, some entirely new phases can emerge such as the π-spin glass or Floquet time crystal which do not exist in equilibrium dynamics [269]. In interacting Bose gases, a Kapitza or a dynamically stabilized state manifests in stabilizing a BEC on harmonically varying the scattering length [270] or a 2D soliton against collapse [271, 272]. Likewise, in spinor BEC condensates, spin mixing dynamics can be frozen by modulation of spin-exchange interaction [273] or by applying periodic microwave pulses [274, 275]. A temporal modulation leads to stabilization of a classically unstable phase (π-mode) in a bosonic Josephson junction [276], or stable trapping of a ferromagnetic spin system near an unstable paramagnetic configuration [277], that has no equilibrium counterparts. Additionally, dynamical stabilization has been useful in controlling the bosonic superfluid to Mott insulator quantum phase transition in an optical lattice [168]. Periodic driving in an array of ultracold Rydberg atoms is proposed to exhibit dynamical localization [137] and may be useful in the implementation of robust quantum gates [230, 278, 279].

We study population trapping in a periodically driven two-level atom as well as in a pair of periodically driven interacting two-level ultracold atoms, in which the ground state is coupled to a Rydberg state. We identify a simple scheme for locating the regimes of population trapping for any initial state, relying on driving induced resonances and the Floquet spectrum. We also introduce the quantity inverse participation ratio (IPR), calculated from the overlap of the initial state with the Floquet eigenstates, as a measure of population trapping. Our work shows that finite interactions cause (initial) state-dependent population trapping in the periodically driven two-atom system.

5.2 Setup, Model, and Techniques

We consider an array of two Rydberg atoms each of which have a two-level scheme consisting of an electronic ground state $|g\rangle$ and a Rydberg state $|r\rangle$. The states are coupled via a classical light field and the corresponding atom-light detuning is periodically changed with time t. The closed system is understood to exist in the frozen gas limit. We obtain the time-dependent Hamiltonian ($\hbar = 1$) as,

$$\hat{H} = -\Delta(t)\sum_{i=1}^{2}\hat{\sigma}^{i}_{rr} + \frac{\Omega}{2}\sum_{i=1}^{2}\hat{\sigma}^{i}_{x} + V_0\hat{\sigma}^{1}_{rr}\hat{\sigma}^{2}_{rr}, \tag{5.1}$$

where $\hat{\sigma}_{ab} = |a\rangle\langle b|$ with $a, b \in \{r, g\}$ is the atomic operator which describes both projection $\hat{\sigma}_{rr}$, and transition operators $\hat{\sigma}_x = \hat{\sigma}_{rg} + \hat{\sigma}_{gr}$. Also, Ω is the Rabi frequency and $\Delta(t) = \Delta_0 + \delta \sin \omega t$ is the time-dependent detuning with modulation frequency ω and modulation amplitude δ. The Rydberg excited atoms interact via strong van der Waals interaction, $V_0 = C_6/R^6$, where C_6 is the interaction coefficient, and R is the separation between two Rydberg excitations [76]. The exact dynamics of the system is obtained by numerically solving the Schrödinger equation: $i\partial\psi(t)/\partial t = \hat{H}(t)\psi(t)$.

Going forward, we are more interested in the high-frequency regime ($\omega \gg \Omega$) in the system. This is motivated by the example of the Kapitza pendulum wherein to stabilize the pendulum bob the driving should be fast compared to the natural oscillation period. Furthermore, localization of a particle/wavepacket in a periodic potential also requires the drive to be faster than the interaction scale. Essentially, under a high-frequency drive, the system doesn't absorb much energy from the drive which culminates in the dressing of the low-energy Hamiltonian from virtual mechanisms [206]. Motivated by the above examples, we aim to find an effective Hamiltonian in the high-frequency regime.

5.2.1 Effective Hamiltonian

First, we move to the rotating frame of high frequency parameters $|\psi'\rangle = \hat{U}(t)|\psi\rangle$, with unitary transformation $\hat{U}(t) = \exp\Big[if(t)\sum_j \hat{\sigma}^j_{rr} + itV_0\hat{\sigma}^1_{rr}\hat{\sigma}^2_{rr}\Big]$ where $f(t) = (\delta/\omega)\cos\omega t - \Delta_0 t$. Here $|\psi'\rangle$ and $|\psi\rangle$ is the wave function in the rotating and laboratory frame respectively. The new Hamiltonian in the rotating frame is $\hat{H}'(t) = \hat{U}\hat{H}\hat{U}^\dagger - i\hbar\hat{U}\dot{\hat{U}}^\dagger$ which after using the Jacobi-Anger expansion $\exp(\pm iz\cos\omega t) = \sum_{m=-\infty}^{\infty} J_m(z)\exp(\pm im[\omega t + \pi/2])$, can be written as [137]

$$\hat{H}' = \frac{\Omega}{2}\sum_{j=1}^{2}\sum_{m=-\infty}^{\infty} i^m J_m(\alpha) g_m(t) e^{iV_0\sum_{k\neq j}\hat{\sigma}^k_{rr}t}\hat{\sigma}^j_{rg} + \text{H.c.}, \tag{5.2}$$

where $J_m(\alpha)$ is the mth order Bessel function of the first kind with $\alpha = \delta/\omega$ and $g_m(t) = \exp[i(m\omega - \Delta_0)t]$. The transformation allows for removal of detuning $\Delta(t)$ and interaction energy V_0 terms in Eq. (5.1) in favour of oscillations in Eq. (5.2). On a comparison of Eq. (5.2) with Eq. (5.1), we conclude that the periodic detuning has effectively modified the Rabi coupling in this frame which influences the excitation dynamics distinctly. Upon further expansion of the operator, $e^{\pm iV_0\sum_{k\neq j}\hat{\sigma}^k_{rr}t} = \prod_{k\neq j}\Big[\hat{\sigma}^k_{rr}(e^{\pm itV_0} - 1) + \mathcal{I}\Big]$, with $\mathcal{I}$ being the identity operator, we may rewrite the Hamiltonian in Eq. (5.2) as

$$\hat{H}' = \frac{\Omega}{2}\sum_{m=-\infty}^{\infty} i^m J_m(\alpha)\left[e^{i(m\omega-\Delta_0)t}\left(\sum_{j=1}^{2}\hat{\sigma}^j_{rg} - \hat{X}\right) + \hat{X}\; e^{i(m\omega-\Delta_0+V_0)t}\right] + \text{H.c.}, \tag{5.3}$$

where the operator $\hat{X} = \hat{\sigma}^1_{rg}\hat{\sigma}^2_{rr} + \hat{\sigma}^1_{rr}\hat{\sigma}^2_{rg}$ produces the correlated Rabi coupling [86, 137]. It underpins the processes in which the first atom gets excited only if the second atom is already present in the excited state, and vice-versa. This correlated Rabi excitation process resembles the density assisted inter-band tunneling [209] or density dependent hopping of atoms [280] observed in optical lattices.

At high modulation frequencies ($\omega/\Omega \gg 1$), the resonant terms in Eq. (5.2) will have a higher contribution towards the summation as compared to oscillatory terms whose overall effect tends to average out in the long time dynamics. In other words, a high frequency modulation may lead to emergence of an effective Floquet Hamiltonian [170, 208]. We regard the zeroth-order term, at high-frequency limit ($\omega \gg \Omega$), as the effective Hamiltonian which is simply the time-averaged Hamiltonian

$$H_{\text{eff}} = 1/T \int_0^T dt\ \hat{H}'(t),$$

where $T = 2\pi/\omega$. The higher order terms scale as $H^{(n)} \sim \omega^{(-n)}$ and become increasingly smaller for large ω. We derive the effective Hamiltonian on a case-by-case basis in the respective sections. Note that all the figures shown in this chapter are obtained from numerics using the complete Hamiltonian given in Eq. (5.1). We use the effective Hamiltonian to build physical insights for the exact results wherever possible, especially to identify driving-induced resonances and regions of population trapping.

5.2.2 Floquet Theory

Now, we briefly review Floquet Theory. Floquet's theorem gives a very powerful tool to analyze periodically driven systems which is why they are also equivalently called Floquet systems. According to Floquet's theorem, the evolution operator of a periodically driven quantum system $\hat{H}(t) = \hat{H}(t+T)$ can be written in the form

$$\hat{U}(t,0) = \hat{P}(t)e^{-\mathrm{i}\hat{H}_F t} \tag{5.4}$$

where the Hermitian operator $\hat{H}_F$ is referred to as Floquet Hamiltonian and $\hat{P}(t) = \hat{P}(t+T)$ is a unitary operator which has same the periodicity as that of the Hamiltonian [281]. Without any loss of generality, we assume that the period is defined by $T = 2\pi/\omega$. At integer multiples of time period, $t_n = nT$, the operator $\hat{P}(t) = \mathbb{1}$ and the evolution operator over one period simplifies to $\hat{U}(T,0) = e^{-\mathrm{i}\hat{H}_F T}$. We can write the set of unit eigenvalues of $\hat{U}(T,0)$ as $e^{\mathrm{i}\epsilon_k T}$, and eigenstates as $|\phi_k(0)\rangle$, which gives us the spectral decomposition of unit period evolution operator

$$\hat{U}(T,0) = e^{-\mathrm{i}\hat{H}_F T} = \sum_k e^{-\mathrm{i}\epsilon_k T}|\phi_k(0)\rangle\langle\phi_k(0)| \tag{5.5}$$

where ϵ_k are called quasienergies and can be shifted by integer multiples of ω. The Floquet modes $\{|\phi_k(0)\rangle\}$ form a complete and orthogonal set of square-integrable states. Evidently, the Floquet modes are also eigenstates of Hamiltonian $\hat{H}_F$ with quasienergies ϵ_k as eigenvalues, *i.e.* $\hat{H}_F = \sum\limits_k \epsilon_k|\phi_k(0)\rangle\langle\phi_k(0)|$. Using Floquet mode eigenbasis, we can write the state of system at $t = 0$ as $|\psi(0)\rangle = \sum\limits_k c_k|\phi(0)\rangle$ where the time-independent co-efficient $c_k = \langle\phi(0)|\psi(0)\rangle$ gives the probability amplitude of finding the system in the Floquet mode $|\phi_k(0)\rangle$ at $t = 0$. Furthermore, using both the expansion of the initial state and Eq. (5.4), a general state of the system can be written as,

$$\begin{aligned} |\psi(t)\rangle &= \sum_k c_k \exp(-\mathrm{i}\epsilon_k t)\hat{P}(t)|\phi_k(0)\rangle \qquad (5.6)\\ &= \sum_k c_k \exp(-\mathrm{i}\epsilon_k t)|\phi_k(t)\rangle, \qquad (5.7)\end{aligned}$$

where the general Floquet mode is defined as

$$|\phi_k(t)\rangle \equiv \hat{P}(t)|\phi_k(0)\rangle = \exp(\mathrm{i}\epsilon_k t)\hat{U}(t,0)|\phi_k(0)\rangle \qquad (5.8)$$

which inherits the periodicity of the Hamiltonian $\hat{H}(t)$. Strikingly, since the time dependence is absorbed in the basis, the same constant c_k gives the probability for finding the system state $|\psi_k(t)\rangle$ in the Floquet mode $|\phi_k(t)\rangle$ as does for initial state in $|\phi_k(0)\rangle$ *i.e.* c_k remains time-independent. This means that the population in respective Floquet modes remains preserved in a periodic Hamiltonian.

We shift our focus to the case of strongly driven systems, *i.e.* we concern ourselves with the high-frequency limit of the system. In this limit, the time-period of driving is very short while the time-scales in which system dynamics occurs is much larger. Consequently, the time-dependent Floquet modes are periodic but with a small time-period. Hence their temporal evolution loses significance in the long time-scales and effectively ($|\phi_k(t)\rangle \approx |\phi_k(0)\rangle$) [282]. With this approximation, the system dynamics is effectively governed by the quasienergies ϵ_k and coefficients c_k,

$$|\psi(t)\rangle \approx \sum_k c_k \exp(-\mathrm{i}\epsilon_k t)|\phi_k(0)\rangle. \qquad (5.9)$$

We now define the criteria for population trapping: $|\langle\psi(0)|\psi(t)\rangle| \approx 1$. The quasienergies ϵ_k and the modes $\{|\phi_k(0)\rangle\}$ are calculated numerically by obtaining the eigenvalues, $\lambda_k = \exp(-i\epsilon_k T)$ of the unit period operator $\hat{U}(T,0)$ [282, 283]. Below we analyze how the quasienergies ϵ_k and Floquet coefficients c_k indicate population trapping.

Quasienergies: If all the quasienergies approach degeneracy, the dynamics of the system on this time-scale will appear to be frozen irrespective of the initial state, resulting in state-independent population trapping. However, as we will see for two Rydberg atoms, this is only true if the atoms are non-interacting making it a trivial case of localization of a single two-level atom [Sec 5.3]. More interestingly, in the two-atom system, if some quasienergies (among the 4 levels) approach degeneracy, it leads to a state-dependent population trapping [see Fig 5.4]. Nevertheless, the

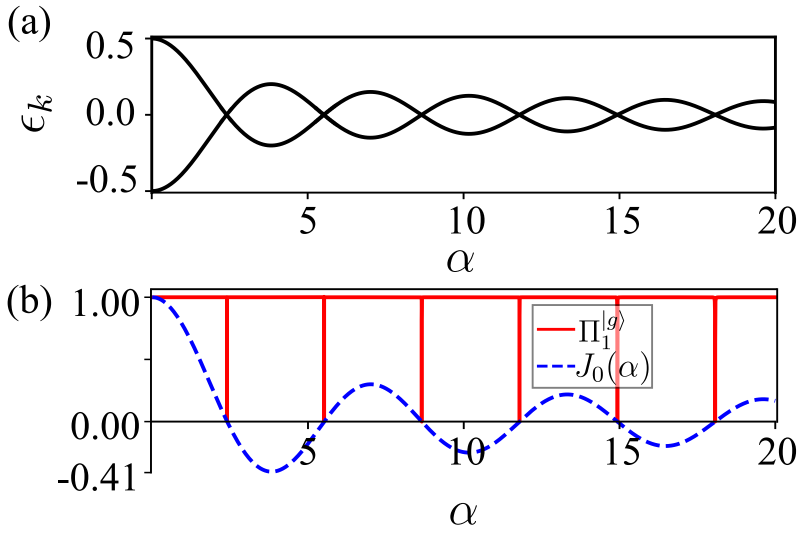

Figure 5.1: Floquet mode properties of a driven single two-level atom with $\omega = 8\Omega$ for the case of primary resonance, $\Delta_0 = 0$ ($n_1 = 0$). The crossings of ϵ_k in (a) and the zeros of $\Pi_0^{|g\rangle}$ in (b) coincides with the zeros of $J_0(\alpha)$. The plots (a) and (b) are the special case of population trapping corresponding to the dynamical stabilization. The parameter α is varied by changing δ and keeping ω constant.

crossing of quasienergies doesn't completely characterize population trapping as soon as more than two levels are present which is the case for two atoms.

Floquet coefficients: Irrespective of quasienergy value, if the initial state coincides with one of the Floquet modes, the population trapping occurs. This is true for both single and two-atoms. As a measure of overlap, we use the inverse participation ratio (IPR) to further characterize the Rydberg excitation dynamics. We define the IPR as,

$$\Pi_N^{|I\rangle} = \frac{1}{\sum_k p_k^2} - 1, \tag{5.10}$$

where $p_k = |c_k|^2 = |\langle\phi_k(0)|\psi(0)\rangle|^2$, is the projection of the initial state $|\psi(0)\rangle$ on the Floquet mode $|\phi_k(0)\rangle$ for N atoms. If the initial state coincides with one of the Floquet modes, IPR vanishes. Since, the population in Floquet mode doesn't vary significantly on the system time-scales, $\Pi_N^{|I\rangle} = 0$ indicates population trapping of the state $|I\rangle$. In the same spirit, a smaller value of $\Pi_N^{|I\rangle}$ indicates a slower transition from the state $|\psi(0)\rangle$ to other states and maximum value of IPR indicates a maximum mixing *i.e.* resonances.

5.3 A two-level atom ($N = 1$)

In this section we briefly review the population trapping in a periodically driven single two-level atom with ground state $|g\rangle$ and excited state $|r\rangle$. The driving is same as mentioned in Eq. (5.1). We also discuss the criteria under which the

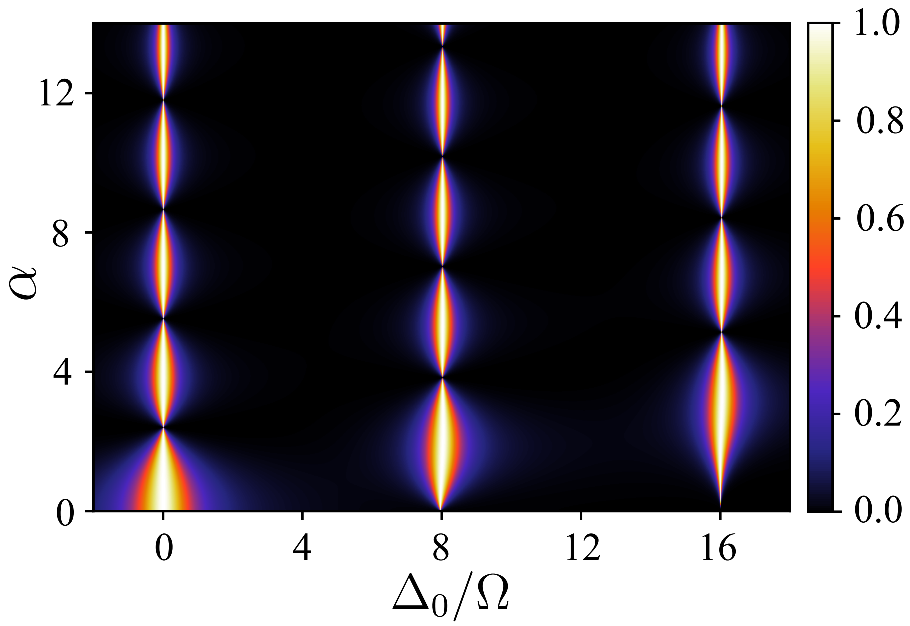

Figure 5.2: The IPR ($\Pi_1^{|g\rangle}$) as a function of α and Δ_0 for $\omega = 8\Omega$. The pearl-stripes are along the α axis at the resonances $n\omega = \Delta_0$. The local minima ($\Pi_1^{|g\rangle} = 0$) along the first stripe are the points of DS for which $J_0(\alpha)$=0. The parameter α is varied by changing δ and keeping ω constant.

population trapping can be identified as dynamical stabilization. For $N = 1$, the Hamiltonian in Eq. (5.2) takes the simplest form [146, 159, 160],

$$\hat{H}' = \frac{\Omega}{2} \sum_{m=-\infty}^{\infty} i^m J_m(\alpha) e^{i(m\omega - \Delta_0)t} \hat{\sigma}_{rg} + \text{H.c.}, \tag{5.11}$$

where $\alpha = \delta/\omega$. In the high-frequency limit ($\omega \gg \Omega$), if a term satisfies the resonance condition, $n_1\omega = \Delta_0$, where $n_1 \in \mathbb{Z}$ it becomes the only relevant term in the summation of Eq. (5.11). Based upon the discussion in Sec. 5.2.1, we can safely drop the non-resonant terms in the summation, and $\hat{H}' \approx i^{n_1} \frac{\Omega J_{n_1}(\alpha)}{2} \hat{\sigma}_{rg} + \text{H.c.}$. This is equivalent to making a second rotating-wave approximation. When the resonance condition holds true, the population in states $|g\rangle$ and $|r\rangle$ exhibit coherent Rabi oscillations. For exhaustiveness, if the resonance condition is not satisfied, multiple terms have significant contribution towards the sum. At the resonances $n_1\omega = \Delta_0$, the effective Rabi coupling between the states $|g\rangle$ and $|r\rangle$ is proportional to $J_{n_1}(\alpha)$. Therefore, if the parameters δ and ω are such that they correspond to the Bessel roots [$J_{n_1}(\alpha) = 0$], the dynamics freezes. This gives rise to a state-independent population trapping. It can be further verified by plotting the quasienergies ϵ_k as a function of α while keeping the resonance condition satisfied. The quasienergies or the energy gap between them oscillate as a function of α, and crossings occur at the zeros of the Bessel function [282]. Fig. 5.1(a) and 5.1(b) show the quasienergies for the case of $\Delta_0 = 0$ and Bessel zero function, respectively. The quasienergy crossings occur at the zeros of $J_0(\alpha)$. At the crossings, the degenerate Floquet modes become purely $|g\rangle$ and $|e\rangle$, which results in a vanishing $\Pi_1^{|g\rangle}$ or $\Pi_1^{|r\rangle}$ as seen in Fig. 5.1(b). Since the Floquet modes do not evolve in time, the population in states $|g\rangle$ or $|r\rangle$ freezes. Note that at the crossings, an arbitrary superposition of $|g\rangle$ and $|r\rangle$ is also a Floquet mode making the population trapping independent of the initial state. As we show below, the latter breaks down in the presence of RRI, leading to a state-dependent population trapping. In short, a vanishing IPR at the driving induced resonance indicates the freezing of the initial state or population trapping.

Note that only if the initial state is dynamically unstable in the absence of periodic modulation, then only the corresponding population trapping should be identified as dynamical stabilization. If n_1 is a non-zero integer, in the high-frequency limit, the resonance condition demands a large value of Δ_0, for which there is hardly any dynamics in the states $|g\rangle$ and $|e\rangle$ in the absence of periodic driving due to far off-resonance. Therefore, population trappings for $|n_1| > 0$ cannot be interpreted as dynamical stabilization. The population trapping at the primary resonance ($n_1 = 0$), i.e., when $J_0(\alpha) = 0$ for $\Delta_0 = 0$, provides us the phenomenon of dynamical stabilization. The results for the latter case with an initial state $|I\rangle = |g\rangle$ are shown in Figs. 5.1(a) (quasi-energies) and 5.1(b) (IPR). Note that the leading terms in the excited state population due to $m \neq n_1$ terms in Eq. (5.11) are proportional to $(\Omega/\omega)^2$ in the high-frequency limit, which can be ignored [146]. More extensive results of the IPR ($\Pi_1^{|g\rangle}$) for the initial state $|g\rangle$, are given in Fig. 5.2. In the $\alpha - \Delta_0$ plane, $\Pi_1^{|g\rangle}$ exhibits pearl-chains along α axis at the resonances $n_1\omega = \Delta_0$. The local minima along the chains provide the values of α at which population trapping takes place [at $J_n(\alpha) = 0$], and the minima along α at $\Delta_0 = 0$ are the points of dynamical stabilization. Between the pearl-chains (along Δ_0 axis), $\Pi_1^{|g\rangle}$ vanishes due to the far-off-resonant driving of the atom, as discussed above. Note that for sufficiently small ω, the crossings in Floquet energies deviate slightly from the Bessel zeros.

In summary, at the quasienergy crossings, the population dynamics freezes, and also the IPR vanishes. We term this phenomenon at resonance as Population trapping. Population trapping at the primary resonance is identified as dynamical stabilization. Thus, we have a scheme to identify population trapping (including dynamical stabilization) of any initial state in two steps. First, identify resonances in which the initial state is involved, and second, vary the amplitude of modulation, keeping the resonance condition satisfied. The minima in IPR will indicate population trapping/dynamical stabilization.

5.4 Two-atom chain

In this section, we extend the above analysis of a single two-level atom to a pair of two-level Rydberg atoms and discuss how Rydberg-Rydberg interactions influence the phenomenon of population trapping. In particular, we are interested in the criteria under which the product states $|gg\rangle$, $|rr\rangle$, and maximally entangled Bell states $|+\rangle = (|gr\rangle + |rg\rangle)/\sqrt{2}$, and $|B\rangle = (|gg\rangle + |rr\rangle)/\sqrt{2}$ exhibit dynamically stabilization.

The system Hamiltonian is given in Eq. (5.1). Since both the atoms are identically driven, the dynamics is restricted to the triplet states $\{|gg\rangle, |+\rangle, |rr\rangle\}$ where $|+\rangle$ is the symmetric combination of $|gr\rangle$ and $|rg\rangle$. The anti-symmetric combination of the same is decoupled from the dynamics and thus gives trivial results. Upon choosing the triplet set as the basis, Hamiltonian in rotated frame [see Eq. (5.3)] can be written as,

$$\hat{H}' = \begin{pmatrix} 0 & \sqrt{2}\Omega_1(t) & 0 \\ \sqrt{2}\Omega_1(t) & 0 & \sqrt{2}\Omega_2(t) \\ 0 & \sqrt{2}\Omega_2(t) & 0 \end{pmatrix} \tag{5.12}$$

where the off-diagonal matrix elements provide the time-dependent coupling strengths for $|gg\rangle \leftrightarrow |+\rangle$ and $|+\rangle \leftrightarrow |rr\rangle$ transitions as $\Omega_1(t)$ and $\Omega_2(t)$ respectively,

$$\Omega_1(t) = \frac{\Omega}{2} \sum_{m=-\infty}^{\infty} J_m(\alpha) e^{i(m\omega-\Delta_0)t+im\pi/2} \tag{5.13}$$

$$\Omega_2(t) = \frac{\Omega}{2} \sum_{m=-\infty}^{\infty} J_m(\alpha) e^{i(m\omega-\Delta_0+V_0)t+im\pi/2}, \tag{5.14}$$

and in general $\Omega_1 \neq \Omega_2$. It is evident from the above expressions that multiple resonances exist in the system. In order to duly analyze the population trapping, we first discuss the resonances present in the periodically driven two-atom setup.

5.4.1 Resonances

At large ω, the terms in Eqs. (5.13) and (5.14) which are most relevant in the first order correspond to $n_1\omega = \Delta_0$ ($R1$) and $n_2\omega = \Delta_0 - V_0$ ($R2$). These are the respective resonance criteria for transitions $|gg\rangle \leftrightarrow |+\rangle$ and $|+\rangle \leftrightarrow |rr\rangle$. As a special case, if $V_0 = n\omega$, the criteria for $R1$ and $R2$ gets satisfied simultaneously with $n_1 = n_2 + n$. In general, however, the $R1$ and $R2$ resonances do not overlap. For a large V_0, the resonances can be well separated in the Δ_0 axis [88], and so we work within that regime for analytical predictions.

Assuming only $R1$ is fulfilled, keeping V_0 large, the effective (time-averaged) Rabi couplings become $\Omega_1 \approx \Omega J_{n_1}(\alpha)/2$ for $|gg\rangle \leftrightarrow |+\rangle$ transition, and $\Omega_2 \approx 0$ for the

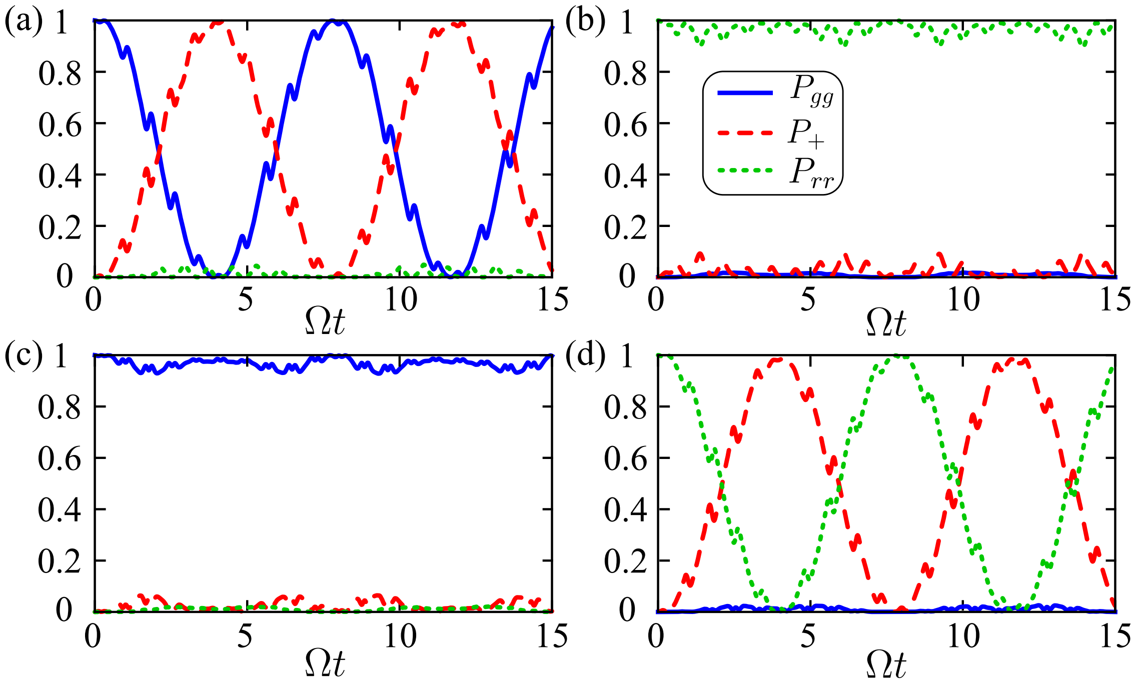

Figure 5.3: Population dynamics for the resonance type R1 ($n_1\omega = \Delta_0$) for the initial states (a) $|I\rangle = |gg\rangle$ and (b) $|I\rangle = |rr\rangle$. The same, but with the resonance type R2 ($n_2\omega = \Delta_0 - V_0$) for the initial state (c) $|I\rangle = |gg\rangle$ and (d) $|I\rangle = |rr\rangle$ with $\Delta_0 = 2\Omega$. In (a) we see the Rabi oscillations between $|gg\rangle$ and $|+\rangle$ states, whereas in (b) we observe no dynamics. Similarly, (c) shows the absence of dynamics, and the Rabi oscillations between $|+\rangle$ and $|rr\rangle$ states is shown in (d). We took $V_0 = 10\Omega$, $\delta = 15\Omega$, and $\omega = 8\Omega$ for all plots. The value of Δ_0 is taken such that $n_1 = 1$ for (a) and (b), and for (c) and (d) we have $n_2 = -1$.

transition between $|+\rangle \leftrightarrow |rr\rangle$. This reduces the three-level system to an effective two-level ($|gg\rangle \leftrightarrow |+\rangle$) and a decoupled isolated level ($|rr\rangle$). Hence, if the initial state is $|\psi(0)\rangle = |gg\rangle$, the system performs coherent Rabi oscillations between $|gg\rangle$ and $|+\rangle$ states [see Fig. 5.3(a) for $n_1 = 1$], similar to the dynamics under the Rydberg blockade. But if the initial state is chosen differently as $|\psi(0)\rangle = |rr\rangle$, the dynamics nearly halts as is shown in Fig. 5.3(b). This behaviour is expected at large V_0, as the state $|rr\rangle$ becomes far off-resonant from $|+\rangle$ making the periodic driving ineffective in changing its dynamics. If the resonance condition for $R2$ is satisfied, we obtain $\Omega_1 \approx 0$ and $\Omega_2 \approx \Omega J_{n_2}(\alpha)/\sqrt{2}$ which means that the $|rr\rangle$ and $|+\rangle$ states are Rabi-coupled while the $|gg\rangle$ state is decoupled from dynamics. Consequently, we see Rabi oscillation between $|rr\rangle$ and $|+\rangle$ for initial state $|rr\rangle$ while barely any significant change of population in case the initial state is $|gg\rangle$. Both of the results are shown in Figs. 5.3(c) and 5.3(d) for $n_2 = -1$, respectively. In addition to resonances $R1$ and $R2$, there also exists a third resonance, which is given by $n_3\omega = 2\Delta_0 - V_0$ ($R3$), which is not directly visible from Eqs. (5.13) and (5.14), but is revealed upon using adiabatic impulse approximation [87]. $R3$ corresponds to direct resonant transitions between ground state $|gg\rangle$ and doubly-excited Rydberg state $|rr\rangle$.

5.4.2 Dynamical stabilization of product states

In this section, we discuss the dynamical stabilization of the product states $|gg\rangle$ and $|rr\rangle$ in the high-frequency limit. The regions of dynamical stabilization will be located across the primary resonances in each of conditions $R1$, $R2$ and $R3$, i.e., $n_{j\in 1,2,3} = 0$. To identify these regimes, we vary the value of ratio α by varying the amplitude of modulation δ while keeping ω constant. With this scheme of parameters, we are able to scan across the Bessel roots while keeping the resonance condition satisfied.

$R1$: To identify dynamical stabilization (DS), we probe the dynamics of the two-atom system at primary resonance of $R1$ ($\Delta_0 - n_1\omega = 0$) which is satisfied for $n_1 = 0$ ($\Delta_0 = 0$). We use insights from effective Hamiltonian, Floquet quasienergies, and IPR to characterize the DS.

Noninteracting case—. For the case of two non-interacting atoms ($V_0 = 0$) the dynamical stabilization occurs at the roots of $J_0(\alpha)$: α_k^0, identical to the results obtained for a single atom [see discussion in Sec. 5.3]. Furthermore, these points are accompanied by the crossing of all quasienergy levels [dashed lines in Fig. 5.4(a)]. From Floquet expansion [also see Eq. (5.9)] we can write at the triple quasienergy crossings,

$$|\psi(t)\rangle \approx e^{-\mathrm{i}\epsilon t}\left(c_1|\phi_1(0)\rangle + c_2|\phi_2(0)\rangle + c_3|\phi_3(0)\rangle\right). \tag{5.15}$$

with $|\psi(0)\rangle = \sum_{k=1}^{3} c_k|\phi_k(0)\rangle$. Hence, at these points, dynamical stabilization occurs by virtue of triple quasienergy crossing, and is independent of the initial state. In particular, both $|gg\rangle$ and $|ee\rangle$ state exhibit DS at the same value of α. This is the case of state-independent dynamical stabilization, as shown in Fig. 5.4(a). Note that the fourth quasienergy level (not shown) corresponds to the anti-symmetric state $|-\rangle = (|rg\rangle - |gr\rangle)/\sqrt{2}$ which remains decoupled from the dynamics and hence is irrelevant to the discussion. Each quasienergy [in Fig. 5.4(a)-(c)] has a color value given by $|\langle gg|\phi_n(0)\rangle|^2$.

$V_0 \ll \Omega$—. A non-zero but small value of V_0 ($V_0 \ll \Omega$) partly lifts the degeneracy of ϵ_n at the Bessel zero roots α_k^0 [see solid coloured lines in Fig. 5.4(a)] but still shows a close approach. It is expected that the points of close approach, the two-level system still exhibits dynamical localization [282]. We examine the case using effective Hamiltonian. When $R1$ resonance ($n_1\omega = \Delta_0$) is satisfied, we can write the

Hamiltonian in the rotated frame [Eq. (5.3)] in the high-frequency limit ($\omega \gg \Omega$) as

$$\begin{aligned}\hat{H}' &= \frac{\Omega}{2} i^{n_1} J_{n_1}(\alpha) \left(\sum_{j=1}^{2} \hat{\sigma}_{rg}^{j} + \hat{X}(e^{iV_0 t} - 1) \right) \\ &+ \frac{\Omega}{2} \sum_{m \neq n_1} i^m J_m(\alpha) e^{i(m-n_1)\omega t} \left(\sum_{j=1}^{2} \hat{\sigma}_{rg}^{j} + \hat{X}(e^{iV_0 t} - 1) \right) + \text{H.c.}, \qquad (5.16)\end{aligned}$$

where the first term gives the resonant contribution and the second term provides off-resonant fast oscillations. For $\omega \gg \Omega$ the sum total in the second term become negligible in comparison to the first term at large times. Furthermore, for $V_0 \ll \Omega$, the Hamiltonian becomes periodic with $T = 2\pi/\omega$, and thereby we can obtain an effective time-independent Floquet Hamiltonian as $\hat{H}_{eff} \approx \int_0^T dt \hat{H}'(t)$ [137, 170, 206–208].

$$\begin{aligned}\hat{H}_{eff} &\approx \frac{\Omega}{2} i^{n_1} J_{n_1}(\alpha) \left(\sum_{j=1}^{2} \hat{\sigma}_{rg}^{j} + \hat{X} \left(\frac{e^{iV_0 T} - 1}{iV_0 T} - 1 \right) \right) \\ &+ \frac{\Omega}{2} \sum_{m \neq n_1} i^m J_m(\alpha) \hat{X} \left(\frac{e^{iV_0 T} - 1}{i[(m-n_1)\omega V_0]T} - 1 \right) + \text{H.c.}. \qquad (5.17)\end{aligned}$$

In leading orders of V_0/ω, we obtain

$$\begin{aligned}\hat{H}_{eff}^{(V_0 \ll \omega)} &\simeq \frac{i^{n_1} \Omega J_{n_1}(\alpha)}{2} \sum_{j=1}^{2} \hat{\sigma}_{rg}^{j} + \frac{i^{n_1}\Omega}{2} \left(i\pi J_{n_1}(\alpha) + \sum_{m \neq n_1} \frac{i^{m-n_1} J_m(\alpha)}{(m-n_1)} \right) \frac{V_0}{\omega} \hat{X} \\ &+ \mathcal{O}\left(V_0^2/\omega^2\right) + \text{H.c.}. \qquad (5.18)\end{aligned}$$

Equation (5.18) implies that in the infinite-frequency limit ($V_0/\omega \to 0$), population trapping happens at the zeros of Bessel function ($J_{n_1}(\alpha) = 0$) irrespective of the initial state, identical to the case of non-interacting atoms. At the primary resonance ($n_1 = 0$), population trapping results in a dynamical stabilization.

For non-zero but small values of V_0/ω, the second term which is linear in V_0/ω also contributes to the effective Hamiltonian. Focusing on the primary resonance, $n_1 = 0$, we note that the third term in Eq. (5.18) vanishes exactly due to symmetry in $J_{\pm m}(\alpha)$. It means that at $J_0(\alpha) = 0$, $\hat{H}_{eff} \approx 0$, which implies that a dynamical stabilization will occur for any choice of the initial state. A further analyses for the same is made by investigating IPR values for both $|gg\rangle$ and $|rr\rangle$ state as a function of α. Both $\Pi_2^{|gg\rangle}$ and $\Pi_2^{|rr\rangle}$ are shown in Figs. 5.4(d) and 5.4(e) respectively for $V_0 = 0.2\Omega$ with $\Delta_0 = 0$ (green dashed lines). As expected, both the values vanish at $J_0(\alpha) = 0$, indicating a dynamical stabilization in both $|gg\rangle$ and $|rr\rangle$ state. Even at secondary resonances $n_1 \neq 0$, the third term in Eq. (5.18) remains vanishingly small at the Bessel roots $\alpha_{n_1}^k$ and thus adds nothing significant to the Hamiltonian.

This term, however, may introduce a tiny shift in the value of α at which the DS occurs from α_0^k for the case of $|I\rangle = |rr\rangle$.

Thus, in conclusion, for small values of V_0/ω with $R1$ holding, as per the effective Hamiltonian, the population trapping happens at the roots of the Bessel function $J_{n_1}(\alpha)$. This is validated by looking at IPR values of dashed lines in Fig. 5.4(d) and Fig. 5.4(e). The avoided crossings in the quasienergy spectrum are in concurrence with DS at α_0^k, which do not get significantly altered at small values of V_0. However, the condition of dynamical stabilization remains independent of initial state $|gg\rangle$ and $|ee\rangle$.

$V_0 \gg \Omega$—. For larger values of V_0 (excluding $V_0 = n\omega$ where n is a non-zero positive integer), the quasienergy spectrum neither shows an exact triple crossing or a close approach. This means that now there is no reason to expect DS independent of the initial state. We plot the quasienergy levels to analyze the information that still can be extracted.

At the primary resonance $n_1 = 0$, one of the quasienergies [topmost level in Fig. 5.4(a) and Fig. 5.4(b)] become separated from the other two levels. At large V_0, the topmost state completely overlaps with $|rr\rangle$ for any value of α [see Fig. 5.4(b)]. Identical to the energy of $|rr\rangle$ in the blockade regime which is far off-resonant from $|+\rangle$ state, the corresponding quasienergy is non-resonant with the other Floquet modes. Nevertheless, the two base Floquet modes exhibit crossings among them, as shown in Fig. 5.4(b). These levels are a superposition of the remaining $|gg\rangle$ and $|+\rangle$ states, except at the level crossings. At the crossings, one Floquet mode completely overlaps with $|gg\rangle$ and the other one fully overlaps with $|+\rangle$ state. Therefore $|gg\rangle$ (as well as $|+\rangle$) is dynamically stabilized. The crossings occur at the Bessel zeros α_0^k. We can verify that the zeros of Bessel function $J_{n_1}(\alpha)$ lead to population trapping analytically. Let's invoke the coupling between states $|gg\rangle \leftrightarrow |+\rangle$ [Eq. (5.13)] and $|+\rangle \leftrightarrow |rr\rangle$ [Eq. (5.14)] in the rotated frame. For $V_0 \gg \Omega$, with $n_1 = 0$ (excluding $V_0 = n\omega$), in the zeroth order $\Omega_1 \approx \Omega J_0(\alpha)/2$ while $\Omega_2 \approx 0$. The system, thus, resembles an effective two-level crossing of $|gg\rangle$ and $+\rangle$ with coupling Ω_1 whilst $|ee\rangle$ remains isolated. Therefore, the dynamical stabilization in $|gg\rangle$ takes place when $\Omega_1 \to 0$ *i.e.*, at the zeros of $J_0(\alpha)$, whereas any population in $|ee\rangle$ is always trapped due to blockade. The dynamical stabilization can also be confirmed by the IPR values of $\Pi_2^{|gg\rangle}$ [see Fig. 5.4(d)], which vanishes at the quasienergy crossings, α_0^k. Furthermore, it can be noted that $\Pi_2^{|gg\rangle} = 1$ depicts the regime of Rydberg blockade for which we obtain an effective two-level system consisting of $|gg\rangle$ and $|+\rangle$ states. In the blockade regime, population in the state $|rr\rangle$ is trapped even in the absence of periodic driving, which makes $\Pi_2^{|rr\rangle} \sim 0$ independent of α [see Fig. 5.4(e) for $V_0 = 5\Omega$].

$V_0 = n\omega$ —. When $V_0 = n\omega$, where n is a positive integer, both $R1$ and $R2$ are

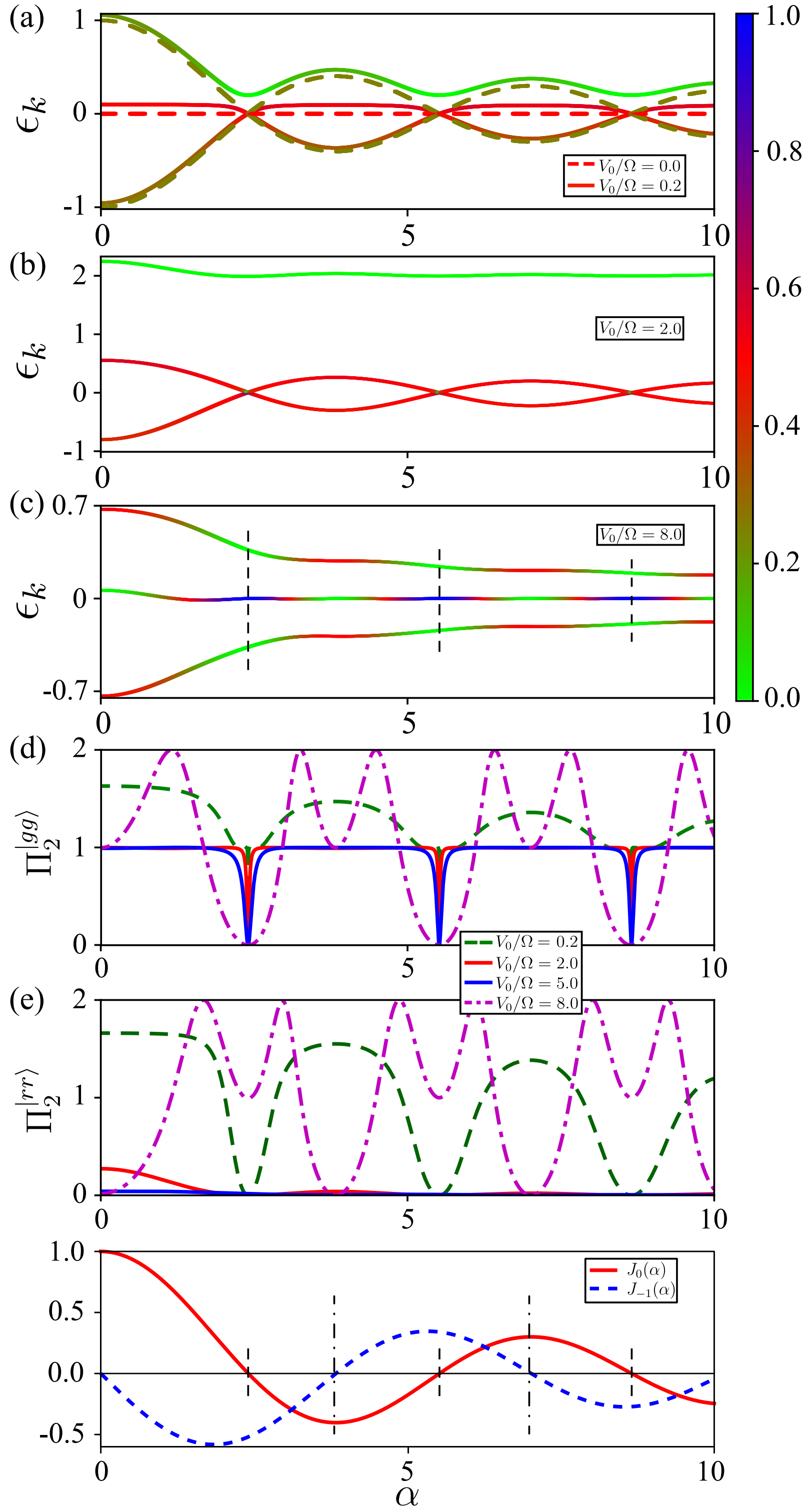

Figure 5.4: The quasi-energy spectrum ϵ_k and IPR ($\Pi_2^{|gg\rangle}$, $\Pi_2^{|rr\rangle}$) for $N = 2$, $\Delta_0 = 0$, and $\omega = 8\Omega$, as a function of α for different V_0. (a) shows ϵ_n for $V_0 = 0\Omega$ (dashed lines), and $V_0 = 0.2\Omega$ (solid lines), and (b) and (c) show the same for $V_0 = 2\Omega$ and $V_0 = 8\Omega$, respectively. Since $\Delta_0 = 0$, in (a) and (b), the level crossings take place at the zeros of $J_0(\alpha)$. In (a)-(c) the color bar indicates the probability of the finding the state $|gg\rangle$ in each of the Floquet modes. The dashed vertical lines in (c) mark $J_0(\alpha) = 0$, and at those points the central Floquet mode consists purely of $|gg\rangle$ state, which indicates dynamical stabilization. (d) and (e) show the IPR $\Pi_2^{|gg\rangle}$ and $\Pi_2^{|rr\rangle}$, respectively. In (f), we show the Bessel functions $J_0(\alpha)$ (solid line) and $J_{-1}(\alpha)$ (dashed line). The parameter α is varied by changing δ and keeping ω constant.

simultaneously satisfied. In that case, the Bessel functions $J_{n_1}(\alpha)$ and $J_{n_2=n_1-n}(\alpha)$ [counter refer Eqs. (5.13) and (5.14)] determine the couplings for the transitions $|gg\rangle \leftrightarrow |+\rangle$ and $|+\rangle \leftrightarrow |rr\rangle$, respectively. This is truly the case of three coupled levels as both $\Omega_1 \approx \Omega/2J_{n1}(\alpha)$ and $\Omega_1 \approx \Omega/2J_{n2}(\alpha)$ are in general non-zero. Thus, the dynamical stabilization of $|gg\rangle$ will occur when $\Omega_1 \to 0$ or when $J_0(\alpha) = 0$. Similarly, population trapping in $|ee\rangle$ takes place when $\Omega_1 \to 0$ or at the zeros of $J_{-1}(\alpha) = 0$. Note, however, that both conditions cannot be satisfied together. In Figs. 5.4(c)-5.4(e), we show the results for $\Delta_0 = 0$ with $V_0 = \omega = 8\Omega$, for which both resonances are satisfied at $n_1 = 0$ and $n_2 = n_1 - n = -1$.

In the case of simultaneous resonance, both the quasienergies ϵ_k and the inverse participation ratio $\Pi_2^{|gg\rangle}$ demonstrate qualitatively different features compared to the relatively simpler case when only one resonance condition, either $R1$ or $R2$, is satisfied. The first anomalous attribute is that the quasienergy spectrum ϵ_k does not have any level crossings when plotted as a function of α [see Fig. 5.4(c)]. Despite that, we observe dynamical stabilization of both $|gg\rangle$ at $J_0(\alpha) = 0$ [marked by dashed vertical lines in Fig. 5.4(c)] and $|ee\rangle$ state at $J_{-1}(\alpha) = 0$. This is in stark contrast to the case of a single two-level atom for which the dynamical stabilization is always accompanied by a level crossing in the quasi-particle spectrum. To further look at the regions of dynamical stabilization of $|gg\rangle$, we color code quasienergies with the overlap $|\langle gg|\phi_n(0)\rangle|^2$. We observe that at the values of α_0^k, one of the Floquet modes [the central one in Fig. 5.4(c)] becomes completely $|gg\rangle$ state. A similar colour profile is observed upon plotting the overlap of Floquet modes with $|rr\rangle$ state (not shown). Interestingly, $\Pi_2^{|gg\rangle}$ and $\Pi_2^{|rr\rangle}$ exhibit both primary and secondary minima as a function of α [see Figs. 5.4(d) and 5.4(e) for $V_0 = \omega$]. The primary minima in $\Pi_2^{|gg\rangle}$ occurs when $J_0(\alpha) = 0$ and it coincide with the secondary minima of $\Pi_2^{|rr\rangle}$ ($J_{n_2=-1}(\alpha) = 0$), and vice versa. At the primary minima of $\Pi_2^{|gg\rangle}$, the state $|gg\rangle$ shows DS while at the secondary minima, the system exhibits blockade dynamics and undergoes Rabi oscillations between the states $|+\rangle$ and $|rr\rangle$. Furthermore, even the maxima of $\Pi_2^{|gg\rangle}$ and $\Pi_2^{|rr\rangle}$ do not coincide as shown in Figs. 5.4(d) and 5.4(e) for $V_0 = \omega$. At the maxima ($\Pi_2^{|gg\rangle} \sim 2$ or $\Pi_2^{|rr\rangle} \sim 2$), the system undergoes Rabi oscillations between $|gg\rangle$ and $|rr\rangle$ via the intermediate state $|+\rangle$ with an effective Rabi frequency $\propto \sqrt{J_0^2(\alpha) + J_{-1}^2(\alpha)}$. Therefore, the maximum value ($\Pi_2^{|gg\rangle} = 2$) in Fig. 5.4(d) correspond to driving-induced Rydberg anti-blockades [137, 284].

Figures 5.5(a) and 5.5(b) show $\Pi_2^{|gg\rangle}$ and $\Pi_2^{|rr\rangle}$, respectively for a broader range of V_0 and α. In Fig. 5.5(a), we identify three different regions: (i) dynamical stabilization (shown by horizontal dark regions with $\Pi_2^{|gg\rangle} \sim 0$), (ii) anti-blockade (bright loops with $\Pi_2^{|gg\rangle} \sim 2$ around $V_0 = n\omega$) and (iii) population trapping of $|rr\rangle$ ($\Pi_2^{|gg\rangle} \sim 1$ and $\Pi_2^{|rr\rangle} = 0$) (red-orange backdrop) in the remaining majority of the parameter space. In Fig. 5.5(b), the dominant regions with a small IPR value ($\Pi_2^{|rr\rangle} \sim 0$) is

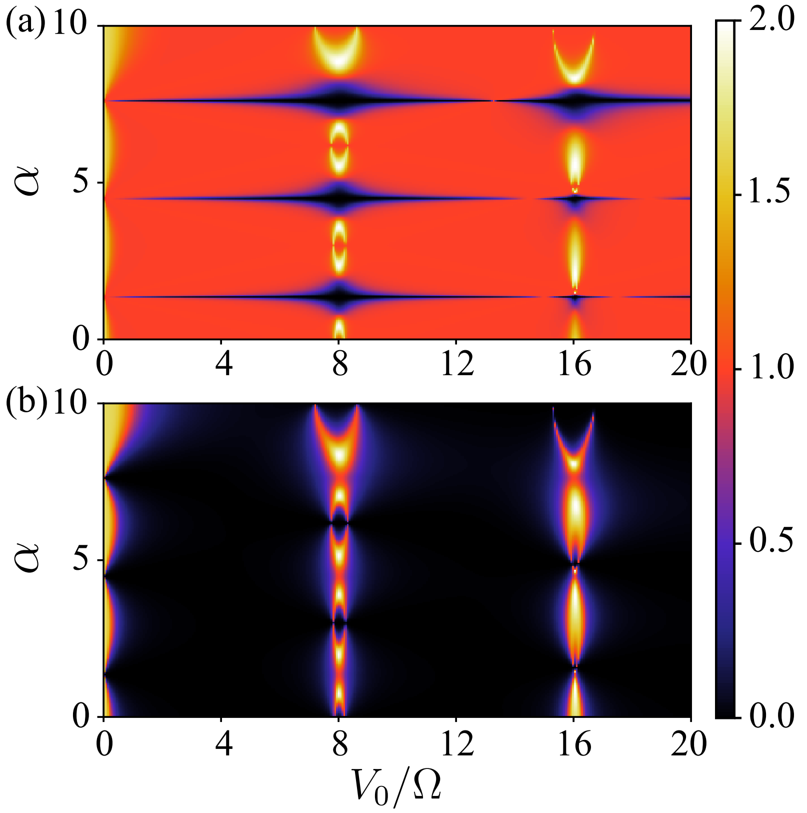

Figure 5.5: The IPR (a) $\Pi_2^{|gg\rangle}$ and (b) $\Pi_2^{|rr\rangle}$ as a function of V_0 and α for $N = 2$, $\Delta_0 = 0$ (R1 resonance), and $\omega = 8\Omega$. The regions of $\Pi_2^{|gg\rangle} = 0$ correspond to the dynamical stabilization of $|gg\rangle$, those where both $\Pi_2^{|gg\rangle} \sim 1$ and $\Pi_2^{|rr\rangle} \sim 0$ indicate the population trapping of $|rr\rangle$, and $\Pi_2^{|gg\rangle} = 2$ signals the Rydberg anti-blockade in which the system exhibits Rabi oscillations between $|gg\rangle$ and $|rr\rangle$ via the intermediate state $|+\rangle$. The intricate patterns arise due to the competition between the Rabi-couplings for the transitions $|gg\rangle \leftrightarrow |+\rangle$ $[\propto J_{n_1}(\alpha)]$ and $|+\rangle \leftrightarrow |rr\rangle$ $[\propto J_{n_2}(\alpha)]$. If R2 is satisfied with $V_0 = \Delta_0$ instead of R1 (a) is $\Pi_2^{|rr\rangle}$ and (b) is $\Pi_2^{|gg\rangle}$. The parameter α is varied by changing δ and keeping ω constant.

primarily due to the Rydberg blockade of $|rr\rangle$. At resonance, $\Pi_2^{|rr\rangle}$ becomes non-zero in the vicinity of $V_0 = n\omega$, except when $J_{n_2} \sim 0$ which leads to population trapping. In the $\alpha - V_0$ plane, the non-trivial patterns in IPR [shown in Fig. 5.5] emerge due to the interplay between the two Rabi-couplings corresponding to the transitions $|gg\rangle \leftrightarrow |+\rangle$ $[\propto J_{n_1}(\alpha)]$ and $|+\rangle \leftrightarrow |rr\rangle$ $[\propto J_{n_2}(\alpha)]$.

*R*2**:** We now consider the dynamical stabilization of both $|gg\rangle$ and $|rr\rangle$ states when R2: $n_2\omega = \Delta_0 - V_0$ is satisfied at primary resonance *i.e.* $n_2 = 0$ $(\Delta_0 = V_0)$. For $V_0 \ll \Omega$, in succession to the aforementioned discussions on $R1$, it can be deduced that the dynamical stabilization of both $|rr\rangle$ and $|gg\rangle$ states is given by the condition, $J_0(\alpha) = 0$. On the other hand, for $V_0 \gg \Omega$, we also have a large Δ_0, and therefore the state $|gg\rangle$ gets decoupled from the dynamics (except when $\Delta_0 = V_0 = n\omega$). Similar to $R1$, in this case the dynamical stabilization of $|rr\rangle$ is provided by $J_0(\alpha) = 0$. In the exceptional case where $\Delta_0 = V_0 = n\omega$, both $R1$ and $R2$ are satisfied simultaneously.

Thus the population trapping of $|gg\rangle$ is provided by $J_n(\alpha) = 0$ while the dynamical stabilization of $|rr\rangle$ is given by $J_0(\alpha) = 0$, as described above. In conclusion, the results for $R2$ are identical to that of $R1$ with $\Delta_0 = 0$, $V_0 = n\omega$, except that the role of $|rr\rangle$ and $|gg\rangle$ are interchanged. Therefore, Figs. 5.5(a) and 5.5(b) alternatively show $\Pi_2^{|rr\rangle}$ and $\Pi_2^{|gg\rangle}$ for $V_0 = \Delta_0$, respectively.

$R3$: Now, we consider the case of third resonance $R3$: $n_3\omega = 2\Delta_0 - V_0$. When $R3$ is satisfied, the system exhibits Rabi oscillations between $|gg\rangle$ and $|rr\rangle$ states. As mentioned earlier, the resonance condition for $R3$ cannot be extracted directly from the Hamiltonian in Eq. (5.3) or from the Rabi couplings in Eqs. (5.13) and (5.14). Hence, the couplings do not provide us with any physical picture of how dynamical stabilization is related to the Bessel roots. For $V_0 \gg \Omega$, the values of Δ_0 for which $R3$ gets satisfied is far away from Δ_0 corresponding to $R1$ or $R2$ resonances. This means that there is no overlap in the resonances [88]. In that case, neither $|gg\rangle$ nor $|rr\rangle$ can be stabilized as both of the states take part in Rabi oscillations coerced by $R3$ resonance. Consequently, the population in $|+\rangle$ state remains negligible, except when $\Delta_0 = V_0 = n\omega$.

For $V_0 \ll \Omega$, there is an overlap among the resonances as $R1$, $R2$, and $R3$ are not well isolated. Thus all three states ($|gg\rangle$, $|+\rangle$, $|rr\rangle$) and resonances are relevant in the dynamics. This situation leads to the population transfer between $|gg\rangle$ and $|rr\rangle$ via the intermediate $|+\rangle$ state. For small values of both RRIs and Δ_0 compared to the driving frequency, i.e., for $\Delta_0/\omega \ll 1$ and $V_0/\omega \ll 1$ the effective Hamiltonian can be approximately obtained as,

$$\hat{H}_{eff}^{(\Delta_0 \ll \omega)} \simeq \frac{\Omega J_0(\alpha)}{2}\left(1 - i\pi\frac{\Delta_0}{\omega}\right)\sum_{j=1}^{2}\hat{\sigma}_{rg}^{j} + \frac{i^{n_3}\Omega}{2}\left(J_{n_3}(\alpha) - J_0(\alpha)\right)\left(1 + i\pi\frac{\Delta_0}{\omega}\right)\hat{X} + \text{H.c.}. \tag{5.19}$$

When $n_3 = 0$, the second term with $\hat{X}$ in Eq. (5.19) vanishes, and the dynamical stabilization of both $|gg\rangle$ and $|rr\rangle$ is provided by the zeros of $J_0(\alpha)$. This result has been further verified by numerical calculations of the Schrödinger equation, using the crossings in the Floquet spectrum and IPR [see Fig. 5.6(a)]. In contrast with $R1$ and $R2$, as V_0 increases, the dynamical stabilization for $R3$ requires both stronger driving frequencies (ω) and larger modulation amplitudes (α). As shown in Fig. 5.6(a), for $V_0 = 0.01\Omega$, we get the IPR profile nearly identical to that of the non-interacting or single atom case [see Fig. 5.1(a)], which exhibits sharp minima at $J_0(\alpha) = 0$. For a fixed ω, increasing V_0 makes the minima broader, and in particular, those at small values of α stop reaching zero. It means that on increasing V_0/ω, the dynamical stabilization at small values of α gets disrupted, as seen for $V_0 = 0.2\Omega$ and $V_0 = 1\Omega$ in Fig. 5.6(a). In Fig. 5.6(b), we show IPR at a sufficiently large value of RRIs ($V_0 = 6\Omega$) and for different ω, and we see that the sharp minima with

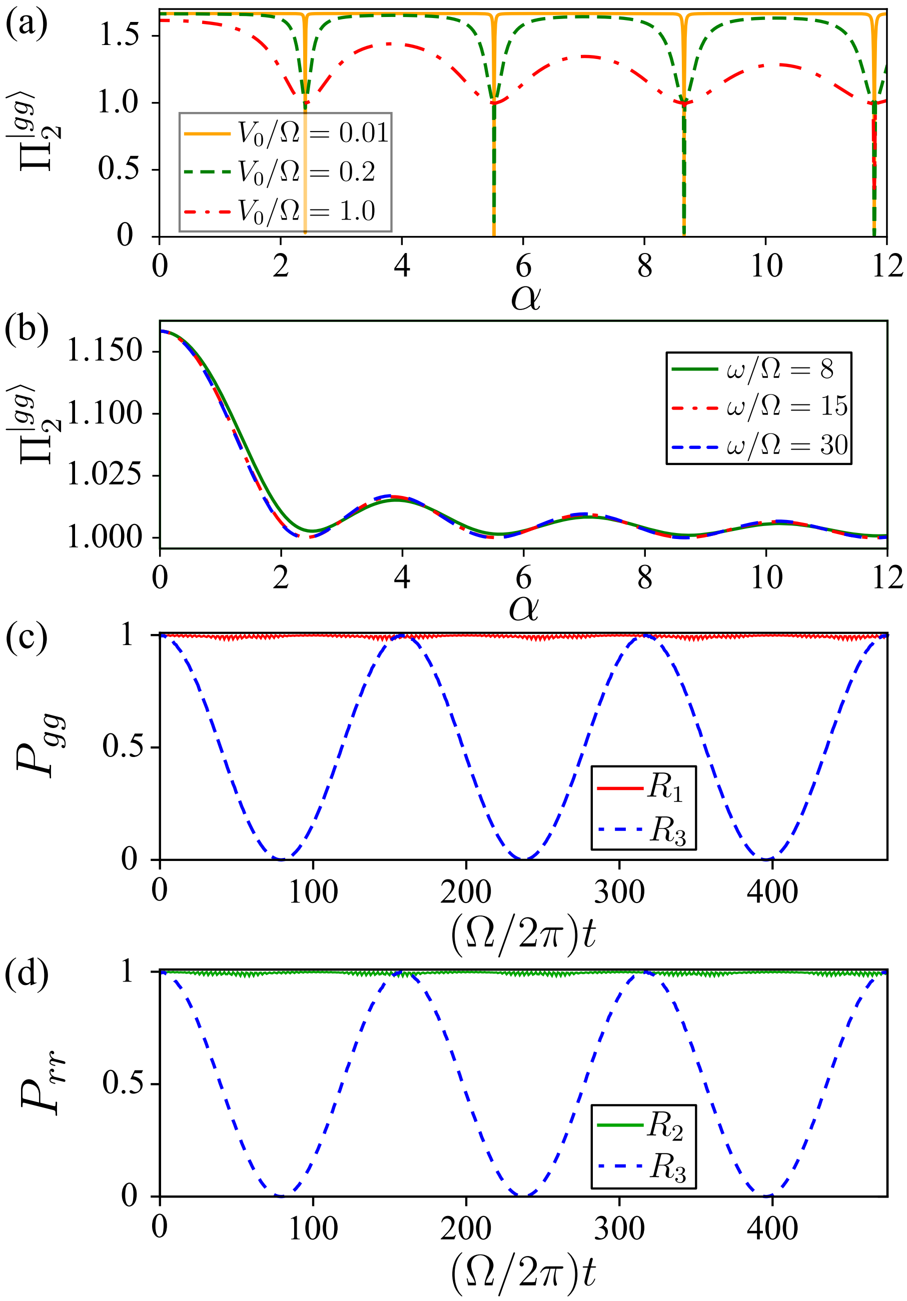

Figure 5.6: (a) The IPR ($\Pi_2^{|gg\rangle}$) as a function of α for $\omega = 30\Omega$ for different V_0 satisfying the R3 resonance with $n_3 = 0$, i.e., $2\Delta_0 = V_0$. (b) The same as in (a), but for different ω and $V_0 = 6\Omega$. In (c), we show the dynamics for the initial state $|gg\rangle$ assuming R1 and R3 are met ($n_1 = n_3 = 0$) at the first root of $J_0(\alpha)$, $\omega = 15\Omega$ and $V_0 = 6\Omega$. In (d), we show the same as in (c), except that the initial state is $|rr\rangle$ and for the resonances R2 and R3, i.e. for $n_2 = n_3 = 0$. The parameter α is varied by changing δ and keeping ω constant.

vanishing IPR have disappeared completely leaving behind the broader minima. These results can be understood from Eqs. (5.13) and (5.14). For sufficiently large V_0, satisfying the primary resonance condition $2\Delta_0 = V_0$ does not result in the selection of a particular Bessel function in the Rabi couplings, which in turn prevents the dynamical stabilization of the initial state. Furthermore, the oscillations saturate to an IPR value of 1 which implies that at strong modulation amplitudes, coherent oscillations between $|gg\rangle$ and $|rr\rangle$ states persist.

The strong dependence of V_0 on the dynamical stabilization of $|gg\rangle$ and $|rr\rangle$ under $R3$ resonance, is in stark contrast to that of $R1$ and $R2$. To explicitly demonstrate it, we plot the dynamics at the first Bessel zero of $J_0(\alpha)$ for the three resonances $R1$, $R2$, and $R3$ for sufficiently large V_0 [see Figs. 5.6(c) and 5.6(d)]. In Fig. 5.6(c), we show the dynamics for the initial state $|gg\rangle$, one case satisfying the resonance $R1$ and the other case $R3$, and in Fig. 5.6(c), the dynamics are shown for the initial state $|rr\rangle$ satisfying $R2$ and $R3$ in the two cases. In both figures, we observe Rabi oscillations in the population dynamics of $R3$, indicating the clear absence of dynamical stabilization at large RRI.

5.4.3 Dynamical stabilization of maximally entangled Bell states

In the following, we consider the dynamical stabilization of entangled states, commonly known as Bell states. These are a set of four particular maximally entangled states of the two-atom system

$$|\pm\rangle \quad = (|gr\rangle \pm |rg\rangle)/\sqrt{2}, \tag{5.20}$$

$$|{}^{B1}/_{B2}\rangle \quad = (|gg\rangle \pm |rr\rangle)/\sqrt{2}. \tag{5.21}$$

We analyze the dynamical stabilization of maximally entangled $|+\rangle$, $|B1\rangle$ and $|B2\rangle$ states. The $|-\rangle$ state is decoupled from the dynamics and hence trivially exhibits stabilization. With $|+\rangle$ state as the initial state, we also inspect if the *entanglement* remains preserved with time. We quantify the quantum correlations or entanglement between the two atoms using bipartite Von Neumann entropy. For a detailed discussion on quantum correlations in two atoms see Sec. 1.5. In the abridged version, we first partition the system identically thereby labelling the two subsystems as A and B each containing one atom. The entanglement entropy is then defined with respect to subsystem A as $\mathcal{S}_A = -\mathrm{Tr}(\rho_\mathrm{A} \log_2 \rho_\mathrm{A}) = -\sum_\mathrm{k} \lambda_\mathrm{k} \log_2 \lambda_\mathrm{k}$, where ρ_A is the reduced subsystem density matrix corresponding to the atom A and λ_k are the eigenvalues of ρ_A. Since, $\mathcal{S}_A = \mathcal{S}_B$, it uniquely defines entanglement in the two-atom system. Each Bell state is maximally entangled with $\mathcal{S}_A = 1$, and under the condition of dynamical stabilization, we expect $\mathcal{S}_A$ to be preserved.

$|+\rangle$ state:

Among all of the Bell states, the $|+\rangle$ state is unique as it is involved in three types of resonances: when (i) only $R1$ is satisfied, (ii) only $R2$ holds, (iii) both of these

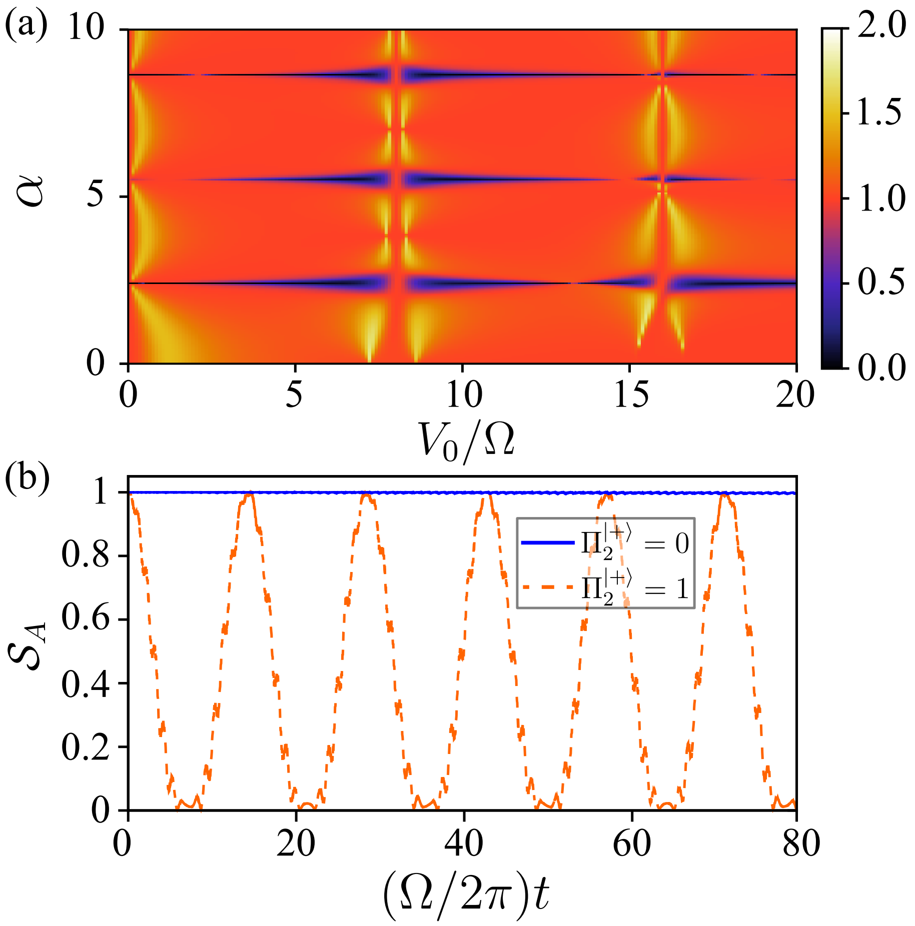

Figure 5.7: (a) IPR $\Pi_2^{|+\rangle}$ as a function of α and V_0 for $\omega = 8\Omega$ and $\Delta_0 = 0$. The parameter α is varied by changing δ and keeping ω constant. (b) The general behavior of the dynamics of the entanglement entropy $\mathcal{S}_A$ for $\Pi_2^{|+\rangle} = 0$ (solid line), indicating dynamical stabilization and for $\Pi_2^{|+\rangle} = 1$ (dashed line).

are simultaneously satisfied.

For $V_0 \ll \Omega$, the resonances $R1$ and $R2$ are not entirely separable and both are partially satisfied. This means that both the couplings Ω_1 from $|+\rangle \rightarrow |gg\rangle$ and Ω_2 from $|+\rangle \rightarrow |rr\rangle$ [see Eqs. (5.14)] are non zero and nearly identical to $\Omega J_0(\alpha)/2$. As a result, on an average the population from $|+\rangle$ state transfers nearly equally to both $|gg\rangle$ and $|rr\rangle$ states. Following Eq. (5.18) for $V_0/\omega \ll 1$, we can see that dynamical stabilization of $|+\rangle$ occurs when $J_0(\alpha) = 0$. This is validated by the apprehension that both Ω_1 and Ω_2 vanish at zeros of $J_0(\alpha)$. For $V_0 \gg \Omega$ (excluding the case of simultaneous resonance $V_0 = n\omega$), the resonances $R1$ and $R2$ are isolated from each other. Nevertheless, the dynamical stabilization of $|+\rangle$ is still determined by the zeros of $J_0(\alpha)$ if either one of $R1$ and $R2$ holds true. Suppose only $R1$ is satisfied with $n_1 = 0$. This results in $\Omega_1 \approx \Omega J_0(\alpha)/2$ and $\Omega_2 \approx 0$. Consequently, $|+\rangle$ to $|gg\rangle$ state transition occurs which is dictated by an effective Rabi coupling of Ω_1 whereas no population from $|+\rangle$ is transferred to $|rr\rangle$ state which can be attributed to Rydberg blockade. The $|+\rangle$ state can thus be stabilized dynamically when Ω_1

vanishes *i.e.* at the zeros of $J_0(\alpha)$ provided the blockade condition is satisfied. On the other hand, the resonance condition $R2$ demands a large initial detuning, which prevents a coherent population transfer from $|+\rangle$ to $|gg\rangle$ state. This helps in the dynamical stabilization of state $|+\rangle$ at the roots of $J_0(\alpha)$.

For simultaneous resonances at $V_0 = n\omega$ with n being a non-zero integer both $R1$ and $R2$ (as well as $R3$) are satisfied. We examine the primary resonance of $R1$ with $n_1 = 0$. The dynamical stabilization of $|+\rangle$ state requires both $J_0(\alpha) = 0$ and $J_{-n}(\alpha) = 0$. The latter criteria can never be satisfied with $n \neq 0$, which prevents population trapping of $|+\rangle$ at simultaneous resonances. The discussion implies that the dynamics of an entangled state is harder to freeze than the product states $|gg\rangle$ or $|rr\rangle$. The above results are summarized in Fig. 5.7(a), in which we show the IPR value $\Pi_2^{|+\rangle}$ in the plane of α and V_0. The broken horizontal blue stripes in Fig. 5.7(a) correspond to the regions of dynamical stabilization of $|+\rangle$ state. The regions with $\Pi_2^{|+\rangle} = 1$ correspond to the blockade dynamics and those with $\Pi_2^{|gg\rangle} = 2$ indicate that all three states are very involved in the dynamics. For R2 resonance and $V_0 = \Delta_0$, we get the same results as above, with the only key difference being that the regions with $\Pi_2^{|+\rangle} = 1$ indicate the Rabi oscillations between $|+\rangle$ and $|rr\rangle$. Further, the time evolution of the entanglement entropy $\mathcal{S}_A$ for the initial state $|+\rangle$ with minimum and maximum value IPR is shown in Fig. 5.7(b). When $\Pi_2^{|+\rangle} = 0$, we see that $\mathcal{S}_A$ freezes, which indicates that the correlation between two atoms is preserved under the periodic drive. In the regimes where $\Pi_2^{|+\rangle} = 1$, the entropy $\mathcal{S}_A$ undergoes coherent oscillations, and for the particular case depicted in Fig. 5.7(b), the oscillations in $\mathcal{S}_A$ are due to the Rabi oscillations of the entangled state $|+\rangle$ with product state $|gg\rangle$.

$|B1\rangle$ and $|B2\rangle$ states:

To discuss the dynamical stabilization of the Bell states $|^{B1}/_{B2},\rangle$, we need to consider all the resonances which includes either $|gg\rangle$ or $|rr\rangle$, or both. Satisfying any of these resonances drives the system away from the $|^{B1}/_{B2},\rangle$ state. This simple-looking state is not trivial to apprehend. We comment on the stabilization of states $|B1\rangle$ and $|B2\rangle$ in conjunction with the case where both $|gg\rangle$ and $|rr\rangle$ are primarily engaged in resonance. The latter happens when either $R3$ is satisfied or both $R1$ and $R2$ are met simultaneously. As already mentioned, at the primary resonance of $R3$ (with $2\Delta_0 = V_0$), the system exhibits Rabi oscillations between $|gg\rangle$ and $|rr\rangle$ via $|+\rangle$ except at the roots of $J_0(\alpha)$ where both $|gg\rangle$ and $|rr\rangle$ populations come to a halt and are dynamical stabilized.

The final state can be expanded in the triplet basis $|\psi(t)\rangle = c_{gg}|gg\rangle + c_+|+\rangle + c_{rr}|rr\rangle$. Accordingly, the probability of system being in product states is $|\langle gg|\psi(t)\rangle|^2 = |c_{gg}|^2$ and $|\langle rr|\psi(t)\rangle|^2 = |c_{rr}|^2$. However, for the entangled states $|B1\rangle$ and $|B2\rangle$ the final probabilities also depend upon the real and imaginary part of the amplitudes c_{gg} and c_{rr} in addition to the product state probabilities,

$$\begin{aligned}
|\langle B1|\psi(t)\rangle|^2 &= \frac{|c_{gg}+c_{rr}|^2}{2} \neq \frac{|c_{gg}|^2+|c_{rr}|^2}{2} \\
&= \frac{|c_{gg}|^2+|c_{rr}|^2}{2} + (\mathrm{Re}[c_{gg}]\mathrm{Re}[c_{rr}] + \mathrm{Im}[c_{gg}]\mathrm{Im}[c_{rr}])\,. \qquad (5.22)\\
|\langle B2|\psi(t)\rangle|^2 &= \frac{|c_{gg}-c_{rr}|^2}{2} \neq \frac{|c_{gg}|^2-|c_{rr}|^2}{2} \\
&= \frac{|c_{gg}|^2+|c_{rr}|^2}{2} - (\mathrm{Re}[c_{gg}]\mathrm{Re}[c_{rr}] + \mathrm{Im}[c_{gg}]\mathrm{Im}[c_{rr}])\,. \qquad (5.23)
\end{aligned}$$

The above expressions crucially indicate that even if the states $|gg\rangle$ and $|rr\rangle$ are dynamically stabilized (implying a constant value of $|c_{gg}|^2$ and $|c_{rr}|^2$), it does not naturally translate to a dynamical stabilization of $|B1\rangle$ or $|B2\rangle$ due to the additional terms in Eqs. (5.22) and (5.23). As an example, the states $|gg\rangle$ and $|rr\rangle$ are dynamically stabilized with small RRIs $V_0/\omega \ll 1$ at the roots of $J_0(\alpha)$ which can be easily seen from Eq. (5.19). However, the same does not imply a dynamical stabilization of $|B1\rangle$ (or $|B2\rangle$) as shown in Fig. 5.8(a). On the other hand, satisfying $R1$ and $R2$ conditions simultaneously requires two different Bessel functions to vanish at the same value of α which is not possible, thereby ruling out the possibility of dynamical stabilization of $|B1\rangle$ or $|B2\rangle$ state. For $V_0 \gg \Omega$ and letting $\Delta_0 = V_0/2$ without periodic driving, with $|B1\rangle$ (or $|B2\rangle$) as initial state, we obtain the population in both $|gg\rangle$ and $|rr\rangle$ nearly 1/2, due to blockade. At the same time, the population in $|B1\rangle$ (or $|B2\rangle$) remains maximally frozen and it acts like a stationary state in absence of modulation [see Fig 5.8(b)]. However, a periodic driving makes $|B1\rangle$ and $|B2\rangle$ dynamically unstable.

5.5 Experimental Parameters

Finally, we comment on the experimental setup and parameters, which can be used to investigate our findings. We consider a Rydberg $nS_{1/2}$ state of a rubidium atom. The two atom setups are easily realizable in labs using either optical tweezers or optical micro traps [76]. Moreover, the interaction strengths between the Rydberg atoms can be controlled precisely by adjusting the separation between the atoms or using external fields [76]. As we mentioned before, the periodic modulation can be generated by applying an additional oscillating RF field, which creates sidebands in the Rydberg state as shown in [285–288]. Further control over the sidebands, selecting even or odd bands, are accessible via ac or dc electric fields [285]. An alternative way, as demonstrated in a recent experiment, an intensity-modulated off-resonance laser is used to vary the energy of the intermediate excited state sinusoidally, in a

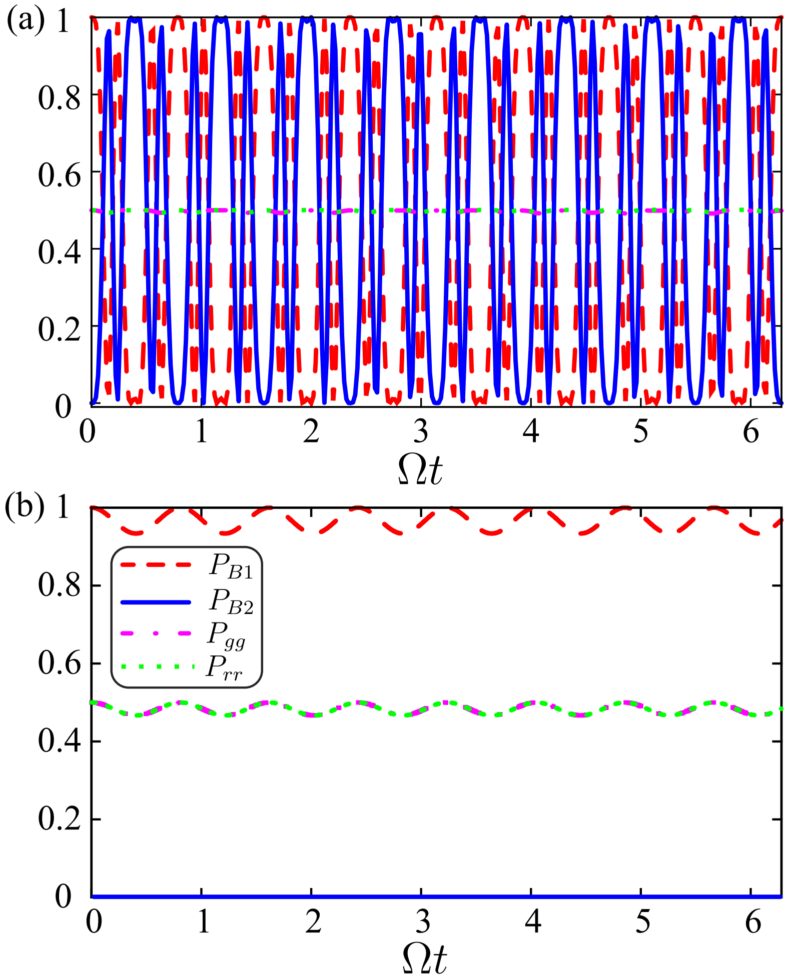

Figure 5.8: Population dynamics in $|B1\rangle$ (red-dashed lines), $|B2\rangle$ (blue-solid), $|gg\rangle$ (magenta dash-dotted) and $|rr\rangle$ (green-dotted) conditioned to initial state $|B1\rangle = (|gg\rangle + |rr\rangle)/\sqrt{2}$, (a) with small interaction strengths $V_0 = 0.01\Omega$, $\omega/\Omega = 8.0$ and modulation amplitude corresponding to first Bessel root $\delta = 2.404\omega$, (b) for strong interactions, $V_0/\Omega = 15$ but without periodic modulation, $\delta = 0$.

two-photon transition to the Rydberg state from the ground state [289]. The latter approach is equivalent to modulating the effective light field, which couples the ground to the Rydberg state.

For a typical experiment involving two Rubidium Rydberg atoms, we consider the Rydberg state to be $|r\rangle \equiv |45S_{1/2}\rangle$ which is coupled from the ground state $|5S, F = 2, m_F = 2\rangle$ via the $|5P, F = 3, m_F = 3\rangle$. A two-photon excitation by diode lasers at 780 and 480nm is used for the 5S-5P-nS transition [102]. On applying a large detuning to the intermediate $5P$ state, the three-level system can be reduced to an effective two-level system with a typical Rabi frequency of $\Omega \sim 1$ MHz. In our studies, we use interaction strengths $V_0 = 0 - 20$ MHz, and modulation frequency $\omega = 0 - 30$ MHz. The typical distance between Rydberg atoms corresponding to this interaction strength would be about 8μm or larger which is feasible in atom traps. The suitable modulation in frequency can also be generated by the above-mentioned methods. As we can see, the frequency differences between neighboring states are $(E_{45S_{1/2}} - E_{44S_{1/2}})/\hbar = 92.96$ GHz and $(E_{46S_{1/2}} - E_{45S_{1/2}})/\hbar = 86.53$ GHz, ensures that sidebands generated by the periodic modulation do not populate the nearest Rydberg states. The latter can also be suppressed by taking a moderately strong intensity of the oscillating RF field [285, 288].

5.6 Summary

In summary, we have studied the Dynamical stabilization of a set of experimentally relevant product and entangled states in a Rydberg atom pair. The presence of Rydberg-Rydberg interactions leads to state-dependent population trapping. As we have shown, unlike in the case of a single two-level atom, the population trapping or dynamical stabilization in two interacting Rydberg atoms may not be accompanied by level crossings in the Floquet spectrum. We have discussed the dynamical stabilization of a few selected states, including both product and entangled Bell states. The latter case offers a way to preserve entanglement or correlation between two qubits for sufficiently long times, with limitations arising only from the decoherent processes. Our analysis reveals that the driving parameters are more restricted to stabilize the entangled states compared to the product states dynamically. The results we have discussed here on population trapping or dynamical stabilization are valid for a pair of any interacting two-level systems.

Our studies immediately raise the question of population trapping or dynamical stabilization in extended systems, i.e., beyond a pair of atoms. For instance, it would be interesting to analyze how the population trapping affects the bipartite and tripartite entanglement of W and GHZ-states in three or more atoms setup. As the number of qubits or atoms increases, the Floquet spectrum's complexity also increases, making the scenario more intriguing.

Chapter 6

Summary and Outlook

Systems of many-body interacting Rydberg atoms have an enormous potential to solve long-standing problems in physics. On the other hand, the interest in two-body Rydberg systems is motivated by applications of local quantum control and deterministic local state preparation in a larger array. Technological progress has allowed for a very active research community where the experimentalists can probe and discover exciting physics which the theorists explain with great insights. Similarly, remarkable theoretical predictions may be verified with controlled experiments. It is therefore of fundamental importance to understand the underlying physics of such systems. We focused on the setup of two atoms which forms the basis for all entanglement operations. In this thesis, we studied systems of two interacting Rydberg atoms and propose mechanisms to engineer the quantum state of the collective system. Our work pertains to manipulating the state dynamics of the two-atom system which is achieved by tuning the atom-light couplings and detunings, both in weakly and strongly interacting systems. We have probed the population dynamics when the atoms are applied with (i) distinct Rabi couplings (ii) a linearly varying detuning, and (iii) a periodically varying detuning. We numerically solve the Schrödinger equation through Trotter's decomposition and employ analytical techniques such as Effective Hamiltonian and Adiabatic Impulse approximation to bring physical insights into the system dynamics.

In keeping pace with the experimental progress which allows for individual atom addressability, we studied a system in which both the atoms are driven distinctly by different light fields. We focused on finding the effect of a Rabi frequency offset on the excitation dynamics and quantum correlations of two atoms. When the atoms are strongly interacting with each other, we identified the novel feature of Rydberg-biased freezing, where augmenting the driving in one atom attenuates the population dynamics of the second atom. In the same regime, the quantum correlations get significantly suppressed, based on which we propose a scheme to dynamically control the quantum correlations. Rydberg biased freezing has since been experimentally observed through quantum simulation in two and three NMR spin qubits by another group. The latter study verifies that local control of excitation can be achieved by Rydberg-biased freezing. In our study, we also investigated the condition of Rydberg Blockade, of double excitation, which remains unaffected by positive Rabi frequency offsets. However, in the double excitation dynamics, an interesting non-monotonic behaviour is observed at small Rabi-offsets and small interaction strengths. We explained the feature using effective Hamiltonians in different limits of system parameters. To test the robustness of the above novel features in a real system, we included a dissipation term that arises from the spontaneous emission in the Rydberg state. We conclude that Rydberg-biased freezing is a robust phenomenon even with dissipation.

The atom-light detuning is another externally controllable system parameter. We studied two variations of time-dependent detuning: linear and periodic. The linear detuning in combination with tunable Rydberg-Rydberg interactions allows the two-atom system to probe various three-level Landau-Zener models. Our setup can emulate three and four-level bow-tie models, triangular Landau-Zener models, as well as anisotropic spin models. Such models are ubiquitously present across all fields of physics. Particularly in quantum simulation and computing, the Landau-Zener transitions have been proposed as an efficient mechanism to prepare the system in deterministic quantum states, and as a method of implementation of robust quantum gates. Furthermore, the three-level system has also been used as an atom interferometer. In consideration of this bigger picture, we analyzed the Landau-Zener transition dynamics in the two-atom system with a linear quench. The Landau-Zener dynamics showed a non-trivial dependence on the initial state, the quench rate, and the interaction strength. The nontrivial patterns are further analytically explained at strong interactions using the Adiabatic impulse approximation. Moreover, at weak interactions corrections to the non-interacting LZ model are proposed based on scaling arguments. The detailed information of population and phases revealed by analytical models can be used in a deterministic preparation of quantum states, as well as in atom-interferometry.

A periodic variation of detuning creates an even richer dynamics in the two-atom system. Often, periodic driving leads to the emergence of non-trivial phases which have no counterparts in equilibrium dynamics. For a single-atom, periodic driving emerged as a tool to manipulate excitation dynamics. We showed that even the simple system of a single-two level atom has still interesting unexplored features. In particular, we identified an interesting resemblance between the excitation probability in the periodically driven two-level atom and the intensity distribution pattern from N-slits. Furthermore, we have studied population trapping/dynamical stabilization in the two-level atom using three approaches (i) Floquet quasienergy crossings, (ii) Inverse participation ratio (IPR), and (iii) using effective Hamiltonian. We identified IPR as a suitable indicator of population trapping.

In an array of Rydberg atoms, it has been previously shown that periodic driving leads to enhancement of blockade and emergence of antiblockade regimes. A lot of research has been going on implementing a scheme for entangled phase gates using periodic driving. We analyzed the population dynamics of the periodically driven system of two Rydberg atoms using numerics and Adiabatic impulse approximation. It revealed the various resonances present in the system. We further discussed the validity of Adiabatic impulse approximation in detail. Furthermore, we focused specifically on population trapping in two two-level atoms for a set of experimentally relevant states. The presence of Rydberg-Rydberg interactions leads to state-dependent population trapping. We showed that unlike in the case of a single two-level atom, the population trapping or dynamical stabilization in two interacting Rydberg atoms may not be accompanied by level crossings in the Floquet spectrum. We have discussed the dynamical stabilization of product and entangled Bell states. The latter case offers a way to preserve entanglement or correlation between two qubits for sufficiently long times, with limitations arising only from the decoherent processes. Our analysis reveals that the driving parameters are more restricted to stabilize the entangled states compared to the product states dynamically. The results we have discussed here on population trapping or dynamical stabilization are valid for a pair of any interacting two-level systems.

Our study of two periodically driven atoms can be extended to three or more two-level atoms, for which it will not be so straightforward to assume AIA would work at large interactions due to the complexity in the level structure. We also note that for weak interactions, it is required to develop a multi-level AIA in which the LZTs take place among multiple levels at the same time. A study of entanglement dynamics of such systems may reveal mechanisms for a dynamical control of quantum correlation. Moreover, population trapping in extended systems can be studied. It would be interesting to analyze how the population trapping affects the bipartite and tripartite entanglement of W and GHZ-states in three or more atoms setup. As the number of qubits or atoms increases, the Floquet spectrum's complexity also increases, making the scenario more intriguing.

Appendix A

Steady State Results

A.1 Analytical results for the steady state density matrices and purity of the system and subsystems

On solving $\dot{\rho}(t) = 0$, the steady state density matrix of the system is obtained as:

$$
\begin{aligned}
\rho_{AB} = \frac{1}{\kappa} \Big[& \Big(V_0^2 \left(\Gamma^2 + \Omega^2 + (\Omega+\omega)^2 \right) + (\Gamma^2 + \Omega^2) \left(\Gamma^2 + (\Omega+\omega)^2 \right) \Big) |gg\rangle\langle gg| \\
& + \left(V_0^2 + \Gamma^2 + \Omega^2 \right) (\Omega+\omega)^2 \, |gr\rangle\langle gr| + \Omega^2 \left(V_0^2 + \Gamma^2 + (\Omega+\omega)^2 \right) |rg\rangle\langle rg| \\
& + \Omega^2 (\Omega+\omega)^2 |rr\rangle\langle rr| + \Omega \left(V_0^2 + \Gamma^2 \right) (\Omega+\omega) \left(|gr\rangle\langle rg| + \text{H.c.} \right) \\
& + \Big((\Omega+\omega)(i\Gamma - V_0) \left(\Gamma^2 + \Omega^2 - iV_0\Gamma \right) |gg\rangle\langle gr| + \text{H.c.} \Big) \\
& + \Big(\Omega(-V_0 + i\Gamma) \left(\Gamma^2 + (\Omega+\omega)^2 - iV_0\Gamma \right) |gg\rangle\langle rg| + \text{H.c.} \Big) \\
& + \left(-\Gamma(iV_0 + \Gamma)\Omega(\Omega+\omega) |gg\rangle\langle rr| + \text{H.c.} \right) \\
& + \Big((-V_0 + i\Gamma)\Omega(\Omega+\omega)^2 |gr\rangle\langle rr| + \text{H.c.} \Big) + \Big((iV_0 + \Gamma)\Omega^2(\Omega+\omega) |rg\rangle\langle rr| + \text{H.c.} \Big) \Big],
\end{aligned}
\tag{A.1}
$$

and that of subsystems are,

$$
\begin{aligned}
\rho_A = \frac{1}{\kappa} \Big[& \Big(V_0^2 \left(\Gamma^2 + 2\omega^2 + 4\omega\Omega + 3\Omega^2 \right) + \left(\Gamma^2 + \Omega^2 \right) \left(\Gamma^2 + 2(\Omega+\omega)^2 \right) \Big) |g\rangle\langle g| \\
& + \Omega^2 \left(V_0^2 + \Gamma^2 + 2(\Omega+\omega)^2 \right) |r\rangle\langle r| \\
& + \Big(\Omega \left(iV_0^2\Gamma - 2V_0(\Omega+\omega)^2 + i\Gamma \left(\Gamma^2 + 2(\Omega+\omega)^2 \right) \right) |g\rangle\langle r| + \text{H.c.} \Big) \Big] \\
\rho_B = \frac{1}{\kappa} \Big[& \Big(V_0^2 \left(\Gamma^2 + \omega^2 + 2\omega\Omega + 3\Omega^2 \right) + \left(\Gamma^2 + 2\Omega^2 \right) \left(\Gamma^2 + (\Omega+\omega)^2 \right) \Big) |g\rangle\langle g| \\
& + (\Omega+\omega)^2 \left(V_0^2 + \Gamma^2 + 2\Omega^2 \right) |r\rangle\langle r| - \Big((\Omega+\omega) (V_0 - i\Gamma) \left(\Gamma^2 + 2\Omega^2 - iV_0\Gamma \right) |g\rangle\langle r| + \text{H.c.} \Big) \Big],
\end{aligned}
\tag{A.2}
$$

where

$$\kappa = V_0^2\left(\Gamma^2 + 2\omega^2 + 4\Omega\omega + 4\Omega^2\right) + (\Gamma^2 + 2\Omega^2)\left(\Gamma^2 + 2(\Omega+\omega)^2\right). \tag{A.3}$$

The purity of the system and subsystems are obtained as:

$$\begin{aligned}
\mathrm{Tr}\left(\rho_{\mathrm{AB}}^2\right) = \frac{1}{\kappa^2}\Big[&\left(\Gamma^4 + 4\Gamma^2\Omega^2 + 2\Omega^4\right)\left(\Gamma^4 + 4\Gamma^2(\Omega+\omega)^2 + 2(\Omega+\omega)^4\right) \\
&+V_0^4\left(\Gamma^4 + 4\Gamma^2\left(2\Omega^2 + 2\Omega\omega + \omega^2\right) + 2\left(2\Omega^2 + 2\Omega\omega + \omega^2\right)^2\right) \\
&+V_0^2\Big(\Gamma^6 + 4\Gamma^4\left(2\Omega^2 + 2\Omega\omega + \omega^2\right) + 4\Omega^2(\Omega+\omega)^2\left(2\Omega^2 + 2\Omega\omega + \omega^2\right) \\
&+2\Gamma^2\left(\omega^4 + 4\omega^3\Omega + 11\omega^2\Omega^2 + 14\omega\Omega^3 + 7\Omega^4\right)\Big)\Big)\Big] \\
\mathrm{Tr}\left(\rho_{\mathrm{A}}^2\right) = \frac{1}{\kappa^2}\Big[&\Omega^4\left(V_0^2 + \Gamma^2 + 2(\Omega+\omega)^2\right)^2 + 2(V_0^2 + \Gamma^2)\Omega^2\left(\left(\Gamma^2 + 2(\Omega+\omega)^2\right)^2 + V_0^2\Gamma^2\right) \\
&+\left(\Gamma^4 + 2\Omega^2(\Omega+\omega)^2 + V_0^2\left(\Gamma^2 + 2\omega^2 + 3\Omega^2\right) + 4\Omega\omega V_0^2 + \Gamma^2\left(2\omega^2 + 3\Omega^2 + 4\Omega\omega\right)\right)^2\Big] \\
\mathrm{Tr}\left(\rho_{\mathrm{B}}^2\right) = \frac{1}{\kappa^2}\Big[&(\Omega+\omega)^4\left(V_0^2 + \Gamma^2 + 2\Omega^2\right)^2 + 2(V_0^2 + \Gamma^2)(\Omega+\omega)^2\left(\left(\Gamma^2 + 2\Omega^2\right)^2 + V_0^2\Gamma^2\right) \\
&+\left(\Gamma^4 + 2\Omega^2(\Omega+\omega)^2 + V_0^2\left(\Gamma^2 + \omega^2 + 3\Omega^2\right) + 2\Omega\omega V_0^2 + \Gamma^2\left(\omega^2 + 3\Omega^2 + 2\Omega\omega\right)\right)^2\Big].
\end{aligned} \tag{A.4}$$

For $\omega = 0$, the expressions for purity become:

$$\begin{aligned}
\mathrm{Tr}\left(\rho_{\mathrm{A}}^2\right) = \mathrm{Tr}\left(\rho_{\mathrm{B}}^2\right) = \frac{1}{\kappa^2}\Big[&\mathrm{V}_0^4\left(\Gamma^4 + 8\Gamma^2\Omega^2 + 10\Omega^4\right) + \mathrm{V}_0^2\left(2\Gamma^6 + 16\Gamma^4\Omega^2 + 32\Gamma^2\Omega^4 + 24\Omega^6\right) \\
&+\Gamma^8 + 8\Gamma^6\Omega^2 + 22\Gamma^4\Omega^4 + 24\Gamma^2\Omega^6 + 8\Omega^8\Big]
\end{aligned} \tag{A.5}$$

$$\begin{aligned}
\mathrm{Tr}\left(\rho_{\mathrm{AB}}^2\right) = \frac{1}{\kappa^2}\Big[&\left(\Gamma^4 + 4\Gamma^2\Omega^2 + 2\Omega^4\right)^2 + V_0^4\left(\Gamma^4 + 8\Gamma^2\Omega^2 + 8\Omega^4\right) \\
&+2V_0^2\left(\Gamma^6 + 8\Gamma^4\Omega^2 + 14\Gamma^2\Omega^4 + 8\Omega^6\right)\Big],
\end{aligned} \tag{A.6}$$

and for $\omega = 0$, the parameter κ reduces to,

$$\kappa = V_0^2\left(\Gamma^2 + 4\Omega^2\right) + \left(\Gamma^2 + 2\Omega^2\right)^2 \tag{A.7}$$

Appendix B

Underlying Group Symmetries

B.1 Two-level system and SU(2)

The underlying symmetry in the time evolution of the two-level system (TLS) is $SU(2)$ rotational symmetry. The evolution matrix of the two-level system falls under the $SU(2)$ symmetry group which comprises of all 2×2 unitary matrices. In particular, the full evolution matrix of the LZ problem under AIA is given by $\hat{F} = U(t_a, +0)\hat{G}_{LZ}U(-0, t_{-a})$ with $t_a \to \infty$. In the adiabatic basis it reads as follows

$$\begin{aligned} \hat{F} &= e^{i\phi_G} \begin{pmatrix} \sqrt{(1-P_{LZ})}e^{-i(2\zeta+\tilde{\phi}_s)} & -\sqrt{P_{LZ}} \\ \sqrt{P_{LZ}} & \sqrt{(1-P_{LZ})}e^{i(2\zeta+\tilde{\phi}_s)} \end{pmatrix} \quad \text{(B.1)} \\ &= e^{i\phi_G} \begin{pmatrix} \alpha_1 & -\alpha_2^* \\ \alpha_2 & \alpha_1^* \end{pmatrix} \quad \text{(B.2)} \end{aligned}$$

where $\phi_G = \int_0^{t_a} \Delta(t)dt$ and $\zeta = \int_0^{t_a} \bar{\Omega}(t)dt$ is an element of the $SU(2)$ group. The matrix on the second equality is the most general element of set $SU(2)$. The elements in $SU(2)$ have the property $\{\alpha_1, \alpha_2\} \in \mathbb{C}$ and $|\alpha_1|^2 + |\alpha_2|^2 = 1$. It describes a general rotation of the state (a_+, a_-) by an angle θ about the axis $\mathbf{n} = (n_x, n_y, n_z)$

$$R(\theta) = \exp\left(\frac{-i\sigma \cdot \mathbf{n}\theta}{2}\right) \quad \text{(B.3)}$$

where σ are the 2×2 Pauli operators. Explicitly, the full matrix $\hat{F}$ represents a rotation by an angle $\theta = \arccos[\sqrt{1-P_{LZ}}\cos\left(2\zeta + \tilde{\phi}_s\right)]$ in the Bloch sphere about the axis $\mathbf{n} = \left(0, -\frac{\sqrt{1-P_{LZ}}\sin\left(2\zeta+\tilde{\phi}_s\right)}{\sin(\theta/2)}, \frac{\sqrt{P_{LZ}}}{\sin(\theta/2)}\right)$.

Because of this symmetry, even repeated traversal across the avoided-crossings can be understood as rotations in the Bloch sphere about an axis $\mathbf{n}$ by an amount θ. Both values depend on the LZ transition probability and the dynamical phases gained during the traversal.

B.2 Three level system and SU(3)

B.2.1 SU(3)

The Lie group $SU(3)$ is the set of all (3×3) unitary matrices with a unity determinant whose generators are eight traceless Hermitian matrices of dimension 3, called Gell-Mann matrices. The unitary evolution of the two-atom follows $SU(3)$ symmetry where the Hamiltonian is a linear combination of the Gell-Mann matrices ($\vec{\Lambda}$),

$$\hat{H}_s = \vec{B}(t) \cdot \vec{\Lambda} \tag{B.4}$$

$$\text{where,} \quad B(t) = (\Omega/\sqrt{2}, 0, \Delta(t), 0, 0, \Omega/\sqrt{2}, 0, \sqrt{3}\Delta(t)), \tag{B.5}$$

and the 8 independent Gell-Mann matrices $\vec{\Lambda} = (\lambda_1, \cdots, \lambda_8)$ are

$$\lambda_1 = \begin{pmatrix} 0 & 1 & 0 \\ 1 & 0 & 0 \\ 0 & 0 & 0 \end{pmatrix}, \quad \lambda_2 = \begin{pmatrix} 0 & -i & 0 \\ i & 0 & 0 \\ 0 & 0 & 0 \end{pmatrix}, \quad \lambda_3 = \begin{pmatrix} 1 & 0 & 0 \\ 0 & -1 & 0 \\ 0 & 0 & 0 \end{pmatrix},$$

$$\lambda_4 = \begin{pmatrix} 0 & 0 & 1 \\ 0 & 0 & 0 \\ 1 & 0 & 0 \end{pmatrix}, \quad \lambda_5 = \begin{pmatrix} 0 & 0 & -i \\ 0 & 0 & 0 \\ i & 0 & 0 \end{pmatrix}, \quad \lambda_+ = \begin{pmatrix} 1 & 0 & 0 \\ 0 & 0 & 0 \\ 0 & 0 & -1 \end{pmatrix},$$

$$\lambda_6 = \begin{pmatrix} 0 & 0 & 0 \\ 0 & 0 & 1 \\ 0 & 1 & 0 \end{pmatrix}, \quad \lambda_7 = \begin{pmatrix} 0 & 0 & 0 \\ 0 & 0 & -i \\ 0 & i & 0 \end{pmatrix}, \quad \lambda_- = \begin{pmatrix} 0 & 0 & 0 \\ 0 & 1 & 0 \\ 0 & 0 & -1 \end{pmatrix},$$

$$\lambda_8 = \frac{1}{\sqrt{3}} \begin{pmatrix} 1 & 0 & 0 \\ 0 & 1 & 0 \\ 0 & 0 & -2 \end{pmatrix}, \tag{B.6}$$

alongwith $\lambda_\pm = (\sqrt{3}\lambda_8 \pm \lambda_3)/2$. This describes a three-level Hamiltonian where the diabatic energies form a triangular shape with their crossings. Furthermore, the

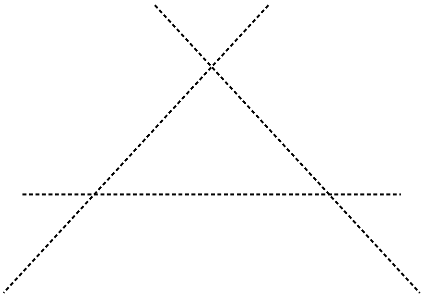

Figure B.1: Each crossing in the triangular shaped $SU(3)$ model can be considered as a combination of three crossings each having $SU(2)$ symmetry.

$SU(3)$ algebra which can be expressed in terms of 3 $SU(2)$ subalgebras

$$3 \times SU(2) = \begin{cases} \vec{s}_1 = & \frac{1}{2}(\lambda_1, \lambda_2, \lambda_3) \\ \vec{s}_2 = & \frac{1}{2}(\lambda_4, \lambda_5, \lambda_+) \\ \vec{s}_3 = & \frac{1}{2}(\lambda_6, \lambda_7, \lambda_-) \end{cases} \tag{B.7}$$

is representative of local $SU(2)$ symmetry at each crossing. Thus when each crossing is distinct, the evolution can be confined to the subspace(s) of two-level crossings where each crossing has a $SU(2)$ symmetry.

B.2.2 LZT matrix

The complete evolution matrix in AIA is given by $\hat{F}_L = \hat{U}_4 \hat{G}3_{LZ} \hat{U}_3 \hat{G}2_{LZ} \hat{U}_2 \hat{G}1_{LZ} \hat{U}_1$. As it is a 3×3 unitary matrix, it also represents a rotation in eight-dimensional hypersphere akin to three-dimensional rotational symmetry found in two-level systems [see Sec. B.1]. Any rotation in the $SU(3)$ group can be generated by a linear combination of the eight Gell-mann matrices λ_i. Hence, the rotation of 3-spinors is written as:

$$\hat{U} = \exp\Big(-i\hat{\lambda} \cdot \hat{\mathbf{n}}\theta\Big) \tag{B.8}$$

where $\hat{n}$ is a unit vector in the eight-dimensional hyperspace. Unlike the simplified expansion of the rotation matrix of $SU(2)$,

$$\exp(-i\hat{\sigma} \cdot \hat{\mathbf{n}}\theta) = \mathbb{1}\cos\theta - i\,(\hat{\sigma} \cdot \hat{\mathbf{n}})\sin\theta \tag{B.9}$$

where $\hat{\sigma}_\mathbf{i}$ are the 2×2 representation of Pauli matrices, the elementary form of an element of rotational matrix in $SU(3)$ is rather unapparent. Upon using Caley-Hamilton theorem [290], an algebraic form of the element can be written as

$$\exp(-iG\theta) = \sum_{k=0,1,2} \left(G^2 + \frac{2}{\sqrt{3}} G \sin(\phi_k) - \frac{\mathbb{1}}{3}\left(1 + 2\cos\left(2\phi_k\right)\right)\right) \frac{\exp\left(-\frac{2}{\sqrt{3}} i\theta \sin(\phi_k)\right)}{1 - 2\cos\left(2\phi_k\right)}, \tag{B.10}$$

where θ is the angular rotation normalized with $\mathrm{tr}(G^2) = 2$ with $\phi_k = \phi + 2\pi k/3$ and ϕ is an angle determined by

$$\phi = \frac{1}{3}\left(\arccos\left(\frac{3}{2}\sqrt{3}\det(G)\right) - \frac{\pi}{2}\right). \tag{B.11}$$

The matrix G is a generalized traceless Hermitian matrix,

$$G = \begin{pmatrix} a & c & d \\ c^* & b & e \\ d^* & e^* & -a-b \end{pmatrix} \tag{B.12}$$

obtained from the generators λ_i, where $\{a, b\} \in \mathbb{R}$ and $\{c, d, e\} \in \mathbb{C}$. The eight unknowns in the above matrix can be easily written in terms of n_i as $a = n_3 + n_8/\sqrt{3}, b = -n_3 + n_8/\sqrt{3}, c = n_1 - in_2, d = n_4 - in_5, e = n_6 - in_7$. To identify a unique rotation, we need to identify the values of the components n_i and angle θ. The most general rotation element in $SU(3)$ is obtained by substituting the matrix in Eq. (B.12) into Eq. (B.10),

$$\hat{U} = \sum_{k=0,1,2} e^{\frac{2i\theta \sin\phi_k}{\sqrt{3}}} \times$$
$$\begin{pmatrix} \frac{a^2+|c|^2+|d|^2-1-2\cos 2\phi_k+\frac{2a\sin\phi_k}{\sqrt{3}}}{1-2\cos 2\phi_k} & \frac{(a+b)c+de^*+\frac{2c\sin\phi_k}{\sqrt{3}}}{1-2\cos 2\phi_k} & \frac{-bd+ce+\frac{2d\sin\phi_k}{\sqrt{3}}}{1-2\cos 2\phi_k} \\ \frac{(a+b)c^*+d^*e+\frac{2c^*\sin\phi_k}{\sqrt{3}}}{1-2\cos 2\phi_k} & \frac{b^2+|c|^2+|e|^2-1-2\cos 2\phi_k+\frac{2b\sin\phi_k}{\sqrt{3}}}{1-2\cos 2\phi_k} & \frac{-ae+c^*d+\frac{2e\sin\phi_k}{\sqrt{3}}}{1-2\cos 2\phi_k} \\ \frac{-bd^*+c^*e^*+\frac{2d^*\sin\phi_k}{\sqrt{3}}}{1-2\cos 2\phi_k} & \frac{-ae^*+cd^*+\frac{2e^*\sin\phi_k}{\sqrt{3}}}{1-2\cos 2\phi_k} & \frac{(a+b)^2+|d|^2+|e|^2-1-2\cos 2\phi_k-\frac{2(a+b)\sin\phi_k}{\sqrt{3}}}{1-2\cos 2\phi_k} \end{pmatrix}. \tag{B.13}$$

The above matrix can be compared with the evolution matrix given by $\hat{F}_L$ to obtain the values of n_i and θ uniquely.

Bibliography

[1]M. H. Anderson, J. R. Ensher, M. R. Matthews, C. E. Wieman, and E. A. Cornell, "Observation of bose-einstein condensation in a dilute atomic vapor", Science **269**, 198–201 (1995).

[2]C. C. Bradley, C. A. Sackett, J. J. Tollett, and R. G. Hulet, "Evidence of bose-einstein condensation in an atomic gas with attractive interactions", Phys. Rev. Lett. **75**, 1687–1690 (1995).

[3]K. B. Davis, et al., "Bose-einstein condensation in a gas of sodium atoms", Phys. Rev. Lett. **75**, 3969–3973 (1995).

[4]J. Stenger, et al., "Spin domains in ground-state bose–einstein condensates", Nature **396**, 345–348 (1998).

[5]T.-L. Ho, "Spinor bose condensates in optical traps", Phys. Rev. Lett. **81**, 742–745 (1998).

[6]D. M. Stamper-Kurn, et al., "Optical confinement of a bose-einstein condensate", Phys. Rev. Lett. **80**, 2027–2030 (1998).

[7]P. Courteille, R. S. Freeland, D. J. Heinzen, F. A. van Abeelen, and B. J. Verhaar, "Observation of a feshbach resonance in cold atom scattering", Phys. Rev. Lett. **81**, 69–72 (1998).

[8]S. Inouye, et al., "Observation of feshbach resonances in a bose–einstein condensate", Nature **392**, 151–154 (1998).

[9]B. DeMarco, and D. S. Jin, "Onset of fermi degeneracy in a trapped atomic gas", Science **285**, 1703–1706 (1999).

[10]M. Greiner, C. A. Regal, and D. S. Jin, "Emergence of a molecular bose–einstein condensate from a fermi gas", Nature **426**, 537–540 (2003).

[11]S. Jochim, et al., "Bose-einstein condensation of molecules", Science **302**, 2101–2103 (2003).

[12]C. Chin, et al., "Observation of the pairing gap in a strongly interacting fermi gas", Science **305**, 1128–1130 (2004).

[13] M. W. Zwierlein, J. R. Abo-Shaeer, A. Schirotzek, C. H. Schunck, and W. Ketterle, “Vortices and superfluidity in a strongly interacting fermi gas”, Nature **435**, 1047–1051 (2005).

[14] A. Griesmaier, J. Werner, S. Hensler, J. Stuhler, and T. Pfau, “Bose-einstein condensation of chromium”, Phys. Rev. Lett. **94**, 160401 (2005).

[15] T. Lahaye, et al., “Strong dipolar effects in a quantum ferrofluid”, Nature **448**, 672–675 (2007).

[16] M. Lu, N. Q. Burdick, S. H. Youn, and B. L. Lev, “Strongly dipolar bose-einstein condensate of dysprosium”, Phys. Rev. Lett. **107**, 190401 (2011).

[17] K. Aikawa, et al., “Bose-einstein condensation of erbium”, Phys. Rev. Lett. **108**, 210401 (2012).

[18] I. Ferrier-Barbut, H. Kadau, M. Schmitt, M. Wenzel, and T. Pfau, “Observation of quantum droplets in a strongly dipolar bose gas”, Phys. Rev. Lett. **116**, 215301 (2016).

[19] M. Schmitt, M. Wenzel, F. Böttcher, I. Ferrier-Barbut, and T. Pfau, “Self-bound droplets of a dilute magnetic quantum liquid”, Nature **539**, 259–262 (2016).

[20] G. Natale, et al., “Excitation spectrum of a trapped dipolar supersolid and its experimental evidence”, Phys. Rev. Lett. **123**, 050402 (2019).

[21] L. Anderegg, et al., “An optical tweezer array of ultracold molecules”, Science **365**, 1156–1158 (2019).

[22] H. Weimer, M. Müller, I. Lesanovsky, P. Zoller, and H. P. Büchler, “A rydberg quantum simulator”, Nature Physics **6**, 382–388 (2010).

[23] M. Saffman, T. G. Walker, and K. Mølmer, “Quantum information with rydberg atoms”, Rev. Mod. Phys. **82**, 2313–2363 (2010).

[24] D. Jaksch, et al., “Fast quantum gates for neutral atoms”, Phys. Rev. Lett. **85**, 2208–2211 (2000).

[25] M. D. Lukin, et al., “Dipole blockade and quantum information processing in mesoscopic atomic ensembles”, Phys. Rev. Lett. **87**, 037901 (2001).

[26] L. Isenhower, et al., “Demonstration of a neutral atom controlled-not quantum gate”, Phys. Rev. Lett. **104**, 010503 (2010).

[27] T. Wilk, et al., “Entanglement of two individual neutral atoms using rydberg blockade”, Phys. Rev. Lett. **104**, 010502 (2010).

[28] A. Browaeys, and T. Lahaye, “Many-body physics with individually controlled rydberg atoms”, Nature Physics **16**, 132–142 (2020).

[29] N. Henkel, R. Nath, and T. Pohl, "Three-dimensional roton excitations and supersolid formation in rydberg-excited bose-einstein condensates", Phys. Rev. Lett. **104**, 195302 (2010).

[30] G. Pupillo, A. Micheli, M. Boninsegni, I. Lesanovsky, and P. Zoller, "Strongly correlated gases of rydberg-dressed atoms: quantum and classical dynamics", Phys. Rev. Lett. **104**, 223002 (2010).

[31] O. Firstenberg, C. S. Adams, and S. Hofferberth, "Nonlinear quantum optics mediated by rydberg interactions", Journal of Physics B: Atomic, Molecular and Optical Physics **49**, 152003 (2016).

[32] T. Peyronel, et al., "Quantum nonlinear optics with single photons enabled by strongly interacting atoms", Nature **488**, 57–60 (2012).

[33] R. Grimm, M. Weidemüller, and Y. B. Ovchinnikov, *Optical dipole traps for neutral atoms*, edited by B. Bederson, and H. Walther, Vol. 42, Advances In Atomic, Molecular, and Optical Physics (Academic Press, 2000), pp. 95–170.

[34] I. Bloch, J. Dalibard, and S. Nascimbène, "Quantum simulations with ultracold quantum gases", Nature Physics **8**, 267–276 (2012).

[35] C. Gross, and I. Bloch, "Quantum simulations with ultracold atoms in optical lattices", Science **357**, 995–1001 (2017).

[36] F. Nogrette, et al., "Single-atom trapping in holographic 2d arrays of microtraps with arbitrary geometries", Phys. Rev. X **4**, 021034 (2014).

[37] H. Kim, et al., "In situ single-atom array synthesis using dynamic holographic optical tweezers", Nature Communications **7**, 13317 (2016).

[38] M. Endres, et al., "Atom-by-atom assembly of defect-free one-dimensional cold atom arrays", Science **354**, 1024–1027 (2016).

[39] D. Barredo, S. de Léséleuc, V. Lienhard, T. Lahaye, and A. Browaeys, "An atom-by-atom assembler of defect-free arbitrary two-dimensional atomic arrays", Science **354**, 1021–1023 (2016).

[40] D. Jaksch, and P. Zoller, "The cold atom hubbard toolbox", Annals of Physics **315**, Special Issue, 52–79 (2005).

[41] D. Jaksch, C. Bruder, J. I. Cirac, C. W. Gardiner, and P. Zoller, "Cold bosonic atoms in optical lattices", Phys. Rev. Lett. **81**, 3108–3111 (1998).

[42] M. Greiner, O. Mandel, T. Esslinger, T. W. Hänsch, and I. Bloch, "Quantum phase transition from a superfluid to a mott insulator in a gas of ultracold atoms", Nature **415**, 39–44 (2002).

[43] M. Köhl, H. Moritz, T. Stöferle, K. Günter, and T. Esslinger, "Fermionic atoms in a three dimensional optical lattice: observing fermi surfaces, dynamics, and interactions", Phys. Rev. Lett. **94**, 080403 (2005).

[44] K. Günter, T. Stöferle, H. Moritz, M. Köhl, and T. Esslinger, "Bose-fermi mixtures in a three-dimensional optical lattice", Phys. Rev. Lett. **96**, 180402 (2006).

[45] E. G. Dalla Torre, E. Berg, and E. Altman, "Hidden order in 1d bose insulators", Phys. Rev. Lett. **97**, 260401 (2006).

[46] D. M. Weld, and W. Ketterle, "Towards quantum magnetism with ultracold atoms", Journal of Physics: Conference Series **264**, 012017 (2011).

[47] C. Becker, et al., "Ultracold quantum gases in triangular optical lattices", New Journal of Physics **12**, 065025 (2010).

[48] G.-B. Jo, et al., "Ultracold atoms in a tunable optical kagome lattice", Phys. Rev. Lett. **108**, 045305 (2012).

[49] L. Balents, "Spin liquids in frustrated magnets", Nature **464**, 199–208 (2010).

[50] H. Labuhn, et al., "Tunable two-dimensional arrays of single rydberg atoms for realizing quantum ising models", Nature **534**, 667–670 (2016).

[51] H. Ott, "Single atom detection in ultracold quantum gases: a review of current progress", Reports on Progress in Physics **79**, 054401 (2016).

[52] P. Schauß, et al., "Observation of spatially ordered structures in a two-dimensional rydberg gas", Nature **491**, 87–91 (2012).

[53] A. W. Glaetzle, et al., "Designing frustrated quantum magnets with laser-dressed rydberg atoms", Phys. Rev. Lett. **114**, 173002 (2015).

[54] R. Samajdar, W. W. Ho, H. Pichler, M. D. Lukin, and S. Sachdev, "Quantum phases of rydberg atoms on a kagome lattice", Proceedings of the National Academy of Sciences **118** (2021).

[55] M. Schreiber, et al., "Observation of many-body localization of interacting fermions in a quasirandom optical lattice", Science **349**, 842–845 (2015).

[56] A. Lukin, et al., "Probing entanglement in a many-body–localized system", Science **364**, 256–260 (2019).

[57] M. Marcuzzi, et al., "Facilitation dynamics and localization phenomena in rydberg lattice gases with position disorder", Phys. Rev. Lett. **118**, 063606 (2017).

[58] E. Zohar, J. I. Cirac, and B. Reznik, "Quantum simulations of lattice gauge theories using ultracold atoms in optical lattices", Reports on Progress in Physics **79**, 014401 (2015).

[59] F. M. Surace, et al., "Lattice gauge theories and string dynamics in rydberg atom quantum simulators", Phys. Rev. X **10**, 021041 (2020).

[60] M. J. Martin, et al., "A quantum many-body spin system in an optical lattice clock", Science **341**, 632–636 (2013).

[61] A. Goban, et al., "Emergence of multi-body interactions in a fermionic lattice clock", Nature **563**, 369–373 (2018).

[62] I. S. Madjarov, et al., "An atomic-array optical clock with single-atom readout", Phys. Rev. X **9**, 041052 (2019).

[63] W. S. Bakr, J. I. Gillen, A. Peng, S. Fölling, and M. Greiner, "A quantum gas microscope for detecting single atoms in a hubbard-regime optical lattice", Nature **462**, 74–77 (2009).

[64] J. F. Sherson, et al., "Single-atom-resolved fluorescence imaging of an atomic mott insulator", Nature **467**, 68–72 (2010).

[65] D. Greif, et al., "Site-resolved imaging of a fermionic mott insulator", Science **351**, 953–957 (2016).

[66] L. W. Cheuk, et al., "Observation of spatial charge and spin correlations in the 2d fermi-hubbard model", Science **353**, 1260–1264 (2016).

[67] F. Schäfer, T. Fukuhara, S. Sugawa, Y. Takasu, and Y. Takahashi, "Tools for quantum simulation with ultracold atoms in optical lattices", Nature Reviews Physics **2**, 411–425 (2020).

[68] S. Ebadi, et al., "Quantum phases of matter on a 256-atom programmable quantum simulator", Nature **595**, 227–232 (2021).

[69] P. Scholl, et al., "Quantum simulation of 2d antiferromagnets with hundreds of rydberg atoms", Nature **595**, 233–238 (2021).

[70] D. Bluvstein, et al., "Controlling quantum many-body dynamics in driven rydberg atom arrays", Science **371**, 1355–1359 (2021).

[71] H. Bernien, et al., "Probing many-body dynamics on a 51-atom quantum simulator", Nature **551**, 579–584 (2017).

[72] M. Serbyn, D. A. Abanin, and Z. Papić, "Quantum many-body scars and weak breaking of ergodicity", Nature Physics **17**, 675–685 (2021).

[73] M. Marcuzzi, et al., "Facilitation dynamics and localization phenomena in rydberg lattice gases with position disorder", Phys. Rev. Lett. **118**, 063606 (2017).

[74] P. Xu, et al., "Interaction-induced decay of a heteronuclear two-atom system", Nature communications **6**, 7803–7803 (2015).

[75]M. Lemeshko, "Manipulating scattering of ultracold atoms with light-induced dissipation", Frontiers in Physics **1**, 17 (2013).

[76]L. Béguin, A. Vernier, R. Chicireanu, T. Lahaye, and A. Browaeys, "Direct measurement of the van der waals interaction between two rydberg atoms", Phys. Rev. Lett. **110**, 263201 (2013).

[77]I. I. Ryabtsev, D. B. Tretyakov, I. I. Beterov, and V. M. Entin, "Observation of the stark-tuned förster resonance between two rydberg atoms", Phys. Rev. Lett. **104**, 073003 (2010).

[78]S. Ravets, H. Labuhn, D. Barredo, T. Lahaye, and A. Browaeys, "Measurement of the angular dependence of the dipole-dipole interaction between two individual rydberg atoms at a förster resonance", Phys. Rev. A **92**, 020701 (2015).

[79]S. de Léséleuc, D. Barredo, V. Lienhard, A. Browaeys, and T. Lahaye, "Optical control of the resonant dipole-dipole interaction between rydberg atoms", Phys. Rev. Lett. **119**, 053202 (2017).

[80]C. J. Picken, R. Legaie, K. McDonnell, and J. D. Pritchard, "Entanglement of neutral-atom qubits with long ground-rydberg coherence times", Quantum Science and Technology **4**, 015011 (2018).

[81]H. Levine, et al., "High-fidelity control and entanglement of rydberg-atom qubits", Phys. Rev. Lett. **121**, 123603 (2018).

[82]Y.-Y. Jau, A. M. Hankin, T. Keating, I. H. Deutsch, and G. W. Biedermann, "Entangling atomic spins with a rydberg-dressed spin-flip blockade", Nature Physics **12**, 71–74 (2016).

[83]J.-L. Wu, et al., "Resilient quantum gates on periodically driven rydberg atoms", Phys. Rev. A **103**, 012601 (2021).

[84]H. Labuhn, et al., "Single-atom addressing in microtraps for quantum-state engineering using rydberg atoms", Phys. Rev. A **90**, 023415 (2014).

[85]X.-P. Du, Q. Cao, N. Dang, and L. Tan, "Quantum router modulated by two rydberg atoms in a x-shaped coupled cavity array", The European Physical Journal D **75**, 79 (2021).

[86]V. Srivastava, A. Niranjan, and R. Nath, "Dynamics and quantum correlations in two independently driven rydberg atoms with distinct laser fields", J. Phys. B: At. Mol. Opt. Phys. **52**, 184001 (2019).

[87]A. Niranjan, W. Li, and R. Nath, "Landau-zener transitions and adiabatic impulse approximation in an array of two rydberg atoms with time-dependent detuning", Phys. Rev. A **101**, 063415 (2020).

[88] S. K. Mallavarapu, A. Niranjan, W. Li, S. Wüster, and R. Nath, "Population trapping in a pair of periodically driven rydberg atoms", Phys. Rev. A **103**, 023335 (2021).

[89] E. Altman, et al., "Quantum simulators: architectures and opportunities", PRX Quantum **2**, 017003 (2021).

[90] J. W. Britton, et al., "Engineered two-dimensional ising interactions in a trapped-ion quantum simulator with hundreds of spins", Nature **484**, 489–492 (2012).

[91] H.-S. Zhong, et al., "Quantum computational advantage using photons", Science **370**, 1460–1463 (2020).

[92] D. E. Chang, V. Vuletić, and M. D. Lukin, "Quantum nonlinear optics — photon by photon", Nature Photonics **8**, 685–694 (2014).

[93] M. J. Hartmann, "Quantum simulation with interacting photons", Journal of Optics **18**, 104005 (2016).

[94] C. Noh, and D. G. Angelakis, "Quantum simulations and many-body physics with light", Reports on Progress in Physics **80**, 016401 (2016).

[95] M. H. Devoret, and R. J. Schoelkopf, "Superconducting circuits for quantum information: an outlook", Science **339**, 1169–1174 (2013).

[96] R. Hanson, L. P. Kouwenhoven, J. R. Petta, S. Tarucha, and L. M. K. Vandersypen, "Spins in few-electron quantum dots", Rev. Mod. Phys. **79**, 1217–1265 (2007).

[97] A. A. Houck, H. E. Türeci, and J. Koch, "On-chip quantum simulation with superconducting circuits", Nature Physics **8**, 292–299 (2012).

[98] M. V. G. Dutt, et al., "Quantum register based on individual electronic and nuclear spin qubits in diamond", Science **316**, 1312–1316 (2007).

[99] J. A. Jones, "Quantum computing and nuclear magnetic resonance", PhysChemComm **4**, 49–56 (2001).

[100] T. F. Gallagher, *Rydberg atoms*, Cambridge Monographs on Atomic, Molecular and Chemical Physics (Cambridge University Press, 1994).

[101] D. P. Fahey, and M. W. Noel, "Excitation of rydberg states in rubidium with near infrared diode lasers", Opt. Express **19**, 17002–17012 (2011).

[102] R. Löw, et al., "An experimental and theoretical guide to strongly interacting rydberg gases", Journal of Physics B: Atomic, Molecular and Optical Physics **45**, 113001 (2012).

[103] W. R. Anderson, J. R. Veale, and T. F. Gallagher, "Resonant dipole-dipole energy transfer in a nearly frozen rydberg gas", Phys. Rev. Lett. **80**, 249–252 (1998).

[104] I. Mourachko, et al., "Many-body effects in a frozen rydberg gas", Phys. Rev. Lett. **80**, 253–256 (1998).

[105] Y. Miroshnychenko, et al., "Coherent excitation of a single atom to a rydberg state", Phys. Rev. A **82**, 013405 (2010).

[106] M. Marinescu, H. R. Sadeghpour, and A. Dalgarno, "Dispersion coefficients for alkali-metal dimers", Phys. Rev. A **49**, 982–988 (1994).

[107] N. Šibalić, J. Pritchard, C. Adams, and K. Weatherill, "Arc: an open-source library for calculating properties of alkali rydberg atoms", Computer Physics Communications **220**, 319–331 (2017).

[108] J. Pritchard, *Cooperative optical non-linearity in a blockaded rydberg ensemble*, Springer Theses (Springer Berlin Heidelberg, 2012).

[109] D. Comparat, and P. Pillet, "Dipole blockade in a cold rydberg atomic sample", J. Opt. Soc. Am. B **27**, A208–A232 (2010).

[110] E. Urban, et al., "Observation of rydberg blockade between two atoms", Nature Physics **5**, 110–114 (2009).

[111] A. Gaëtan, et al., "Observation of collective excitation of two individual atoms in the rydberg blockade regime", Nature Physics **5**, 115–118 (2009).

[112] D. Tong, et al., "Local blockade of rydberg excitation in an ultracold gas", Phys. Rev. Lett. **93**, 063001 (2004).

[113] K. M. Birnbaum, et al., "Photon blockade in an optical cavity with one trapped atom", Nature **436**, 87–90 (2005).

[114] T. A. Fulton, and G. J. Dolan, "Observation of single-electron charging effects in small tunnel junctions", Phys. Rev. Lett. **59**, 109–112 (1987).

[115] Y. O. Dudin, L. Li, F. Bariani, and A. Kuzmich, "Observation of coherent many-body rabi oscillations", Nature Physics **8**, 790–794 (2012).

[116] A. S. Sørensen, C. H. van der Wal, L. I. Childress, and M. D. Lukin, "Capacitive coupling of atomic systems to mesoscopic conductors", Phys. Rev. Lett. **92**, 063601 (2004).

[117] D. Petrosyan, and M. Fleischhauer, "Quantum information processing with single photons and atomic ensembles in microwave coplanar waveguide resonators", Phys. Rev. Lett. **100**, 170501 (2008).

[118] L. H. Pedersen, and K. Mølmer, "Few qubit atom-light interfaces with collective encoding", Phys. Rev. A **79**, 012320 (2009).

[119] M. Müller, I. Lesanovsky, H. Weimer, H. P. Büchler, and P. Zoller, "Mesoscopic rydberg gate based on electromagnetically induced transparency", Phys. Rev. Lett. **102**, 170502 (2009).

[120] M. Saffman, and T. G. Walker, “Creating single-atom and single-photon sources from entangled atomic ensembles”, Phys. Rev. A **66**, 065403 (2002).

[121] I. Bouchoule, and K. Mølmer, “Spin squeezing of atoms by the dipole interaction in virtually excited rydberg states”, Phys. Rev. A **65**, 041803 (2002).

[122] E. Brion, K. Mølmer, and M. Saffman, “Quantum computing with collective ensembles of multilevel systems”, Phys. Rev. Lett. **99**, 260501 (2007).

[123] M. Saffman, and K. Mølmer, “Scaling the neutral-atom rydberg gate quantum computer by collective encoding in holmium atoms”, Phys. Rev. A **78**, 012336 (2008).

[124] T. Langen, R. Geiger, M. Kuhnert, B. Rauer, and J. Schmiedmayer, “Local emergence of thermal correlations in an isolated quantum many-body system”, Nature Physics **9**, 640–643 (2013).

[125] A. M. Kaufman, et al., “Quantum thermalization through entanglement in an isolated many-body system”, Science **353**, 794–800 (2016).

[126] R. Islam, et al., “Measuring entanglement entropy in a quantum many-body system”, Nature **528**, 77–83 (2015).

[127] A. Elben, B. Vermersch, M. Dalmonte, J. I. Cirac, and P. Zoller, “Rényi entropies from random quenches in atomic hubbard and spin models”, Phys. Rev. Lett. **120**, 050406 (2018).

[128] K. Wang, et al., “Simulating dynamic quantum phase transitions in photonic quantum walks”, Phys. Rev. Lett. **122**, 020501 (2019).

[129] A. Keesling, et al., “Quantum kibble–zurek mechanism and critical dynamics on a programmable rydberg simulator”, Nature **568**, 207–211 (2019).

[130] B. P. Lanyon, et al., “Efficient tomography of a quantum many-body system”, Nature Physics **13**, 1158–1162 (2017).

[131] J. Dziarmaga, “Dynamics of a quantum phase transition: exact solution of the quantum ising model”, Phys. Rev. Lett. **95**, 245701 (2005).

[132] J.-M. Cui, et al., “Experimental trapped-ion quantum simulation of the kibble-zurek dynamics in momentum space”, Scientific Reports **6**, 33381 (2016).

[133] L. W. Clark, L. Feng, and C. Chin, “Universal space-time scaling symmetry in the dynamics of bosons across a quantum phase transition”, Science **354**, 606–610 (2016).

[134] C.-J. Lin, V. Calvera, and T. H. Hsieh, “Quantum many-body scar states in two-dimensional rydberg atom arrays”, Phys. Rev. B **101**, 220304 (2020).

[135] E. Pachniak, and S. A. Malinovskaya, “Creation of quantum entangled states of rydberg atoms via chirped adiabatic passage”, Scientific Reports **11**, 12980 (2021).

[136] T. Pohl, E. Demler, and M. D. Lukin, “Dynamical crystallization in the dipole blockade of ultracold atoms”, Phys. Rev. Lett. **104**, 043002 (2010).

[137] S. Basak, Y. Chougale, and R. Nath, “Periodically driven array of single rydberg atoms”, Phys. Rev. Lett. **120**, 123204 (2018).

[138] X.-R. Huang, et al., “Robust rydberg gate via landau-zener control of förster resonance”, Phys. Rev. A **98**, 052324 (2018).

[139] D.-D. Ma, K.-Y. Zhang, and J. Qian, “Properties of collective rabi oscillations with two rydberg atoms”, Chinese Physics B **28**, 013202 (2019).

[140] X.-Y. Xu, et al., “Quantum simulation of landau-zener model dynamics supporting the kibble-zurek mechanism”, Phys. Rev. Lett. **112**, 035701 (2014).

[141] L. D. Landau, Phys. Z. Sowjetunion **2**, 46 (1932).

[142] C. Zener, Proc. R. Soc. Lond. A **137**, 696 (1932).

[143] E. Majorana, “Atomi orientati in campo magnetico variabile”, Il Nuovo Cimento (1924-1942) **9**, 43–50 (1932).

[144] E. K. G. Stückelberg, “Theorie der unelastischen stösse zwischen atomen”, (1933).

[145] S. Ashhab, J. R. Johansson, A. M. Zagoskin, and F. Nori, “Two-level systems driven by large-amplitude fields”, Phys. Rev. A **75**, 063414 (2007).

[146] B. M. Garraway, and N. V. Vitanov, “Population dynamics and phase effects in periodic level crossings”, Phys. Rev. A **55**, 4418–4432 (1997).

[147] N. V. Vitanov, “Transition times in the landau-zener model”, Phys. Rev. A **59**, 988–994 (1999).

[148] J. R. Rubbmark, M. M. Kash, M. G. Littman, and D. Kleppner, “Dynamical effects at avoided level crossings: a study of the landau-zener effect using rydberg atoms”, Phys. Rev. A **23**, 3107–3117 (1981).

[149] H. Maeda, J. H. Gurian, and T. F. Gallagher, “Population transfer by multiphoton adiabatic rapid passage”, Phys. Rev. A **83**, 033416 (2011).

[150] C. W. S. Conover, M. C. Doogue, and F. J. Struwe, “Chirped-pulse multiphoton transitions between rydberg states”, Phys. Rev. A **65**, 033414 (2002).

[151] J. Lambert, M. W. Noel, and T. F. Gallagher, “Rydberg-atom population transfer by population trapping in a chirped microwave pulse”, Phys. Rev. A **66**, 053413 (2002).

[152] A. Gürtler, and W. J. van der Zande, " L-state selective field ionization of rubidium rydberg states", Phys. Lett. A **324**, 315–320 (2004).

[153] S. S. Zhang, W. Gao, H. Cheng, L. You, and H. P. Liu, "Symmetry-breaking assisted landau-zener transitions in rydberg atoms", Phys. Rev. Lett. **120**, 063203 (2018).

[154] R. Feynman, et al., "Quantum interference in the field ionization of rydberg atoms", Phys. Rev. A **92**, 043412 (2015).

[155] N. Saquet, et al., "Landau-zener transitions in frozen pairs of rydberg atoms", Phys. Rev. Lett. **104**, 133003 (2010).

[156] M. A. Lieberman, and A. J. Lichtenberg, "Stochastic and adiabatic behavior of particles accelerated by periodic forces", Phys. Rev. A **5**, 1852–1866 (1972).

[157] B. V. Chirikov, F. Izrailev, and D. Shepelyansky, "Dynamical stochasticity in classical and quantum mechanics", Sov. Scient. Rev. C **2**, 209–267 (1981).

[158] S. Fishman, D. R. Grempel, and R. E. Prange, "Chaos, quantum recurrences, and anderson localization", Phys. Rev. Lett. **49**, 509–512 (1982).

[159] G. S. Agarwal, and W. Harshawardhan, "Realization of trapping in a two-level system with frequency-modulated fields", Phys. Rev. A **50**, R4465–R4467 (1994).

[160] M. W. Noel, W. M. Griffith, and T. F. Gallagher, "Frequency-modulated excitation of a two-level atom", Phys. Rev. A **58**, 2265–2273 (1998).

[161] F. Grossmann, T. Dittrich, P. Jung, and P. Hänggi, "Coherent destruction of tunneling", Phys. Rev. Lett. **67**, 516–519 (1991).

[162] M. Grifoni, and P. Hänggi, "Driven quantum tunneling", Physics Reports **304**, 229–354 (1998).

[163] E. Kierig, U. Schnorrberger, A. Schietinger, J. Tomkovic, and M. K. Oberthaler, "Single-particle tunneling in strongly driven double-well potentials", Phys. Rev. Lett. **100**, 190405 (2008).

[164] S. Raghavan, V. M. Kenkre, D. H. Dunlap, A. R. Bishop, and M. I. Salkola, "Relation between dynamic localization in crystals and trapping in two-level atoms", Phys. Rev. A **54**, R1781–R1784 (1996).

[165] D. H. Dunlap, and V. M. Kenkre, "Dynamic localization of a charged particle moving under the influence of an electric field", Phys. Rev. B **34**, 3625–3633 (1986).

[166] H. Lignier, et al., "Dynamical control of matter-wave tunneling in periodic potentials", Phys. Rev. Lett. **99**, 220403 (2007).

[167] A. Eckardt, T. Jinasundera, C. Weiss, and M. Holthaus, “Analog of photon-assisted tunneling in a bose-einstein condensate”, Phys. Rev. Lett. **95**, 200401 (2005).

[168] A. Zenesini, H. Lignier, D. Ciampini, O. Morsch, and E. Arimondo, “Coherent control of dressed matter waves”, Phys. Rev. Lett. **102**, 100403 (2009).

[169] C. E. Creffield, F. Sols, D. Ciampini, O. Morsch, and E. Arimondo, “Expansion of matter waves in static and driven periodic potentials”, Phys. Rev. A **82**, 035601 (2010).

[170] J. Gong, L. Morales-Molina, and P. Hänggi, “Many-body coherent destruction of tunneling”, Phys. Rev. Lett. **103**, 133002 (2009).

[171] C. Chen, J.-H. An, H.-G. Luo, C. P. Sun, and C. H. Oh, “Floquet control of quantum dissipation in spin chains”, Phys. Rev. A **91**, 052122 (2015).

[172] R. Horodecki, P. Horodecki, M. Horodecki, and K. Horodecki, “Quantum entanglement”, Rev. Mod. Phys. **81**, 865–942 (2009).

[173] J. Eisert, M. Cramer, and M. B. Plenio, “Colloquium: area laws for the entanglement entropy”, Rev. Mod. Phys. **82**, 277–306 (2010).

[174] K. Modi, A. Brodutch, H. Cable, T. Paterek, and V. Vedral, “The classical-quantum boundary for correlations: discord and related measures”, Rev. Mod. Phys. **84**, 1655–1707 (2012).

[175] L. Amico, R. Fazio, A. Osterloh, and V. Vedral, “Entanglement in many-body systems”, Rev. Mod. Phys. **80**, 517–576 (2008).

[176] R. Dillenschneider, “Quantum discord and quantum phase transition in spin chains”, Phys. Rev. B **78**, 224413 (2008).

[177] J. I. Latorre, and A. Riera, “A short review on entanglement in quantum spin systems”, Journal of Physics A: Mathematical and Theoretical **42**, 504002 (2009).

[178] Y.-A. Chen, S. D. Huber, S. Trotzky, I. Bloch, and E. Altman, “Many-body landau–zener dynamics in coupled one-dimensional bose liquids”, Nat. Phys. **7**, (2010).

[179] C. Wang, Y.-Y. Zhang, and Q.-H. Chen, “Quantum correlations in collective spin systems”, Phys. Rev. A **85**, 052112 (2012).

[180] A. Bera, et al., “Quantum discord and its allies: a review of recent progress”, Reports on Progress in Physics **81**, 024001 (2017).

[181] M. Levin, and X.-G. Wen, “Detecting topological order in a ground state wave function”, Phys. Rev. Lett. **96**, 110405 (2006).

[182] A. Kitaev, and J. Preskill, “Topological entanglement entropy”, Phys. Rev. Lett. **96**, 110404 (2006).

[183] H.-C. Jiang, Z. Wang, and L. Balents, “Identifying topological order by entanglement entropy”, Nature Physics **8**, 902–905 (2012).

[184] S. V. Isakov, M. B. Hastings, and R. G. Melko, “Topological entanglement entropy of a bose–hubbard spin liquid”, Nature Physics **7**, 772–775 (2011).

[185] Y. Zhang, T. Grover, and A. Vishwanath, “Entanglement entropy of critical spin liquids”, Phys. Rev. Lett. **107**, 067202 (2011).

[186] A. K. Rajagopal, and R. W. Rendell, “Decoherence, correlation, and entanglement in a pair of coupled quantum dissipative oscillators”, Phys. Rev. A **63**, 022116 (2001).

[187] M. F. Santos, P. Milman, L. Davidovich, and N. Zagury, “Direct measurement of finite-time disentanglement induced by a reservoir”, Phys. Rev. A **73**, 040305 (2006).

[188] T. Yu, and J. H. Eberly, “Finite-time disentanglement via spontaneous emission”, Phys. Rev. Lett. **93**, 140404 (2004).

[189] T. Yu, and J. Eberly, “Sudden death of entanglement: classical noise effects”, Optics Communications **264**, 393–397 (2006).

[190] C. H. Bennett, D. P. DiVincenzo, J. A. Smolin, and W. K. Wootters, “Mixed-state entanglement and quantum error correction”, Phys. Rev. A **54**, 3824–3851 (1996).

[191] C. H. Bennett, H. J. Bernstein, S. Popescu, and B. Schumacher, “Concentrating partial entanglement by local operations”, Phys. Rev. A **53**, 2046–2052 (1996).

[192] L. Henderson, and V. Vedral, “Classical, quantum and total correlations”, Journal of Physics A: Mathematical and General **34**, 6899–6905 (2001).

[193] H. Ollivier, and W. H. Zurek, “Quantum discord: a measure of the quantumness of correlations”, Phys. Rev. Lett. **88**, 017901 (2001).

[194] A. Datta, A. Shaji, and C. M. Caves, “Quantum discord and the power of one qubit”, Phys. Rev. Lett. **100**, 050502 (2008).

[195] B. P. Lanyon, M. Barbieri, M. P. Almeida, and A. G. White, “Experimental quantum computing without entanglement”, Phys. Rev. Lett. **101**, 200501 (2008).

[196] M. Okrasa, and Z. Walczak, “Quantum discord and multipartite correlations”, EPL (Europhysics Letters) **96**, 60003 (2011).

[197] G. Adesso, and A. Datta, “Quantum versus classical correlations in gaussian states”, Phys. Rev. Lett. **105**, 030501 (2010).

[198] V. Vedral, M. B. Plenio, M. A. Rippin, and P. L. Knight, “Quantifying entanglement”, Phys. Rev. Lett. **78**, 2275–2279 (1997).

[199] V. Vedral, and M. B. Plenio, “Entanglement measures and purification procedures”, Phys. Rev. A **57**, 1619–1633 (1998).

[200] S. Kuhr, “Quantum-gas microscopes: a new tool for cold-atom quantum simulators”, National Science Review **3**, 170–172 (2016).

[201] Y. Zeng, et al., “Entangling two individual atoms of different isotopes via rydberg blockade”, Phys. Rev. Lett. **119**, 160502 (2017).

[202] S. de Léséleuc, D. Barredo, V. Lienhard, A. Browaeys, and T. Lahaye, “Analysis of imperfections in the coherent optical excitation of single atoms to rydberg states”, Phys. Rev. A **97**, 053803 (2018).

[203] K. M. Maller, et al., “Rydberg-blockade controlled-not gate and entanglement in a two-dimensional array of neutral-atom qubits”, Phys. Rev. A **92**, 022336 (2015).

[204] A. Browaeys, D. Barredo, and T. Lahaye, “Experimental investigations of dipole–dipole interactions between a few rydberg atoms”, Journal of Physics B: Atomic, Molecular and Optical Physics **49**, 152001 (2016).

[205] C. Ates, T. Pohl, T. Pattard, and J. M. Rost, “Antiblockade in rydberg excitation of an ultracold lattice gas”, Phys. Rev. Lett. **98**, 023002 (2007).

[206] M. Bukov, L. D’Alessio, and A. Polkovnikov, “Universal high-frequency behavior of periodically driven systems: from dynamical stabilization to floquet engineering”, Ad. Phy. **64**, 139–226 (2015).

[207] M. Bukov, M. Kolodrubetz, and A. Polkovnikov, “Schrieffer-wolff transformation for periodically driven systems: strongly correlated systems with artificial gauge fields”, Phys. Rev. Lett. **116**, 125301 (2016).

[208] L. D’Alessio, and M. Rigol, “Long-time behavior of isolated periodically driven interacting lattice systems”, Phys. Rev. X **4**, 041048 (2014).

[209] Y. Chougale, and R. Nath, “Ab initio calculation of hubbard parameters for rydberg-dressed atoms in a one-dimensional optical lattice”, Journal of Physics B: Atomic, Molecular and Optical Physics **49**, 144005 (2016).

[210] C.-H. Fan, D. Yan, Y.-M. Liu, and J.-H. Wu, “Coopetition and manipulation of quantum correlations in rydberg atoms”, Journal of Physics B: Atomic, Molecular and Optical Physics **50**, 115501 (2017).

[211] D. Manzano, “A short introduction to the lindblad master equation”, AIP Advances **10**, 025106 (2020).

[212] V. R. Krithika, S. Pal, R. Nath, and T. S. Mahesh, "Observation of interaction induced blockade and local spin freezing in a nmr quantum simulator", Phys. Rev. Research **3**, 033035 (2021).

[213] D. Burgarth, et al., "Scalable quantum computation via local control of only two qubits", Phys. Rev. A **81**, 040303 (2010).

[214] S. N. Shevchenko, S. Ashhab, and F. Nori, "Landau–zener–stückelberg interferometry", Phys. Rep. **492**, 1–30 (2010).

[215] C. E. Carroll, and F. T. Hioe, "Transition probabilities for the three-level landau-zener model", **19**, 2061–2073 (1986).

[216] Y. N. Demkov, and V. N. Ostrovsky, "Multipath interference in a multistate landau-zener-type model", Phys. Rev. A **61**, 032705 (2000).

[217] V. S. Malinovsky, and J. L. Krause, "General theory of population transfer by adiabatic rapid passage with intense, chirped laser pulses", Eur. Phys. J. D **14**, 147–155 (2001).

[218] M. Førre, and J. P. Hansen, "Selective-field-ionization dynamics of a lithium $m = 2$ rydberg state: landau-zener model versus quantal approach", Phys. Rev. A **67**, 053402 (2003).

[219] A. V. Shytov, "Landau-zener transitions in a multilevel system: an exact result", Phys. Rev. A **70**, 052708 (2004).

[220] Y. B. Band, and Y. Avishai, "Three-level landau-zener dynamics", Phys. Rev. A **99**, 032112 (2019).

[221] M. B. Kenmoe, and L. C. Fai, "Periodically driven three-level systems", Phys. Rev. B **94**, 125101 (2016).

[222] M. N. Kiselev, K. Kikoin, and M. B. Kenmoe, "Su(3) landau-zener interferometry", Eur. Phys. Lett. **104**, 57004 (2013).

[223] S. Ashhab, "Landau-zener transitions in an open multilevel quantum system", Phys. Rev. A **94**, 042109 (2016).

[224] N. A. Sinitsyn, "Exact transition probabilities in a 6-state landau–zener system with path interference", J. Phys. A: Math. The. **48**, 195305 (2015).

[225] N. A. Sinitsyn, and F. Li, "Solvable multistate model of landau-zener transitions in cavity qed", Phys. Rev. A **93**, 063859 (2016).

[226] N. A. Sinitsyn, and V. Y. Chernyak, "The quest for solvable multistate landau-zener models", **50**, 255203 (2017).

[227] F. Li, C. Sun, V. Y. Chernyak, and N. A. Sinitsyn, "Multistate landau-zener models with all levels crossing at one point", Phys. Rev. A **96**, 022107 (2017).

[228] N. A. Sinitsyn, J. Lin, and V. Y. Chernyak, "Constraints on scattering amplitudes in multistate landau-zener theory", Phys. Rev. A **95**, 012140 (2017).

[229] A. V. Parafilo, and M. N. Kiselev, "Landau–zener transitions and rabi oscillations in a cooper-pair box: beyond two-level models", L. Temp. Phys. **44**, 1325–1330 (2018).

[230] B. Militello, "Detuning-induced robustness of a three-state landau-zener model against dissipation", Phys. Rev. A **99**, 063412 (2019).

[231] Q. Niu, X.-G. Zhao, G. A. Georgakis, and M. G. Raizen, "Atomic landau-zener tunneling and wannier-stark ladders in optical potentials", Phys. Rev. Lett. **76**, 4504–4507 (1996).

[232] B. Wu, and Q. Niu, "Nonlinear landau-zener tunneling", Phys. Rev. A **61**, 023402 (2000).

[233] J.-Y. Yan, S. Duan, W. Zhang, and X.-G. Zhao, "Observation of landau-zener tunneling through atomic current in the optical lattices", Phys. Rev. A **79**, 053613 (2009).

[234] T. Salger, C. Geckeler, S. Kling, and M. Weitz, "Atomic landau-zener tunneling in fourier-synthesized optical lattices", Phys. Rev. Lett. **99**, 190405 (2007).

[235] C. Kasztelan, et al., "Landau-zener sweeps and sudden quenches in coupled bose-hubbard chains", Phys. Rev. Lett. **106**, 155302 (2011).

[236] S. F. Caballero-Benıétez, and R. Paredes, "Phase diagram of landau-zener phenomena in coupled one-dimensional bose quantum fluids", Phys. Rev. A **85**, 023605 (2012).

[237] J. Larson, "Interaction-induced landau-zener transitions", Eur. Phys. Lett. **107**, 30007 (2014).

[238] H. Zhong, et al., "Photon-induced sideband transitions in a many-body landau-zener process", Phys. Rev. A **90**, 023635 (2014).

[239] K. Saito, and Y. Kayanuma, "Nonadiabatic electron manipulation in quantum dot arrays", Phys. Rev. B **70**, 201304 (2004).

[240] L. Gaudreau, et al., "Coherent control of three-spin states in a triple quantum dot", Nature Physics **8**, 54–58 (2012).

[241] G. Cao, et al., "Ultrafast universal quantum control of a quantum-dot charge qubit using landau–zener–stückelberg interference", Nat. Commun. **4**, (2013).

[242] W. D. Oliver, et al., "Mach-zehnder interferometry in a strongly driven superconducting qubit", Science **310**, 1653 (2005).

[243] M. W. Noel, W. M. Griffith, and T. F. Gallagher, “Frequency-modulated excitation of a two-level atom”, Phys. Rev. A **58**, 2265–2273 (1998).

[244] V. N. Ostrovsky, and H. Nakamura, “Exact analytical solution of the n-level landau-zener type bow-tie model”, J. Phys. A: Math. Gen. **30**, 6939–6950 (1997).

[245] Y. N. Demkov, and V. N. Ostrovsky, “The exact solution of the multistate landau-zener type model: the generalized bow-tie model”, J. Phys. B: At. Mol. Opt. Phys. **34**, 2419–2435 (2001).

[246] V. Y. Chernyak, N. A. Sinitsyn, and C. Sun, “A large class of solvable multistate landau–zener models and quantum integrability”, Journal of Physics A: Mathematical and Theoretical **51**, 245201 (2018).

[247] R. M. W. van Bijnen, S. Smit, K. A. H. van Leeuwen, E. J. D. Vredenbregt, and S. J. J. M. F. Kokkelmans, “Adiabatic formation of rydberg crystals with chirped laser pulses”, J. Phys. B: At. Mol. Opt. Phys. **44**, 184008 (2011).

[248] P. Schauß, et al., “Crystallization in ising quantum magnets”, Science **347**, 1455 (2015).

[249] H. Bernien, et al., “Probing many-body dynamics on a 51-atom quantum simulator”, Nature **551**, 579–584 (2017).

[250] J.-L. Wu, J. Song, and S.-L. Su, “Resonant-interaction-induced rydberg antiblockade and its applications”, Phys. Lett. A, 126039 (2019).

[251] M. Sillanpää, T. Lehtinen, A. Paila, Y. Makhlin, and P. Hakonen, “Continuous-time monitoring of landau-zener interference in a cooper-pair box”, Phys. Rev. Lett. **96**, 187002 (2006).

[252] Y. Kayanuma, and K. Saito, “Coherent destruction of tunneling, dynamic localization, and the landau-zener formula”, Phys. Rev. A **77**, 010101 (2008).

[253] C. M. Wilson, et al., “Coherence times of dressed states of a superconducting qubit under extreme driving”, Phys. Rev. Lett. **98**, 257003 (2007).

[254] A. Izmalkov, et al., “Consistency of ground state and spectroscopic measurements on flux qubits”, Phys. Rev. Lett. **101**, 017003 (2008).

[255] J. R. Petta, H. Lu, and A. C. Gossard, “A coherent beam splitter for electronic spin states”, Science **327**, 669–672 (2010).

[256] T. Ota, K. Hitachi, and K. Muraki, “Landau-zener-stückelberg interference in coherent charge oscillations of a one-electron double quantum dot”, Sci. Rep. **8**, 5491 (2018).

[257] J. Stehlik, et al., “Landau-zener-stückelberg interferometry of a single electron charge qubit”, Phys. Rev. B **86**, 121303 (2012).

[258] F. Forster, et al., “Characterization of qubit dephasing by landau-zener-stückelberg-majorana interferometry”, Phys. Rev. Lett. **112**, 116803 (2014).

[259] E. Dupont-Ferrier, et al., “Coherent coupling of two dopants in a silicon nanowire probed by landau-zener-stückelberg interferometry”, Phys. Rev. Lett. **110**, 136802 (2013).

[260] H. Liu, M. Dai, and L. F. Wei, “Simulating the landau-zener transitions and landau-zener-stückelberg interferometers with compacted optical waveguides: an invariant method”, Phys. Rev. A **99**, 013820 (2019).

[261] S. H. Autler, and C. H. Townes, “Stark effect in rapidly varying fields”, Phys. Rev. **100**, 703–722 (1955).

[262] T. F. Gallagher, and P. Pillet, *Dipole–dipole interactions of rydberg atoms*, Vol. 56 (Academic Press, 2008), pp. 161–218.

[263] I. S. Averbukh, and N. Perel’man, “Quasienergy and optical spectra of a two-level system in a low-frequency field of arbitrary strength”, Sov. Phys. JETP **61**, 665 (1985).

[264] B. Damski, “The simplest quantum model supporting the kibble-zurek mechanism of topological defect production: landau-zener transitions from a new perspective”, Phys. Rev. Lett. **95**, 035701 (2005).

[265] M. P. Silveri, J. A. Tuorila, E. V. Thuneberg, and G. S. Paraoanu, “Quantum systems under frequency modulation”, Rep. Prog. Phys. **80**, 056002 (2017).

[266] B. Damski, and W. H. Zurek, “Adiabatic-impulse approximation for avoided level crossings: from phase-transition dynamics to landau-zener evolutions and back again”, Phys. Rev. A **73**, 063405 (2006).

[267] S. N. Shevchenko, S. Ashhab, and F. Nori, “Inverse landau-zener-stückelberg problem for qubit-resonator systems”, Phys. Rev. B **85**, 094502 (2012).

[268] C. Roychoudhuri, “Demonstrations using a fabry–perot. i. multiple-slit interference”, American Journal of Physics **43**, 1054–1056 (1975).

[269] R. Moessner, and S. L. Sondhi, “Equilibration and order in quantum floquet matter”, Nature Physics **13**, 424–428 (2017).

[270] F. K. Abdullaev, J. G. Caputo, R. A. Kraenkel, and B. A. Malomed, “Controlling collapse in bose-einstein condensates by temporal modulation of the scattering length”, Phys. Rev. A **67**, 013605 (2003).

[271] H. Saito, and M. Ueda, “Dynamically stabilized bright solitons in a two-dimensional bose-einstein condensate”, Phys. Rev. Lett. **90**, 040403 (2003).

[272] H. Saito, R. G. Hulet, and M. Ueda, “Stabilization of a bose-einstein droplet by hyperfine rabi oscillations”, Phys. Rev. A **76**, 053619 (2007).

[273] W. Zhang, B. Sun, M. S. Chapman, and L. You, "Localization of spin mixing dynamics in a spin-1 bose-einstein condensate", Phys. Rev. A **81**, 033602 (2010).

[274] T. M. Hoang, et al., "Dynamic stabilization of a quantum many-body spin system", Phys. Rev. Lett. **111**, 090403 (2013).

[275] Y. Huang, H.-N. Xiong, Y. Yang, Z.-D. Hu, and Z. Xi, "Quantum control of spin-nematic squeezing in a dipolar spin-1 condensate", Scientific Reports **7**, 43159 (2017).

[276] E. Boukobza, M. G. Moore, D. Cohen, and A. Vardi, "Nonlinear phase dynamics in a driven bosonic josephson junction", Phys. Rev. Lett. **104**, 240402 (2010).

[277] A. Lerose, J. Marino, A. Gambassi, and A. Silva, "Prethermal quantum many-body kapitza phases of periodically driven spin systems", Phys. Rev. B **100**, 104306 (2019).

[278] J.-L. Wu, et al., "Resilient quantum gates on periodically driven rydberg atoms", Phys. Rev. A **103**, 012601 (2021).

[279] X. Shi, "Quantum logic and entanglement by neutral rydberg atoms: methods and fidelity", Quantum Science and Technology (2021).

[280] O. Dutta, et al., "Non-standard hubbard models in optical lattices: a review", Reports on Progress in Physics **78**, 066001 (2015).

[281] M. Holthaus, "Floquet engineering with quasienergy bands of periodically driven optical lattices", Journal of Physics B: Atomic, Molecular and Optical Physics **49**, 013001 (2015).

[282] C. Creffield, "Location of crossings in the floquet spectrum of a driven two-level system", Phys. Rev. B **67**, 165301 (2003).

[283] C. E. Creffield, and G. Platero, "Ac-driven localization in a two-electron quantum dot molecule", Phys. Rev. B **65**, 113304 (2002).

[284] J.-L. Wu, J. Song, and S.-L. Su, "Resonant-interaction-induced rydberg antiblockade and its applications", Physics Letters A **384**, 126039 (2020).

[285] S. A. Miller, D. A. Anderson, and G. Raithel, "Radio-frequency-modulated rydberg states in a vapor cell", New Journal of Physics **18**, 053017 (2016).

[286] M. G. Bason, et al., "Enhanced electric field sensitivity of rf-dressed rydberg dark states", New Journal of Physics **12**, 065015 (2010).

[287] A. Tauschinsky, C. S. E. van Ditzhuijzen, L. D. Noordam, and H. B. v. L. van den Heuvell, "Radio-frequency-driven dipole-dipole interactions in spatially separated volumes", Phys. Rev. A **78**, 063409 (2008).

[288] Y. Jiao, et al., “Spectroscopy of cesium rydberg atoms in strong radio-frequency fields”, Phys. Rev. A **94**, 023832 (2016).

[289] L. W. Clark, et al., “Interacting floquet polaritons”, Nature **571**, 532–536 (2019).

[290] T. L. Curtright, and T. S. V. Kortryk, “On rotations as spin matrix polynomials”, Journal of Physics A: Mathematical and Theoretical **48**, 025202 (2014).